

Quasi-static and Dynamic Constitutive Behavior of Precipitate Strengthened Al and Mg
Alloys: An Experimental and Crystal Plasticity Modeling Investigation

A Dissertation

Presented to
the faculty of the School of Engineering and Applied Science
University of Virginia

in partial fulfillment
of the requirements for the degree

Doctor of Philosophy

by

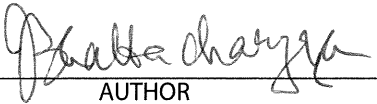
Jishnu J. Bhattacharyya

August

2016

APPROVAL SHEET

The dissertation
is submitted in partial fulfillment of the requirements
for the degree of
Doctor of Philosophy


AUTHOR

The dissertation has been read and approved by the examining committee:

Sean R Agnew

Advisor

Haydn .N.G Wadley

Ed Starke

Haitham El-Kadiri

Baoxing Xu

Accepted for the School of Engineering and Applied Science:



Craig H. Benson, Dean, School of Engineering and Applied Science

August
2016

Abstract

A present challenge in material science lies in applying the knowledge of single crystal level deformation behavior to predict the polycrystalline response. Mean field polycrystal plasticity models such as Elasto-Plastic Self-Consistent (EPSC) and Visco-Plastic Self-Consistent (VPSC) models provide computationally efficient tools to link the single crystal response to the polycrystal aggregate.

Many commercial alloys are precipitation hardenable, and the introduction of second phase particles in the matrix leads to an increase in strength and changes the work hardening behavior. Besides affecting the uniaxial flow behavior, the precipitates also alter the anisotropy of the material. The flow response and anisotropy of two commercial precipitation-hardenable alloys were measured experimentally, as well as modeled and predicted using the crystal plasticity approach.

In the first part of the dissertation, EPSC modeling was employed to describe the flow behavior, anisotropy and texture evolution of Mg alloy WE43 in the T5 (hot worked and artificially peak aged) temper, which has recently been proposed as a potential lightweight metallic armor. The independent contribution of texture, grain size and various strengthening mechanisms were determined and their impact on individual slip modes was quantified. Additionally, the strain rate sensitivities of each individual mode were determined. The results show that deformation twinning and basal slip can be treated as rate insensitive at least up to the strain rate regime investigated here. The modeling efforts led to the development of a set of parameters which were then validated using data obtained from T3 and T6 tempered samples which possessed microstructures which were far from that of the material used to develop the model. Furthermore, the aging response and the fracture behavior of this alloy was explored and

it was established that the T5 temper has the optimum combination of strength and ductility. The results confirm the notion that the poor ageing hardening characteristics of WE43, as compared to Al alloys, is due to a low number density/volume fraction of the strengthening phases.

The second part of the dissertation focuses on modeling the homogenous deformation response of Al-7085 alloy, a new high strength precipitation hardenable alloy which is used for aerospace applications and has also been considered as a lightweight metallic armor. First, the texture evolution and large strain behavior was measured and then modeled using the VPSC code, which permitted the role of latent hardening and grain shape effects to be explored. These initial experimental modeling results highlighted the potential importance of ‘*backstresses*’ generated by non-shearable precipitates. To account for this, a micromechanical model of kinematic hardening was implemented within the EPSC framework. This modified EPSC model was then used to predict the flow stress and strain anisotropy of this alloy in various tempers. The results demonstrate that incorporation of precipitate-induced backstresses do result in strength and strain anisotropy trends which qualitatively match the trends observed experimentally. However, to quantitatively predict all of the generalized Bauschinger (or backstress) effects, it is suggested that a dislocation-density based intragranular approach must also be taken into consideration.

Keywords: Self-consistent modeling, precipitation hardenable alloys, high strain rate, anisotropy, backstress

Table of Contents

1	Introduction	1
1.1	Motivation: developing the microstructure-mechanical property relationship	1
1.2	Constitutive modeling of thermally activated deformation.....	3
1.3	Polycrystal plasticity modeling.....	6
1.4	Plastic anisotropy	8
1.5	Choice of alloys for the research	9
1.6	Mg alloys	12
1.7	Al alloys	15
1.8	Thesis organization	17
1.9	References	18
2	Demonstration of alloying, thermal activation, and latent hardening effects on quasi-static and dynamic polycrystal plasticity of Mg alloy, WE43-T5, plate.....	22
2.1	Abstract	22
2.2	Introduction	23
2.3	Experimental methods.....	26
2.3.1	Materials, texture and microstructure	26
2.3.2	Mechanical testing	28
2.4	Modeling approach	29
2.4.1	The EPSC model.....	30
2.4.2	Grain level constitutive response.....	30
2.4.3	Twinning model.....	31
2.4.4	Latent hardening	32
2.5	Results	35
2.5.1	Characterization of as received WE43-T5 plate.....	35
2.5.2	Modeling the quasistatic response	38
2.5.3	Modeling the high strain rate response	49
2.6	Analysis and Discussion.....	56
2.6.1	Rate sensitivity of individual deformation modes	56
2.6.2	Plastic anisotropy and tension-compression strength asymmetry	61
2.6.3	Strengthening mechanisms.....	62
2.6.4	Influence of strain rate on the strain hardening rate	71
2.6.5	In-plane compression vs. ND tension – role of twin nucleation	74
2.7	Summary and conclusions.....	75
2.8	Acknowledgements.....	77
2.9	Appendix 1	77
2.10	Appendix 2	80
2.11	References	81
3	Deformation and fracture behavior of magnesium alloy WE43 after various aging heat treatments.....	86
3.1	Abstract	86
3.2	Introduction	87
3.3	Experimental.....	88

3.3.1	Heat treatment.....	88
3.3.2	Microhardness	89
3.4	Results	90
3.4.1	Texture and microstructure after solutionizing heat treatment.....	90
3.4.2	Temperature dependence of aging response	91
3.4.3	Effect of pre-deformation on aging response	93
3.4.4	Effect of two-step aging	93
3.4.5	Flow behavior after aging	95
3.4.6	Fracture behavior after aging.....	97
3.5	Discussion.....	102
3.5.1	Effect on flow behavior.....	103
3.5.2	Effect on ductility	107
3.6	Conclusions	108
3.7	Acknowledgements.....	109
3.8	References	110
4	Measuring and modeling the anisotropic, high strain rate deformation of Al alloy, 7085, plate in T711 temper.....	113
4.1	Abstract	113
4.2	Introduction	114
4.2.1	Background.....	114
4.2.2	Dynamic deformation of Al alloys	115
4.2.3	Role of anisotropic grain shape	116
4.3	Experimental methods.....	118
4.3.1	Materials, texture and microstructure	118
4.3.2	Mechanical testing	123
4.4	Modeling approach	125
4.4.1	The VPSC model	125
4.4.2	Simulation methodology	128
4.5	Results	130
4.5.1	Compressive flow behavior.....	130
4.5.2	Modeling the quasistatic compressive response	131
4.5.3	Modeling the dynamic compressive response	135
4.5.4	Failure and shear banding	142
4.6	Discussion.....	145
4.6.1	Strain rate sensitivity of Al-7085-T711	145
4.6.2	Flow behavior and strength anisotropy	146
4.6.3	Plastic strain anisotropy and texture evolution.....	148
4.7	Summary and conclusions.....	151
4.8	Acknowledgements.....	153
4.9	References	154
5	Effect of precipitates on anisotropy: Application to AA7085 at various tempers – Part 1: Experiments	158
5.1	Abstract	158
5.2	Introduction	159
5.2.1	The Bauschinger effect	159

5.2.2	Effect on plastic anisotropy	162
5.3	Experimental methods.....	163
5.3.1	Materials, texture and microstructure	163
5.3.2	Mechanical testing	165
5.4	Results	168
5.4.1	Compressive flow behavior	169
5.4.2	Plastic strain anisotropy (r-value)	174
5.4.3	Bauschinger tests	178
5.5	Discussion.....	183
5.5.1	The strength and strain anisotropy	183
5.5.2	Bauschinger data.....	185
5.6	Conclusion.....	187
5.7	Acknowledgements.....	188
5.8	References	188
6	Effect of precipitates on anisotropy: Application to AA7085 at various tempers – Part 2: Modeling.....	191
6.1	Abstract	191
6.2	Introduction	191
6.3	The EPSC model.....	194
6.3.1	Grain level constitutive behavior	195
6.3.2	Self-consistent formulation	197
6.4	Grain with elastic particles	199
6.4.1	The heterogeneous grain	200
6.4.2	Yield criteria for the heterogeneous grain	201
6.4.3	Constitutive relation of the equivalent grain	204
6.5	Modifications.....	206
6.5.1	Eliminating the grain compliance	207
6.5.2	Incorporating relaxation effects	208
6.6	Simulation methodology	210
6.7	Results	212
6.7.1	Modeling Bauschinger effect	212
6.7.2	Modeling W51	214
6.7.3	Modeling T721	218
6.8	Discussion.....	221
6.8.1	Bauschinger effect	221
6.8.2	Role of precipitates on anisotropy	222
6.9	Conclusions	223
6.10	Acknowledgements.....	224
6.11	References	225
7	Conclusions and future work.....	229
7.1	Overall contribution	229
7.2	Future work	233
8	Appendix A.....	236
8.1	Experimental - Split Hopkinson Pressure Bar	236
8.2	Calibration	237
8.3	Constitutive response	241

8.4	SHPB data analysis - Assumptions.....	244
8.5	References	247

List of Figures

Figure 1.1: Experimental stress-strain curves for WE43-T5 plate and AM30 extrusion under quasistatic and dynamic compression (Agnew et al., 2014).	14
Figure 1.2: Experimental stress-strain curves for AZ31-H24 under compression from Tucker et al. (2009).	15
Figure 2.1: 1010, 0002 and 1011 pole figures obtained by discretizing the experimental texture into 16000 grains (a) for plate # 9849 and (b) plate # 6457.	35
Figure 2.2: ND-IPF map from plate # 9849, showing grain structure of the as-received WE43-T5 plate.	36
Figure 2.3: TEM characterization of precipitate microstructure of WE43-T5 including (a) bright-field TEM, (b) high angle annular dark field (HAADF) STEM, and (c-e) selected area electron diffraction patterns along 0001, 1120 and 1010 zone axes, respectively.	38
Figure 2.4: Flow curves and variation of r value with strain : (a) and (b) for RD-t, (c) and (d) for RD-c and (e) and (f) for ND-c at QSR with “same” LH parameters (i.e. all coefficients equal to 1) and LH parameters given in Table 2-1.	40
Figure 2.5: Experimental and simulated results for TD tension tested at QSR (a) flow curves, (b) relative activities of deformation modes, (c) and (d) texture evolution after 14% strain.	43
Figure 2.6: EBSD maps from a RD tension sample deformed at QSR (a) Band contrast	43
Figure 2.7: Experimental and simulated results for TD compression tested at QSR (a) flow curves, (b) relative activities of deformation modes, (c) experimental texture measured using XRD, (d) simulated texture evolution and (e) ND-IPF map showing the grains which have the twin orientation have reoriented completely.	45
Figure 2.8: Experimental and simulated twin volume fraction as a function of strain for RD compression, TD compression and ND tension for both quasistatic and dynamic strain rate. The experimental data points are based on $\theta = 33^\circ$, while the error bars represent the lower and upper bounds, obtained based on $\theta = 30^\circ$ and $\theta = 40^\circ$ respectively.	45
Figure 2.9: Experimental and simulated results for ND compression tested at QSR (a) relative activities of deformation modes, (b) and (c) texture evolution and (d) band contrast map highlighting various twin boundaries, same color coding as Figure 2-6.	47
Figure 2.10: Experimental and simulated results for ND tension tested at QSR (a) flow curves (b) relative activities of deformation modes, (c) and (d) texture evolution, and (e) ND-IPF map showing most grains have reoriented by twinning while a few thin lamellae of a single variant is present within the grains.	48
Figure 2.11: Experimental and simulated flow curves for samples tested at HSR (a) for RD tension (b) TD tension (c) relative activities plot, (d) and (e) texture evolution and (f) ND-IPF map revealing dislocation substructures for the TD case.	50
Figure 2.12: Experimental and simulated result for ND compression tested at HSR (a) flow curves (b) and (c) texture evolution and (d) band contrast map showing contraction and double twins are rare even at dynamic rates (same color coding as Figure 2-6).	53
Figure 2.13: Experimental and simulated flow curves for samples tested at HSR (a) RD compression (b) TD compression and (c) and (d) shows experimental and simulated pole figures for TD compression.	53
Figure 2.14: Experimental and simulated results for ND tension at HSR (a) flow curves (b) relative activity plot (c) and (d) experimental and simulated pole figures respectively and (e) ND-IPF showing multiple variants of twins present as twin intersecting lamellae.	54

Figure 2.15: (a) A fractograph of RD tension sample tested at QSR showing presence of dimples associated with particles as well as grain/twin boundary cracks (b) a higher magnification micrograph from the region showing presence of grain boundary precipitates and a crack associated with them.	72
Figure 2.16: Experimental and simulated flow curves for TD tension and compression using WE43T5 plate # 9849 texture (a) with AZ31B parameters from Wang et al.,(2012) and (b) with parameters listed in Table 2.10.	81
Figure 3.1: Optical micrographs showing the grain size for (a) T5 material and (b) T3 material.	90
Figure 3.2: Crystallographic texture shown as recalculated $\{1010\}$ and $\{0002\}$ pole figures averaged from data collected at various depths within the 1.5" thick plate of WE43B in T5 (top) and T3 (bottom) condition. The T5 sample shows a stronger texture than T3.	91
Figure 3.3: Variation of microhardness with aging duration at 250°C with the starting material as T3 and T5. The as-received T5 and T7 are also shown.	92
Figure 3.4: Age hardening plots showing the variation of microhardness as a function of aging time at 210 °C for solutionized + aged and F-temper + aged. The plot for solutionized + aged at 250 °C is also shown for comparison.	92
Figure 3.5: Variation of microhardness with aging duration for T8 treatment, where the specimens were stretched along RD. The T6 age-hardening curves are shown for comparison. For both cases, aging was carried out at 210 °C.	94
Figure 3.6: Variation of microhardness with aging duration for T8 treatment, where the specimens were compressed along ND (with RD tension T8 shown for comparison).	94
Figure 3.7: Variation of microhardness as a function of aging duration for the 2-step aging treatment where pre-aging was carried out at 140 °C for 4h, followed by aging at 210 °C. The T6 curve and T5 hardness value is shown for comparison.	95
Figure 3.8: Stress-strain curves for various samples along the ND and TD direction. These curves show that the T5 treated samples show both a higher tensile strength and ductility than T6.	96
Figure 3.9: Backscattered fractographs for a T5 specimen tested in tension along ND, showing (a) clusters of dispersoids and (b) dimples and grain boundary precipitates.	98
Figure 3.10: Backscattered fractographs for a T5 specimen tested in tension along RD, showing dimples and grain boundary precipitates, but absence of dispersoid clusters.	98
Figure 3.11: Backscattered fractographs for a T3 specimen tested in tension along TD, showing (a) smooth cracks associated with twins/grain boundaries (b) ductile dimples associated with Y rich cuboids.	99
Figure 3.12: Backscattered fractographs for an under-aged (aging at 210°C for 8h) specimen tested in tension along ND, showing (a) smooth features indicative of less ductile damage and cracks associated with twins/grain boundaries. (b) the clusters of dispersoids still present after solutionizing treatment.	100
Figure 3.13: Backscattered fractographs for an under-aged (aging at 210°C for 8h) specimen tested in tension along TD, showing (a) smooth features indicative of less ductile damage and cracks associated with twins/grain boundaries. (b) some ductile dimples in between regions of smooth faceted regions.	100
Figure 3.14: Backscattered fractographs for peak-aged (aging at 210 °C for 64h) specimen tested in tension along TD, showing (a) extensive intergranular failure with twin related cracks within the grains (b) presence of grain boundary precipitates.	101

Figure 3.15: Backscattered fractographs for peak-aged (aging at 210 °C for 64h) specimen tested in tension along ND, showing (a) some ductile dimples associated with Y-rich cuboid dispersoids (b) dispersoid clusters (c) and (d) twin/grain boundary cracks.	102
Figure 3.16: Experimental and simulated flow curves for TD tension for WE43-T3, and.....	106
Figure 3.17: Experimental and simulated flow curves for ND tension for WE43-T6 temper and only experimental flow curve for ND tension for an under-aged specimen. The simulations were carried out using Voce parameters given in Tables 3.4 and 3.6.....	106
Figure 4.1: Texture gradient of AA7085-T711 plate –Recalculated experimental{111}, {200} and {220} pole figures at various depths from the surface (a) 0 mm(surface) (b) 5mm (1/8 th plane) (c) 9 mm (1/4 th plane) (d) 15 mm (3/8 th plane) and (e) 20 mm (midplane).	120
Figure 4.2: Texture gradient of AA7085-T711 plate - $\phi_2 = 45^\circ$, 65° , and 90° sections (after imposing orthotropic symmetry) at: a) surface b) 1/4 th plane c) midplane and d) variation of β -fibre intensity in these sections.....	121
Figure 4.3: EBSD ND-IPF maps of the as-received AA7085-T711 plate obtained at: a) near the surface, showing mostly {001} oriented grains, and b) near the midplane, showing a predominance of {011} oriented grains c) relative frequency distribution of aspect ratio of the grains in the two above mentioned cases.....	123
Figure 4.4: Discretized 2000 grains {111}, {200} and {220} pole figures for (a) average of surface, 1/8 th and 1/4 th plane (b) average of 3/8 th and midplane.....	130
Figure 4.5: Experimental true stress-strain curves for RD, ND and TD compression at a) 0.001 s^{-1} and b) 1000 s^{-1}	131
Figure 4.6: Experimental and simulated data for compression at 0.001 s^{-1} along TD a) flow curves and b) r-values. Isotropic grain shape is denoted by '111' and '531' represents grain shape RD:TD:ND = 5:3:1.....	132
Figure 4.7: Experimental and simulated data for compression at 0.001 s^{-1} along RD a) flow curves and b) r-values. Isotropic grain shape is denoted by '111' and '531' represents grain shape RD:TD:ND = 5:3:1.....	133
Figure 4.8: Experimental and simulated data for compression at 0.001 s^{-1} along ND a) flow curves and b) r-values. Isotropic grain shape is denoted by '111' and '531' represents grain shape RD:TD:ND = 5:3:1.....	133
Figure 4.9: {111}, {200} and {220} pole figures for a specimen tested in ND compression at 0.001 s^{-1} up to 26% strain a) experimental recalculated pole figures b) simulated with isotropic grain shape c) simulated with the actual average grain shape (5:3:1).	134
Figure 4.10: Experimental and simulated data for compression at 1000 s^{-1} along RD a) flow curves and b) r-values. 'mid' and 'surf' indicate the average texture used. The grain shape is given in parentheses.	136
Figure 4.11: Texture evolution for RD compression after 43% strain at 1000 s^{-1} a) experimental recalculated pole figures b) simulated texture with isotropic grain shape and c) simulated texture with the actual average grain shape (5:3:1).	136
Figure 4.12: Experimental and simulated data for compression at 1000 s^{-1} along TD a) flow curves and b) r-values.	138
Figure 4.13: Texture evolution for TD compression after 40% strain at 1000 s^{-1} a) experimental recalculated pole figures b) simulated texture with isotropic grain shape and c) simulated texture with grain shape (5:3:1).....	138
Figure 4.14: Experimental and simulated data for compression along ND from midplane a) flow curves at 1000 s^{-1} and b) r-values at 1000 s^{-1} and 0.001 s^{-1}	140

Figure 4.15: Texture evolution for a midplane ND compression specimen after 9% strain at 1000 s^{-1} a) experimental recalculated pole figures b) simulated texture with isotropic grain shape and c) simulated texture with grain shape (5:3:1).....	140
Figure 4.16: Experimental and simulated data for compression along ND from near surface a) flow curves at 1000 s^{-1} and b) r-values at 1000 s^{-1} and 0.001 s^{-1}	141
Figure 4.17: Texture evolution for a ND compression specimen extracted from near surface, after 32% strain at 1000 s^{-1} a) experimental recalculated pole figures b) simulated texture with isotropic grain shape and d) simulated texture with grain shape (3:2:1).	141
Figure 4.18: An EBSD RD-IPF map from a specimen compressed along RD up to 40 % strain at 1000 s^{-1} . The black (non-indexed) region shows a shear band on the TD plane, at an angle $\sim 45^{\circ}$ with the loading axis. Another shear band at angle $\sim 60^{\circ}$ with the loading axis is also present, identified by poorly indexed diffraction pattern.	144
Figure 4.19: (a)ND-IPF map and (b) band contrast map of a specimen compressed to 26% strain at 0.001 s^{-1} showing diffuse shear band formation on the TD plane, oriented $\sim 42^{\circ}$ to the horizontal (RD). RD is to the right, ND up.	144
Figure 4.20: Simulated r-values of AA7085-T711: (a) in-plane variation for different strain levels and (b) evolution of in-plane r-values with strain.....	149
Figure 4.21: Plane stress yield surface at representative strain levels 0.04 and 0.12 for clarity. Arrows indicate the normal to the yield surface for RD and TD compression. The plane strain condition is also indicated along with the ND compression case, approximated as equibiaxial tension.	150
Figure 5.1: Textures measured at the plate mid-plane in the a) as-quenched and stretched temper (W51) and b) the over-aged condition known as T721.....	165
Figure 5.2: Stress strain curve obtained from Bauschinger test of a T711 specimen, where the compressive data during the reload has been plotted in the first quadrant.	168
Figure 5.3: Experimental flow curves for T3 temper a) at 0.001 s^{-1} and b) at $\sim 1000 s^{-1}$	170
Figure 5.4: Experimental flow curves for W51 temper at a) 0.001 s^{-1} and b) $\sim 1000 s^{-1}$	171
Figure 5.5: Experimental flow curves for T6 temper at 0.001 s^{-1}	172
Figure 5.6: Experimental flow curves for T711 temper at a) 0.001 s^{-1} and b) $\sim 1000 s^{-1}$	173
Figure 5.7: Experimental flow curves for T721 temper at a) 0.001 s^{-1} and b) $\sim 1000 s^{-1}$	174
Figure 5.8: The variation of r-value as a function of plastic strain, for T3, W51, T6, T711 and T721 temper, at both quasistatic and dynamic strain rates a) along RD b) along TD	176
Figure 5.9: The variation of r-value as a function of plastic strain, for T3, W51, T6, T711 and T721 temper, at both quasistatic and dynamic strain rates a) along ND b) along 45	177
Figure 5.10: Tension compression flow curves for T3 material after different prestrains.....	179
Figure 5.11: Tension compression flow curves for T711 material after different prestrains.....	180
Figure 5.12: The variation of backstress as a function of plastic prestrain and offset used to obtain compressive yield stress. a) computed according to Eq. 5. 3 and b) based on permanent softening	182
Figure 5.13: Evolution of Bauschinger strain as a function of plastic prestrain.....	182
Figure 6.1: Experimental and simulated tension-compression curves for the T3 material, after 1.5% and 3.5% prestrains, showing the effect of β parameter.	214
Figure 6.2: Experimental tension-compression curves for the T3 material after different prestrains, along with simulations, carried out using $\beta = 0.5$	214
Figure 6.3: Experimental and simulated flow curves for W51 a) (fitted) along TD b) predicted along RD.....	216

Figure 6.4: Experimental and predicted flow curves for W51 a) along ND and b) along 45.	216
Figure 6.5: Experimental and predicted r-values for W51 a) along RD and b) along ND	217
Figure 6.6: Experimental and predicted r-values for W51 a) along 45 and b) along TD	217
Figure 6.7: Experimental and simulation (fitted) flow curves for T721 along TD.....	219
Figure 6.8: Experimental and predicted flow curves for T721 along RD.....	219
Figure 6.9: Experimental and predicted flow curves for T721 along ND.....	220
Figure 6.10: Experimental and predicted flow curves for T721 along 45 direction.	220
Figure 6.11: Experimental and predicted r-values for T721 a) along ND and b) along RD.	221
Figure 6.12: Experimental and predicted r-values for T721 a) along 45 and b) along RD.....	221
Figure 8.1: A schematic of the compression Split Hopkinson Pressure Bar (G.T. Gray, 2000).	236
Figure 8.2: A ‘bars apart’ test raw data showing the signal measured by strain gages attached to the incident and transmitted bar. The compressive incident wave is chosen as positive.....	240
Figure 8.3: A ‘bars together’ test raw data showing the signal measured by strain gages attached to the incident and transmitted bar. The compressive incident wave is chosen as positive.	240
Figure 8.4: A schematic of the tension Split Hopkinson Pressure Bar (Isakov et al., 2014). The arrow indicates the direction in which the striker tube moves.	244
Figure 8.5: The variation of strain rate with strain for tests with and without a pulse shaper, showing constant strain rate as well as high frequency oscillations are eliminated when a pulse shaper is used.	246
Figure 8.6: Dynamic test results for AA7085-T711 along TD obtained at UVa, MSU and ARL (a) Flow curves (b) strain rate as a function of strain.	246

List of Tables

Table 2.1: List of dislocation-dislocation interactions and the corresponding FZ coefficients as obtained from Bertin et al., (2014) along with the “mode on mode” interaction coefficients obtained by weighted average of FZ value by the number of slip systems.	34
Table 2.2: Voce hardening parameters for simulating experimental data at 0.001/s (units in MPa).	41
Table 2.3: The r-values obtained experimentally and from the EPSC model along with the strain at which the measurements were conducted.	42
Table 2.4: Voce hardening parameters for simulating experimental data at 1000 /s (units in MPa).	49
Table 2.5: A comparison of CRSS for single crystal pure Mg, for AZ31 alloy and for WE43-T5 used in this study. The single crystal CRSS were obtained from the following references: a.(Roberts, 1960), b. (Yoshinaga and Horiuchi, 1964), c. (Akhtar and Teghtsoonian, 1969) d. (Flynn et al., 1961), e. (Obara et al., 1973), f. (Stohr and Poirier, 1972), g. (Bettles and Barnett, 2012)	62
Table 2.6: The contribution of grain refinement on individual deformation modes obtained using Hall Petch coefficient. The first values of total strength are based on HP coefficient of Wang and Choo (2014) and the second is based on Raeisia et al. (2010), respectively.	65
Table 2.7: Contributions to the CRSS of individual modes from various strengthening mechanisms: lattice resistance, solutes, grain size refinement, forest dislocations and precipitates. The total strength based on the single crystal (∞), the EPSC CRSS values for T3 material and EPSC CRSS from Stanford et al., (2014) are highlighted in grey (all values in MPa). When two values appear separated by commas, the first is based on HP coefficient of Wang and Choo (2014) and the second is based on Raeisia et al. (2010).	70
Table 2.8: Thermal properties and densities of some commercial structural alloys along with WE43-T5 alloy.	73
Table 2.9: Temperature rise according to equation 2-21 for different loading conditions for samples tested at dynamic rates.	74
Table 2.10: Comparison of VPSC CRSS for AZ31B (after Wang et.al) and for WE43-T5 employed in this study.	81
Table 3.1: Yield anisotropy of WE43 for different aging conditions	96
Table 3.2: Voce hardening parameters for T5 temper obtained from Bhattacharyya et al., (2016).	105
Table 3.3: The effect of grain size on individual deformation modes obtained using Hall Petch coefficients Wang and Choo (2014) and Raeisia et al. (2010), respectively.	105
Table 3.4: CRSS values for T3 temper, obtained by subtracting the contribution of precipitates, forest dislocations, and grain size of T5 and adding T3 grain size contribution to the CRSS values given in Table 3.2.....	105
Table 3.5: CRSS values for T6 temper, obtained by subtracting the contribution of grain size of T5 and adding T3 contribution to the CRSS values given in Table 3.2.	105
Table 4.1: Volume fraction of texture components calculated with 20° radius (triclinic symmetry).....	121
Table 4.2: Voce hardening parameters for simulating flow curves at 0.001 s^{-1} and 1000 s^{-1}	134

Table 5.1: Values of strain rate sensitivity m calculated from RD flow curves, with stress values at 2% offset.....	170
Table 5.2: Various Bauschinger parameters computed for T3 and T711 material.	181
Table 6.1: Voce hardening parameters for $\{111\}\langle 110 \rangle$ slip mode for T3, W51 and T721 simulations.....	215

1 Introduction

1.1 Motivation: developing the microstructure-mechanical property relationship

The knowledge of mechanical properties of structural materials is of utmost importance for nearly every industry including aerospace, automotive, biomedical, construction, energy, manufacturing, military, etc. Starting from the electron density around the constituent atoms, at the subatomic level, to the macroscale residual stresses, at the component level, various factors determine the mechanical responses of a material. In a broad sense, every length scale, spanning over 12 orders of magnitude, 10^{-12} to 10^0 m, can be defined as the *microstructure*. Most structural materials of interest are polycrystalline; composed of individual crystals (grains) of different orientations. Thus, it is the crystal structure, which determines the maximum level of anisotropy which the physical properties such as elastic stiffness, coefficient of thermal expansion etc. may exhibit (governed by Neumann's principle (Nye, 1985)). On a polycrystal level, the primary cause of anisotropy is crystallographic texture, which can be defined as the statistical distribution of certain preferred orientations of grains with respect to the sample reference frame. The development of texture is intricately related to the deformation and thermal history of the material. If the single crystal properties are anisotropic, then a non-random distribution of these anisotropic crystals is expected to be anisotropic.

At a fixed chemical composition, it is the lattice defects, particularly the dislocations, their collective behavior, as well as interaction with other defects that generally dictate the mechanical behavior of materials. Thus, the most relevant length scale ranges from an individual dislocation segment (nanometers) and spacing up to the size of individual grains (microns to millimeters), which henceforth, shall conveniently be referred to as the *microstructure*. One reason that makes

this length scale attractive to scientists/engineers is because this *microstructure* can be tailored in a controlled manner to obtain the desired properties. Thus the main goal is to quantitatively relate the macroscopic sample level response to this microstructure.

One way to establish these connections is to perform a large number of experiments, on a trial and error basis, to fully characterize the mechanical response. This, however, is generally not viewed as most efficient and cost effective. Rather, constitutive models, which are calibrated and validated by limited number of experiments, are often preferred over the former approach. These models then can be used by engineers for materials selection and design. In the field of plasticity, a wide variety of models can generally be employed; ranging from phenomenological macroscopic models, which typically require a large number of empirical fitting parameters and generally disregard the microstructure details. While the phenomenological models are computationally inexpensive and easier to employ in large-scale finite element (FE) simulations of interest to manufacturing and design engineers, they are often specific to the problem used for calibration. As such, they generally lack good predictive capabilities outside the specific conditions used to experimentally constrain the large number of fitting parameters they require.

An alternative approach is discrete dislocation dynamics (DDD) simulation (e.g., Kubin et al., 1992; Giessen and Needleman, 1999), which computes the interactions between individual dislocation segments with all other sources of applied and internal stress fields which act upon them. The disadvantage of such fine scale modeling approaches like DDD is that it is computationally quite impossible to use such a model to predict the macroscopic responses at the macroscopic sample or component level.

The *mesoscopic* polycrystal plasticity models (described later) provide a middle ground, which uses classical homogenization theory to obtain the aggregate response from single crystal

properties without directly invoking defects dynamics. In these models, the highly complex microstructures of real materials is replaced by appropriate constitutive description at the individual grain level, and the aggregate is treated as a *homogeneous effective medium* (HEM). The transition from the microscale to macroscale is performed using suitable homogenization and localization schemes. This middle path, so to speak, is the approach employed in the present work. Concepts related to the individual dislocation are invoked from lower-level theory and simulation approaches such as DDD and up-scaled for use within the mesoscale model.

1.2 Constitutive modeling of thermally activated deformation

The interaction of dislocations with various microstructural features such as grain boundaries (Hall-Petch effect), solutes (solid solution hardening/softening), precipitates (precipitation strengthening) and other dislocations (forest hardening) control the deformation behavior of a material at the single crystal level. These interactions are thermally activated and thus have unique strain rate and temperature dependence. At a given temperature and strain rate, the flow behavior (strength and strain hardening) and strain anisotropy exhibited by a polycrystal is a net result of such interactions at the grain level and explicitly influenced by the presence of crystallographic texture. This latter aspect, crystallographic texture, is explicitly accounted for in the mesoscopic polycrystal plasticity approaches employed in this thesis work.

The strain rate dependence of flow stress is often approximated as a power law and the exponent is termed as strain rate sensitivity parameter m , defined as:

$$m = \frac{\partial \ln \sigma(\epsilon)}{\partial \ln \dot{\epsilon}} \quad (1-1)$$

calculated at a fixed plastic strain and temperature. Generally, most metals exhibit rather small values of $m \sim 0.01$, within a factor of 3, at room temperature. From an engineering perspective, a higher value of m is generally desirable, since it provides a larger resistance to strain localization.

The strain rates that can be applied using a conventional laboratory uniaxial testing machine range from about 10^{-4} to 10 s^{-1} . In order to test at strain rates that are relevant to ballistic impact applications, $\dot{\epsilon} \sim 10^3\text{-}10^4 \text{ s}^{-1}$ which is several orders of magnitude higher, a *Split Hopkinson Pressure Bar* (SHPB), also known as the *Kolsky Bar* is typically used. This apparatus was first conceived by J. Hopkinson in 1872 (Hopkinson, 1901) and was revisited by his son B. Hopkinson in 1914 when he developed the *Hopkinson Pressure Bar* (Hopkinson, 1914). However, a major shortcoming of the apparatus was that the stress-time history in the bar could not be obtained. Davies, in 1948, conducted the first dynamic axial and radial strain measurements in a Hopkinson Pressure Bar and devised a way to record the pressure-time history (Davies, 1948). He also discussed the limitations of the Hopkinson Pressure Bar. Kolsky (1949) modified the loading mechanism of the original apparatus and measured the axial and radial displacements using Davies' design. This modified apparatus came to be known as the *Split Hopkinson Pressure Bar* (SHPB), or the *Kolsky Bar*. Using this, he made the first measurements of dynamic mechanical properties of several different materials. Since then, several researchers have developed and/or modified the SHPB technique to test materials under tension (Harding et al., 1960; Lindholm and Yeakley, 1968), torsion (Baker and Yew, 1966), biaxial loading (Lindholm and Yeakley, 1967), dynamic indentation (Subhash, 2000) and even and fracture toughness (Costin et al., 1977).

A commonly used constitutive model that takes into account strain-rate and temperature dependence is the Johnson-Cook Model (Johnson and Cook, 1983). While this model can be efficiently implemented within finite element codes, they are representative of the aforementioned phenomenological approaches which require careful calibration for a specific material for them to accurately represent the strain, strain-rate and temperature dependence of

that material. The approach does not respect the fact that microstructure has a strong influence on the response.

Zerilli and Armstrong (1987) were among the first to point out that the functional form of the empirical Johnson-Cook relationship fails to account for the differences between metals of different crystal structures, particularly at high levels of plastic strain. They also noted the potential impact that mechanical twinning would have, relative to dislocation motion. Other research groups have demonstrated the utility of a physics-based description of thermally activated slip first systematized by Kocks, Argon and Ashby (Kocks et al., 1975) in their models of the flow strength of metals in the quasi-static through dynamic loading regimes. Follansbee et al. (Follansbee and Kocks, 1988) and Nemat-Nasser et al. (e.g., 2001, 1998, 1994) made notable contributions, demonstrating improved success (relative to Johnson-Cook) for modeling the temperature and rate sensitivity of fcc (e.g., Cu), bcc (e.g., Ta), hcp (e.g., Zr) and two-phase mixtures (e.g., α plus β Ti-64). While these studies have highlighted the differences in properties of these broad classes of metals and alloys, there appear to have been far fewer studies of the detailed effects of alloying and temper on the deformation behavior at high strain rates. This is the key gap in our present understanding, which this thesis work seeks to fill. In all honesty, this is a very lofty goal, but discernable progress has been made to connect detailed microstructural features (many of which are already reported in the literature) with the experimentally measured response.

The strain hardening response can also be modeled in a variety of ways; starting from a power law type relation, known as the Hollomon equation, as commonly employed in Johnson-Cook models to the physics based approach accounting for the evolution of the dislocation accumulation and recovery via the Kocks-Mecking formulation (Mecking and Kocks, 1981;

Kocks and H. Mecking, 2003; Beyerlein and Tomé, 2008). Such an approach recognizes the fact that plasticity is path dependent (i.e., plastic strain is not a state variable). Again, there is a middle-path which does not require dealing explicitly with dislocation densities, but accounts for the dislocation-based physics of the problem. The so-called Voce hardening rule can be used for this purpose:

$$\frac{d\sigma}{d\varepsilon} = \theta_0 \left(1 - \frac{\sigma}{\sigma_s}\right) \quad (1-2)$$

where the strain hardening rate is a function of stress and is controlled by two parameters, the initial hardening rate θ_0 and saturation stress σ_s . In principle, these parameters could have strain rate and temperature dependence. In this dissertation, this form of the functional dependence will be implemented at the slip-system level, in a crystal plasticity model, which allows for investigating the strain hardening behavior of individual slip modes and it will be shown that it is of utmost importance for Mg alloys where more than one slip mode is active.

1.3 Polycrystal plasticity modeling

Polycrystal plasticity models provide a convenient framework to relate the single crystal properties to the aggregate level behavior. At the grain level, the deformation is described by the crystallography of dislocation slip or twinning, which is the fundamental mechanism of plasticity. On the other hand, the polycrystalline aggregate is represented by its crystallographic texture, the statistical distribution of preferred grain orientations, which can be measured experimentally using diffraction based techniques (x-rays, neutron, and electron). In this way, real materials with different textures can be investigated. This makes the model independent of the initial material state. Furthermore, the models fully account for the 6-dimensional¹ nature of

¹ Note that only 5 dimensions are accounted for in the rigid-viscoplastic approach employed in some of the work, since crystal plasticity is known to be incompressible (deviatoric) and insensitive to hydrostatic pressure.

stress and strain space, allowing a full description of these tensorial quantities instead of relying on scalar measure of stress or strain (e.g., Von Mises equivalent stress/strain). These models also explicitly account for the anisotropic elastic and plastic properties, at both grain and aggregate level. Any constitutive description of strength and strain hardening (e.g., empirical Voce or dislocation density based Kocks-Mecking formulation), can be implemented at the grain level and thus a wide variety of microstructural complexities can be addressed using such a model. These polycrystal models mainly differ with respect to how the individual grains interact with the aggregate. For instance, the first of these kinds of model was developed by Sachs (1928) (Reuss (1930) lower-bound model for elasticity) where it was emphasized that stress equilibrium must be maintained between the grains and thus each grain has the same stress state as the aggregate. This model violates strain compatibility and would allow grain to separate or overlap, which clearly is against experimental observations. Taylor (1934) on the other hand, argued that strain compatibility is more important than stress equilibrium (Voigt (1910) upper-bound rule of mixtures model for elasticity). Thus according to this model, the strain state of each grain is the same as the macroscopically imposed strain. These two models clearly provide the lower and upper bound and in reality the stresses and strains on each grain would be within these two extrema. Eshelby (1957) employed Hooke's law, stress equilibrium and strain compatibility to obtain the stress and strain in an elastic ellipsoidal inclusion that undergoes a shape change while embedded in an infinite matrix. Based on Eshelby's solution, Kroner (1958) formulated a self-consistent model which imposed the condition that the volume average of grain level quantities (stresses, strains) should be equal to that in the aggregate level. Subsequently, Hill (1965a, 1965b) and Hutchinson (1970) refined these ideas for application within elasto-plastic and viscoplastic contexts, respectively, by incrementally linearizing the response within infinitesimal

straining steps. Although other researchers, most notably Molinari (1987), Berveiller (1978; 1989), and Nemat-Nasser (1986) employed these concepts, the development of the *Viscoplastic Self Consistent* (VPSC) code by Lebensohn and Tomé (1993) broadened the application of the modeling concept to a wide range of materials and research problems by rigorously accounting for fully anisotropic, rigid-viscoplastic grains of arbitrary ellipsoidal shape and orientation within an aggregate of arbitrary anisotropy. The VPSC approach was used throughout the earlier phases of the present research. Around the same time as the development of VPSC, Turner and Tomé (Turner and Tomé, 1994) developed the *Elastoplastic Self-Consistent* (EPSC) code, which enabled modeling of fully anisotropic, elasto-plastic grains of arbitrary ellipsoidal shape and orientation within an aggregate of arbitrary anisotropy. EPSC serves as the backbone for the later phases of the present research.

1.4 Plastic anisotropy

Fundamentally, the anisotropy of plastic properties stems from the anisotropy of the crystallographic slip. It is interesting to note that both the strength/flow stress as well as the plastic strains is anisotropic. The strength anisotropy can be quantified by taking the ratios of the yield strength/flow stress along different directions. In case of strain anisotropy, a useful parameter, commonly used in sheet metal forming industry, is the r-value, which is ratio of the width strain ε_w to the thickness strain ε_t , for a specimen tested in tension along the rolling direction (RD):

$$R = \frac{\varepsilon_w}{\varepsilon_t} \quad (1-3)$$

Plastic isotropy results in an r-value of 1, whereas r-values greater than 1 indicate resistance to thinning. This commonly used definition can be readily extended to the transverse

(TD), normal (ND) or any other oblique directions. The r -value can be directly related to the activity of the slip systems at the grain level. Thus these r -values can be used to calibrate as well as validate polycrystal plasticity models.

1.5 Choice of alloys for the research

Light metal alloys with high strength to weight ratio and adequate ballistic and blast resistant properties are potential candidates for military applications, such as armor, because of their ability to increase the fuel efficiency of vehicles. Aluminum and magnesium based alloys can serve as ballistic protection in lightly armored vehicles or can be used in composite armor systems, e.g., as a backing plate to a ceramic-based system, where the ceramic face degrades the projectile tip and the backing absorbs the kinetic energy of the projectile and traps the ceramic and projectile debris (Gonçalves et al., 2004; Ben-Dor et al., 2005).

Recently, the Army Research Laboratory (ARL) conducted blast and ballistic tests on two such lightweight alloys; a rare earth (RE) element containing magnesium alloy, WE43, and a 7000 series aluminum alloy (AA) 7085, which has recently replaced AA7050 for aerospace applications. The results demonstrated the superior ballistic properties of both alloys, as compared to their predecessors. WE43 in the T5 temper performed better than both AZ31B-H24 (another Mg alloy) and, the concurrent acceptance specification MIL-DTL-46027K, which was based on AA 5083-H131. AA7085 also showed a higher performance as compared to existing AA7039 acceptance limits and lead to a new mil specification, MILDTL-32375 (Doherty et al., 2012). AA7085 material was tested in two different tempers: T711 for enhanced ballistic protection and T721 for improved blast protection (Gallardy, 2012). Both are in the over-aged (T7) condition, though T711 is only slightly overaged and T721 is more overaged.

The present research is not intended to evaluate the ballistic performance of these alloys; the current work was motivated by such promising results. However, it is important to identify the mechanical and thermal properties that are of interest for ballistic applications. This work focuses on investigating the constitutive response of these alloys and aims to develop process-structure-property relationships which could help explain current successes and chart directions for improvements through improved process control. In what follows next, a brief introduction to the failure mechanisms and constitutive properties relevant for ballistic applications are presented.

When a projectile impacts a target, a compressive stress wave is generated and several types of interactions can occur depending on the constitutive properties and the geometry of the projectile and the target. The most commonly observed failure mechanisms for a ductile target upon projectile impact are: discing, petalling, plugging, spallation, ductile hole enlargement and fragmentation (Backman and Goldsmith, 1978). The first two mechanisms are prevalent in thin targets while fragmentation is generally observed in materials with poor ductility, where fracture initiates at early stages, before extensive plastic deformation. Increasing the **ductility** enhances the fragmentation resistance by increasing the energy absorbing capacity, which can be roughly approximated as the product of the strength and strain-to-failure.

In thicker materials, projectile-target interactions lead to a cavity formation by plastic deformation in order to accommodate the volume of the projectile. For instance, it has been shown (e.g., Bishop et al., 1945; Corbett et al., 1996) that due to the lateral constraint by the surrounding undeformed material, the pressure that the projectile has to impart to perforate through the target is about 3-4 times the yield strength of the target. Thus, another mechanical property of interest is the material **yield strength**; a material with a higher strength would

provide a larger resistance to the penetrator, all other factors remaining the same. In Mg alloys, besides the normal strengthening mechanisms of solute atoms, precipitation, and grain refinement, other additional factors, such as crystallographic texture and the resulting anisotropy, play a decisive role in determining the yield strength for a given loading condition. One objective of the present research is to determine the contribution from each of these individual mechanisms that are operative in the alloy WE43, as well as to employ various heat treatment strategies to explore the possibility of increasing the strength of the alloy.

The other commonly observed failure mechanism is plugging, which results from severe shear deformation near the projectile-target interface. This extensive plastic deformation leads to an increase in the local temperature and results in thermoplastic instability known as ‘adiabatic shear localization’ (Borvik et al., 2010; Pedersen et al., 2011). Thus, for enhancing the ballistic resistance, the general objective is to delay the onset of this shear instability.

A material’s resistance to adiabatic shear localization is determined by both its thermal and mechanical properties. In general, the plastic instability criterion can be expressed as (Clifton et al., 1984; Semiatin et al., 1984; Molinari and Clifton., 1987):

$$\frac{d\sigma}{d\varepsilon} = \left. \frac{\partial\sigma}{\partial\varepsilon} \right|_{T,\dot{\varepsilon}} + \left. \frac{\partial\sigma}{\partial\dot{\varepsilon}} \right|_{T,\varepsilon} \frac{\partial\dot{\varepsilon}}{\partial\varepsilon} + \left. \frac{\partial\sigma}{\partial T} \right|_{\varepsilon,\dot{\varepsilon}} \frac{\partial T}{\partial\varepsilon} = 0 \quad (1-4)$$

where $\frac{\partial\sigma}{\partial\varepsilon}$ is the strain hardening rate, $\frac{\partial\sigma}{\partial\dot{\varepsilon}}$ is the strain rate hardening, and $\frac{\partial\sigma}{\partial T}$ is the thermal softening rate. Since the last term is always negative, a high strain hardening as well as a positive strain rate sensitivity are required to delay the shear instability. The term $\frac{\partial T}{\partial\varepsilon}$ is dependent on the thermal properties. For instance, a high volume specific heat capacity, ρC_p (where ρ is the density and C_p is the specific heat capacity) and a high thermal conductivity are considered beneficial since the former reduces the amount of heat generated during plastic deformation and the latter enables effective dissipation of the energy (Staker, 1981; Timothy, 1985). However, for

a given metal or alloy (the choice of which is dictated by the application, cost and expediency), the thermal properties are less sensitive to microstructure, as compared to mechanical properties. Thus, improving the latter provides a pathway for optimizing the ballistic performance, since they can be tailored by suitable thermomechanical treatments. In the present research, the strain rate sensitivities as well as the strain hardening behavior of both WE43 and AA7085, in various tempers, were investigated.

When the initial compressive wave, generated during impact, reflects from the free surface at the back end of the target as a tensile wave, the target is reloaded in tension and these high stresses can result in tensile failure, leading to yet another failure mechanism, known as ‘spallation’. A recent study carried out by Hamilton et al., (2012) showed evidence of extensive spallation when WE43-T5 plates were impacted by high velocity projectiles, along the plate through-thickness direction (ND). Their study serves as motivation to further examine the fracture behavior of this alloy, especially along ND. More importantly, several heat treatment strategies were employed, in order to explore the possibility of improving the fracture resistance of this alloy. In the next two sections, a brief background on Mg and Al-based alloys is presented to set the stage for the upcoming chapters.

1.6 Mg alloys

The high anisotropy of plastic deformation in textured Mg alloys originates from its hexagonal close packed (hcp) crystal structure with multiple slip and twinning modes having a wide range of critical resolved shear stress (CRSS) values. This creates unique challenges in the understanding and prediction of deformation behavior. Most notably, loading conditions which favor extension twinning (on the $\{10\bar{1}2\}$ planes), lead to unique deformation and fracture behavior as compared to slip dominated deformation. For plates/sheets with basal texture (c-axis

|| plate thickness direction (ND)), the strain is accommodated by $\langle c+a \rangle$ pyramidal slip or contraction twinning, which result in parabolic hardening behavior under ND compression. However, during in-plane compression, soft $\{10\bar{1}2\}$ extension twinning dominates the flow at lower strains, leading to a yield “plateau” at low plastic strains followed by rapid strain hardening. Due to this fact, a tension–compression yield strength and hardening asymmetry is observed in conventional wrought Mg alloys.

The addition of rare earth (RE) elements has been noted to have a positive effect of weakening the texture and, thus, reducing the strong anisotropy (Ball and Prangnell, 1994). The present research attempts to quantify to what extent such randomization of texture is responsible for the relatively low level of anisotropy observed in WE43-T5. Moreover, RE containing alloys develop plate shaped precipitates on prismatic planes, which have been shown to provide good age hardening response (Nie and Muddle, 2000; Nie et al., 2001; Robson et al., 2011). However, the effect of precipitation hardening is different for each deformation mode. Although it is not examined in detail within the present research, the possibility of short range ordering of solute is of interest, especially as it pertains to operation of the twinning modes (Nie et al., 2013). Other factors such as grain size also have a significant effect on the slip and twinning behavior (Barnett et al., 2004; Raeisinha et al., 2010; Wang and Choo, 2014).

Preliminary examinations of WE43-T5 plate tested at both quasistatic and high strain rates, during the early phases of the present research, revealed that the WE43-T5 behavior is in striking contrast to the strongly anisotropic behavior which is typical of wrought Mg alloys mentioned above. Despite being moderately textured, the compressive strength and ductility of WE43-T5 were surprisingly similar (isotropic) along different plate directions (RD and ND) as compared to other Mg alloys, including extruded alloy AM30-F (Figure 1.1). Thus, the question

remains as to what effect the rare earth alloying additions (and/or microstructure details) had on the deformation mechanisms, which render the material more isotropic. When compared with the results obtained by Tucker et al. for rolled AZ31-H24 alloy of similar texture and plate thickness (Figure 1.2), the first thing that stands out is that this alloy is stronger (on average) as compared to AZ31. In AZ31, the in-plane compression and through-thickness compression yield strength difference is $\sim 100\text{MPa}$ and is even higher at dynamic strain rates. Based on these results it was hypothesized that the various strengthening mechanisms operative in this alloy increase the strength of the soft deformation modes more than the hard modes, which renders this material more isotropic and less asymmetric as compared to conventional alloys like AZ31.

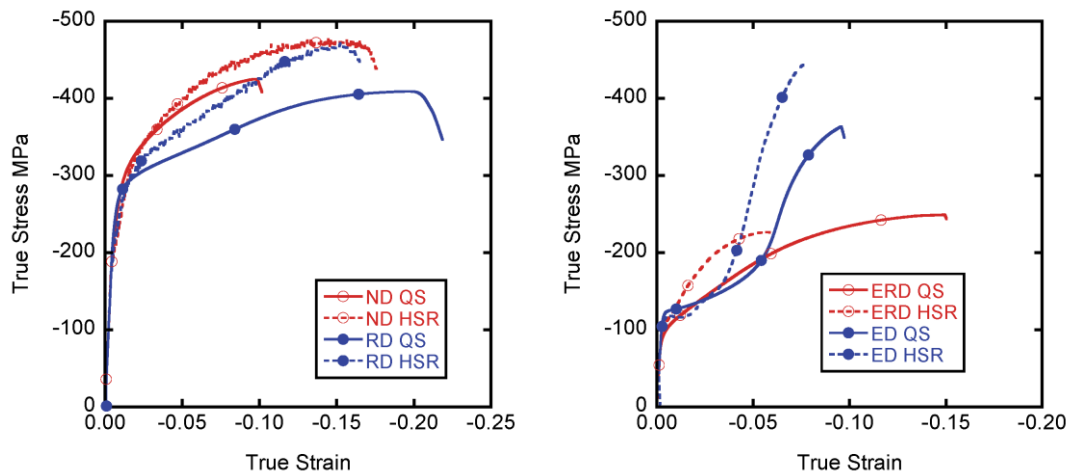


Figure 1.1: Experimental stress-strain curves for WE43-T5 plate and AM30 extrusion under quasistatic and dynamic compression (Agnew et al., 2014).

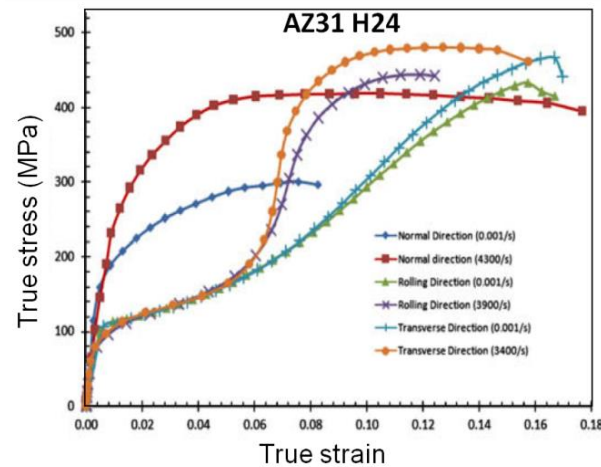


Figure 1.2: Experimental stress-strain curves for AZ31-H24 under compression from Tucker et al. (2009).

One of the objectives of this dissertation is to quantify the influence of microstructure (solutes, precipitates, texture and grain size), on deformation behavior of WE43 plate under quasistatic and dynamic loading conditions. The deformation behavior of this alloy is studied by systematically varying: i) the crystallographic texture (i.e. strong and weak texture), ii) the strain rate (i.e. 0.001/s and 1000/s), and iii) second phase content in the microstructure (i.e. solution-treated vs. variously aging conditions).

1.7 Al alloys

The literature that exists even for only 7XXX series Al alloys is enormous. The whole range of alloy development strategies: solid solution strengthening, cold-work, precipitate strengthening, and grain size refinement, have been studied systematically in Al alloys. Although there are many recent publications focused on Mg, the vast majority tend to be more focused on trial-and-error alloy and process development studies, rather than on systematic analyses of the effects of specific microstructure features on the mechanical properties. The goal of this section is not to provide a detailed literature review on Al 7XXX series alloys. Pertinent literature is presented in the subsequent chapters where ever relevant. Rather, this section provides a

motivation for the final three chapters of the dissertation. Even though the quasistatic behavior of Al 7XXX alloys is well studied, there have not been many studies investigating the temper dependence on high strain rate deformation behavior of these alloys. One notable exception is the work by the group at Norwegian University of Science and Technology (NTNU), which has focused on studying the dynamic deformation and fracture behavior at high strain rates. They have shown that the 7XXX alloys have slightly positive SRS, but were susceptible to strain localization at dynamic strain rates (Oosterkamp et al., 2000; Chen et al., 2009). Furthermore, Pedersen et al. (2008) found that although the strength and strain hardening anisotropy were quite low, there was strong plastic strain anisotropy, which did not vary much within different tempers (W, T4, T6, T7) in extruded AA7030. Lademo et al., (2002) and Reyes et al., (2006) found that both W and T6 temper of AA7108 have the similar level of strength anisotropy, however, the r -values were different along 45° from extrusion direction. Reyes et al., (2006) also investigated AA7003 in T1 (Cooled from hot forming and naturally aged to stable condition).and T79 tempers and found smaller differences in the r -values. Moreover, they found strong normal strain anisotropy during through-thickness compression tests, large scatter in the data, and a large difference in the r -values of the W and T6 tempers. All these results indicate that there is some temper-dependence of the r -values and whether the texture or other microstructural features are responsible for such observations is still not clear. An initial investigation of AA 7085 in T711 temper explored the role of texture gradients, grain shape and latent hardening on the constitutive response of this alloy at both quasistatic and dynamic strain rates. It was found that all these variables were unable to capture all the aspects of strength and strain anisotropy, in this material. It has been known for quite a while that the presence of precipitates can induce a backstress which leads to strong Bauschinger effect. However, the effect on plastic anisotropy is a relatively

less studied area. Thus, in order to investigate the role of precipitates on plastic anisotropy, several different tempers were tested and a micromechanical model was incorporated in the EPSC code to quantitatively explore the possibility that precipitate-induced backstress may be responsible for the observed changes in anisotropy that occur with aging.

1.8 Thesis organization

This is a manuscript thesis where each chapter (2-6) is a self-contained study representing a journal publication. At the time of writing, Chapter 2 has been published in *International Journal of Plasticity* (Bhattacharyya et al., 2016). That chapter builds upon a previously published paper in the proceedings of the *Magnesium Technology 2015* symposium (Bhattacharyya et al., 2015), by adding more experimental data and modeling with EPSC, rather than the previously employed VPSC. Incidentally, the Magnesium Technology 2015 paper was awarded the best student paper award at the symposium. Chapter 4 was presented at the 2016 International Symposium on Plasticity held in January 2016, Hawaii and is under review with the *International Journal of Plasticity*. The rest of the chapters (3, 5 and 6) are in preparation for submission. Additionally, a detailed description of the SHPB instrumentation and experimental analysis is presented as an appendix.

More specifically, **Chapter 2** consists of EPSC modeling of WE43-T5 temper at quasistatic and dynamic strain rates. The model developed in this chapter is then validated in **Chapter 3** by making application to T3 and T6 tempers of the same alloy. Additionally, the response to various ageing treatments and the effect of plasticity and fracture behavior is presented in this chapter. **Chapter 4** presents the quasistatic and dynamic strain rate data of AA 7085 in T711 temper with a focus on modeling the texture evolution and anisotropy using the VPSC model. The effects of microstructural features such as grain shape and latent hardening are

examined. Based on the results of chapter 4, the temper dependence of anisotropy is further examined in **Chapter 5**, where experimental results for different tempers of AA7085 are presented. In **Chapter 6**, a model is developed to take into account the effect of precipitate-induced backstresses on anisotropy is presented and validated using the data presented in chapter 5. The dissertation is concluded with a summary of the key overall conclusions and suggestions for future work for both Mg and Al alloys. Since each chapter is in journal format, they contain a review of the appropriate literature. Though each individual chapter is written in a way that they can be read independently, each of them uses crystal plasticity modeling to interpret the role of microstructure on the slip system-level deformation behavior of precipitation hardenable light alloys. As a result of this research, two models with predictive capabilities have been developed and validated against experimental data.

1.9 References

- Agnew, S., Whittington, W., Oppedal, A., El Kadiri, H., Shaeffer, M., Ramesh, K.T., Bhattacharyya, J., Delorme, R., Davis, B., 2014. Dynamic Behavior of a Rare-Earth-Containing Mg Alloy, WE43B-T5, Plate with Comparison to Conventional Alloy, AM30-F. *Jom* 66, 277–290. doi:10.1007/s11837-013-0830-x
- Backman, M.E., Goldsmith, W., 1978. The mechanics of penetration of projectiles into targets. *Int. J. Eng. Sci.* 16, 1–99.
- Baker, W.E., Yew, C.H., 1966. Strain-rate effects in the propagation of torsional plastic waves. *J. Appl. Mech.* 33, 917–923.
- Ball, E.A., Prangnell, P.B., 1994. Tensile compressive yield asymmetries in high strength wrought magnesium alloys. *Scr. Metall.* 31, 111–116.
- Barnett, M.R., Keshavarz, Z., Beer, a. G., Atwell, D., 2004. Influence of grain size on the compressive deformation of wrought Mg-3Al-1Zn. *Acta Mater.* 52, 5093–5103. doi:10.1016/j.actamat.2004.07.015
- Ben-Dor, G., Dubinsky, A., Elperin, T., 2005. Optimization of two-component composite armor against ballistic impact. *Compos. Struct.* 69, 89–94. doi:10.1016/j.compstruct.2004.05.014
- Beyerlein, I.J., Tomé, C.N., 2008. A dislocation-based constitutive law for pure Zr including temperature effects. *Int. J. Plast.* 24, 867–895. doi:10.1016/j.ijplas.2007.07.017
- Bhattacharyya, J., Agnew, S., Wu, P., Whittington, W., El Kadiri, H., 2015. Crystal Plasticity Modeling of the Dynamic Behavior of Magnesium Alloy, WE43-T5, Plate, in: *Magnesium Technology*. pp. 165–170.
- Bhattacharyya, J.J., Wang, F., Wu, P.D., Whittington, W.R., El Kadiri, H., Agnew, S.R., 2016. Demonstration of alloying, thermal activation, and latent hardening effects on quasi-static and dynamic polycrystal plasticity of Mg alloy, WE43-T5, plate. *Int. J. Plast.* 81, 123–151. doi:10.1016/j.ijplas.2016.01.005
- Bishop, R.F., Hill, R., Mott, N.F., 1945. The theory of indentation and hardness tests. *Proc. Phys. Soc.* 57,

147.

- Borvik, T., Hopperstad, O.S., Pedersen, K.O., 2010. Quasi-brittle fracture during structural impact of AA7075-T651 aluminium plates. *Int. J. Impact Eng.* 37, 537–551. doi:10.1016/j.ijimpeng.2009.11.001
- Chen, Y., Pedersen, K.O., Clausen, A.H., Hopperstad, O.S., 2009. An experimental study on the dynamic fracture of extruded AA6xxx and AA7xxx aluminium alloys. *Mater. Sci. Eng. A* 523, 253–262. doi:10.1016/j.msea.2009.06.007
- Clifton, R.J., Duffy, J., Hartley, K.A., Shawki, T.G., 1984. On critical conditions for shear band formation at high strain rates. *Scr. Metall.* 18, 443–448. doi:10.1016/0036-9748(84)90418-6
- Corbett, G.G., Reid, S.R., Johnson, W., 1996. Impact loading of plates and shells by free-flying projectiles: A review. *Int. J. Impact Eng.* 18, 141–230. doi:10.1016/0734-743X(95)00023-4
- Costin, L.S., Duffy, J., Freund, L.B., 1977. Fracture initiation in metals under stress wave loading conditions, in: *Fast Fracture and Crack Arrest*. ASTM International.
- Davies, R., 1948. A critical study of the Hopkinson pressure bar. *Philos. Trans. R. Soc. London. Ser. A, Math. Phys. Sci.* 240, 375–457.
- Djapic Oosterkamp, L., Ivankovic, a., Venizelos, G., 2000. High strain rate properties of selected aluminium alloys. *Mater. Sci. Eng. A* 278, 225–235. doi:10.1016/S0921-5093(99)00570-5
- Doherty, K., Squillacioti, R., Cheeseman, B., Placzankis, B., Gallardy, D., 2012. Expanding the Availability of Lightweight Aluminum Alloy Armor Plate Procured From Detailed Military Specifications. *ICAA13 13th Int. Conf. Alum. Alloy.* 541–546.
- Eshelby, J.D., 1957. The Determination of the Elastic Field of an Ellipsoidal Inclusion, and Related Problems. *Proc. R. Soc. A Math. Phys. Eng. Sci.* 241, 376–396. doi:10.1098/rspa.1957.0133
- Follansbee, P.S., Kocks, U.F., 1988. A constitutive description of the deformation of copper based on the use of the mechanical threshold stress as an internal state variable. *Acta Metall.* 36, 81–93. doi:10.1016/0001-6160(88)90030-2
- Gallardy, D., 2012. Ballistic Evaluation of 7085 Aluminum ARL-TR-5952.
- Giessen, E. Van Der, Needleman, a, 1999. Discrete dislocation plasticity: a simple planar model. *Model. Simul. Mater. Sci. Eng.* 3, 689–735. doi:10.1088/0965-0393/3/5/008
- Gonçalves, D.P., De Melo, F.C.L., Klein, A.N., Al-Qureshi, H.A., 2004. Analysis and investigation of ballistic impact on ceramic/metal composite armour. *Int. J. Mach. Tools Manuf.* 44, 307–316. doi:10.1016/j.ijmachtools.2003.09.005
- Harding, J., Wood, E.O., Campbell, J.D., 1960. Tensile testing of materials at impact rates of strain. *J. Mech. Eng. Sci.* 2, 88–96.
- Hill, R., 1965a. A self-consistent mechanics of composite materials. *J. Mech. Phys. Solids* 13, 213–222. doi:10.1016/0022-5096(65)90010-4
- Hill, R., 1965b. Continuum Micro-Mechanics of Elastoplastic polycrystals. *J. Mech. Phys. Solids* 13, 89–101.
- Hopkinson, B., 1914. A method of measuring the pressure produced in the detonation of high explosives or by the impact of bullets. *Philos. Trans. R. Soc. London. Ser. A, Contain. Pap. a Math. or Phys. Character* 213, 437–456.
- Hopkinson, J., 1901. *Original Papers by the Late John Hopkinson...* At the University Press.
- Hutchinson, J., 1970. Elastic-Plastic Behavior of Polycrystalline Metals and Composites. *Proc. R. Soc. London A Math. Phys. Eng. Sci.* 319, 247–272.
- Johnson, G.R., Cook, W.H., 1983. A constitutive model and data for metals subjected to large strains, high strain rates and high temperatures, in: *Proceedings of the 7th International Symposium on Ballistics*. pp. 541–547.
- Kocks, U., H. Mecking, 2003. Physics and phenomenology of strainhardening: the FCC case. *Prog. Mater. Sci.* 48, 171–273.
- Kocks, U.F., Argon, A.S., Ashby, M.F., 1975. Thermodynamics and Kinetics of Slip. *Prog. Mater. Sci. B. Chalmers, JW Christ. TB Massalsk, Eds.* 19.
- Kolsky, H., 1949. An investigation of the mechanical properties of materials at very high rates of loading.

- Proc. Phys. Soc. Sect. B 62, 676.
- Kroner, E., 1958. No Title. *Z. Phys.* 151, 504.
- Kubin, L.P., Canova, G., Condat, M., Devincere, B., Pontikis, V., Bréchet, Y., 1992. Dislocation microstructures and plastic flow: a 3D simulation, in: *Solid State Phenomena*. pp. 455–472.
- Lademo, O.G., Hopperstad, O.S., Malo, K.A., Pedersen, K.O., 2002. Modelling of plastic anisotropy in heat-treated aluminium extrusions. *J. Mater. Process. Technol.* 125-126, 84–88. doi:10.1016/S0924-0136(02)00289-3
- Lebensohn, R.A., Tome, C.N., 1993. A self-consistent anisotropic approach for the simulation of plastic deformation and texture development of polycrystals: application to zirconium alloys. *Acta Metall.* 41, 2611–2624.
- Lindholm, U.S., Yeakley, L.M., 1968. High strain-rate testing: tension and compression. *Exp. Mech.* 8, 1–9.
- Lindholm, U.S., Yeakley, L.M., 1967. A dynamic biaxial testing machine. *Exp. Mech.* 7, 1–7.
- Mecking, H., Kocks, U.F., 1981. Kinetics of flow and strain hardening. *Acta Metall.* 29, 1865–1875.
- Molinari, A., Clifton, R.J., 1987. Analytical characterization of shear localization in thermoviscoplastic materials. *J. Appl. Mech.* 4, 806–812.
- Nemat-Nasser, S., Guo, W.G., Nesterenko, V.F., Indrakanti, S.S., Gu, Y.B., 2001. Dynamic response of conventional and hot isostatically pressed Ti-6Al-4V alloys: Experiments and modeling. *Mech. Mater.* 33, 425–439. doi:10.1016/S0167-6636(01)00063-1
- Nemat-Nasser, S., Issacs, J.B., Liu, M., 1998. Microstructure of high strain, high strain rate deformed Tantalum. *Acta Metall.* 46, 1307–1325.
- Nemat-Nasser, S., Li, Y.-F., Isaacs, J.B., 1994. Experimental/ computational evaluation of flow stress at high strain rates with application to adiabatic shear banding. *Mech. Mater.* 17, 111–134. doi:10.1016/0167-6636(94)90053-1
- Nie, J.F., Muddle, B.C., 2000. Characterisation of strengthening precipitate phases in a Mg–Y–Nd alloy. *Acta Mater.* 48, 1691–1703. doi:10.1016/S1359-6454(00)00013-6
- Nie, J.F., Xiao, X.L., Luo, C.P., Muddle, B.C., 2001. Characterisation of precipitate phases in magnesium alloys using electron microdiffraction. *Micron* 32, 857–863. doi:10.1016/S0968-4328(00)00094-9
- Nie, J.F., Zhu, Y.M., Liu, J.Z., Fang, X.Y., 2013. Periodic segregation of solute atoms in fully coherent twin boundaries. *Science* 340, 957–60. doi:10.1126/science.1229369
- Nye, J.F., 1985. *Physical properties of crystals: their representation by tensors and matrices*. Oxford university press.
- Pedersen, K.O., Roven, H.J., Lademo, O.-G., Hopperstad, O.S., 2008. Strength and ductility of aluminium alloy AA7030. *Mater. Sci. Eng. A* 473, 81–89. doi:10.1016/j.msea.2007.03.089
- Pedersen, K.O., Børvik, T., Hopperstad, O.S., 2011. Fracture mechanisms of aluminium alloy AA7075-T651 under various loading conditions. *Mater. Des.* 32, 97–107. doi:10.1016/j.matdes.2010.06.029
- Raeisinia, B., Agnew, S.R., Akhtar, A., 2010. Incorporation of Solid Solution Alloying Effects into Polycrystal Modeling of Mg Alloys. *Metall. Mater. Trans. A* 42, 1418–1430. doi:10.1007/s11661-010-0527-5
- Reuss, A., 1930. *Mathematik und Mechanik* 10, 266.
- Reyes, A., Hopperstad, O.S., Lademo, O.-G., Langseth, M., 2006. Modeling of textured aluminum alloys used in a bumper system: Material tests and characterization. *Comput. Mater. Sci.* 37, 246–268. doi:10.1016/j.commatsci.2005.07.001
- Robson, J.D., Stanford, N., Barnett, M.R., 2011. Effect of precipitate shape on slip and twinning in magnesium alloys. *Acta Mater.* 59, 1945–1956. doi:10.1016/j.actamat.2010.11.060
- Sachs, G., 1928. *Z. Verein Deutsch Ingen* 72, 734.
- Semiatin, S.L., Staker, M.R., Jonas, J.J., 1984. Plastic instability and flow localization in shear at high rates of deformation. *Acta Metall.* 32, 1347–1354. doi:10.1016/0001-6160(84)90080-4
- Staker, M.R., 1981. The Relation Between Adiabatic Shear Instability and Material Properties. *Acta Metall.* 29, 683–689. doi:10.1016/0001-6160(81)90151-6
- Subhash, G., 2000. *Dynamic Indentation Testing*. Mater. Park. OH ASM Int. 2000. 519–529.

- Taylor, G., 1934. The Mechanism of Plastic Deformation of Crystals . Proc. R. Soc. A Math. Phys. Eng. Sci. 145, 362–387.
- Timothy, S.P., 1985. The Structure of Adiabatic Shear Bands in Metals: A critical Review. Acta Metall. 35, 301–306.
- Tucker, M.T., Horstemeyer, M.F., Gullett, P.M., El Kadiri, H., Whittington, W.R., 2009. Anisotropic effects on the strain rate dependence of a wrought magnesium alloy. Scr. Mater. 60, 182–185. doi:10.1016/j.scriptamat.2008.10.011
- Turner, P.A., Tomé, C.N., 1994. A study of residual stresses in Zircaloy-2 with rod texture. Acta Metall. Mater. 42, 4143–4153. doi:10.1016/0956-7151(94)90191-0
- Voigt, W., 1910. Lehrbuch der Kristallphysik. Leipzig-Berlin: Teubner.
- Wang, Y., Choo, H., 2014. Influence of texture on Hall–Petch relationships in an Mg alloy. Acta Mater. 81, 83–97. doi:10.1016/j.actamat.2014.08.023
- Zerilli, F.J., Armstrong, R.W., 1987. Dislocation-mechanics-based constitutive relations for material dynamics calculations. J. Appl. Phys. 61, 1816–1825. doi:10.1063/1.338024

2 Demonstration of alloying, thermal activation, and latent hardening effects on quasi-static and dynamic polycrystal plasticity of Mg alloy, WE43-T5, plate

J.J. Bhattacharyya¹, F. Wang¹, P.D. Wu², W. Whittington³, H. El Kadiri³, and S.R. Agnew¹

¹Materials Science and Engineering, University of Virginia, Charlottesville, Virginia, U.S.A.

²Mechanical Engineering, McMaster University, Hamilton, Ontario, Canada

³Mechanical Engineering, Mississippi State University, Mississippi, U.S.A.

2.1 Abstract

The mechanical response of rare earth containing Mg alloy, WE43, plates is found to be more isotropic, as compared to conventional alloys like AZ31, despite a moderately strong texture. In order to understand the grain-level deformation mechanisms which are responsible, the elastoplastic self-consistent (EPSC) polycrystal plasticity code, including the recently developed twinning-detwinning (TDT) model, is used to describe the homogeneous plastic flow of WE43-T5, plate at quasistatic and dynamic strain rates. Latent hardening of the slip modes is based on a recent discrete dislocation dynamics study in order to reduce the number of empirical fitting parameters without sacrificing model fidelity. The approach accounts for the presence of the initial texture and its evolution during deformation. The observed flow stress, strain, and strain hardening anisotropies and asymmetries are well-described. A single set of parameters was used to fit the entire set of results, at a given strain rate, thus enabling determination of strain rate sensitivities of individual deformation modes. Basal slip and extension twinning are rate-insensitive, within the strain rate regime examined, whereas the prismatic and $\langle c+a \rangle$ slip exhibit strain rate sensitivities of 0.008 and 0.005, respectively. Various strengthening mechanisms such as precipitation, grain refinement and solid solution hardening effects on each individual deformation modes are assessed. The softer modes, basal slip and extension twinning, are greatly

strengthened in this alloy, as compared to the harder modes such as prismatic and $\langle c+a \rangle$ slip, which renders this material more isotropic, even at the grain-level, as compared to conventional Mg alloys.

Keywords: A. strengthening mechanisms; B. crystal plasticity; B. constitutive behavior; latent hardening; thermal activation

2.2 Introduction

Recent ballistic tests carried out by Army Research Laboratory (ARL) have shown that the rare earth (RE) containing magnesium alloy WE43 have superior properties compared to Al-Mg alloy, 5083, and conventional Mg alloy, AZ31 (Cho et al., 2009). Thus, it is considered to be a potential armor material. In an earlier study (Agnew et al., 2014), the constitutive behavior of this alloy was examined and it was found that this material exhibited a more isotropic response as compared to AZ31 and AM30, despite being moderately textured. Moreover, it showed some tension-compression strength asymmetry which was highest along the normal direction (ND) of the plate. Furthermore, the strain rate sensitivity was found to be a function of loading direction as well as strain level. Recent studies by Tucker et al. (2009) and Ulacia et al. (2010) demonstrated the strong role that texture plays in the dynamic response of Mg alloy sheets and plates respectively. The goal of the present study is to determine the role of individual deformation modes, which render this material more isotropic in spite of being moderately textured. Crystal plasticity modeling is an effective technique to study the grain-level deformation mechanisms. Such technique allows one to assess the strength and strain hardening behavior of individual slip systems. Thus, for the present study, an elasto-plastic self-consistent (EPSC) model (Turner and Tomé, 1994) has been employed. Importantly, the crystal plasticity model itself is completely rate independent. By determining the model parameters which

describe the experimental response at different strain rates, the strain rate sensitivities of individual deformation modes are evaluated. This information is, in turn, used to inform our understanding of how the various strengthening mechanisms affect the individual deformation modes.

WE43 (containing 3.7–4.3 wt% yttrium, 2.4–4.4 wt% neodymium and at least 0.4 wt% zirconium) alloy is a precipitation hardenable alloy, which exhibits good age-hardening response among Mg alloys. The precipitation hardening behavior in Mg alloys is quite complicated as compared to face centered cubic alloys e.g. heat treatable Al alloys, because of multiple deformation modes that are active in Mg alloys. Moreover, for a given deformation mode, the effect of precipitation hardening depend on the shape and orientation of the precipitates with respect to the matrix. In WE43, primarily, plate shaped precipitates form on the prismatic planes (Nie and Muddle, 2000; Nie et al., 2001). The effects of precipitate shape on the deformation behavior of Mg alloys have been investigated in several prior works (Nie, 2003; Robson et al., 2011, 2012), where calculations based upon the Orowan bowing mechanism has been used to obtain the shear resistance imposed by the precipitates. These calculations reveal that the prismatic plates, such as those in WE43 alloys, are most effective in blocking basal $\langle a \rangle$ type dislocations. Using in-situ neutron diffraction and EPSC modeling Agnew et al. (2013) studied the effect of age-hardening on the deformation of an as-cast WE43 alloy, and found that basal $\langle a \rangle$ slip is considerably strengthened as compared to prismatic and $\langle c+a \rangle$ pyramidal slip. Interestingly, a possible reduction in the critical resolved shear stress (CRSS) for twinning with age-hardening was reported.

Besides age-hardening, solutes can have a profound impact on the active deformation modes (e.g. Akhtar and Teghtsoonian, 1969; Raeisinha et al., 2010). Using first principles

calculation, Yasi et al. (2010) tabulated the potency of 29 solutes for strengthening basal slip, including Y. Regarding non-basal slip and twinning modes, only recently, some investigations have started to shed light on the effects of RE solutes. For instance, Stanford et al. (2014) used in-situ neutron diffraction and EPSC modeling to investigate the deformation of binary Mg-Y alloys and found that Y solute can significantly increase the CRSS of $\langle c+a \rangle$ pyramidal slip. Nie et al. (2013) using HAADF STEM have shown Gd segregation in tensile twin boundaries, leading to retardation in twin growth during subsequent deformation. Lentz et al. (2014; 2015), while studying WE54 using in-situ neutron diffraction and EPSC modeling, found that the strength of the twinning mode is significantly higher than that in conventional Mg alloys. Stanford et al. (2015) recently observed that Y addition leads to reduced $\{10\bar{1}2\}$ extension twinning activity and can even lead to the formation of $\{11\bar{2}1\}$ twins in Mg-10Y alloys. All these aforementioned works indicate a significant effect of precipitates and solutes on the deformation behavior of RE containing Mg alloys. One goal of this paper is to investigate the effects of these strengthening mechanisms on individual deformation modes under dynamic loading conditions, with a goal of informing researchers interested in maximizing the ballistic performance of Mg alloys.

Despite possessing superior mechanical properties than AZ31, the dynamic behavior of WE43 alloy is less extensively investigated. Nevertheless, one of the earliest published high-strain-rate deformation studies on Mg alloys was performed on WE43 (Mukai et al., 1998). They showed that a significant improvement in energy absorption could be achieved by strong grain refinement (down to 1.4 μm) via conventional extrusion. This fine-grained WE43 exhibited high ductility, which resulted in significantly higher energy absorption per unit mass due to the low density of Mg alloys.

Asgari et al. (2014) recently examined the high strain rate behavior of Mg alloy, WE43, and employed the visco-plastic self-consistent (VPSC) model (Lebensohn and Tomé, 1993) to simulate texture evolution during in-plane and ND compression. However, they did not seek to simulate the constitutive response (flow stress or plastic anisotropy), nor did they consider prismatic slip in their simulations, which is known to be active in Mg alloys and has recently been reemphasized as an important contributor to deformation texture evolution (Steiner et al., 2015). Furthermore, they suggested that the activity of extension twinning decreases with increase in strain rate, based upon EBSD data (Asgari et al., 2014). Finally, they suggested a higher activity of pyramidal $\langle c + a \rangle$ slip with increasing strain rate and attributed this to adiabatic heating during dynamic deformation, although the extent of temperature rise was not mentioned.

The goal of the present study is to determine the strength, hardening behavior, and rate sensitivity of individual deformation (slip and twinning) modes. These mode-level behaviors are interpreted in terms of various operative strengthening mechanisms (solute, precipitates, grain size, etc.). The relative effects of texture and deformation mode behavior in determining the constitutive behavior are discussed.

2.3 Experimental methods

2.3.1 Materials, texture and microstructure

Two 38 mm (1.5 inch) thick plates of WE43B alloy in T5 (artificially peak aged at 210 °C for 48 h) condition were used in this study. The details of the processing technique are described elsewhere (Agnew et al., 2014). X-ray diffraction was used to measure the crystallographic texture of the plate at various depths, from the surface up to mid-plane, in order to assess the possibility of through-thickness texture gradients. Tension and compression

specimens were wire cut electrical discharge machined (EDM'd) from both plates along rolling direction (RD), transverse direction (TD) and normal direction (ND). The quasistatic tensile, compression and dynamic compression tests were carried out on a plate obtained from Magnesium Electron North America (MELNA) having lot # 9849, while dynamic tensile and compression tests were carried out on plate MELNA with lot # 6457.

Electron backscattered diffraction (EBSD) measurements were carried out on both the as-received and deformed WE43-T5 material, in order to investigate the microstructure and texture evolution. The samples were cold-mounted in epoxy, mechanically ground down to 1200-grit SiC paper, polished with 3 and 1 μm oil-based diamond paste, and final polished with 0.06 μm colloidal silica. After this metallographic procedure, the samples were cleaned with a plasma etching and coating system to remove the deformation layer and facilitate indexing. A FEI Quanta 650 FEG scanning electron microscope, equipped with Oxford /HKL system with a Nordys EBSD detector, was used for EBSD measurements. The operating voltage and the spot size was 20 kV and 5.5 (corresponding to a beam current of 11 nA), respectively. For the data collection, a working distance of 15-20 mm at a magnification of 500X was used along with step sizes between 0.5-1 μm . The fraction of points successfully indexed was 75–95%, for the samples presented. To obtain the texture of the deformed sample, multiple (3-4) areas of $\sim 200 \mu\text{m}^2$ were scanned and the orientation distribution function (ODFs) of the individual measurements were averaged to obtain the recalculated pole figures with sufficient grain-count statistics. Band contrast and inverse pole figure (IPF) maps of different directions were constructed using HKL Channel 5 software to analyze the microstructure evolution post deformation. The twin boundaries were identified based on their misorientation: $86^\circ \pm 5^\circ$ about $\langle 11\bar{2}0 \rangle$ axis for extension twins, $56^\circ \pm 5^\circ$ $\langle 11\bar{2}0 \rangle$ for contraction twins and $38^\circ \pm 5^\circ$ about

$\langle 11\bar{2}0 \rangle$ axis for double twins. It is to be noted that the “clean-up” procedure based on extrapolation of data from nearest neighbors were not carried out because such extrapolation increases the chance of introducing artifacts in the data. The twin volume fraction were obtained according to the method described in Jain and Agnew, 2007. A cut-off radius of 30° - 40° was used to determine the twin volume fraction. A radius of 33° gave the best overall match and the upper and lower bound were calculated based on a radius of 40° and 30° respectively.

Characterization of the precipitate morphology and distribution was performed on a JEOL 2000FX TEM operating at 200 kV and a TEI Titan 880-300 TEM operating at 300 kV. High angle annular dark field scanning TEM (HAADF-STEM) images were obtained from the latter. TEM samples were produced from the transverse direction (TD) and normal direction (ND) respectively. Thin foils were prepared via mechanical grinding and subsequently electropolishing in a Fischione double-jet polisher. The electrolyte is a solution of 500 ml methanol, 100 ml butyl cellosolve, 11.16 g magnesium perchlorate and 5.3 g lithium chloride. The regional thickness of the TEM foil was measured by convergent beam electron diffraction (CBED), following the approach as described in the literature (Allen and Hall, 1982; Allen, 1981; Fultz and Howe, 2012).

2.3.2 Mechanical testing

High strain rate (~ 1000 /s) uniaxial tension and compression tests were carried out using a Split Hopkinson pressure (or Kolsky) bar testing apparatus. The tests were carried out along RD, ND and transverse direction (TD) of the plate. The testing procedure, sample geometry and data processing are discussed in detail in an earlier publication (Agnew et al., 2014). Notably, cylindrical pulse shapers of 10 mm diameter and 2 mm length cut from AA-1100 alloy were used in case of compression tests to maintain reasonably constant strain rates. During data processing,

the force on the incident and transmitted ends of the specimen were compared in order to ensure stress equilibrium and uniform loading conditions. A universal testing machine was used to assess the quasistatic uniaxial compression and tensile response. An extensometer was used to record the strain during the tests. The plastic strain anisotropy was evaluated by measuring the r -values which are defined as (Jain and Agnew, 2007):

$$r_{RD} = \epsilon_{TD}/\epsilon_{ND} \quad (2-1)$$

$$r_{TD} = \epsilon_{RD}/\epsilon_{ND} \quad (2-2)$$

$$r_{ND} = \epsilon_{RD}/\epsilon_{TD} \quad (2-3)$$

In case of quasistatic tests, the samples were strained up to a specific strain level and unloaded. Subsequently a digital caliper was used to measure the two lateral strains. For the high strain rate tests, the r -values were obtained by measuring the lateral strains on the tested samples post-mortem. The r -values were measured 3 times on each individual sample and on 3-5 different samples and the average value was reported along with the standard deviations as error bars. For the tensile specimens, the measurements were carried out on each sample, within the region of uniform deformation (at regions away from the neck). The constancy of volume condition ($\epsilon_{ii} = 0$) was assessed in all cases to check the accuracy of the measurements.

2.4 Modeling approach

It may initially sound counterintuitive, but because the goal of this work is to determine the strain rate sensitivities of individual deformation modes, the rate-independent elastoplastic self-consistent (EPSC) model is used in preference over the rate-dependent viscoplastic self-consistent (VPSC) model, in which the rate sensitivity is implicit in the model itself. The rationale for this is explained below. In addition, for the desired analysis of individual mechanisms, it was necessary to model the elasto-plastic transition. Nevertheless, some insights with respect to

anisotropy obtained from VPSC simulations are presented in the appendix. In both cases, a polycrystal is represented as a collection of crystal orientations with volume fractions chosen to reproduce the experimentally measured initial texture. To simulate uniaxial tension and compression along RD, TD and ND straining increments of 2×10^{-5} were imposed parallel to one direction while the normal stresses along the other two perpendicular directions and all shear stresses were set to zero. The simulations were carried out to the experimental strain level associated with failure. This enables the comparison between the experimentally obtained textures after deformation and the simulated textures.

2.4.1 The EPSC model

The EPSC model was first developed by Turner and Tome (1994) and makes use of the solution to the Eshelby inclusion problem (Eshelby, 1957). In the model, a grain (defined by its orientation) is considered as an anisotropic elastoplastic ellipsoidal inclusion embedded in a homogeneous anisotropic effective medium (HEM) which represents the polycrystalline aggregate. The properties and macroscopic response of the HEM are calculated via weighted averages of all the grains. The model accounts for the crystallographic reorientation due to twinning (Clausen et al., 2008; Wang et al., 2012) and that due to slip (Neil et al., 2010).

2.4.2 Grain level constitutive response

Slip and twin activation is dictated by Schmid law, viz. the resolved shear stress on the slip/twin plane in the slip/ twin direction has to reach the critical resolved shear stress (CRSS), for the activation of the particular deformation mode. Moreover, for a given straining step, the resolved shear stress of active slip systems must remain on the yield surface, while the yield surface evolves due to strain hardening and reorientation. At the individual slip-system level, the

EPSC model employed incorporates an initial threshold stress τ_0^α , and an empirical Voce strain hardening rule for the evolution of the CRSS τ_{ref}^α :

$$\frac{\partial \tau_{ref}^\alpha}{\partial \Gamma} = \theta_0^\alpha \left(1 - \left(\frac{\tau^\alpha - \tau_0^\alpha}{\tau_1^\alpha} \right) \right) \quad (2-4)$$

where, $\Gamma = \sum_\alpha \gamma^\alpha$ is the accumulated shear strain in a grain, τ_{ref}^α is the reference shear resistance of slip system α , $\tau_0^\alpha + \tau_1^\alpha$ is the saturation stress, and θ_0 is the initial strain rate, respectively.

Thus, there are three parameters per slip mode.

2.4.3 Twinning model

For twinning, a linear hardening model, $\frac{\partial \tau_{ref}^\alpha}{\partial \Gamma} = \theta_0^\alpha$, is assumed. Furthermore, according to the twinning-detwinning (TDT) model employed, deformation twinning consists of four processes: a) twin nucleation and immediate propagation across the parent grain, b) twin growth, c) twin shrinkage, and d) re-twinning (Wang et al., 2012). In the original TDT model, two empirical parameters $A1$ and $A2$ are employed to control the volume fraction evolution of the twins, according to the following relation:

$$V^{th} = \min \left(1.0, A1 + A2 \frac{V^{eff}}{V^{acc}} \right) \quad (2-5)$$

where, V^{th} is the threshold volume fraction, V^{acc} is the accumulated twin fraction and V^{eff} is the effective twinned fraction. $A1$ determines the level of strain which a grain undergoes before twinning starts to exhaust and $A2$ controls the rate at which the twins exhaust. The combination of $A1$ and $A2$ controls the length of the plateau and the subsequent strain hardening rate. One effect of these two parameters is to prevent a grain from twinning 100%. However, in the present case, EBSD observations reveal that the grains are completely twinned (reoriented), and hence these two parameters are set to 1. This enables the grains to be completely consumed by the twins within them, should the local boundary conditions be favorable. The key point of the TDT

model, for this application, is that stress conditions within the twinned material are permitted to drive further growth of the twins. Previous models (e.g., Clausen et al., 2008) only polled the parent grain stress conditions to determine whether a twin will grow during a given strain step. In summary, there are four parameters ($\tau_0^\alpha, \theta_0, A1$, and $A2$) to describe the critical stress and hardening behavior of twinning.

2.4.4 Latent hardening

Dislocation interactions, especially when multiple slip modes are active, may lead to considerable latent hardening (LH). LH equal to 1 implies that the secondary (latent) system is hardened equally to self-hardening. A value of LH greater than 1 indicates that the latent system is hardened more and a value of LH less than 1 means it is hardened less than self-hardening. In the EPSC model, the actual slip/twin mode hardening occurs via a hardening matrix, $h^{\alpha\beta}$, as follows:

$$\Delta\tau^\alpha = \frac{\partial\tau_c^\alpha}{\partial\Gamma} \sum_\beta h^{\alpha\beta} \Delta\gamma^\beta \quad (2-6)$$

where, $\delta\Gamma = \sum_\beta \Delta\gamma^\beta$. The components of the LH matrix determine the extent to which mode α is hardened by to activity of mode β . Until recently, the latent hardening parameters employed for modeling non-cubic metals have been determined empirically, i.e., as fitting parameters. In this study, an attempt has been made to use a physics-based approach to incorporate latent hardening in the simulations, without introducing any additional fitting parameters. Recent discrete dislocation dynamics simulations (Bertin et al., 2014) have shown that the Franciosi-Zaoui (FZ) latent hardening formulation :

$$\tau_c^s = \tau_0^s + \mu^s b^s \sqrt{\sum_{s'} a_{FZ}^{ss'} \rho^{s'}} \quad (2-7)$$

is most suitable, and thus, they generated the full (system-by-system) LH matrix for pure Mg. In the above equation, τ_c^s and τ_0^s is the CRSS and lattice friction stress on system s , respectively. μ^s

is the shear modulus and b^s is the Burgers vector of system s . $a_{FZ}^{ss'}$ is the FZ interaction coefficient between systems s and s' and $\rho^{s'}$ is the dislocation density of the latent system s' . Since the present EPSC model takes into account only “mode-hardening,” the complete system-by-system LH matrix cannot be directly applied. Table 2.1 summarizes the hardening coefficient values used in the simulations. As a first approximation, the average FZ interaction coefficients as given in Bertin et al., 2014, weighted by the number of slip systems associated with each interaction were employed for a given slip mode. The value thus obtained is normalized with respect to self-hardening (F-Z value = 0.15) such that it is 1, which maintains the relative strength ratios of various interactions. For example, in case of pyramidal $\langle c+a \rangle$ slip, there are 6 systems involved in self-interaction with FZ = 0.15, which is set to 1. Out of the remaining possible interactions, 6 are involved in semi-collinear with FZ = 0.018 and 24 in non-collinear interaction with FZ = 0.042. Thus, the weighted average of the $\langle c+a \rangle$ mode is then:

$$LH_{c+a} = \left[\frac{(6 \times 0.018) + (24 \times 0.042)}{(6+24)(0.15)} \right] = 0.25 \quad (2-8)$$

The relationship between the FZ coefficients and the LH coefficients used in EPSC has been derived in Appendix 2.9. In short, the coefficients are linearly related. Hence, the weighted average values shown in Table 2.1 are used for the simulations. Note that our definition of “mode on mode” hardening, as employed within the EPSC model, is distinct from the “mode” hardening of Bertin et al (2014). In their “mode” hardening approach, slip systems only interact with other slip systems of the same mode, with interaction coefficients equal to that of self-hardening. In our case, we assign a single latent hardening value for all possible interactions between the different slip systems of one mode and another. For the present study, the important point is that $\langle c+a \rangle$ slip experiences very little latent hardening due to basal and prismatic slip, whereas basal is significantly hardened by prismatic and $\langle c+a \rangle$ slip. It was not deemed

necessary to incorporate high latent hardening of slip due to twin and thus to avoid any empirical latent hardening coefficient, it was set to 1.

Table 2.1: List of dislocation-dislocation interactions and the corresponding FZ coefficients as obtained from Bertin et al., (2014) along with the “mode on mode” interaction coefficients obtained by weighted average of FZ value by the number of slip systems.

Interaction	systems	FZ value	normalized	wt avg
basal self-hardening	3	0.150	1.00	1.00
basal/basal coplanar	6	0.150	1.00	1.00
basal/prismatic collinear	3	0.707	4.71	1.81
basal/prismatic non-collinear	6	0.054	0.36	
basal/pyramidal semi-collinear	6	0.367	2.45	2.12
basal/ pyramidal non-collinear	12	0.293	1.95	
prismatic self-hardening	3	0.150	1.00	1.00
prismatic/basal collinear	3	0.535	3.57	1.46
prismatic/basal non-collinear	6	0.060	0.40	
prismatic/prismatic	6	0.038	0.25	0.25
prismatic/ pyramidal semi-collinear	6	0.068	0.45	0.54
prismatic/ pyramidal non-collinear	12	0.088	0.59	
pyramidal self-hardening	6	0.150	1.00	1.00
pyramidal /basal semi-collinear	6	0.017	0.11	0.09
pyramidal /basal non-collinear	12	0.011	0.07	
pyramidal /prismatic semi-collinear	6	0.025	0.17	0.12
pyramidal /prismatic non-collinear	12	0.015	0.10	
pyramidal / pyramidal semi-collinear	6	0.018	0.12	0.25
pyramidal /pyramidal non-collinear	24	0.042	0.28	

2.5 Results

2.5.1 Characterization of as received WE43-T5 plate

The recalculated pole figures from plate # 9849 were presented in an earlier publication (Agnew et al., 2014) and the texture of plate # 6457 is very similar, albeit slightly stronger (Figure 2.1). Both the plates exhibit a near-basal texture, with a peak intensity of ~ 4 multiples of random distribution (mrd), where the basal poles are tilted by $\sim 25^\circ$ towards RD. A ND-IPF map of a sample extracted from plate # 9849 is shown in Figure 2.2. The map shows some elongated fine grains forming banded structure which is probably shear bands forming as a result of the hot rolling process.

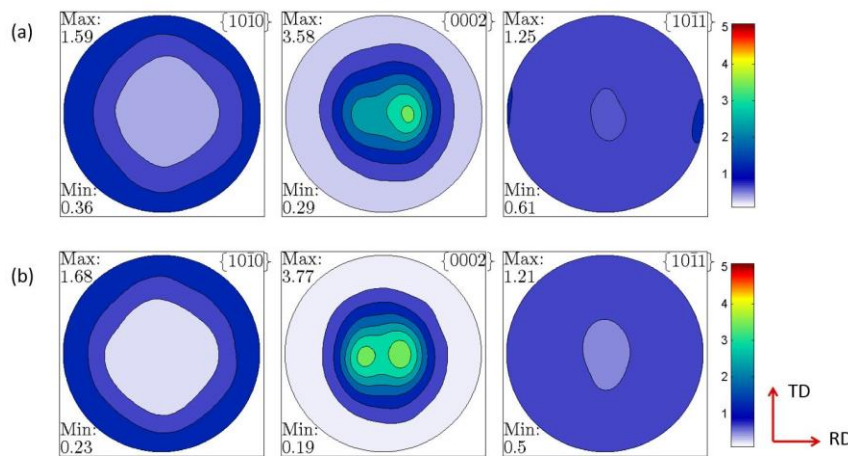


Figure 2.1: $\{10\bar{1}0\}$, $\{0002\}$ and $\{10\bar{1}1\}$ pole figures obtained by discretizing the experimental texture into 16000 grains (a) for plate # 9849 and (b) plate # 6457.

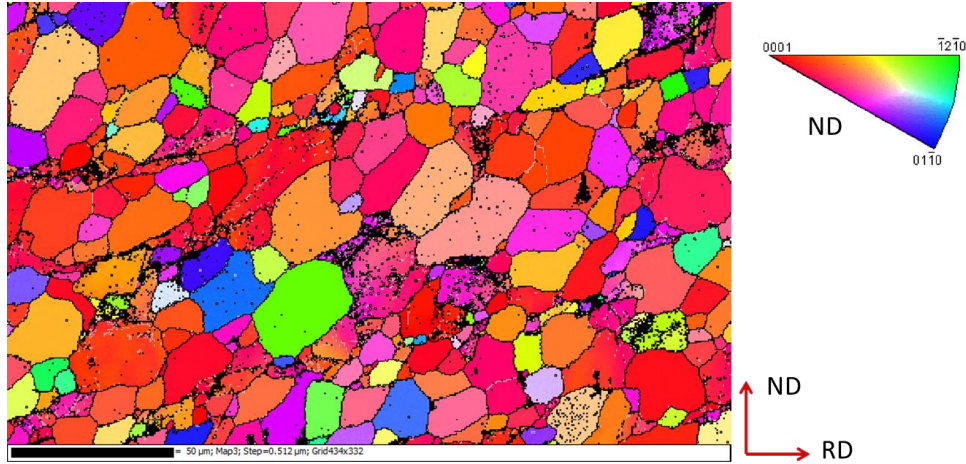


Figure 2.2: ND-IPF map from plate # 9849, showing grain structure of the as-received WE43-T5 plate.

Figure 2.3 presents a typical microstructure of WE43 in the T5 temper. The majority of the precipitates assume a globular shape, though many of the globules are connected to plate-shaped precipitates. All the precipitates exhibit fringe contrast in the transmission electron microscope (TEM) bright-field (BF) image (Figure 2.3a), with a fringe spacing of 1.13 nm. The high angle annular dark field (HAADF) scanning transmission electron microscope (STEM) image (Figure 2.3b) shows that the precipitates are rich in rare earth (high atomic number) solute atoms, and these atoms distribute in layers, of same spacing as in the BF image. SAED patterns were recorded from three perspectives: $[0001]_{\text{Mg}}$, $\langle 11\bar{2}0 \rangle_{\text{Mg}}$ and $\langle 10\bar{1}0 \rangle_{\text{Mg}}$. The diffraction patterns (Figure 2.3c-e) are consistent with a single base-centered orthorhombic β' phase (Antion et al., 2003; Nie and Muddle, 2000), with the reported orientation relationship of $(100)_{\beta'}/(1\bar{2}10)_{\text{Mg}}$ and $[001]_{\beta'}/[0001]_{\text{Mg}}$. Furthermore, the angle between the plate precipitate and the fringes in the globular precipitate is about 30° . Therefore, the plate precipitates lie on the $\{11\bar{2}0\}_{\text{Mg}}$ prismatic planes. It has been shown by using phase field simulations (Liu et al., 2013)

that the morphology of the β' precipitates is strongly determined by the anisotropy in interfacial and in elastic strain energies. In order to obtain the size of these precipitates, TEM micrographs recorded with electron beam parallel to $[0001]_{\text{Mg}}$ and $\langle 11\bar{2}0 \rangle_{\text{Mg}}$ were used. The precipitates were treated as ellipsoids and using Image J software, the major and minor axes were measured from each direction. Following this procedure, the average dimensions of the globular β' precipitates were obtained as 9 nm along $[100]_{\beta'}$, 19 nm along $[010]_{\beta'}$ and 14 nm along $[001]_{\beta'}$. The average foil thickness of the specimen was determined to be ~400 nm and, together with measurements of number density from a small number of high resolution images, yielded a range of volume fraction estimates from 0.2 % - 0.9 % for the globular β' phase precipitates. In the strength estimates performed later in the paper, an estimated ~0.5 volume % is employed for the globules. A similar approach for the thin plate shaped precipitates yielded an average size of 14 nm x 1.6 nm x 25 nm and a volume fraction of 0.2%. Thus, the total volume fraction of strengthening precipitates is estimated to be about 0.7 %. It is to be noted that X-ray powder diffraction and Rietveld analysis (not described in the interest of space), yielded a total second phase volume fraction of 5.6%, and SEM imaging that reveals a significant volume fraction of larger grain boundary particles which would not contribute to strengthening.

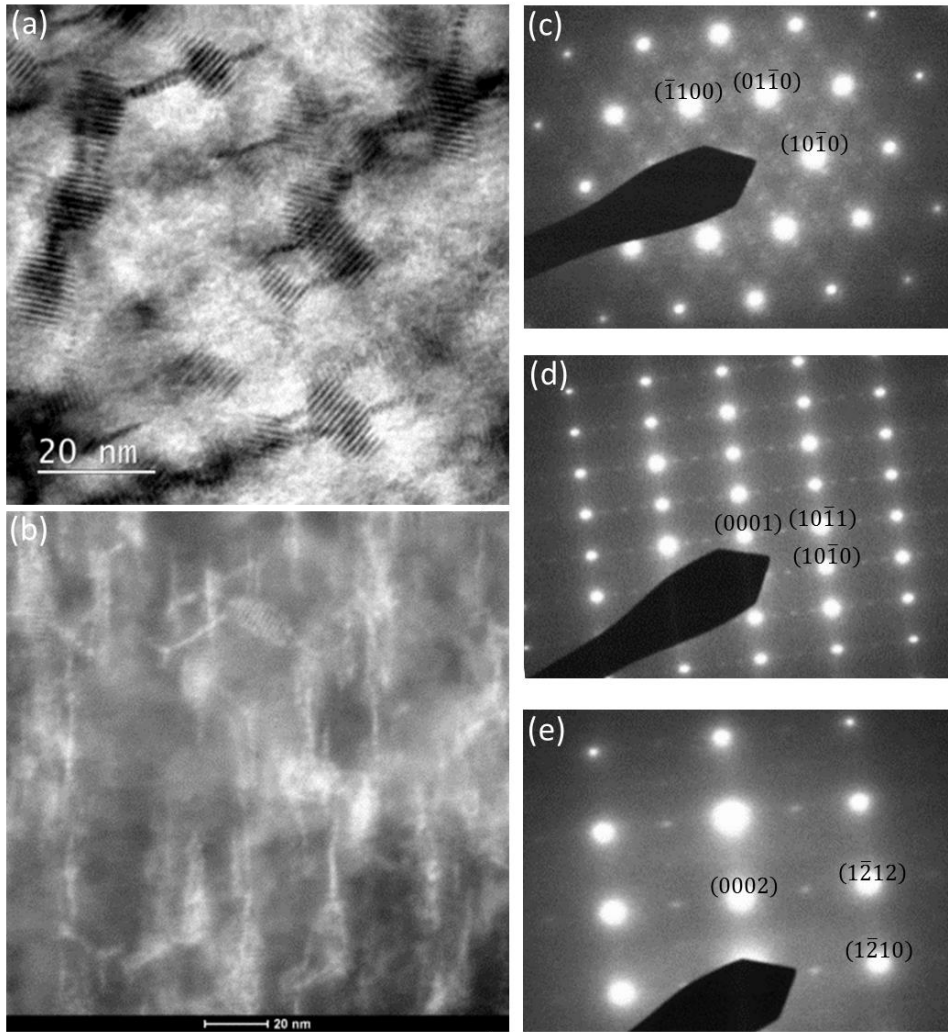


Figure 2.3: TEM characterization of precipitate microstructure of WE43-T5 including (a) bright-field TEM, (b) high angle annular dark field (HAADF) STEM, and (c-e) selected area electron diffraction patterns along $[0001]$, $[11\bar{2}0]$ and $[10\bar{1}0]$ zone axes, respectively.

2.5.2 Modeling the quasistatic response

The experimental texture obtained from various depths of both the WE43-T5 plates were averaged and discretized to obtain a set of 2000 and 16000 orientations with volume fractions representing the measured textures (Figure 2.1). The initial fitting of the crystal plasticity model was carried out with the smaller (more computationally efficient) grain set after which the larger grain set was employed for obtaining the final parameters. Little change was observed when

employing the larger grain set. However, it is notable that the predicted twin volume fraction decreased slightly when the larger grain set is used.

The modeling strategy is similar to that used in earlier studies (Jain and Agnew, 2007; Bhattacharyya et al., 2015). The initial texture of the material is such that, during in-plane (RD and TD) tension, most of the strain is accommodated by the basal and prismatic slip modes. Hence, the tensile data are used to determine the appropriate parameters governing these two modes. Again, due to the initial texture, the c-axes of many grains are near parallel to ND and thus, prismatic slip and extension twinning is not favored during ND compression. The strain is accommodated by pyramidal $\langle c+a \rangle$ slip. Hence, the ND compression data is used to determine the parameters of this mode. It is to be noted that the basal slip parameters influence the yield strength and the hardening rate for all loading conditions. After the initial round of fitting, the r-value of RD tension is used to constrain the ratio between the CRSS values $\tau_{\text{prism}} : \tau_{\text{basal}}$ and $\tau_{\langle c+a \rangle} : \tau_{\text{basal}}$. For instance, increasing the ratio of prismatic to basal CRSS, decreases the r-value for RD and TD tension. On the other hand, increasing the ratio of the $\langle c+a \rangle$ to basal CRSS values leads to an increase in the r-value (Agnew and Duygulu, 2005). Once the CRSS values are determined, the hardening parameters of these two modes are adjusted to fit the macroscopic hardening behavior, while ensuring that the relative activities are still appropriate to model the r-values. Finally, in-plane compression data were used to obtain the parameters for $\{10\bar{1}2\}$ extension twinning. The twinning is modeled with a linear hardening, where the experimentally observed twin volume fraction served as guide to select the values of τ_0 and θ_0 .

It is to be noted that the initial round of fitting was carried out with “same” latent hardening, where all the coefficients of the LH matrix are equal to 1. For this case, the in-plane tension r-values were consistently over-predicted to values greater than 2, depending on the

strength ratios used, and no set of CRSS values could be obtained which fitted the flow curves and simultaneously gave the correct r -values. Thus it was deemed necessary to include the latent hardening as described in Section 2.4.4. The key effect of incorporating the latent hardening can be understood from the coefficients presented in Table 2.1. It can be seen that the basal slip mode is hardened considerably by both prismatic and $\langle c+a \rangle$ slip modes, whereas the $\langle c+a \rangle$ mode is not strongly hardened by either basal or prismatic. The nature of the interactions leading to formation of such weak obstacles in the latter case, compared to the strong ones for the former case, has been discussed by Bertin et al., (2014). Figure 2.4 shows an example where the parameters shown in Table 2.2 were used with LH coefficients all equal to 1 (same hardening) in one case and in another with the LH matrix given in Table 2.1. The in-plane tension r -values evolve in a significantly different manner while the flow curves and ND and RD compression r -values remains essentially unaffected. In absence of latent hardening, a higher value of $\langle c+a \rangle$ slip strength is required to match the ND compression flow curve which leads to a significant increase in the r -value for in-plane tension. The Voce thus parameters obtained for the quasistatic case are presented in Table 2.2.

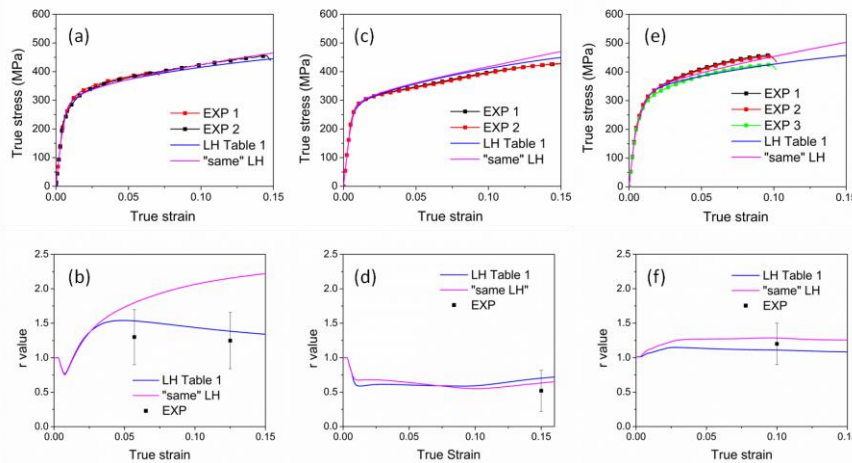


Figure 2.4: Flow curves and variation of r value with strain : (a) and (b) for RD-t, (c) and (d) for RD-c and (e) and (f) for ND-c at QSR with “same” LH parameters (i.e. all coefficients equal to 1) and LH parameters given in Table 2-1.

Table 2.2: Voce hardening parameters for simulating experimental data at 0.001/s (units in MPa).

	τ_0	τ_I	θ_0
Basal	68	40	170
Prismatic	145	90	170
$\langle c+a \rangle$ 2 nd order	210	205	350
Tensile twin	130	0	150

Notice that the initial hardening rates for $\langle a \rangle$ slip are in the range of $\mu/100$, which is typical of FCC metals and alloys (Kocks and Mecking, 2003), whereas that of $\langle c+a \rangle$ slip is a factor of 2 larger, which respects the fact that the Burgers vector is about a factor of 2 larger. Notice also that many researchers have required much higher strain hardening rates in their modeling work, particularly if VPSC is employed. This is due to the fact that the apparent strain hardening in Mg is initially dominated by a protracted elasto-plastic transition and not due to dislocation interactions alone (Agnew et al., 2003). In the following subsections, the experimental and simulated flow behavior, anisotropy, texture and microstructure evolution for different loading directions examined under quasistatic rates will be presented first, followed by the high strain rate tests.

2.5.2.1 In-plane tension.

For RD and TD tension (Figure 2.4a and Figure 2.5a respectively), the shape of the flow curve is typical of dislocation-mediated plasticity. The relative activities (Figure 2.5b) show that although the basal slip and extension twinning is activated earlier, the macroscopic yielding is associated with the onset of prismatic slip, which occurs at 250 MPa. This is in accordance with previous studies (Agnew et al., 2003) where internal strain evolution and EPSC modeling have shown that during in-plane tension of basal textured Mg, prismatic slip determines the macroscopic yield. The strain accommodation right from the onset of yielding up to higher strain levels is dominated by prismatic slip. The r-value for RD tension (Figure 2.4b) is ~ 1.2 which

indicates only slightly more rapid Poisson contraction along TD than ND. It is interesting to note that, even though the r -values for in-plane uniaxial tension are greater than 1, the RD and TD exhibit similar level of plastic strain anisotropy (Table 2.3). This is contrary to strongly textured AZ31 sheets/plates which exhibit a significantly higher r -value in case of TD tension as compared to RD (Agnew and Duygulu, 2005).

Table 2.3: The r -values obtained experimentally and from the EPSC model along with the strain at which the measurements were conducted.

Loading condition	at 0.001/s			at 1000/s		
	ϵ (%)	Exp	Sim	ϵ (%)	Exp	Sim
RD-t	5.5	1.3 ± 0.4	1.48	9.4	1.5 ± 0.3	1.64
	12.5	1.2 ± 0.4	1.38	-	-	-
TD-t	3	1.3 ± 0.6	1.53	13.8	1.6 ± 0.3	1.42
	10	1.3 ± 0.2	1.40	-	-	-
ND-t	8	1.2 ± 0.3	1.09	5.8	1.2 ± 0.2	1.05
RD-c	15	0.5 ± 0.3	0.67	15	0.5 ± 0.3	0.66
TD-c	8.1	0.5 ± 0.3	0.68	12.8	0.5 ± 0.3	0.65
	-	-	-	15.2	0.6 ± 0.3	0.66
ND-c	10	1.2 ± 0.3	1.09	18	1.2 ± 0.3	1.05

The $\{10\bar{1}0\}$ pole figures (Figure 2.1) show that the initial texture is almost radially symmetric about ND. In comparison, the $\{10\bar{1}0\}$ pole figures of samples deformed under in-plane tension have the highest intensity along loading direction (Figure 2.5c and Figure 2.5d), which is indicative of the activity of prismatic slip. However, a strong 6-fold symmetry is absent even though prismatic slip controls the flow behavior, because other modes like basal and $\langle c+a \rangle$ slip are also significantly active, and this tends to moderate the texture evolution due to prismatic slip alone.

A few extension twins (outlined in green) can be seen in the band contrast map (Figure 2.6a), and this in accordance with the model prediction (activity plot). An ND-IPF map of the same area (Figure 2.6b) shows that most grains have their c -axis parallel to ND, indicating that will have deformed by prismatic slip. Studies of the intragrain misorientation axes (IGMA, not shown in the interest of space) show that these expectations are correct (see (Chun and Davies,

2011; Hadorn et al., 2012) for how IGMA can be employed in such studies). One other observation is that the harder twinning modes, such as $\{10\bar{1}1\}$ and $\{10\bar{1}3\}$ contraction twins and the $\{10\bar{1}1\}$ - $\{10\bar{1}2\}$ “double” twins, are rarely observed in this loading condition.

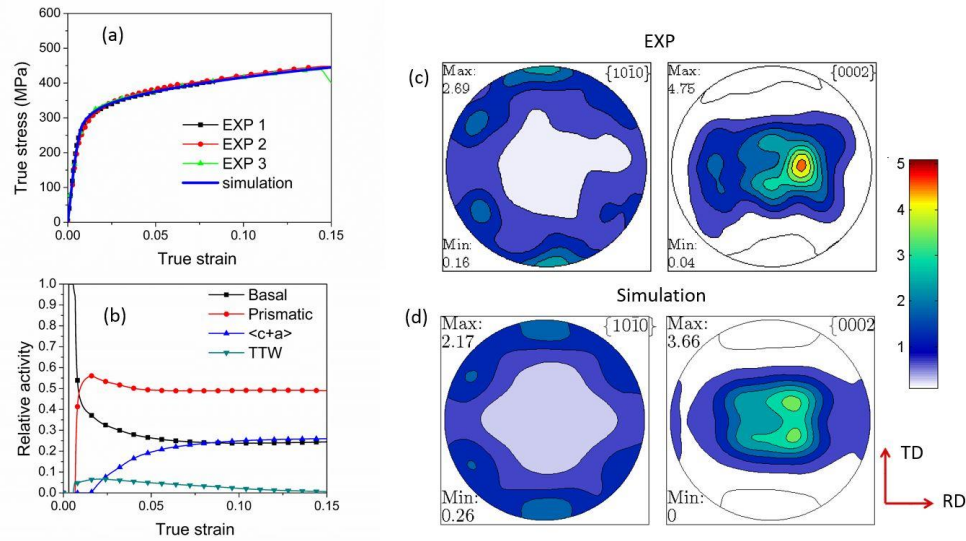


Figure 2.5: Experimental and simulated results for TD tension tested at QSR (a) flow curves, (b) relative activities of deformation modes, (c) and (d) texture evolution after 14% strain.

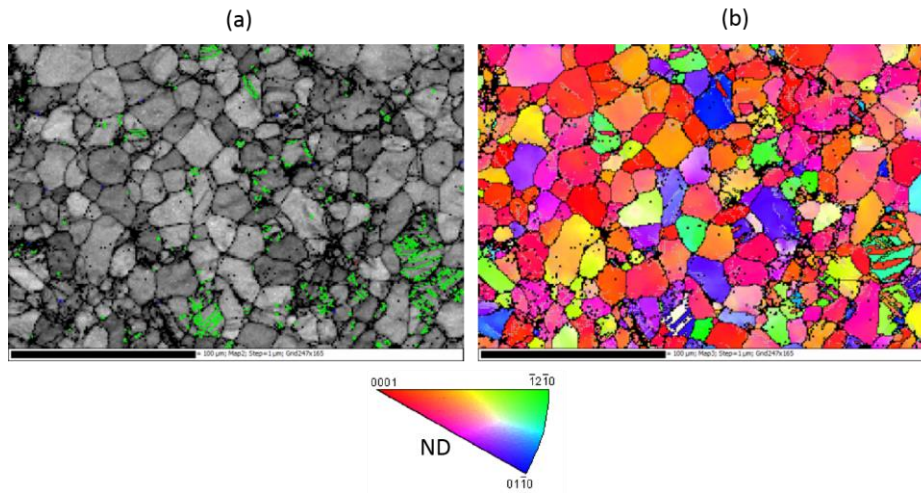


Figure 2.6: EBSD maps from a RD tension sample deformed at QSR (a) Band contrast map showing presence of extension twins (boundaries outlined in green) and (b) ND-IPF map of the same region showing most grains have c-axis parallel to ND post deformation indicating they deformed by prismatic slip.

2.5.2.2 In-plane compression

In the case of RD compression, the flow curve shows a low initial hardening rate followed by a slight increase (Figure 2.4c). The TD compression flow curve is similar (Figure 2-7a). Interestingly, the activity plots (Figure 2.7b) reveal that the sharp macroscopic yielding is controlled by activation of prismatic slip and not by extension twinning alone. In fact, at higher strain levels, both twinning and prismatic slip are similarly active. Another interesting feature is that $\langle c+a \rangle$ slip is also quite active from the start of deformation and tends to dominate the deformation once twinning is exhausted. The r -value is ~ 0.6 (Figure 2-4d) which indicates larger strain accommodation along ND than TD, another indication of extension twinning activity (Lou et al., 2007). The r -value evolution is similar for RD and TD (Table 3) the only slight difference being due to the fact that basal slip is slightly less active and prismatic slip is slightly more active due to the initial texture.

The $\{0002\}$ pole figures (Figure 2.7c and Figure 2.7d) reveal that the texture evolution during in-plane compression is typical of twinning activity, where the c -axis, initially aligned close to ND, reorients towards the loading axis. The splitting in the basal poles is due to $\langle c+a \rangle$ activity in the reoriented grains following twinning exhaustion. Figure 2.7e shows a ND-IPF map of a sample tested in compression along TD up to 12% strain. It can be seen that most of the grains, which have the twin orientation, are fully reoriented. Therefore, only a few twin lamellae, associated with partially twinned grains, can be seen. The twin volume fraction along RD is less than TD (Figure 2.8). This is expected since the initial texture favors basal slip slightly more during RD compression. Another noteworthy feature is that the volume fraction of twinning is only $\sim 40\%$ which is much less than that observed in case of AZ31 (Clausen et al., 2008; Wang et al., 2013), suggesting that twin nucleation and growth are considerably harder in this alloy. In

order to model both the flow stress and twin volume fraction (and texture) evolution; it was deemed necessary to set the CRSS of twinning close to that of prismatic slip.

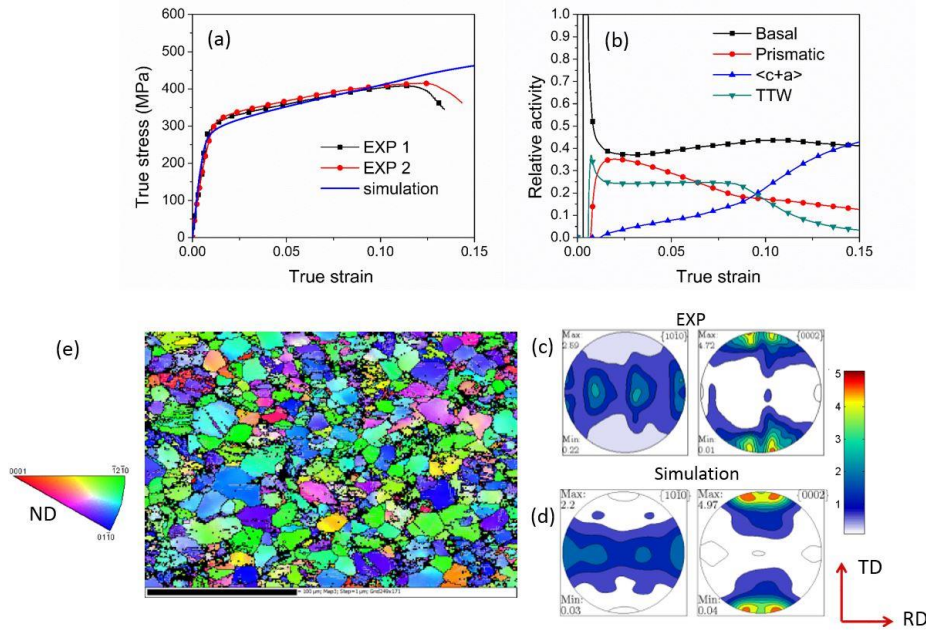


Figure 2.7: Experimental and simulated results for TD compression tested at QSR (a) flow curves, (b) relative activities of deformation modes, (c) experimental texture measured using XRD, (d) simulated texture evolution and (e) ND-IPF map showing the grains which have the twin orientation have reoriented completely.

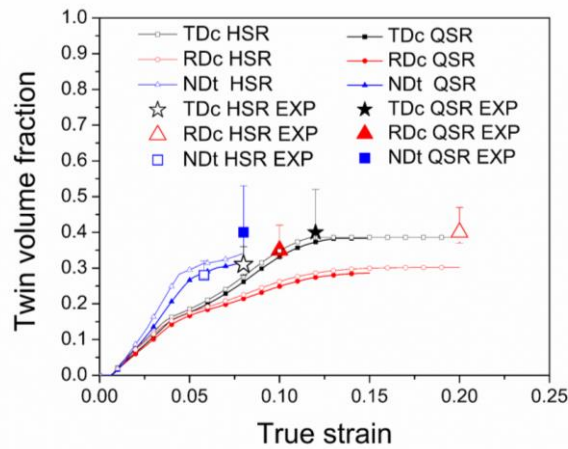


Figure 2.8: Experimental and simulated twin volume fraction as a function of strain for RD compression, TD compression and ND tension for both quasistatic and dynamic strain rate. The experimental data points are based on $\theta = 33^\circ$, while the error bars represent the lower and upper bounds, obtained based on $\theta = 30^\circ$ and $\theta = 40^\circ$ respectively.

In summary, it is noted that the model is successful in reproducing the shape of the compression curves for both RD and TD, however, it slightly (~5%) over-predicts and under-predicts the flow stress for RD compression and TD compression case, respectively. This is most likely related to twin nucleation phenomena and will be discussed later. In any case, the small degree of tension-compression yield strength asymmetry present along RD and TD is captured by the model.

2.5.2.3 Through-thickness compression

The experimental flow curves for ND compression (Figure 2-4e) show some variability. Overall, the simulated flow curve matches well with the experimental data, given the amount of scatter present (Figure 2-4e). After a protracted elasto-plastic microyielding regime, the flow curves exhibit parabolic hardening, which is distinctive from in-plane compression. The r -value (Figure 2-4f) is slightly greater than 1, which implies a slight larger straining along RD than TD. This is again due to the initial texture, where the tilt of the basal poles towards RD, enables basal slip to accommodate a larger fraction of strain along RD than TD. The relative activity plots (Figure 2-9a) reveal that basal and prismatic slip and some twinning activity are responsible for the microyielding behavior, whereas the flow stress is controlled by $\langle c+a \rangle$ slip following macroscopic yielding at ~ 300 MPa.

The $\{0002\}$ pole figures (Figure 2-9b and Figure 2-9c) show a texture evolution which is typical when basal slip and $\langle c+a \rangle$ slip dominates the flow behavior. The splitting of the basal poles along RD is due to the competition between these two modes and is dictated by the relative activities of the two slip modes. One representative band contrast map (Figure 2-9d) shows that secondary twinning modes, such as $\{10\bar{1}1\}$ and $\{10\bar{1}3\}$ contraction twins (highlighted in red) and $\{10\bar{1}1\}$ - $\{10\bar{1}2\}$ “double” twins (highlighted in blue), are rarely present and support the

decision to attempt to capture all such deformation modes under a single mechanism of $\langle c+a \rangle$ slip during the crystal plasticity modeling.

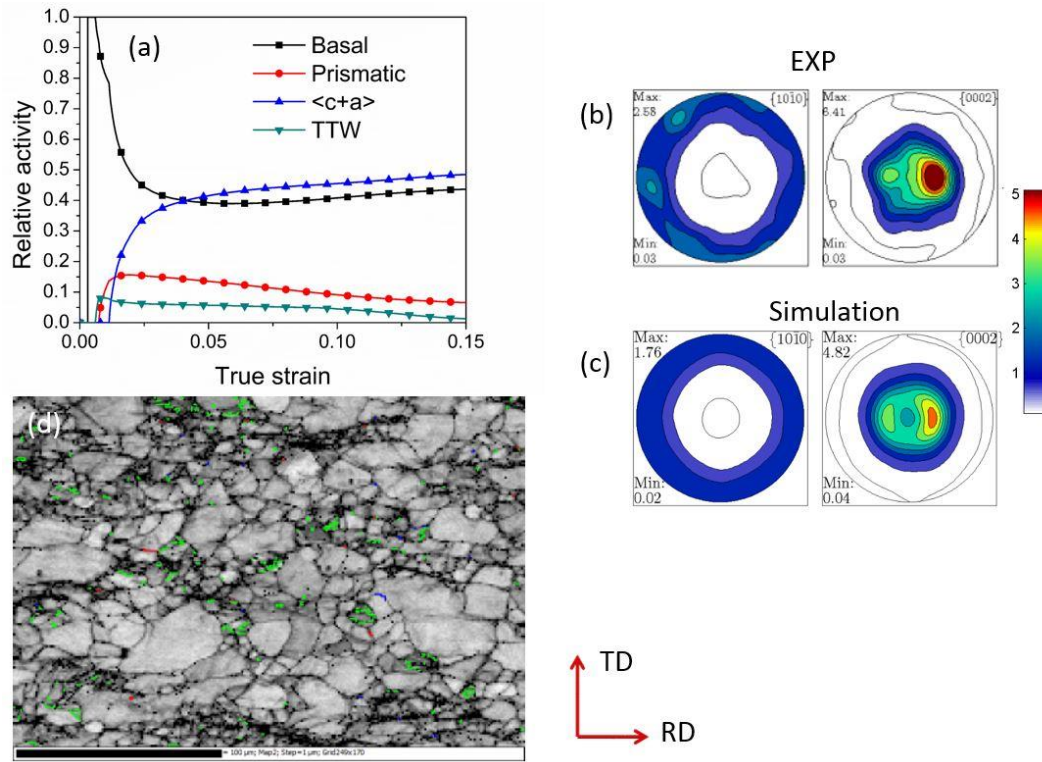


Figure 2.9: Experimental and simulated results for ND compression tested at QSR (a) relative activities of deformation modes, (b) and (c) texture evolution and (d) band contrast map highlighting various twin boundaries, same color coding as Figure 2-6.

2.5.2.4 Through-thickness tension

The ND tension case has the lowest flow stress out of all the tests carried out (Figure 2-10a). Thus, the highest level of tension compression strength asymmetry is along ND. However, since the model over-predicts the ND tension flow stress by $\sim 8\%$, it under-predicts the level of asymmetry along this direction. Following a sharp yield behavior, the flow curve exhibits the same shallow linear hardening observed experimentally. The relative activity plot (Figure 2-10b) shows that the flow stress is controlled by twinning, although prismatic slip is active throughout and dominates at strains $> 5\%$. The r -value evolution for ND tension is similar to that observed

during ND compression (Table 3) being slightly greater than 1, indicating a larger fraction of strain accommodation along RD than TD, due to the initial tilt of the basal poles towards RD.

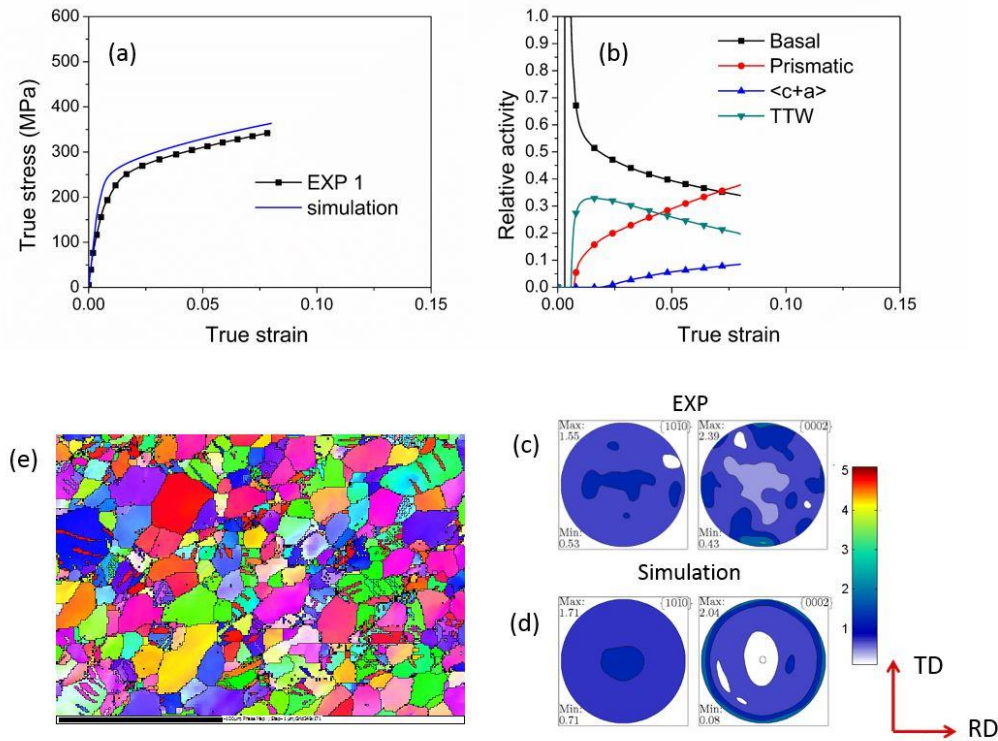


Figure 2.10: Experimental and simulated results for ND tension tested at QSR (a) flow curves (b) relative activities of deformation modes, (c) and (d) texture evolution, and (e) ND-IPF map showing most grains have reoriented by twinning while a few thin lamellae of a single variant is present within the grains.

The texture evolution (Figure 2.10c and Figure 2.10d) is dramatic since extension twinning is the dominant deformation mode. The grains having their c-axis initially along the ND reorients by 90° due to twinning and lies in the plane of the plate and thus leads to a significant weakening of the basal texture intensity. The experimental and simulated twin volume fraction is shown in Figure 2.8. It can be seen that the model is able to capture the volume fraction of twins despite the overestimation of the flow stress. This suggests that the predicted, relative activities of the different modes are correct.

Representative IPF map, is shown in Figure 2.10e. Only a few tensile twin lamellae are present, while the majority of the grains are completely reoriented. This is why the fitting parameters $A1$ and $A2$ of the TDT model were set to 1, allowing complete reorientation of the grains. Out of the remaining grains containing twin lamellae, only a few have more than one twin variant. Moreover, the twin lamellae are thin and needle like indicating that their growth was strongly hindered.

2.5.3 Modeling the high strain rate response

Once the Voce parameters for the quasistatic tests are obtained, the high strain rate data is modeled with these parameters as a baseline. While obtaining the parameters for dynamic rates, the following hypotheses were explored: 1) basal slip and twinning are essentially athermal within the rate regime considered; 2) prismatic and $\langle c+a \rangle$ are thermally activated hence rate sensitive; and 3) the strain hardening rate θ_0 is rate independent although θ_0 / τ_I is proportional to the rate of dynamic recovery. Since the measurement of the response, at the initial stages of the dynamic tests, is inaccurate (Gama et al., 2004), the 1% offset strains have been chosen to obtain the CRSS parameters. The Voce parameters thus obtained are presented in Table 2.4.

Table 2.4: Voce hardening parameters for simulating experimental data at 1000 /s (units in MPa).

	τ_0	τ_I	θ_0
Basal	68	40	170
Prismatic	162	100	170
$\langle c+a \rangle$ 2 nd order	225	230	350
Tensile twin	130	0	150

2.5.3.1 In-plane tension

For in-plane tension at dynamic rates, the yield strength and the flow stress is slightly higher than at quasistatic rates. This can be successfully modeled by increasing the CRSS, τ_0 ,

and the saturation stress, $\tau_0 + \tau_1$, of prismatic slip. As was the case for quasistatic flow, the tensile behavior (Figure 2.11a and Figure 2.11b) and relative activities (Figure 2.11c) along TD are very similar to RD, except for the fact that basal slip is slightly less active along TD due to the initial texture. Note that, for the dynamic tensile tests, the flow curves were smoothed (see Figure 2.11a) using the adjacent averaging algorithm in ORIGIN 7.5 to eliminate the oscillations which are present at low strains due to dispersive wave propagation in the incident bar (Gama et al., 2004).

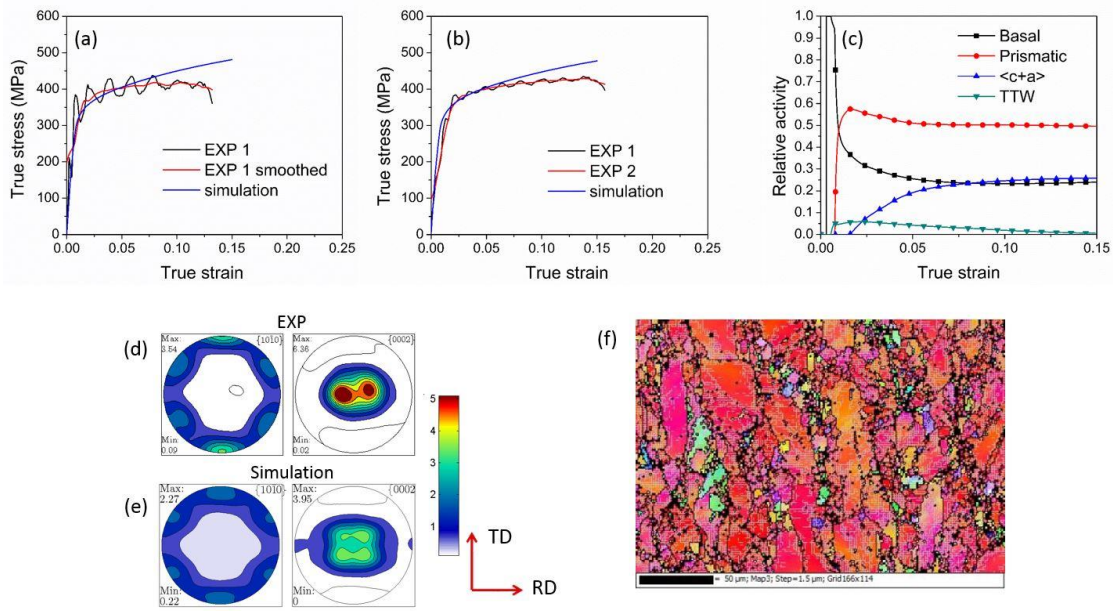


Figure 2.11: Experimental and simulated flow curves for samples tested at HSR (a) for RD tension (b) TD tension (c) relative activities plot, (d) and (e) texture evolution and (f) ND-IPF map revealing dislocation substructures for the TD case.

Unlike the flow stress, the apparent strain hardening rate at dynamic rates is reduced, as compared to the quasistatic case. The authors of this paper hypothesize that this reduction in tensile hardening rate is related to localization and damage evolution and not to the intrinsic thermal activation of dislocations. The possible effect of adiabatic heating will be discussed later. It is to be noted that no attempt has been made to model the softening/localization behavior since

the mean-field EPSC model is not capable of capturing such effects. Hence the same hardening parameters are used for the present high rate simulations as were employed in the quasistatic.

The r -value is ~ 1.5 (Table 2.3) and the increase in the r -value from the quasistatic case is due to two causes. First, there is a change in the relative strength of deformation modes, and second, the initial texture of plate # 6457 is stronger than that of plate # 9849. The $\{10\bar{1}0\}$ pole figures (Figure 2.11d and Figure 2.11e) of the samples deformed in in-plane tension have a more prominent 6-fold appearance than as compared to the quasistatic case. Again, this is due to the fact that the initial texture is slightly stronger, which reduces the activities of other deformation modes (basal and $\langle c+a \rangle$ slip). The slight discrepancy between the experimental and simulated textures for in-plane tension stems from the fact that the simulations overestimate the activity of $\langle c+a \rangle$ slip predicted at the higher strain levels. This is due to the high stresses, which the real sample never experienced, most likely because of the aforementioned premature onset of damage.

One representative ND-IPF map, from a sample tested in TD tension until failure, is shown in Figure 2.11f. The grain boundaries having misorientation $2-15^\circ$ are highlighted in grey. The significant intragranular misorientation and presence of dislocation substructures indicate that slip is the preferred strain accommodation mechanism even at higher rates.

2.5.3.2 Through-thickness compression

In the case of ND compression, by increasing the CRSS, τ_0 , and the saturation stress, $\tau_0 + \tau_1$, of $\langle c+a \rangle$ slip, the yielding hardening behavior and flow strength can be modeled adequately (Figure 2.12a). The splitting of the regions of peak intensity in the basal pole figures (Figure 2.12b and Figure 2.12c), suggests that $\langle c+a \rangle$ is active even at high strain rates. The kinematics demand a very similar level of $\langle c+a \rangle$ slip mode activity under dynamic loading

conditions, even though the strength for this mechanism is increased, consistent with the notion that this thermally activated mechanism is harder at high rates. One representative band contrast map, from a sample tested in ND compression until failure, is shown in Figure 2.12d. Again, the volume fraction of secondary twinning modes, such as $\{10\bar{1}1\}$ and $\{10\bar{1}3\}$ contraction twins and the $\{10\bar{1}1\}$ - $\{10\bar{1}2\}$ “double” twins is much lower than the primary extension twins, indicating that these twinning modes are hard, relative to competing modes, even at dynamic rates. This supports the decision to attempt to capture all such deformation modes under a single mechanism of $\langle c+a \rangle$ slip even up to strain rates investigated in this study, as previously suggested (Agnew et al., 2006).

2.5.3.3 In-plane compression

The RD compression flow curve can be successfully modeled with no further changes to the parameters (Figure 2.13a). Hence, it serves as a validation. Contrary to in-plane tension at high rate, the hardening rate for this case is very similar to the quasistatic case. However, the TD compression flow curve is under predicted by the simulation (Figure 2.13b). As observed for the quasistatic case, the model is unable to capture the asymmetry between RD and TD compression and this deviation is more prominent at dynamic rates. The $\{0002\}$ poles align with the loading axis again indicating the occurrence of twinning (Figure 2.13c and Figure 2.13d) and it can be seen that a higher twin volume fraction is observed for both RD and TD compression under dynamic loading (Figure 2.8). This increase in the relative twin activity as compared to prismatic slip, can be rationalized by the fact that prismatic slip is harder at higher strain rates.

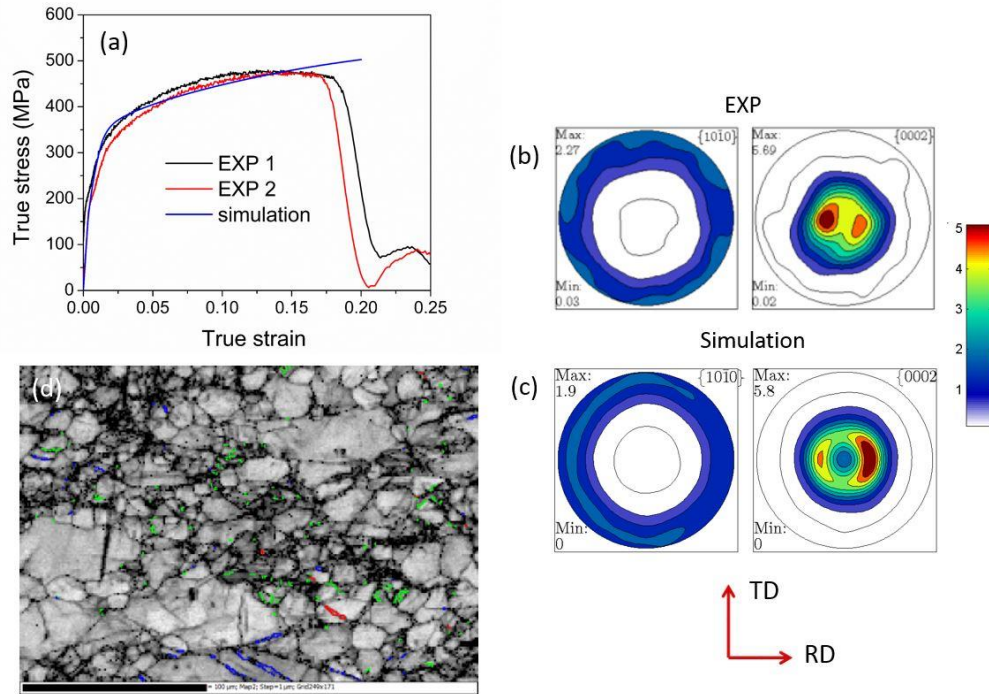


Figure 2.12: Experimental and simulated result for ND compression tested at HSR (a) flow curves (b) and (c) texture evolution and (d) band contrast map showing contraction and double twins are rare even at dynamic rates (same color coding as Figure 2-6).

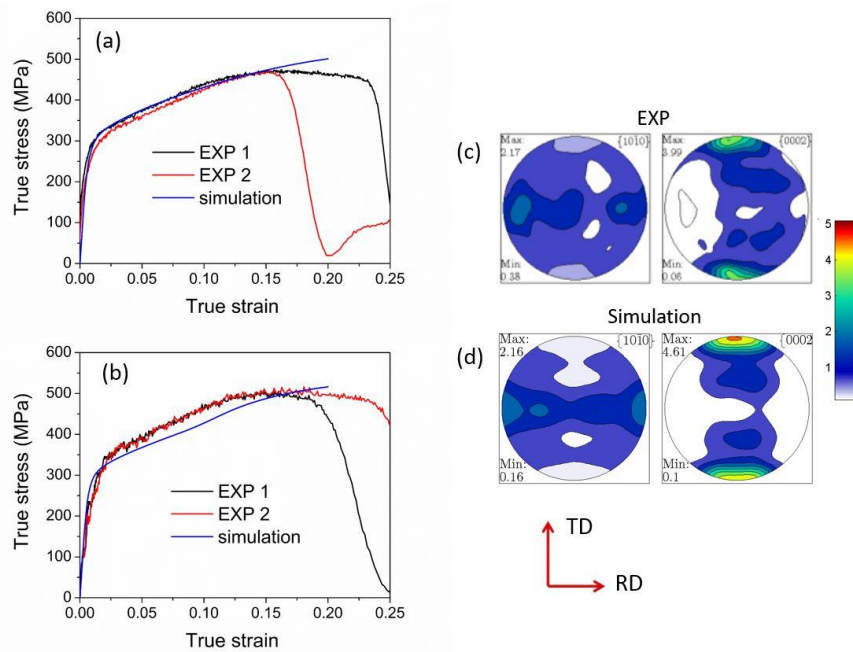


Figure 2.13: Experimental and simulated flow curves for samples tested at HSR (a) RD compression (b) TD compression and (c) and (d) shows experimental and simulated pole figures for TD compression.

2.5.3.4 Through-thickness tension

The simulation of ND tension determines whether or not the twinning parameters (which control yielding) and relative activities of other modes mainly, prismatic slip (which control higher strain plasticity in this case) are appropriate. Similar to the quasistatic case, this loading condition exhibits the lowest flow stress due to extension twinning (Figure 2.14a). The simulated flow curve again overestimates the flow stress slightly, which leads to an underestimation of the strength asymmetry along ND. The relative activities (Figure 2.14b), r -value evolution (Table 2.3) and texture evolution (Figure 2.14c and Figure 2.14d) are quite similar to the quasistatic case, where twinning controls the flow behavior along with some prismatic slip activity.

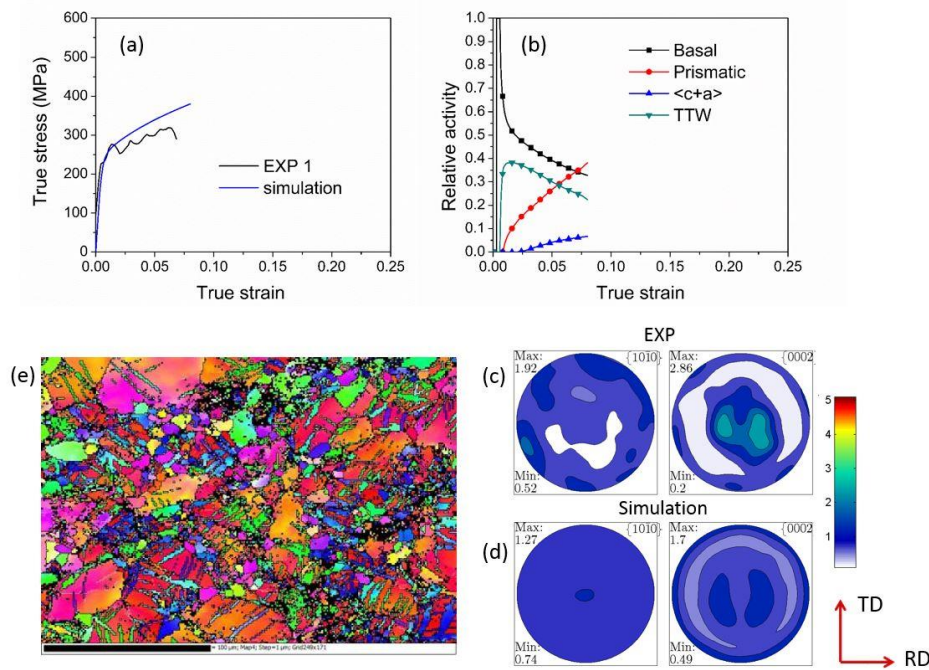


Figure 2.14: Experimental and simulated results for ND tension at HSR (a) flow curves (b) relative activity plot (c) and (d) experimental and simulated pole figures respectively and (e) ND-IPF showing multiple variants of twins present as twin intersecting lamellae.

One representative ND-IPF map, from a sample tested in ND tension until failure, is shown in Figure 2.14e. Contrary to the quasistatic case, quite a few tensile twin lamellae are present while only some of the grains are completely reoriented. One reason for this is because the sample tested at dynamic rates failed at a low strain of $\sim 6\%$ before twinning is exhausted. Out of the remaining grains containing twin lamellae, only a few have more than one twin variants. Again, the twin lamellae are thin and needle like indicating that their propagation is strongly hindered. The twin volume fraction (Figure 2.8) is adequately modeled even though the twin parameters were left unchanged.

From Figure 2.8, it can be seen that the twin volume fraction is higher at higher strain rate for all the three loading conditions which favor extension twinning. This indicates that twinning activity increases with increase in strain rate; which is consistent with earlier results on α -Ti (Chichili et al., 1998) and Mg alloy, AZ31 (Li et al., 2012). The model results suggest that the higher activity of twinning is not due to a decrease in the strength of the twinning mode. Instead, the small but positive strain rate sensitivity of the hard slip modes leads to an increase in the relative activity of twinning.

The fact that the flow curves for samples tested along different directions can be reproduced by changing only the strength of prismatic and $\langle c+a \rangle$ is consistent with the existing literature, where it is well established that prismatic and $\langle c+a \rangle$ slip are thermally activated at ambient temperatures, while basal slip and extension twinning are essentially rate insensitive at ambient temperatures (Conrad et al., 1961; Obara et al., 1973). It is also consistent with recent experimental results on other Mg alloys (Li et al., 2009; Ulacia et al., 2010).

2.6 Analysis and Discussion

The deformation mode activities and texture evolution of this alloy, WE43-T5, are in general rather typical of Mg alloy sheets and plates. However, there are also important distinctions with the conventional alloys. For example, in order to describe the observed yield behavior, it was necessary to set the CRSS of basal slip quite high. Moreover, in order to obtain the appropriate twin volume fraction, it was found necessary to set the CRSS and hardening rate of extension twinning very close to that of the prismatic slip.

2.6.1 Rate sensitivity of individual deformation modes

It is well known that dislocation based plastic deformation is a thermally activated process and the shear strain rate can be described by an Arrhenius type relation (e.g., Argon, 2008):

$$\dot{\gamma} = \dot{\gamma}_0 \exp\left(\frac{-\Delta G(\tau^*)}{kT}\right) \quad (2-9)$$

where, k is the Boltzmann constant, T is the absolute temperature, $\Delta G(\tau^*)$ is the activation energy which is a function of stress: $\tau^* = \tau_a - \tau_\mu$ where, τ_a is the applied stress and τ_μ is the athermal stress resulting from long range obstacles. The pre-exponential term $\dot{\gamma}_0 = NAbv_0$ where N is the number of possible activation sites, A is the area swept by the dislocation, b is the Burgers vector and v_0 is the vibration frequency of the dislocation segment against an obstacle, $\sim 10^{11}/s$ (Diak et al., 1998).

The primary thermodynamic parameters that can be experimentally determined to characterize the material response are the engineering strain rate sensitivity (eSRS) of the flow stress m :

$$m = \frac{\partial \ln \tau}{\partial \ln \dot{\gamma}} \quad (2-10)$$

and the activation volume $V = bA$, which can be obtained by taking the derivative of the activation energy $\Delta G(\tau^*)$ with respect to stress at constant temperature and substructure (Argon, 2008; Caillard and Martin, 2003; Diak et al., 1998):

$$V = - \left[\frac{\partial(\Delta G)}{\partial \tau^*} \right]_{T,S} = kT \left(\frac{\partial \ln \dot{\gamma}}{\partial \tau^*} \right)_{T,S} = \frac{kT}{m\tau} \quad (2-11)$$

The aforementioned activation area can also be represented as $A = l_F d$, where l_F is the length of the dislocation segment involved in the activation process which can be considered equal to the Friedel sampling length, and d is the distance swept out by the dislocation segment during one activation process, i.e. the activation distance. Different obstacles, such as cross-slip by kink pair nucleation mechanism, forest cutting and solute atoms each have a characteristic l_F and d . Thus, an analysis of these thermodynamic parameters V and m can provide insight on the rate controlling mechanisms in the plastic deformation of metals. It is to be emphasized that it is necessary to determine these parameters at constant substructure in order to obtain an accurate description of the rate controlling processes, and we acknowledge that the calculations which follow are thus only an approximation performed in order to provide some insight about the processes involved.

The experimentally observed strain rate sensitivities, m , were published previously (Bhattacharyya et al., 2015). There are some inherent problems with using this approach for the tensile loading condition, because the high and low strain rate data were obtained from two different plates, which had distinct textures (Figure 2.1). On the other hand, employing a polycrystal plasticity model allows one to explicitly account for the fact that the initial textures are distinct. After the grain-level properties are obtained, the polycrystal plasticity model can be used to *predict* the aggregate-level strain rate sensitivities.

The CRSS values, as obtained from the EPSC model, also permit isolation of the strain rate sensitivities of the individual deformation modes. For example, it is found that by keeping the basal and twinning strength constant (same as the quasistatic case) and by increasing the strength of prismatic and $\langle c+a \rangle$ slip, the high strain rate experimental data, can be modeled successfully. This is in line with the well-known athermal nature of basal slip at room temperatures and above (Conrad et al., 1961), as well as the athermal nature of extension twinning (Ulacia et al., 2010). It is important to note that the athermal nature of these deformation modes was not assumed. Rather, neither slight increases nor decreases in the CRSS values of these slip systems was found to improve the model predictions. In fact changes of more than 5 and 10 MPa, for basal and twinning mode, respectively, gave rise to problems in one or more aspects of the predictions. This permits an estimate of the uncertainty in the obtained zero rate sensitivity values of ± 0.007 and ± 0.008 , respectively.

Based on the EPSC model parameters presented in Table 2.2 and Table 2.4, the CRSS of the flow stress (τ_0 and $\tau_0 + \tau_1$) of the prismatic slip mode show a strain rate sensitivity $m = 0.008 \pm 0.006$ and 0.008 ± 0.004 , respectively. The uncertainties in the rate sensitivities have been calculated based on the uncertainties in the stresses and strain rates, using standard error propagation rules. The corresponding activation volume is $105b^3$. The thermally activated nature of prismatic slip is well known (Akhtar and Teghtsoonian, 1969; Raeisinia et al., 2010; Yoshinaga and Horiuchi, 1964). In fact, in-situ measurements on pure Mg single crystals by Couret and Caillard (1985a; 1985b) have established the microscopic and macroscopic activation area to be $9b^2$ and $30b^2$ respectively. They established that the motion of prismatic dislocations on prismatic planes is controlled by the pseudo-Peierls (or Friedel-Escaig) mechanism, which

involves repeated dissociation of $\langle a \rangle$ dislocations on close-packed basal planes, movement by thermally activated kink pair nucleation and subsequently recombining on prism planes.

However, the present alloy contains Y and Nd, and thus interaction of $\langle a \rangle$ dislocations with these solutes can be the rate controlling mechanism, leading to a higher activation volume. In order to investigate this possibility, the activation volume due to glide of dislocations across solutes have been computed. Assuming a Fleischer (1961) approximation, A can be computed:

$$A = \frac{b^2}{c_b} \quad (2-12)$$

where c_b is the atomic concentration of the solute species. Consultation with the phase diagrams (Rokhlin et al., 2004) suggests $c_b = 1.0$ at%. Thus, the activation area $A = 100b^2$ corresponding to an activation volume $V = 100b^3$.

To check the possibility that interaction with forest dislocations is the rate controlling process, the activation volume corresponding to a rectangular force-distance profile is calculated according to the following relationships (e.g., Caillard and Martin, 2003):

$$V = l_F bw \quad (2-13)$$

where, w is the width of the dislocation core $\sim 5b$ and

$$l_F = d \left(\frac{\mu b}{\tau d} \right)^{1/3} \quad (2-14)$$

Since the average forest dislocation spacing $d = \frac{\mu b}{\tau}$, $V = 5\mu b^3/\tau$. Using the CRSS value of prismatic slip i.e. 145 MPa, V is obtained as $\sim 600b^3$, which is much greater than the value obtained based on the modeling results. Thus, it seems that the rate controlling mechanism for prismatic slip in this alloy is mainly due to interaction of $\langle a \rangle$ dislocations with solutes.

The CRSS of $\langle c+a \rangle$ slip mode exhibits a strain rate sensitivity of 0.005 ± 0.004 , which corresponds to an activation volume $V = 17b^3$. If $\tau_0 + \tau_1$ is considered, the rate sensitivity is

0.007 ± 0.002 , $V = 6b^3$. It is to be noted that the activation volume appears to be much lower than prismatic slip but one has to be careful, since the Burgers vector of $\langle c+a \rangle$ is almost twice large as $\langle a \rangle$ type dislocation. The rate sensitivities correlate well with the experimentally observed rate sensitivity during ND compression (Agnew et al., 2014), which is the direction along which $\langle c+a \rangle$ slip is most active. In fact, based on their TD tension and ND compression results, Ulacia et al. (2010) also suggested that the CRSS of prismatic slip is more rate sensitive than that of pyramidal $\langle c+a \rangle$ slip.

$\langle c+a \rangle$ slip is clearly thermally activated, as the strength is shown to dramatically decrease with increasing temperature (Obara et al., 1973). Additionally, there appear to be complex decompositions/dissociations into the basal plane which impart a yield strength anomaly at intermediate temperatures (Stohr and Poirier, 1972; Poirier, 1985; Wu and Curtin, 2015). Based upon the present work, it can only be stated that we are in a regime of slightly positive rate sensitivity. Further, the rate sensitivity increases slightly with straining. This makes sense, as the increase in dislocation density will result in a smaller activation area. $\langle c+a \rangle$ dislocations may be particularly prone to this sort of phenomenon because of the aforementioned decompositions/dissociations may occur more frequently, as the dislocations' motion is more frequently arrested as the dislocation density increases.

For the case of in plane compression (RD and TD), the experimentally obtained rate sensitivities are similar to that of in-plane tension (Bhattacharyya et al., 2015). At first, it may seem contradictory, since twinning is treated as rate independent in the model. However, the activity plots (Figure 2.7a) show that a significant fraction of strain is accommodated initially by the prismatic slip and at later stages, by $\langle c+a \rangle$ slip, both of which are rate sensitive. It also

makes sense that the experimental strain rate sensitivity appears to increase with strain, since less of the strain is accommodated by twinning, at the higher strain levels.

2.6.2 Plastic anisotropy and tension-compression strength asymmetry

Of the 3 directions examined, viz. RD, TD, and ND, the ND exhibits the strongest tension-compression asymmetry at both dynamic and quasistatic strain rates. This can be explained as follows. During in-plane tension, prismatic slip dominates the strain accommodation, and during in-plane compression, a considerable amount of strain is still accommodated by prismatic slip. Because the twinning mode is only slightly softer than prismatic slip, in WE43-T5, the level of asymmetry is lower than in conventional alloys. For ND tension, the extension twinning is the dominant deformation mode with only a minor contribution of prismatic slip. However, during ND compression, $\langle c+a \rangle$ slip is the major strain carrier. Since the $\langle c+a \rangle$ slip is much harder than the other modes, the relative strength differences is larger, and thus, the asymmetry is greater.

The level of in-plane tension-compression asymmetry is lower under quasistatic loading conditions than it is under dynamic conditions. This is because the prismatic slip shows a small but positive strain rate sensitivity and hence is harder at higher rates. The twinning mode however, is rate insensitive. Thus the relative strength difference is larger at higher rates, leading to a higher strength asymmetry at higher strain rates, consistent with prior observations (Ulacia et al., 2010).

The large normal direction asymmetry is crucial for ballistic applications. The low tensile strength and ductility along this direction result in low energy absorption, leading to spallation failures (Hamilton et al., 2012), during ballistic testing.

2.6.3 Strengthening mechanisms

The CRSS values for pure Mg, conventional Mg alloy AZ31B and the presently examined WE43-T5 alloy are presented in Table 2.5. Single crystal studies provided the values for pure Mg and EPSC/EVPSC model parameters for alloy AZ31B (Wang et al., 2010). This comparison reveals that the CRSS values (τ_0) are, in general higher for WE43-T5. The smaller relative strength differences between the slip modes of WE43-T5 renders the material more isotropic at the grain level, because the soft modes (basal slip and extension twinning) are strengthened more than the hard modes (prismatic and pyramidal slip). As a result, the polycrystalline aggregate is significantly more isotropic, despite being moderately textured.

Table 2.5: A comparison of CRSS for single crystal pure Mg, for AZ31 alloy and for WE43-T5 used in this study. The single crystal CRSS were obtained from the following references: a.(Roberts, 1960), b. (Yoshinaga and Horiuchi, 1964), c. (Akhtar and Teghtsoonian, 1969) d. (Flynn et al., 1961), e. (Obara et al., 1973), f. (Stohr and Poirier, 1972), g. (Bettles and Barnett, 2012)

Deformation mode	CRSS of PURE Mg (MPa)	CRSS of AZ31B (MPa)	CRSS used in this study (MPa)	Comparison WE43/AZ31
Basal	0.5 ^a	9-20	68	3.5 – 7.5 X
Prismatic	18-48 ^{b,c,d}	60-90	145	1.6 – 2.5 X
<c+a> 2 nd order	40 ^{e,f}	100-150	210	1.4 – 2.1 X
Extension twin	2-10 ^g	50-60	130	2.2 – 2.6 X

In order to assess the relative strength contributions from solute atoms, precipitation, grain size refinement, and dislocation density on each deformation mode, the increase in shear resistances were calculated based on information available in the literature. Each individual contribution is discussed in the following sub-sections and the results are summarized in Table 2.7. A linear superposition law has been used for most strengthening elements, since it has been

shown that this is a reasonable approximation when there is a mixture of weak (lattice resistance, solutes) and strong (precipitates, dislocations) obstacles (e.g., Ardell, 1985).

$$\tau_{CRSS}^{\alpha} = \tau_l^{\alpha} + \Delta\tau_{HP}^{\alpha} + \Delta\tau_s^{\alpha} + \Delta\tau_f^{\alpha} + \Delta\tau_{ppt}^{\alpha} \quad (2-15)$$

Thus, the critical resolved shear strength, τ_{CRSS}^{α} , of each slip mode α can be predicted, if each of the terms in the sum are known. The intrinsic lattice resistance, τ_l^{α} , is obtained directly from the pure Mg single crystal literature. The influence of grain size, $\Delta\tau_{HP}^{\alpha}$, is introduced via Hall-Petch relationship, as explained in section 2.6.3.1. The impact of solute additions upon each individual slip mode, $\Delta\tau_s^{\alpha}$, were estimated in two different ways. For basal slip first-principles modeling data available in the literature is used. Regarding the other modes, only non RE solute effects on prismatic slip single crystals is known. Thus, previous crystal plasticity modeling of in-situ neutron diffraction experiments performed on alloy WE43 and Mg-Y binary alloys was used to indirectly address the effect of solutes as explained in section 2.6.3.2. The effect of forest dislocations on the critical resolved shear strengths, $\Delta\tau_f^{\alpha}$, of the deformation modes of this dynamically recrystallized and artificially aged material is introduced via the Taylor hardening relation, as detailed in section 2.6.3.3. Finally, as outlined in section 2.6.3.4, the strengthening effects of the precipitates, $\Delta\tau_{ppt}^{\alpha}$, observed by TEM/STEM are computed based upon geometrically specific Orowan bowing relationships that are available in the literature (basal) or derived in parallel to this study (prismatic and pyramidal).

2.6.3.1 Grain size strengthening

The Hall-Petch (HP) relationship has been used to relate the increase in strength due to grain boundaries:

$$\Delta\tau_{HP} = \tau - \tau_i = kD^{-1/2} \quad (2-16)$$

where, τ is the measured critical resolved shear strength, τ_i is the intrinsic strength of the single crystal in the absence of grain boundaries, D is the mean grain diameter, and k is the HP coefficient which determines how strongly the grain size affects the stress. Several researchers have determined the values of k for basal and prismatic slip. However, the values estimated for twinning and pyramidal $\langle c+a \rangle$ slip are relatively scarce. Table 2.6 shows the ranges of k values of the different modes from two different studies (Raeisnia et al., 2010; Wang and Choo, 2014) along with the predicted values of $\Delta\tau_{HP}^\alpha$ for the mean grain size of 18 μm observed in the present material. It is to be noted that two separate studies, resulting in very different HP coefficients, were chosen in order to explore the range of possible strength estimates. In any case, the harder modes are strengthened to a greater extent by grain refinement, as compared to the softer modes such as basal slip and twinning.

It is important to note that the Hall-Petch dependences employed in this study were not developed for alloy WE43. Rather, they were developed for conventional alloy AZ31. Thus, it is implicitly assumed that there is not a strong alloy dependence in the grain size dependence of the strength of Mg alloys. The summary data in Table 2.7 employs the data in Table 2.6 to compute the effect of grain size relative to the single crystal. Equation (2-16) was also employed to *remove* the grain size contribution from the results obtained on a solutionized and quenched (T3 temper), large grained casting examined previously (Agnew et al., 2013) and for Mg - 0.1 at% Y and Mg - 0.6 at% Y binary alloys (Stanford et al., 2014). For these two cases, the intrinsic resistance to shear included both the lattice resistance and the effect of solute additions. Thus, $\tau_i^\alpha = \tau_l^\alpha + \Delta\tau_s^\alpha = \tau - kD_{casting}^{-1/2}$. In this way, the combined effects of solute and lattice resistance were estimated for cases where the effect of solute is unavailable in the literature.

Table 2.6: The contribution of grain refinement on individual deformation modes obtained using Hall Petch coefficient. The first values of total strength are based on HP coefficient of Wang and Choo (2014) and the second is based on Raeisnia et al. (2010), respectively.

Deformation mode	Hall Petch coefficient k (MPa-mm ^{1/2})	$\Delta\tau_{HP}$ (MPa)
Basal	2.61, 0.42	19, 3
Prismatic	5.54, 3.72	41, 28
Pyramidal <c+a>	n/a, 4.71	n/a, 35
Extension twinning	3.48, n/a	26, n/a

2.6.3.2 Solid solution strengthening

The effects of several solutes on basal slip have been studied by (Yasi et al., 2010) using first principles calculations. From their study, it is found that Y has a high potency to strengthen basal slip. With good solubility, Y is thus an effective solute strengthener in Mg alloys. The WE43 alloy contains 3.7-4.3 wt% Y along with 2.4-4.4 wt% Nd. Most of the Nd is used up in forming the precipitates, so the solid solution hardening, is assumed to arise only due to Y, and can be computed using equation 11 from Yasi et al.,

$$\Delta\tau_s^{basal} = 38.9 \left\{ \left(\frac{\varepsilon_b}{0.176} \right)^2 + \left(\frac{\varepsilon_{SFE}}{5.67} \right)^2 - \left(\frac{\varepsilon_b \varepsilon_{SFE}}{2.98} \right) \right\}^{3/2} c_s^{1/2} \quad (2-17)$$

where, ε_b is the size misfit, ε_{SFE} is the chemical misfit and c_s is the atomic concentration of the solute species. For Y, the size and chemical misfit can be obtained from Table 2 of Yasi et al. (2010) as 21.2% and -1.7 respectively. The expected solute concentration of ~1 at% (Rokhlin, 2004; Sitzmann and Marquis, 2015) leads to an increase of ~ 8.3 MPa of the basal CRSS.

For all other deformation modes, there is an absence of such information in the literature. Solute softening of prismatic slip has been observed for single crystals of Mg alloys with Zn and other solutes at low temperatures, whereas solute strengthening is observed at elevated temperatures (e.g. Akhtar and Teghtsoonian, 1969, Raeisnia et al., 2010). Coincidentally, very little effect of solute is observed on the strength of prismatic slip of Mg alloy single crystals at

room temperature. Thus, the existing literature suggests that the strength of prismatic slip is largely independent of the solute content, at ambient temperatures. However, it is to be noted that the effect of RE solutes on prismatic slip has not yet been determined. The effect of Y solute on $\langle c+a \rangle$ slip is largely unknown, except for a single in-situ neutron diffraction and EPSC modeling study by Stanford et al., (2014) where significant strengthening of $\langle c+a \rangle$ slip mode was observed. Similarly, the strengthening effect of Y additions on tension twinning has only been addressed recently. It has very recently been revealed that Y solute potentially strengthen this mode of deformation (Agnew et al., 2013; Stanford et al., 2014, 2015; Lentz et al., 2014, 2015).

Therefore, as introduced above, EPSC modeling parameters for WE43 in the solutionized (T3) condition (Agnew et al., 2013) were used to account for the intrinsic lattice resistance and solid solution strengthening by subtracting the relevant grain size contribution. We acknowledge that this could slightly over-estimate the degree of solute strengthening that will be present in the peak-aged (T5) condition, since the solute level will be reduced by aging. Additionally, EPSC modeling of Mg - 0.1 at% Y and Mg - 0.6 at% Y binary alloys (Stanford et al., 2014) has also been compared by first subtracting the relevant grain size contribution and then extrapolating to the relevant Y solute concentration of ~ 1 at%.

2.6.3.3 Forest dislocation strengthening

TEM analysis did not reveal a high dislocation density, though the dislocations may have been obscured by the coherency strain contrast from the precipitates. For the purpose of the present estimation, the initial forest dislocation density is approximated as $10^{11}/\text{m}^2$. The strengthening contribution from existing dislocation density is calculated from the relation:

$$\Delta\tau_{forest}^s = \alpha\mu b^s \sqrt{\rho} \quad (2-18)$$

where α assumed to be close to 0.5, b^s is the Burgers vector of mode s , μ is the shear modulus and ρ is the dislocation density. Without greater knowledge of the initial dislocation density, it does not make sense to try to discriminate the contributions of individual slip system densities to forest hardening.

2.6.3.4 Precipitation strengthening

Recent studies have shown that RE element containing Mg alloys exhibit some of the most potent precipitation hardening among Mg alloys. The main strengthening precipitates are the β' globules and the plate precipitate of high aspect ratio. It has been shown that the plate shaped precipitates are very effective in blocking basal slip (Nie, 2003; Robson et al., 2011), assuming Orowan bowing. The increase in the basal CRSS $\Delta\tau$ is given by (Nie, 2003) for prismatic plates and for spheres in terms of b , the magnitude of the Burgers vector, the volume fraction of the precipitates f , and the dimensions of the precipitates: d , the diameter of the plates or spheres, and t , the thickness of the plate precipitates. For the present alloy, recall that the volume fraction of globules is ~0.5%, with an equivalent spherical diameter of 14 nm. For the plate shaped precipitates, the volume fraction is estimated to be 0.2% with an average aspect ratio (d/t) of approximately 9. Thus, an increase in the CRSS of basal slip due to the spheres and plates may be approximated as 26 and 33 MPa, respectively. Since both are strong obstacles, a Pythagorean superposition principle, $(\Delta\tau_{ppt}^\alpha)^2 = (\Delta\tau_{spheres}^\alpha)^2 + (\Delta\tau_{plates}^\alpha)^2$ (Kocks et al., 1975; Koppenaal and Kuhlmann-Wilsdorf, 1964) leads to a total increase in CRSS of 42 MPa. Previous theoretical predictions have suggested much larger increases in the CRSS of basal slip > 100 MPa (Ji et al., 2014) because a large volume fraction (> 4 %) of prismatic plate shaped

precipitates was considered. However, in the present commercially processed WE43-T5 samples, the plate-shaped precipitates are present in low volume fraction.

The increase in CRSS of prismatic and $\langle c+a \rangle$ slip modes due to the plate shaped particles has recently been established by Wang et al. (2016). The increase in the CRSS for prismatic slip due to the globular β' and plate shaped precipitates (according to equation 2-19) yields values of 26 MPa and 20 MPa, respectively, with a total increase in CRSS as 33 MPa. In case of $\langle c+a \rangle$ slip, the strength contribution from the globular and plate shaped precipitates (equation 2-20) are 40 MPa and 45 MPa respectively, leading to a total strength of 60 MPa. It is to be noted that one reason there is an appreciable strengthening effect upon $\langle c+a \rangle$ is due to the larger Burgers vector of $\langle c+a \rangle$ slip as compared to $\langle a \rangle$ slip (0.612 nm vs. 0.321 nm).

$$\Delta\tau_{ppt}^{prismatic} = \frac{Gb}{2\pi\sqrt{1-\nu}} \frac{1}{\sqrt{0.605\frac{dt}{f}-1.346t\sqrt{\frac{dt}{f}}+t^2+0.389\sqrt{\frac{dt}{f}}-0.262d}} \ln \frac{1.144\sqrt{dt}}{r_0} \quad (2-19)$$

$$\Delta\tau_{ppt}^{\langle c+a \rangle} = \frac{Gb}{2\pi\sqrt{1-\nu}} \frac{1}{0.935\sqrt{\frac{dt}{f}}-0.386d-1.991t} \ln \frac{1.038\sqrt{dt}}{r_0} \quad (2-20)$$

Note that the core radius, r_0 , is assumed equal to the appropriate b in the above calculations.

2.6.3.5 Summary of strengthening contributions

Table 2.7 presents each of the contributions to the overall strength employed in the sum (Eq. 2-15): intrinsic lattice resistance τ_l^α , solute $\Delta\tau_s^\alpha$, grain size $\Delta\tau_{HP}^\alpha$, forest dislocation $\Delta\tau_f^\alpha$, and precipitation $\Delta\tau_{ppt}^\alpha$ strengthening effects. Three different sets of totals, τ_{CRSS}^α , are presented. One is computed beginning with the single crystal data, one is based upon previous EPSC modeling of alloy WE43 and the third one is based on the EPSC modelling results of Stanford et al. (2014), after removing the grain size effect intrinsic to those results using the Hall-Petch relation, as discussed previously. All three sets of totals include the same values for $\Delta\tau_{HP}^\alpha$, $\Delta\tau_f^\alpha$, and $\Delta\tau_{ppt}^\alpha$,

and compare well with the initial critical resolved shear strength, τ_0^α , determined in the present study using EPSC modeling (last column). This is especially true for basal, where most of the information is available in the literature (less than 5%, provided HP coefficient of Wang and Choo (2014) is employed).

For prismatic slip, the results suggest that there is some solute strengthening due to Y solutes at room temperature, in distinction with observations of other non-rare earth solute (Akhtar and Teghtsoonian, 1969). A similar level of solute strengthening is implied by the work of Lentz et al. (2014), though they were studying more highly alloyed WE54. The totals based upon data from Stanford et al. (2014) appear to be over-estimated ($\sim 20\%$), however, they admitted significant uncertainty in those particular values in their paper.

In the case of $\langle c+a \rangle$ slip, only the second set of totals, which begins with prior EPSC modeling of solutionized WE43, $\tau_l^\alpha + \Delta\tau_s^\alpha$, compares very well with the present EPSC modeling. The results suggest that Y has a significant solute strengthening effect upon $\langle c+a \rangle$ slip, which is in qualitative agreement with Stanford et al. (2014). However, use of numbers from Stanford et al., again appear to be over-estimated. In that paper, the emphasis of the modeling was primarily upon mechanisms responsible for macroscopic yield, basal and twinning, and there was less confidence placed upon values associated with mechanisms responsible for strain hardening, which include the critical resolved shear strengths of prismatic and $\langle c+a \rangle$ slip.

Finally, concerning $\{10\bar{1}2\}$ extension twinning, the results confirm that Y has a potent strengthening effect (e.g., Stanford et al., 2015). Note that including solute effects improve the strength but is still under-predicted ($\sim 20\%$). None of the current estimates incorporate any strengthening effect of precipitates on twinning, since previous studies even suggested the

possibility that precipitation actually reduced the strength of twinning, either by promoting twin nucleation or depleting the matrix of solute (Agnew et al., 2013). In any event, the high strength of twinning helps to explain why the tension-compression strength asymmetry in this rare earth-containing alloy is diminished relative to traditional Mg alloys.

Table 2.7: Contributions to the CRSS of individual modes from various strengthening mechanisms: lattice resistance, solutes, grain size refinement, forest dislocations and precipitates. The total strength based on the single crystal (∞), the EPSC CRSS values for T3 material and EPSC CRSS from Stanford et al., (2014) are highlighted in grey (all values in MPa). When two values appear separated by commas, the first is based on HP coefficient of Wang and Choo (2014) and the second is based on Raeisinha et al. (2010).

Deformation mode	τ_l^α ∞	$\Delta\tau_s^\alpha$	$\Delta\tau_{HP}^\alpha$ $\infty \rightarrow T$ 5	$\Delta\tau_f^\alpha$	$\Delta\tau_{ppt}^\alpha$	τ_{CRSS}^α from ∞	$\tau_l^\alpha + \Delta\tau_s^\alpha$ EPSC T3	τ_{CRSS}^α EPS C T3	$\tau_l^\alpha + \Delta\tau_s^\alpha$ Stanford	τ_{CRSS}^α Stanford	τ_0^α EPS C T5
Basal	0.5	8.3	19, 3	1	42	71, 55	3,11	65, 57	6, 15	68, 61	68
Prismatic	48	n/a	41, 28	1	33	124, 110	59,65	134, 127	104, 112	179, 174	145
<c+a>	40	n/a	n/a, 35	2	60	n/a, 137	n/a, 114	n/a, 210	n/a, 176	n/a, 273	210
TTW	8	n/a	26, n/a	n/a	n/a	34, n/a	73, n/a	99, n/a	80, n/a	106, n/a	130

The broad agreement between the theoretical calculations and the empirical EPSC parameters provides some support for both approaches (though it is admitted there are significant approximations involved), and suggests that combining deformation mode strength modeling together with crystal plasticity modeling is approaching the level required to employed modern alloy development paradigms such as ICME (integrated computational materials engineering) (National Academy of Engineers, 2008) and MGI (Materials Genome Initiative, 2011) in the development of Mg alloys. The one area which merits further investigation is the solute strengthening of non-basal slip and twinning, since the current indirect results highlight a

significant solute strengthening effect of these mechanisms, which has not yet been characterized at the single crystal level.

2.6.4 Influence of strain rate on the strain hardening rate

It has been shown that the strain hardening rate θ_0 increases with increase in strain rate (Follansbee and Kocks, 1988; Klepaczko and Chiem, 1986). However, in this study it has been observed that there is a significant decrease in the strain hardening rate for the dynamic *tensile* tests as compared to the quasistatic tests. The compression tests do not show this behavior. Hence, in absence of sufficient experimental data, it was assumed that θ_0 remains essentially constant. Thus, it is hypothesized that the difference in hardening behavior observed for the tensile tests is more associated with localization and damage accumulation, rather than homogenous flow. Moreover, plate # 6457 had a slight strong texture and thus a stronger plastic anisotropy, which has been shown to have a detrimental effect on strain to failure of another Mg alloy (Kondori and Benzerga, 2014).

Figure 2.15a shows a fractograph of samples tested in tension along RD. Interestingly; the fracture surface shows two different mechanisms operative. On one hand, dimples associated with second phase particles are indicative of a ductile microvoid nucleation and growth mechanisms. On the other hand, there are microcracks associated with twin/grain boundaries that are also present. It has to be noted that EBSD band contrast maps (Figure 2.9d and Figure 2.12d) have revealed the presence of a small amount of secondary and double twins. Although these twins have little effect on the bulk plasticity, they can play a dominant role in the fracture process (Ando et al., 2014; Barnett, 2007). A high magnification micrograph of the region highlighted in Figure 2.15a shows the presence of grain boundary precipitates and a crack associated with them. Further studies are being carried out to identify if there is any particular

grain boundaries which are more susceptible for cracking and/or the presence of precipitate free zones which leads to strain localization at the grain boundaries (Vasudévan and Doherty, 1987). Note that even the grain boundary fracture surfaces exhibit evidence of dimples. Under dynamic loading, the onset of damage occurs early due to accelerated void growth and coalescence as well as increased micro-cracking, which results in a lower tensile ductility. The compression samples on other hand, exhibited ductile shear fracture (Agnew et al., 2014), which is less sensitive to the influence of strain rate and thus exhibit essentially no change in either the strain hardening rate (perhaps the hardening rate increased slightly as mentioned above) or strain to failure (El-Magd and Abouridouane, 2006).

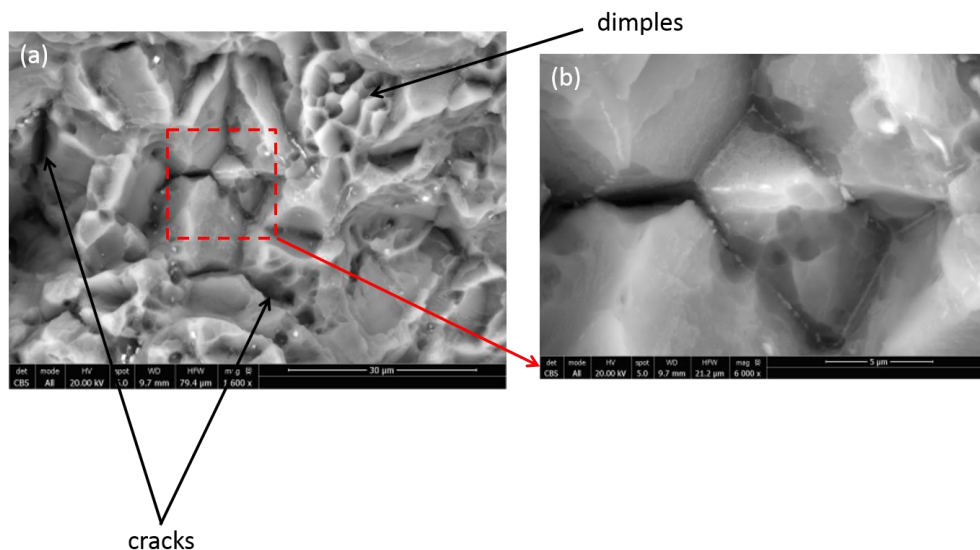


Figure 2.15: (a) A fractograph of RD tension sample tested at QSR showing presence of dimples associated with particles as well as grain/twin boundary cracks (b) a higher magnification micrograph from the region showing presence of grain boundary precipitates and a crack associated with them.

Finally, we consider the role of adiabatic heating, since dissipation of thermal energy can be limited during high strain rate deformation, in contrast to the isothermal conditions of

quasistatic tests. One can estimate the adiabatic temperature rise of the specimen under dynamic loading by the following equation:

$$\Delta T = \frac{\beta}{\rho C_p} \int_0^{\varepsilon_f} \sigma d\varepsilon \quad (2-21)$$

where, β is the efficiency or fraction of mechanical work converted into thermal energy, typically estimated to be 0.95, ρ is the mass density, C_p is the specific heat capacity, and ε_f is the strain to failure. Considering the low melting point of Mg and the tendency to dynamically recrystallize at low homologous temperatures, this adiabatic temperature rise can have a significant effect in the flow response. The mass density, specific heat capacity and the thermal conductivity of WE43-T5 along with some other structural alloys are presented in Table 2.8. The temperature rise for different loading directions is presented in Table 2.9. It can be seen that the adiabatic temperature rise for compression tests could be as high as ~50 K, while that estimated for the tension tests is only ~11 K (due to the lower strain to failure). Thus the reduction of hardening rate in case of tensile loading, is not solely due to adiabatic heating, since, heating is expected to be greater for the compression case, not the tensile. Instead the rate dependence of failure appears to be responsible for the observed behavior, and this will be explored in future studies. In particular, the local temperature rise associated with shear instability can be quite high and can play a significant role in the shear failures observed in case of compression.

Table 2.8: Thermal properties and densities of some commercial structural alloys along with WE43-T5 alloy.

Alloy	Density (g/cc)	Specific heat capacity (J/g-°C)	Thermal conductivity (W/m-K)
WE43 T5	1.84	0.966	51.3
zirconium	6.53	0.285	16.7
Ti 6Al 4V annealed	4.43	0.526	6.7
Al 7075 T6	2.81	0.96	130
copper	7.94	0.385	398
304L stainless steel	8.00	0.5	16.3

Table 2.9: Temperature rise according to equation 2-21 for different loading conditions for samples tested at dynamic rates.

WE43-T5 loading condition	Area under σ - ϵ curve (MPa)	Temperature rise ΔT (K)
RD compression	105.8	56.6
RD tension	23.6	12.6
ND compression	84.7	45.3
ND tension	19.1	10.2

2.6.5 In-plane compression vs. ND tension – role of twin nucleation

The one aspect which challenged the present EPSC modeling framework, was predicting the flow behavior for twin dominated loading conditions, viz. RD and TD compression and ND tension. A good match with TD compression led to over-prediction of the RD compression flow behavior, while a good match with the RD, under-predicts the TD. In either case, the ND tension flow stress is over-estimated. The most plausible explanation for this behavior stems from local effects of interaction between basal slip and grain boundaries leading to twin nucleation. Twin nucleation models (Beyerlein and Tomé, 2010; Beyerlein et al., 2010) and molecular dynamics (MD) simulations (Wang et al., 2014) have shown that twin nucleation occurs at locations where basal $\langle a \rangle$ dislocations impinge on grain boundaries. Thus, the stress at which twins are nucleated could be inversely related to the activity of basal slip, since higher activity will more likely lead to more potent dislocation pile-ups, etc. For this alloy plate, the initial texture is such that basal slip activity is highest for ND tension, followed by RD compression and finally TD compression. Therefore, it may be expected that twin nucleation might occur at the lowest macroscopic applied stress for ND tension and highest for TD compression. Such nearest neighbor effects cannot be captured in a mean field model like EPSC/VPSC. To capture this, full field models like finite element-based (Wang et al., 2011; Zhang et al., 2008) or Fourier transform-based (Lebensohn, 2001) crystal plasticity modeling will be required.

2.7 Summary and conclusions

EPSC modeling of quasistatic and high strain rate deformation behavior of WE43T5 plate has provided useful insights about the grain level deformation mechanisms and the role of individual strengthening mechanisms that are operative in this alloy. The results of the model allow one to conclude the following:

1. Unlike previous crystal plasticity modeling exercises, where latent hardening has been treated empirically, the present study addresses latent hardening due to dislocation-dislocation interactions based on a recent discrete dislocation dynamics calculation carried out by Bertin et al. (2014). It is shown that incorporating such latent hardening was necessary in order to match the flow behavior and the evolution of plastic strain anisotropy (r-value) simultaneously.
2. The quasistatic model results suggest that the basal slip and extension twinning in this alloy are strengthened greatly, whereas harder prismatic and $\langle c+a \rangle$ slip modes are relatively less strengthened. This is one reason that alloy WE43-T5 exhibits lower anisotropy than conventional Mg alloys.
3. The hardening of the twinning mode has a great effect on the behavior. For example, there is an absence of the characteristic sigmoidal shape, reduced tension compression strength asymmetry, and lower twin volume fraction as compared to conventional alloys.
4. It is found that the polycrystal plasticity model cannot precisely capture the flow stress along all directions simultaneously, when extension twinning is the dominant deformation mode (i.e. for ND tension, RD and TD compression). As the recent literature suggests, it appears that it will be necessary to take into account the stress associated with

twin nucleation which is sensitive to the local stress state and cannot be addressed in such mean field approach.

5. The high strain rate deformation behavior can be modeled adequately by treating prismatic and $\langle c+a \rangle$ to be rate sensitive, while basal and extension twinning are revealed to be rate insensitive ($m = 0.000 \pm 0.008$), in the rate regime investigated.
6. The rate sensitivity of the CRSS of prismatic slip is found to be 0.008 ± 0.006 and that for $\langle c+a \rangle$ slip to be 0.005 ± 0.004 , suggesting prismatic slip is more rate sensitive than $\langle c+a \rangle$.
7. The modeling results also suggest that the observed higher twin volume fraction at higher strain rate offset a reduction in prismatic slip, which exhibits the aforementioned small but positive rate sensitivity.
8. By examining the effect of various strengthening mechanisms, it is found that the precipitates have a profound effect in strengthening the slip modes and solute atoms were emphasized as key strengtheners of the $\langle c+a \rangle$ and extension twinning modes.
9. The broad agreement between strength modeling and EPSC estimates suggests that combining deformation mode strength modeling together with crystal plasticity modeling is approaching the level required to employed modern alloy development paradigms such as ICME (integrated computational materials engineering) and MGI (Materials Genome Initiative) in the development of Mg (and other non-cubic metal) alloys.
10. The fracture behavior of the tensile samples comprised of void dominated ductile fracture and ductile intergranular fracture associated with grain boundary precipitates. This behavior may explain the reduction in strain hardening rate, at high strain rates, observed in tension.

2.8 Acknowledgements

The authors would like to acknowledge Christopher Calhoun for incorporating TDT model into EPSC, Prof. Joseph Robson, University of Manchester, UK for fruitful discussions concerning strengthening due to prismatic plate shaped precipitates, and Dr. Bruce Davis of Magnesium Elektron, for providing the plate material explored in this study. The research at U.V.A. and M.S.U. was sponsored by the U.S. Army Research Office under contract number W911NF-12-1-0455 monitored by Drs. Suveen Mathaudhu and David Stepp as well as the U.S. National Science Foundation, grant number 1235259 monitored by Dr. Alexis Lewis. The views and conclusions contained in this document are those of the authors and should not be interpreted as representing the official policies, either expressed or implied, of the Army Research Laboratory or the U.S. Government. The U.S. government is authorized to reproduce and distribute reprints for government purposes notwithstanding any copyright notation hereon.

2.9 Appendix 1

The relationship between the latent hardening matrix $h^{\alpha\beta}$ employed within the EPSC and VPSC (e.g., Lebensohn and Tomé, 1993) models and $a_{FZ}^{\alpha\beta}$ of the dislocation density based model (Bertin et al., 2014) is derived beginning with the total differential of the resolved shear resistance of slip system α with respect to shear strains on β slip systems.

$$d\tau^\alpha = \sum_\beta \frac{\partial \tau^\alpha}{\partial \gamma^\beta} d\gamma^\beta \quad (2-A1.1)$$

Using the chain rule,

$$d\tau^\alpha = \sum_\beta \frac{\partial \tau^\alpha}{\partial \Gamma} \frac{\partial \Gamma}{\partial \gamma^\beta} d\gamma^\beta \quad (2-A1.2)$$

where, $\delta\Gamma = \sum_\beta \Delta\gamma^\beta$ and $\frac{\partial \tau^\alpha}{\partial \Gamma}$, is given by the Voce relation (Eq. 2-4). Rearranging gives,

$$d\tau^\alpha = \frac{\partial \tau^\alpha}{\partial \Gamma} \sum_\beta \frac{\partial \Gamma}{\partial \gamma^\beta} d\gamma^\beta \quad (2-A1.3)$$

where it can be formally shown that, $\frac{\partial \Gamma}{\partial \gamma^\beta} = 1$. In EPSC/VPSC, however, latent hardening is introduced by replacing $\frac{\partial \Gamma}{\partial \gamma^\beta}$ by $h^{\alpha\beta}$, a matrix with coefficients of order 1. Hence,

$$d\tau^\alpha \approx \frac{\partial \tau^\alpha}{\partial \Gamma} \sum_\beta h^{\alpha\beta} d\gamma^\beta \quad (2-A1.4)$$

To relate simple Voce relation to the dislocation density, we use the Taylor hardening relation:

$$\tau^\alpha = \tau_0^\alpha + C\mu b\sqrt{\rho^{total}} \quad (2-A1.5)$$

where, τ^α and τ_0^α is the current shear resistance and initial lattice friction on slip system α , respectively, and μ and b is the shear modulus and Burger's vector associated with the system α . ρ^{total} is the total dislocation density and C is a constant depending on the specific dislocation arrangement. As was done in equation (2-A1.2), applying the chain rule gives

$$\frac{\partial \tau^\alpha}{\partial \Gamma} = \frac{\partial \tau^\alpha}{\partial \rho^{total}} \frac{\partial \rho^{total}}{\partial \Gamma} \quad (2-A1.6)$$

where $\frac{\partial \rho^{total}}{\partial \gamma^{total}}$ is given by the Kocks–Mecking relation:

$$\frac{\partial \rho^{total}}{\partial \Gamma} = k_1\sqrt{\rho^{total}} - k_2\rho^{total} \quad (2-A1.7)$$

Differentiating the Taylor relation gives:

$$\frac{\partial \tau^\alpha}{\partial \rho^{total}} = \frac{C\mu b}{2\sqrt{\rho^{total}}} \quad (2-A1.8)$$

Therefore, equation 2-A1.7 becomes:

$$\frac{\partial \tau^\alpha}{\partial \Gamma} = \frac{C\mu b}{2\sqrt{\rho^{total}}} \left(k_1\sqrt{\rho^{total}} - k_2\rho^{total} \right) \quad (2-A1.9)$$

Substituting $\sqrt{\rho^{total}}$ from the Taylor relation and rearranging, one obtains,

$$\frac{\partial \tau^\alpha}{\partial \Gamma} = \frac{c\mu b k_1}{2} \left(1 - \frac{k_2}{k_1} \left(\frac{\tau^\alpha - \tau_0^\alpha}{c\mu b} \right) \right) \quad (2-A1.10)$$

If we define, $\theta_0^\alpha = \frac{c\mu b k_1}{2}$ and $\tau_1^\alpha = \frac{c\mu b k_1}{k_2}$, then we obtain the Voce relation:

$$\frac{\partial \tau^\alpha}{\partial \Gamma} = \theta_0^\alpha \left(1 - \left(\frac{\tau^\alpha - \tau_0^\alpha}{\tau_1^\alpha} \right) \right) \quad (2-A1.11)$$

Thus, there is a clear connection between the employed Voce relation (Eq. 2-4) and a dislocation density based hardening formulation. Now considering the specific case of Franciosi – Zaoui latent hardening formulation (Eq.2-7), equation 2-A1.1 can be re-written as:

$$d\tau^\alpha = \sum_\beta \frac{\partial \tau^\alpha}{\partial \rho^\beta} \frac{\partial \rho^\beta}{\partial \gamma^\beta} d\gamma^\beta \quad (2-A1.12)$$

Taking the derivative of Eq. 2-7 with respect to ρ^β gives:

$$\frac{\partial \tau^\alpha}{\partial \rho^\beta} = \frac{a_{FZ}^{\alpha\beta}}{2\sqrt{\sum_\beta a_{FZ}^{\alpha\beta} \rho^\beta}} \quad (2-A1.13)$$

Therefore,

$$d\tau^\alpha = \sum_\beta \frac{a_{FZ}^{\alpha\beta}}{2\sqrt{\sum_\beta a_{FZ}^{\alpha\beta} \rho^\beta}} \frac{\partial \rho^\beta}{\partial \gamma^\beta} d\gamma^\beta \quad (2-A1.14)$$

As before, $\frac{\partial \rho^\beta}{\partial \gamma^\beta}$ is given by Kocks-Mecking type relation and $\sqrt{\sum_\beta a_{FZ}^{\alpha\beta} \rho^\beta}$ can be substituted using Eq. 2-7 to obtain:

$$d\tau^\alpha = \sum_\beta \frac{\mu b}{2(\tau^\alpha - \tau_0^\alpha)} \frac{\partial \rho^\beta}{\partial \gamma^\beta} a_{FZ}^{\alpha\beta} d\gamma^\beta \quad (2-A1.15)$$

In the spirit of the approximation made from 2-A1.3 to 2-A1.4, the term $\frac{\mu b}{2(\tau^\alpha - \tau_0^\alpha)} \frac{\partial \rho^\beta}{\partial \gamma^\beta}$ is treated as equivalent to $\frac{\partial \tau^\alpha}{\partial \gamma}$. It is implicitly assumed that any latent hardening effects, which are embedded within the sum over the term $\frac{\partial \rho^\beta}{\partial \gamma^\beta}$, are of second order importance. Thus,

$$d\tau^\alpha \approx \frac{\partial \tau^\alpha}{\partial \gamma} \sum_\beta a_{FZ}^{\alpha\beta} d\gamma^\beta \quad (2-A1.16)$$

Comparing equations 2-A1.4 and 2-A1.16 reveals that the latent hardening coefficients of the two approximations are related as:

$$a_{FZ}^{\alpha\beta} \approx h^{\alpha\beta} \quad (2-A1.17)$$

2.10 Appendix 2

As mentioned in Section 2.4, VPSC model (Lebensohn and Tome, 1993) was used in order to gain some preliminary insights. The WE43-T5 texture from plate # 9849 was employed together with AZ31 parameters from (Wang et al., 2012). The CRSS values employed in the VPSC model are presented in Table 2.10. Figure 2.16 shows the experimental and simulated flow curves. It can be seen that the AZ31 model parameters under-predict strength and over-predict anisotropy. These results support the conclusion that the higher strength and lower anisotropy of WE43-T5 stems from changes in intrinsic grain level deformation mechanisms.

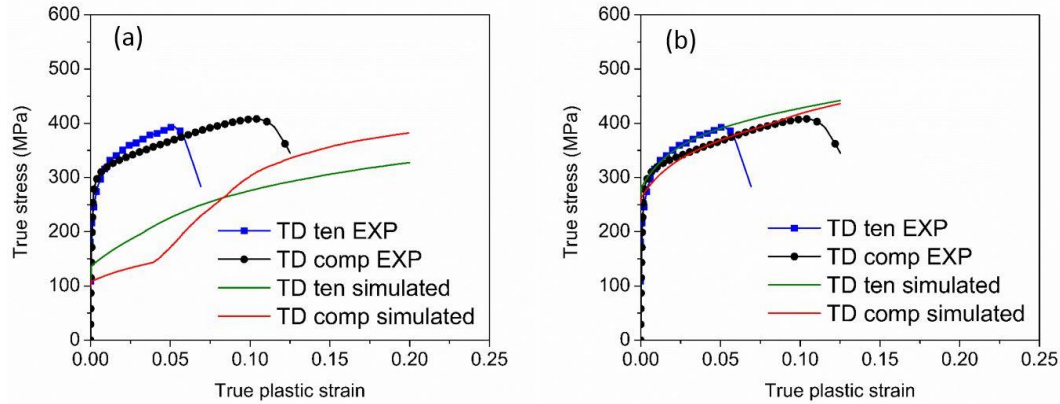


Figure 2.16: Experimental and simulated flow curves for TD tension and compression using WE43T5 plate # 9849 texture (a) with AZ31B parameters from Wang et al.,(2012) and (b) with parameters listed in Table 2.10.

Table 2.10: Comparison of VPSC CRSS for AZ31B (after Wang et.al) and for WE43-T5 employed in this study.

Deformation mode	AZ31B from Wang et al., (2012)	WE43 T5 - VPSC
Basal	12	55
Prismatic	75	135
$\langle c+a \rangle$ 2 nd order	115	170
Tensile twin	40	115

2.11 References

- Agnew, S., Whittington, W., Oppedal, A., El Kadiri, H., Shaeffer, M., Ramesh, K.T., Bhattacharyya, J., Delorme, R., Davis, B., 2014. Dynamic Behavior of a Rare-Earth-Containing Mg Alloy, WE43B-T5, Plate with Comparison to Conventional Alloy, AM30-F. *Jom* 66, 277–290. doi:10.1007/s11837-013-0830-x
- Agnew, S.R., Brown, D.W., Tomé, C.N., 2006. Validating a polycrystal model for the elastoplastic response of magnesium alloy AZ31 using in situ neutron diffraction. *Acta Mater.* 54, 4841–4852. doi:10.1016/j.actamat.2006.06.020
- Agnew, S.R., Duygulu, Ö., 2005. Plastic anisotropy and the role of non-basal slip in magnesium alloy AZ31B. *Int. J. Plast.* 21, 1161–1193. doi:10.1016/j.ijplas.2004.05.018
- Agnew, S.R., Mulay, R.P., Polesak, F.J., Calhoun, C.A., Bhattacharyya, J.J., Clausen, B., 2013. In situ neutron diffraction and polycrystal plasticity modeling of a Mg–Y–Nd–Zr alloy: Effects of precipitation on individual deformation mechanisms. *Acta Mater.* 61, 3769–3780. doi:10.1016/j.actamat.2013.03.010
- Agnew, S.R., Tomé, C.N., Brown, D.W., Holden, T.M., Vogel, S.C., 2003. Study of slip mechanisms in a magnesium alloy by neutron diffraction and modeling. *Scr. Mater.* 48, 1003–1008. doi:10.1016/S1359-6462(02)00591-2
- Akhtar, A., Teghtsoonian, E., 1969. Solid solution strengthening of magnesium single crystals—ii the effect of solute on the ease of prismatic slip. *Acta Metall.* 17, 1351–1356. doi:10.1016/0001-

- 6160(69)90152-7
- Allen, S.M., 1981. Foil thickness measurements from convergent-beam diffraction patterns. *Philos. Mag. A* 43, 325–335.
- Allen, S.M., Hall, E.L., 1982. Foil thickness measurements from convergent-beam diffraction patterns An experimental assessment of errors. *Philos. Mag. A* 46, 243–253.
- Ando, D., Koike, J., Sutou, Y., 2014. The role of deformation twinning in the fracture behavior and mechanism of basal textured magnesium alloys. *Mater. Sci. Eng. A* 600, 145–152. doi:10.1016/j.msea.2014.02.010
- Antion, C., Donnadieu, P., Perrard, F., Deschamps, A., Tassin, C., Pisch, A., 2003. Hardening precipitation in a Mg-4Y-3RE alloy. *Acta Mater.* 51, 5335–5348. doi:10.1016/S1359-6454(03)00391-4
- Ardell, A., 1985. Precipitation Hardening. *Metall. Trans. A* 16, 2131–2165.
- Argon, A.S., 2008. Strengthening mechanisms in crystal plasticity. Oxford: Oxford University Press.
- Asgari, H., Odeshi, A.G., Szpunar, J.A., 2014. On dynamic deformation behavior of WE43 magnesium alloy sheet under shock loading conditions. *Mater. Des.* 63, 552–564. doi:10.1016/j.matdes.2014.06.038
- Barnett, M.R., 2007. Twinning and the ductility of magnesium alloys. Part II. “Contraction” twins. *Mater. Sci. Eng. A* 464, 8–16. doi:10.1016/j.msea.2007.02.109
- Bertin, N., Tomé, C.N., Beyerlein, I.J., Barnett, M.R., Capolungo, L., 2014. On the strength of dislocation interactions and their effect on latent hardening in pure Magnesium. *Int. J. Plast.* 62, 72–92. doi:10.1016/j.ijplas.2014.06.010
- Bettles, C., Barnett, M.R. (Eds.), 2012. *Advances in wrought magnesium alloys: Fundamentals of processing, properties and applications*. Elsevier.
- Beyerlein, I.J., Capolungo, L., Marshall, P., McCabe, R.J., Tomé, C.N., 2010. Statistical analyses of deformation twinning in magnesium. *Philos. Mag.* 90, 2161–2190.
- Beyerlein, I.J., Tomé, C.N., 2010. A probabilistic twin nucleation model for hcp polycrystalline metals. *Proc. R. Soc. A Math. Phys. Eng. Sci.* 466, 2517–2544.
- Bhattacharyya, J., Agnew, S., Wu, P., Whittington, W., El Kadiri, H., 2015. Crystal Plasticity Modeling of the Dynamic Behavior of Magnesium Alloy, WE43-T5, Plate, in: *Magnesium Technology*. pp. 165–170.
- Caillard, D., Martin, J.L., 2003. *Thermally activated mechanisms in crystal plasticity*. Pergamon Materials Series Vol 8, Elsevier.
- Chichili, D.R., Ramesh, K.T., Hemker, K.J., 1998. The high-strain-rate response of alpha-titanium: experiments, deformation mechanisms and modeling. *Acta Mater.* 46, 1025–1043. doi:10.1016/S1359-6454(97)00287-5
- Cho, K., Sano, T., Doherty, K., Yen, C., Gazonas, G., Montgomery, J., Moy, P., Davis, B., Delorme, R., 2009. *Magnesium Technology and Manufacturing for Ultra Lightweight Armored Ground Vehicles*, Army Research Laboratory ARL-RP-236.
- Chun, Y.B., Davies, C.H.J., 2011. Investigation of prism $\langle a \rangle$ slip in warm-rolled AZ31 alloy. *Metall. Mater. Trans. A Phys. Metall. Mater. Sci.* 42, 4113–4125. doi:10.1007/s11661-011-0800-2
- Clausen, B., Tomé, C.N., Brown, D.W., Agnew, S.R., 2008. Reorientation and stress relaxation due to twinning: Modeling and experimental characterization for Mg. *Acta Mater.* 56, 2456–2468. doi:10.1016/j.actamat.2008.01.057
- Conrad, H., Hays, L., Schoeck, G., Wiedersich, H., 1961. On the rate-controlling mechanism for plastic flow of Mg crystals at low temperatures. *Acta Metall.* 9, 367–378. doi:10.1016/0001-6160(61)90230-9
- Council, N.M.A.B.D. on E. and P.S.N.R., 2008. *Integrated Computational Materials Engineering*. National Academies Press.
- Couret, A., Caillard, D., 1985. An in situ study of prismatic glide in magnesium—I. The rate controlling mechanism. *Acta Metall.* 33, 1447–1454. doi:10.1016/0001-6160(85)90045-8
- Couret, A., Caillard, D., 1985. An in situ study of prismatic glide in magnesium—II. Microscopic

- activation parameters. *Acta Metall.* 33, 1455–1462.
- Diak, B.J., Upadhyaya, K.R., Saimoto, S., 1998. Characterization of thermodynamic response by materials testing. *Prog. Mater. Sci.* 43, 223–363. doi:10.1016/S0079-6425(98)00007-3
- El-Magd, E., Abouridouane, M., 2006. Characterization, modelling and simulation of deformation and fracture behaviour of the light-weight wrought alloys under high strain rate loading. *Int. J. Impact Eng.* 32, 741–758. doi:10.1016/j.ijimpeng.2005.03.008
- Eshelby, J.D., 1957. The Determination of the Elastic Field of an Ellipsoidal Inclusion, and Related Problems. *Proc. R. Soc. A Math. Phys. Eng. Sci.* 241, 376–396. doi:10.1098/rspa.1957.0133
- Flynn, P., Mote, J.E.D., Dorn, J., 1961. On the thermally activated mechanism of prismatic slip in magnesium single crystals. *Trans Met Soc AIME* 221, 1148–1154.
- Follansbee, P.S., Kocks, U.F., 1988. A constitutive description of the deformation of copper based on the use of the mechanical threshold stress as an internal state variable. *Acta Metall.* 36, 81–93. doi:10.1016/0001-6160(88)90030-2
- Fultz, B., Howe, J.M., 2012. *Transmission electron microscopy and diffractometry of materials*. Springer Science & Business Media.
- Gama, B.A., Lopatnikov, S.L., Gillespie, J.W., 2004. Hopkinson bar experimental technique: A critical review. *Appl. Mech. Rev.* 57, 223. doi:10.1115/1.1704626
- Hadorn, J.P., Hantzsche, K., Yi, S., Bohlen, J., Letzig, D., Wollmershauser, J.A., Agnew, S.R., 2012. Role of solute in the texture modification during hot deformation of Mg-rare earth alloys. *Metall. Mater. Trans. A Phys. Metall. Mater. Sci.* 43, 1347–1362. doi:10.1007/s11661-011-0923-5
- Hamilton, J., Brennan, S.T., Sohn, Y., Davis, B., Delorme, R., Cho, K., 2012. Microstructural Characteristics of High Rate Plastic Deformation in Elektron™ WE43 Magnesium Alloy.
- Jain, A., Agnew, S.R., 2007. Modeling the temperature dependent effect of twinning on the behavior of magnesium alloy AZ31B sheet. *Mater. Sci. Eng. A* 462, 29–36. doi:10.1016/j.msea.2006.03.160
- Ji, Y.Z., Issa, A., Heo, T.W., Saal, J.E., Wolverton, C., Chen, L.Q., 2014. Predicting β' precipitate morphology and evolution in Mg-RE alloys using a combination of first-principles calculations and phase-field modeling. *Acta Mater.* 76, 259–271. doi:10.1016/j.actamat.2014.05.002
- Klepaczko, J.R., Chiem, C.Y., 1986. On rate sensitivity of f. c. c. metals, instantaneous rate sensitivity and rate sensitivity of strain hardening. *J. Mech. Phys. Solids* 34, 29–54.
- Kocks, U.F., Argon, A.S., Ashby, M.F., 1975. *Thermodynamics and Kinetics of Slip*. *Prog. Mater. Sci. B*. Chalmers, J.W. Christ. T.B. Massalski, Eds. 19.
- Kondori, B., Benzerga, A.A., 2014. Effect of stress triaxiality on the flow and fracture of Mg alloy AZ31. *Metall. Mater. Trans. A Phys. Metall. Mater. Sci.* 45, 3292–3307. doi:10.1007/s11661-014-2211-7
- Koppelaar, T.J., Kuhlmann-Wilsdorf, D., 1964. The effect of prestressing on the strength of neutron-irradiated copper single crystals. *Appl. Phys. Lett.* 4.
- Lebensohn, R.A., 2001. N-site modeling of a 3D viscoplastic polycrystal using Fast Fourier Transform. *Acta Mater.* 49, 2723–2737. doi:10.1016/S1359-6454(01)00172-0
- Lebensohn, R.A., Tomé, C.N., 1993. A self consistent anisotropic approach for the simulation of plastic deformation and texture development of polycrystals: application to zirconium alloys. *Acta metall. Mater.* 41, 2611–2624.
- Lentz, M., Klaus, M., Coelho, R.S., Schaefer, N., Schmack, F., Reimers, W., Clausen, B., 2014. Analysis of the Deformation Behavior of Magnesium-Rare Earth Alloys Mg-2 pct Mn-1 pct Rare Earth and Mg-5 pct Y-4 pct Rare Earth by In Situ Energy-Dispersive X-ray Synchrotron Diffraction and Elasto-Plastic Self-Consistent Modeling. *Metall. Mater. Trans. A* 45, 5721–5735. doi:10.1007/s11661-014-2533-5
- Lentz, M., Klaus, M., Wagner, M., Fahrenson, C., Beyerlein, I.J., Zecevic, M., Reimers, W., Knezevic, M., 2015. Effect of age hardening on the deformation behavior of an Mg–Y–Nd alloy: In-situ X-ray diffraction and crystal plasticity modeling. *Mater. Sci. Eng. A* 628, 396–409. doi:10.1016/j.msea.2015.01.069
- Li, B., Joshi, S., Azevedo, K., Ma, E., Ramesh, K.T., Figueiredo, R.B., Langdon, T.G., 2009. Dynamic testing at high strain rates of an ultrafine-grained magnesium alloy processed by ECAP. *Mater. Sci.*

- Eng. A 517, 24–29. doi:10.1016/j.msea.2009.03.032
- Li, B., Joshi, S.P., Almagri, O., Ma, Q., Ramesh, K.T., Mukai, T., 2012. Rate-dependent hardening due to twinning in an ultrafine-grained magnesium alloy. *Acta Mater.* 60, 1818–1826. doi:10.1016/j.actamat.2011.12.002
- Liu, H., Gao, Y., Liu, J.Z., Zhu, Y.M., Wang, Y., Nie, J.F., 2013. A simulation study of the shape of β' precipitates in Mg-Y and Mg-Gd alloys. *Acta Mater.* 61, 453–466. doi:10.1016/j.actamat.2012.09.044
- Lou, X.Y., Li, M., Boger, R.K., Agnew, S.R., Wagoner, R.H., 2007. Hardening evolution of AZ31B Mg sheet. *Int. J. Plast.* 23, 44–86. doi:10.1016/j.ijplas.2006.03.005
- Materials Genome Initiative (Washington, D.C: The White House, 2011), www.whitehouse.gov/mgi.
- Mukai, T., Mohri, T., Mabuchi, M., Nakamura, M., Ishikawa, K., Higashi, K., 1998. Experimental study of a structural magnesium alloy with high absorption energy under dynamic loading. *Scr. Mater.* 39, 1249–1253. doi:10.1016/S1359-6462(98)00296-6
- Neil, C.J., Wollmershauser, J.A., Clausen, B., Tomé, C.N., Agnew, S.R., 2010. Modeling lattice strain evolution at finite strains and experimental verification for copper and stainless steel using in situ neutron diffraction. *Int. J. Plast.* 26, 1772–1791. doi:10.1016/j.ijplas.2010.03.005
- Nie, J.F., 2003. Effects of precipitate shape and orientation on dispersion strengthening in magnesium alloys. *Scr. Mater.* 48, 1009–1015. doi:10.1016/S1359-6462(02)00497-9
- Nie, J.F., Muddle, B.C., 2000. Characterisation of strengthening precipitate phases in a Mg–Y–Nd alloy. *Acta Mater.* 48, 1691–1703. doi:10.1016/S1359-6454(00)00013-6
- Nie, J.F., Xiao, X.L., Luo, C.P., Muddle, B.C., 2001. Characterisation of precipitate phases in magnesium alloys using electron microdiffraction. *Micron* 32, 857–863. doi:10.1016/S0968-4328(00)00094-9
- Nie, J.F., Zhu, Y.M., Liu, J.Z., Fang, X.Y., 2013. Periodic segregation of solute atoms in fully coherent twin boundaries. *Science* 340, 957–60. doi:10.1126/science.1229369
- Obara, T., Yoshinga, H., Morozumi, S., 1973. $\{1122\}$ $\langle 23 \rangle$ Slip system in magnesium. *Acta Metall.* 21, 845–853. doi:10.1016/0001-6160(73)90141-7
- Raeisinia, B., Agnew, S.R., Akhtar, A., 2010. Incorporation of Solid Solution Alloying Effects into Polycrystal Modeling of Mg Alloys. *Metall. Mater. Trans. A* 42, 1418–1430. doi:10.1007/s11661-010-0527-5
- Roberts, C., 1960. *Magnesium and its alloys*. Wiley.
- Robson, J.D., Stanford, N., Barnett, M.R., 2012. Effect of Precipitate Shape and Habit on Mechanical Asymmetry in Magnesium Alloys. *Metall. Mater. Trans. A* 44, 2984–2995. doi:10.1007/s11661-012-1466-0
- Robson, J.D., Stanford, N., Barnett, M.R., 2011. Effect of precipitate shape on slip and twinning in magnesium alloys. *Acta Mater.* 59, 1945–1956. doi:10.1016/j.actamat.2010.11.060
- Rokhlin, L.L., Dobatkina, T. V., Tarytina, I.E., Timofeev, V.N., Balakhchi, E.E., 2004. Peculiarities of the phase relations in Mg-rich alloys of the Mg–Nd–Y system. *J. Alloys Compd.* 367, 17–19. doi:10.1016/j.jallcom.2003.08.004
- Sandlöbes, S., Zaefferer, S., Schestakow, I., Yi, S., Gonzalez-Martinez, R., 2011. On the role of non-basal deformation mechanisms for the ductility of Mg and Mg–Y alloys. *Acta Mater.* 59, 429–439. doi:10.1016/j.actamat.2010.08.031
- Sitzmann, E., Marquis, E.A., 2015. Chemistry and morphology of β' precipitates in an aged Mg–Nd–Y–Zr alloy. *Philos. Mag. Lett.* 95, 7–13.
- Stanford, N., Cottam, R., Davis, B., Robson, J., 2014. Evaluating the effect of yttrium as a solute strengthener in magnesium using in situ neutron diffraction. *Acta Mater.* 78, 1–13. doi:10.1016/j.actamat.2014.06.023
- Stanford, N., Marceau, R.K.W., Barnett, M.R., 2015. The effect of high yttrium solute concentration on the twinning behaviour of magnesium alloys. *Acta Mater.* 82, 447–456. doi:10.1016/j.actamat.2014.09.022
- Steiner, M., Bhattacharyya, J.J., Agnew, S.R., 2015. The Origin and Enhancement of $\{0001\}\langle 11-20 \rangle$ Texture during Heat Treatment of Rolled AZ31B Magnesium Alloys. *Acta Mater.*

- Stohr, J.F., Poirier, J.P., 1972. Etude en microscopie electronique du glissement pyramidal $\{1122\}$ $\langle 1123 \rangle$ dans le magnesium. *Philos. Mag.* 25, 1313–1329. doi:10.1080/14786437208223856
- Tucker, M.T., Horstemeyer, M.F., Gullett, P.M., El Kadiri, H., Whittington, W.R., 2009. Anisotropic effects on the strain rate dependence of a wrought magnesium alloy. *Scr. Mater.* 60, 182–185. doi:10.1016/j.scriptamat.2008.10.011
- Turner, P.A., Tomé, C.N., 1994. A study of residual stresses in Zircaloy-2 with rod texture. *Acta Metall. Mater.* 42, 4143–4153. doi:10.1016/0956-7151(94)90191-0
- Ulacia, I., Dudamell, N. V., Gálvez, F., Yi, S., Pérez-Prado, M.T., Hurtado, I., 2010. Mechanical behavior and microstructural evolution of a Mg AZ31 sheet at dynamic strain rates. *Acta Mater.* 58, 2988–2998. doi:10.1016/j.actamat.2010.01.029
- Vasudévan, A.K., Doherty, R.D., 1987. Grain boundary ductile fracture in precipitation hardened aluminum alloys. *Acta Metall.* 35, 1193–1219. doi:10.1016/0001-6160(87)90001-0
- Wang, F., Bhattacharyya, J.J., Agnew, S.R., 2016. Effect of precipitate shape and orientation on Orowan strengthening of non-basal slip modes in magnesium alloys. To be submitted.
- Wang, H., Raeisinia, B., Wu, P.D., Agnew, S.R., Tomé, C.N., 2010. Evaluation of self-consistent polycrystal plasticity models for magnesium alloy AZ31B sheet. *Int. J. Solids Struct.* 47, 2905–2917. doi:10.1016/j.ijsolstr.2010.06.016
- Wang, H., Wu, P.D., Tomé, C.N., Wang, J., 2012. A constitutive model of twinning and detwinning for hexagonal close packed polycrystals. *Mater. Sci. Eng. A* 555, 93–98. doi:10.1016/j.msea.2012.06.038
- Wang, H., Wu, P.D., Wang, J., Tomé, C.N., 2013. A crystal plasticity model for hexagonal close packed (HCP) crystals including twinning and de-twinning mechanisms. *Int. J. Plast.* 49, 36–52. doi:10.1016/j.ijplas.2013.02.016
- Wang, J., Beyerlein, I.J., Tomé, C.N., 2014. Reactions of lattice dislocations with grain boundaries in Mg: Implications on the micro scale from atomic-scale calculations. *Int. J. Plast.* 56, 156–172. doi:10.1016/j.ijplas.2013.11.009
- Wang, L., Barabash, R.I., Yang, Y., Bieler, T.R., Crimp, M. a., Eisenlohr, P., Liu, W., Ice, G.E., 2011. Experimental characterization and crystal plasticity modeling of heterogeneous deformation in polycrystalline α -Ti. *Metall. Mater. Trans. A Phys. Metall. Mater. Sci.* 42, 626–635. doi:10.1007/s11661-010-0249-8
- Wang, Y., Choo, H., 2014. Influence of texture on Hall–Petch relationships in an Mg alloy. *Acta Mater.* 81, 83–97. doi:10.1016/j.actamat.2014.08.023
- Wu, Z., Curtin, W.A., 2015. The origins of high hardening and low ductility in magnesium. *Nature.* 526, 62–67. doi:10.1038/nature15364
- Yasi, J.A., Hector, L.G., Trinkle, D.R., 2010. First-principles data for solid-solution strengthening of magnesium: From geometry and chemistry to properties. *Acta Mater.* 58, 5704–5713. doi:10.1016/j.actamat.2010.06.045
- Yoshinaga, H., Horiuchi, R., 1964. On the nonbasal slip in magnesium crystals. *Trans. Japan Insitute Met.* 5, 14–21.
- Zhang, R.Y., Daymond, M.R., Holt, R.A., 2008. A finite element model of deformation twinning in zirconium. *Mater. Sci. Eng. A* 473, 139–146. doi:10.1016/j.msea.2007.04.021

3 Deformation and fracture behavior of magnesium alloy WE43 after various aging heat treatments

J.J. Bhattacharyya, P.J. McQuade and S.R. Agnew

Materials Science and Engineering, University of Virginia, Charlottesville, Virginia, U.S.A.

3.1 Abstract

The deformation and fracture behavior of WE43 after different aging heat treatments were investigated. It is found that the solutionizing heat treatment weakened the initial basal texture of the WE43 plate, which resulted in a reduction of the yield strength anisotropy. Solutionizing followed by peak aging, only lead to a marginal increase in the hardness, as compared to the T5 (hot working followed by aging) heat treatment. Different strategies to increase the number density of the precipitates were explored. First, the T8 treatment (where the solutionized material is deformed prior to aging) was carried out to see if the presence of the dislocations aided in increasing the number density of the precipitates. The results show that although the aging kinetics increased, the peak hardness value did not show any improvement. Furthermore, stretching parallel to the rolling direction (RD) or compression parallel to the normal direction (ND), lead to vary similar hardness profiles. A two-step aging (first at 140°C for 4 hrs, followed by 210°C) treatment also did not provide a measureable increase in hardness over the conventional one-step aging. The T6 samples appeared to exhibit the most intergranular ductile fracture, consistent with localization within a precipitate free zone (PFZ). The lower ductility along ND in the T5 temper appears to be related to stringers of Y-containing cuboidal dispersoids. Strength and flow stress *predictions* using a previously published crystal plasticity model that accounts for the effects of initial

texture, grain size, solid solution additions, and precipitates are accurate to within 13%, for both solutionized and peak-aged material.

Keywords: T8 heat treatment, two-step aging, grain boundary precipitation, intergranular ductile fracture, strength modeling

3.2 Introduction

Rare earth (RE) containing Mg alloys obtain their strength from a combination of solid solution and precipitation hardening and are among one of the strongest age-hardenable Mg alloys, particularly at elevated temperatures (Mordike, 2002). The alloy of interest for the present study is WE43, which has been considered as a potential light weight armor material due to its superior ballistic properties as compared to other Mg alloys, and with conventional lightweight metallic armor material Al alloy 5083-H131(Cho et al., 2009). Recently, a study carried out by Hamilton et al., (2012) showed evidence of extensive spallation when WE43-T5 plates were impacted by high velocity projectiles, along the plate through-thickness direction (ND). Their study serves as motivation to further examine the fracture behavior of this alloy, especially along ND. More importantly, it is worth exploring whether there is any heat treatment which would improve the fracture resistance of this alloy.

On the other hand, the effect of precipitation hardening in Mg alloys is only moderate compared to age-hardenable Al alloys. Several researchers have focused on characterizing the precipitation sequence and the structure of the metastable precipitates (e.g., Nie and Muddle, 2000; Nie et al., 2001;Antion et al., 2003). Moreover, quite a few studies have employed theoretical calculations based on Orowan bowing mechanism to calculate the effect of precipitate geometry on different slip modes (Nie, 2003; Robson et al., 2011; Wang et al., 2016). These calculations reveal that plate shaped precipitates lying on non-basal planes are effective in

strengthening all slip modes. However, in an earlier study on WE43-T5, it was found that the volume fraction of these plate shaped precipitates were much less than 1% with a rather limited number density of $\sim 5 \times 10^{21} \text{ m}^{-3}$ (Bhattacharyya et al., 2016) as compared to Al alloys, where the number density is typically $\sim 10^{23} \text{ m}^{-3}$; two orders of magnitude higher (Deschamps et al., 2001; Gable et al., 2001). Thus, it appears that increasing the number density of these precipitates is a strategy to improve the age hardening response.

A relatively less studied area is the effect of precipitate distribution on the strength and ductility of WE43 alloy. For instance, it is well-known that extensive heterogeneous nucleation on grain boundaries lead to the formation of precipitate free zones (PFZs) which have detrimental effects on mechanical properties (Graf and Hornbogen, 1977; Ludtka and Laughlin, 1982; Pardo et al., 2003). In addition, RE-containing Mg alloys, like WE43, have been known to undergo significant texture randomization during recrystallization and grain growth (Senn and Agnew, 2008). Hence, solution heat treatment after deformation processing, could lead to effects on anisotropy and strain hardening that are not common to other heat treatable alloy systems. Thus, different aging heat treatment strategies, including the so-called T8 treatments involving small pre-deformation prior to aging that have been extensively explored for Al alloys (e.g., Cassada et al., 1991; Gable et al., 2001) but rarely for Mg (e.g., Rosalie et al., 2013) are employed in this study to explore the possibility of improving the properties of WE43.

3.3 Experimental

3.3.1 Heat treatment

Three 38 mm (1.5 inch) thick plates of different tempers: WE43-F, WE43-T5 and WE43-T7 were provided by Magnesium Elektron North America. All heat treatments were carried out in air in a box furnace at constant temperature within $\pm 2 \text{ }^{\circ}\text{C}$. The solutionizing heat treatment

(SHT) was carried out at 525 °C for 8 hours. All solutionized specimens were quenched in water at room temperature.

For T8 treatment in tension, rectangular tensile bars were cut from the parent plate, such that the tensile axis was along the RD of the original plate. For T8 compression, rectangular blocks were cut out with compression axis along the ND of the original plate. These specimens were solution treated, and subsequently stretched or compressed using an Instron universal testing machine, to different strain levels. Following deformation, several pieces (2 mm x 2 mm x 2 mm) were cut from the gage portion of the tensile bar, or for compression, from center of the rectangular block, using slow speed diamond saw blade, and were subjected to aging treatments at 210°C for different durations.

Differential Scanning Calorimetry (DSC) measurements were carried out on the solutionized specimen to determine the pre-ageing temperature. Discs of 5 mm diameter and 1 mm thickness were used for the scans which were carried out at a heating rate of 20 °C/min. The first exothermic peak was observed at 140 °C, hence it was chosen as the pre-ageing temperature. The specimens were aged at this temperature for 4 hours before aging for various durations at 210 °C.

3.3.2 Microhardness

All microhardness measurements were carried out using a Vicker's microhardness tester at load of 0.5 kg and indentation duration of 15s. 10 measurements were carried out for each specimens, the average is reported as the hardness with the standard deviation as error bars.

3.4 Results

3.4.1 Texture and microstructure after solutionizing heat treatment

Optical micrographs (Figure. 3.1) reveal that the material has undergone significant grain growth during the SHT. The average grain size for the T5 material was found to be $\sim 18 \mu\text{m}$ (Bhattacharyya et al., 2016), whereas after solutionizing, the grain size is $\sim 82 \mu\text{m}$.

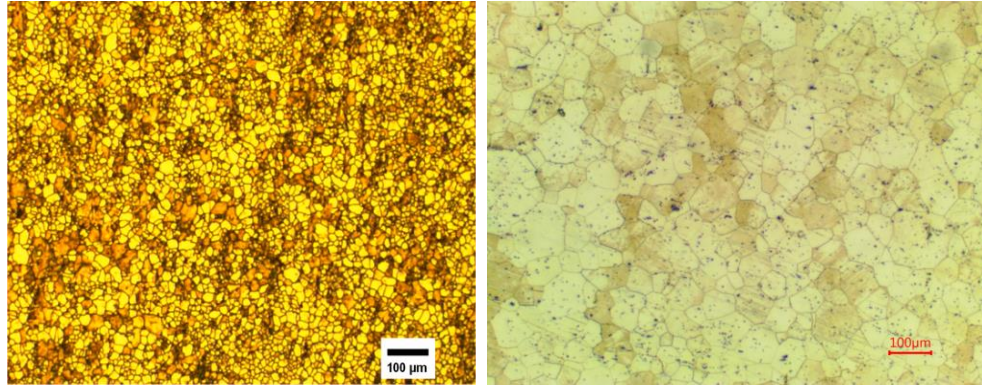


Figure 3.1: Optical micrographs showing the grain size for (a) T5 material and (b) T3 material.

For RE containing Mg alloys like WE43, it is well known that the SHT leads to randomization of the strong texture that is present in wrought alloys (Senn and Agnew, 2008). Figure.3.2 shows the recalculated $\{10\bar{1}0\}$ and $\{0002\}$ pole figures for the T5 and T3 material. The T5 material has a texture strength of 4.5 multiples of random distribution (m.r.d) with the basal poles tilted $\sim 25^\circ$ towards RD. It can be seen that although the SHT did not completely randomize the texture, it considerably weakened it. The spread of the basal poles has increased significantly and the texture strength is reduced to ~ 2.5 m.r.d. This change in texture is expected to have a significant impact upon the mechanical response of the material.

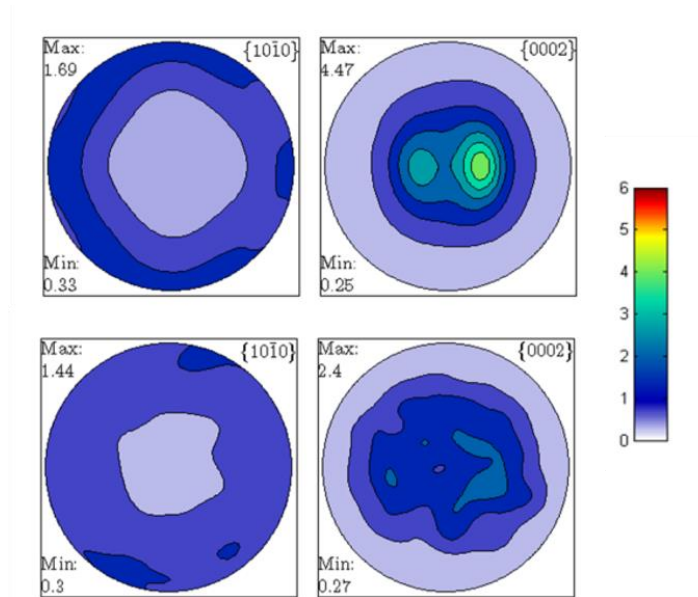


Figure 3.2: Crystallographic texture shown as recalculated $\{10\bar{1}0\}$ and $\{0002\}$ pole figures averaged from data collected at various depths within the 1.5" thick plate of WE43B in T5 (top) and T3 (bottom) condition. The T5 sample shows a stronger texture than T3.

3.4.2 Temperature dependence of aging response

The variation of microhardness with aging time at 250 °C for different starting conditions is shown in Figure 3.3. It is found that the T5 material exhibits the highest hardness of ~96 VHN whereas the peak hardness achieved from the T6 treatment is only ~ 80 VHN. Starting from the T5 condition, further aging does not lead to any increasing in the hardening response; rather it tends towards the T7 condition. This aging temperature was selected based upon prior work on cast alloy WE54 (e.g., Nie and Muddle, 2000) as well as the technical data sheet published by the vendor for cast alloy WE43 (MENA, 2014a).

Aging heat treatments were also carried out at 210 °C, the vendor recommended temperature for wrought WE43 (MENA, 2014b). The results (Figure 3.4) indicate that aging the hot-deformed material at 210 °C gives rise to a significantly higher hardness than that observed in cast and heat treated conditions. A peak (T5) hardness in the range of 90-95 VHN was

obtained after 18-32 hours, up 20-25 from about 70 VHN in the as-deformed (F-temper) condition. A SHT and subsequent aging, on the other hand, gives a moderate improvement (~6%) in the peak aged (T6) hardness of 102 VHN at 64 hrs, which comes with a burden of increased heat treatment cost.

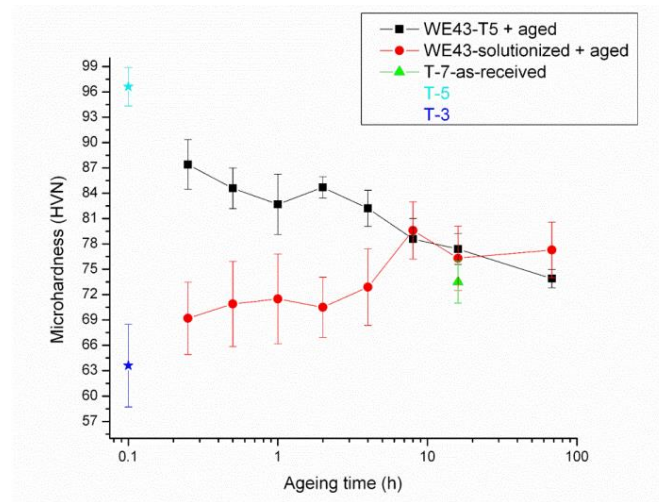


Figure 3.3: Variation of microhardness with aging duration at 250°C with the starting material as T3 and T5. The as-received T5 and T7 are also shown.

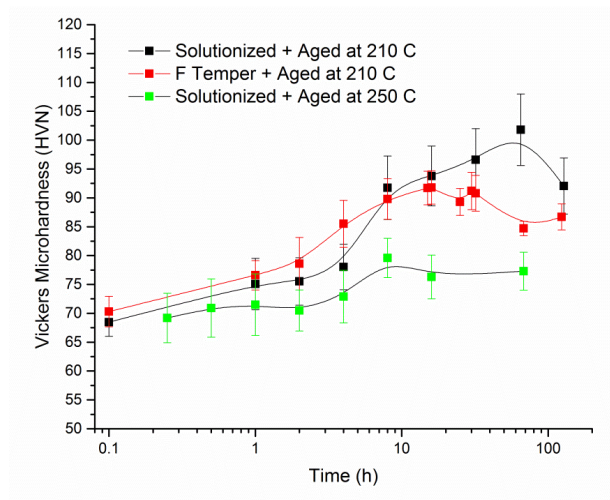


Figure 3.4: Age hardening plots showing the variation of microhardness as a function of aging time at 210 °C for solutionized + aged and F-temper + aged. The plot for solutionized + aged at 250 °C is also shown for comparison.

3.4.3 Effect of pre-deformation on aging response

The present literature suggests that increasing the number density of precipitates is the key to improving the problem of low age hardenability of Mg alloys (Nie, 2012). One strategy to accomplish this goal is the so-called T8 temper, wherein the material is first solutionized and quenched then it is deformed (typically stretched in tension), and finally, it is artificially aged. In fact, recent investigations have suggested that the strengthening phase (β') will preferentially precipitate on pre-existing dislocations (Liu et al., 2014). Furthermore, due to presence of multiple deformation modes, it is of interest to investigate whether basal $\langle a \rangle$ or non-basal $\langle c+a \rangle$ type dislocations have different effects on the age hardening response.

Performing a slight tensile stretch (2%) does not improve the peak hardness, but it does significantly improve the kinetics of aging, such that the peak hardness is reached after only one day of aging rather than 64 hours in the as-quenched condition (Figure 3.5). Stretching more (4-6%) furthered this trend of improved statistics to enable 8-16 hr aging treatments, but with a slight decrement in peak hardness. In summary, a higher level of strain correlates to a faster response time, at the cost of a slightly lower peak hardness. Performing ND compression had a very similar effect to in-plane tension. This seems to rule out the possibility that introducing different kinds of dislocations will yield different levels of age-hardenability (Figure 3.6). These curves illustrate that the mode of deformation for T8 has only a minor effect on the hardening behavior, since similar levels of strain result in similar hardening behavior.

3.4.4 Effect of two-step aging

Another strategy to increase the number density of precipitates is a 2-step heat treatment, where the material is first aged at a low temperature to nucleate a high number density and then finished at a higher temperature to more rapidly grow these nuclei, as demonstrated by (Oh-ishi

et al., 2008) for Mg-Zn-Mn alloys. The results presented in Figure 3.7 show the enhanced kinetics resulting from the 2-step treatment, which is quite similar to the T8 treatment, presented earlier. The hardness after the pre-aging treatment of 4 hrs at 140 °C is up only 8 VHN to 78 VHN, but the peak hardness is a relatively high value of ~100 VHN reached within a day of aging at 210 °C or a total of 28 hrs of aging. The value of the peak hardness is very close to the T6 condition, which was achieved after aging 64h at 210 °C.

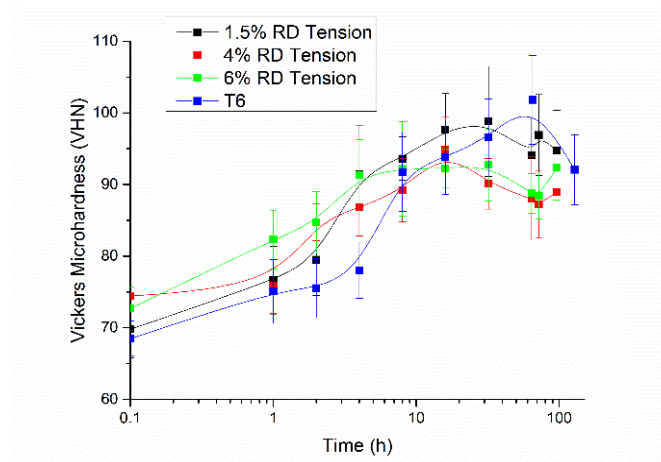


Figure 3.5: Variation of microhardness with aging duration for T8 treatment, where the specimens were stretched along RD. The T6 age-hardening curves are shown for comparison. For both cases, aging was carried out at 210 °C.

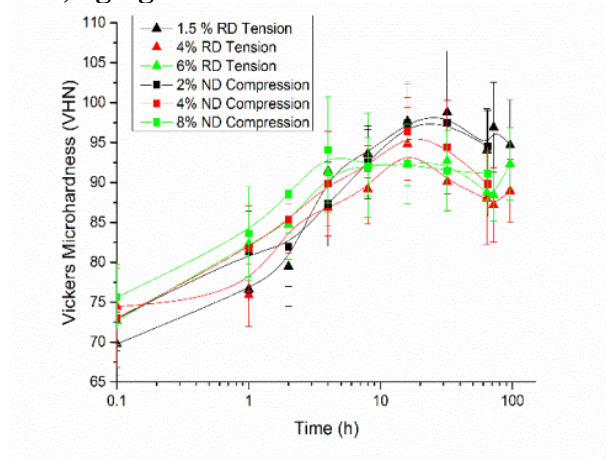


Figure 3.6: Variation of microhardness with aging duration for T8 treatment, where the specimens were compressed along ND (with RD tension T8 shown for comparison).

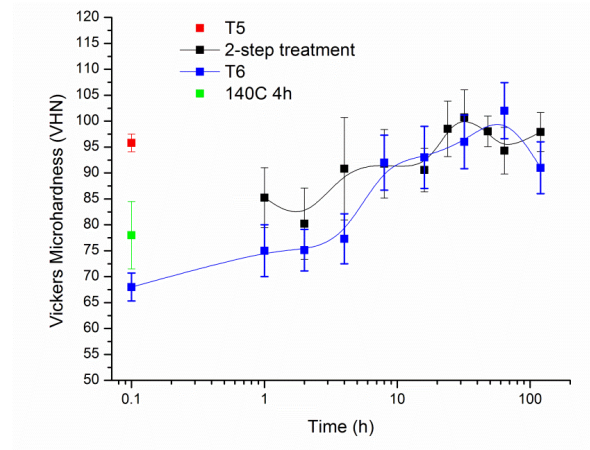


Figure 3.7: Variation of microhardness as a function of aging duration for the 2-step aging treatment where pre-aging was carried out at 140 °C for 4h, followed by aging at 210 °C. The T6 curve and T5 hardness value is shown for comparison.

3.4.5 Flow behavior after aging

Although there is no dramatic change in peak hardness with the various aging treatments, it is of interest to the measure effect of aging on the tensile flow and fracture response specimens in the solutionized (T3), under-aged (210 °C/8h) and peak-aged (T6-210 °C/64h) conditions. The flow curves are shown in Figure 3.8. Because the texture after SHT was found to be dramatically weakened from the original T5 condition, two orientations (viz. TD and ND) were tested to see the effect of that weak texture. The T5 TD data is also shown for comparison. Interestingly, the flow curves show a considerable deterioration of both strength and ductility for the heat treated samples, as compared to the T5 material. The work-hardening rate changed only slightly as compared to the T5 material. The TD specimen tested at T3 condition, has ductility quite similar to the T5 specimen and much lower yield strength of ~140 MPa, as compared to ~ 300 MPa for the T5. After 8h of aging, an increase of strength by ~ 50 MPa is observed. For the same aging condition, ND is softer than TD. Even though the texture is weak, the number of grains favorable to undergo twinning is larger in case of ND as compared to TD, and since twinning is softer than

prismatic slip (Bhattacharyya et al., 2016), the overall flow strength is lower. Further aging to 64h leads to a slight increase in strength. Since the texture strength decreased upon solutionizing, it is interesting to see the effect this has on the flow anisotropy. Table 3.1 shows the yield strength ratios of TD and ND samples for the under aged, T5 and T6 condition. The values were obtained using 0.2% offset yield strength. From these values it is evident that the weakening of the texture resulted in a dramatic reduction (~25%) of the yield anisotropy between T6 and T5 temper.

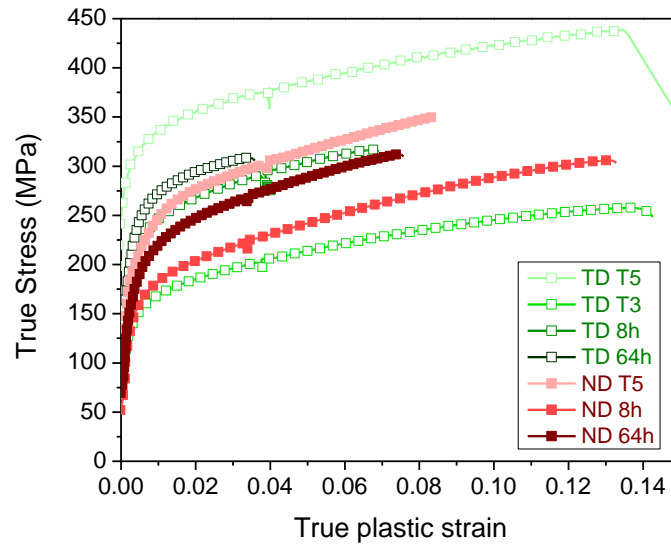


Figure 3.8: Stress-strain curves for various samples along the ND and TD direction. These curves show that the T5 treated samples show both a higher tensile strength and ductility than T6.

Table 3.1: Yield anisotropy of WE43 for different aging conditions

Ageing condition	$\sigma_{TD} / \sigma_{ND}$ at 0.2%
Under-aged (210 °C/8h)	1.4
T5	1.7
Peak aged (T6 - 210 °C/8h)	1.3

There was significant differences in ductility between the two orientations investigated, and TD happens to have a lower ductility than ND for both under-aged and peak-aged conditions. Perhaps this is due to the slightly higher strain hardening rate in the ND samples, presumably also due to the higher incidence of extension twinning, which has previously been noted to delay plastic instability (Barnett, 2007).

3.4.6 Fracture behavior after aging

In order to further investigate the variations in ductility between the different tempers and gain insight about the fracture mechanisms operative in this alloy, SEM based fractography was carried out for selected specimens deformed in tension. Figure 3.9 shows a low magnification fractograph of a T5 specimen tested in tension along ND. It can be seen that various different mechanisms are operative. The fracture surface shows dimples associated with second phase particles which are responsible for nucleation of microvoids. One interesting feature is the region of bright Y rich dispersoid clusters (or stringers), which align themselves on the ND plane during hot rolling. Under ND tension, these particles can simply de-bond and lead to catastrophic failure. Due to this spatial distribution of the dispersoids, the ND samples generally exhibit lower ductility than RD and TD (Agnew et al., 2014). Other features such as cracks associated with twin/grain boundaries are also present. Since this mode of loading favors tensile twinning, cracks nucleating at the intersections of twins, is expected (Somekawa et al., 2009; Kondori and Benzerga, 2014) .

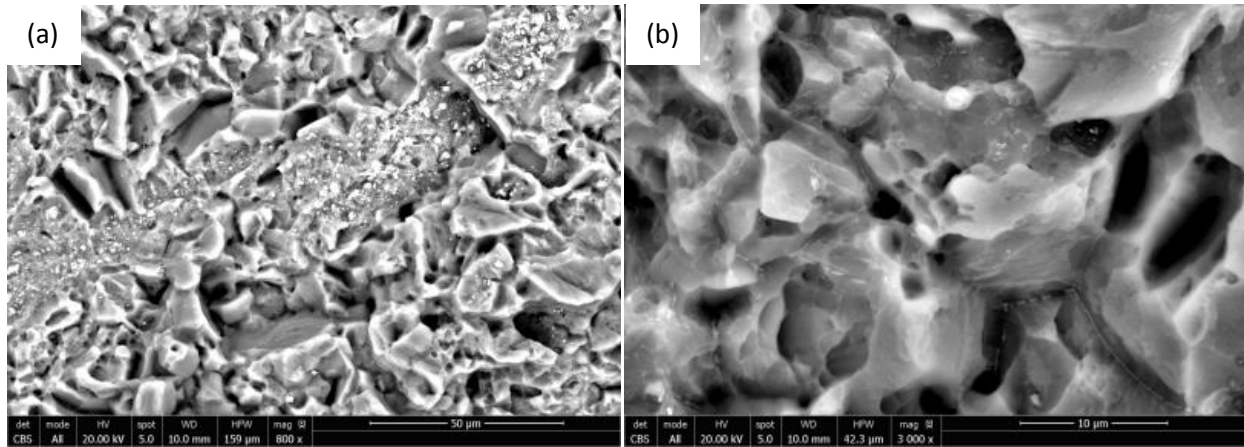


Figure 3.9: Backscattered fractographs for a T5 specimen tested in tension along ND, showing (a) clusters of dispersoids and (b) dimples and grain boundary precipitates.

A high magnification micrograph of the same specimen (Figure 3.9b) reveal network of grain boundary precipitates which may be responsible for nucleating grain boundary cracks. Moreover, the precipitate free zone associated with these particles may also be responsible for the ductile intergranular failure observed (e.g., Vasudévan and Doherty; 1987 Pardo et al., 2003). The RD specimens for the same temper exhibits similar features as that of ND (Figure 3.10), except the presence of dispersoid clusters, which is probably the explanation for the slightly higher ductility of RD samples.

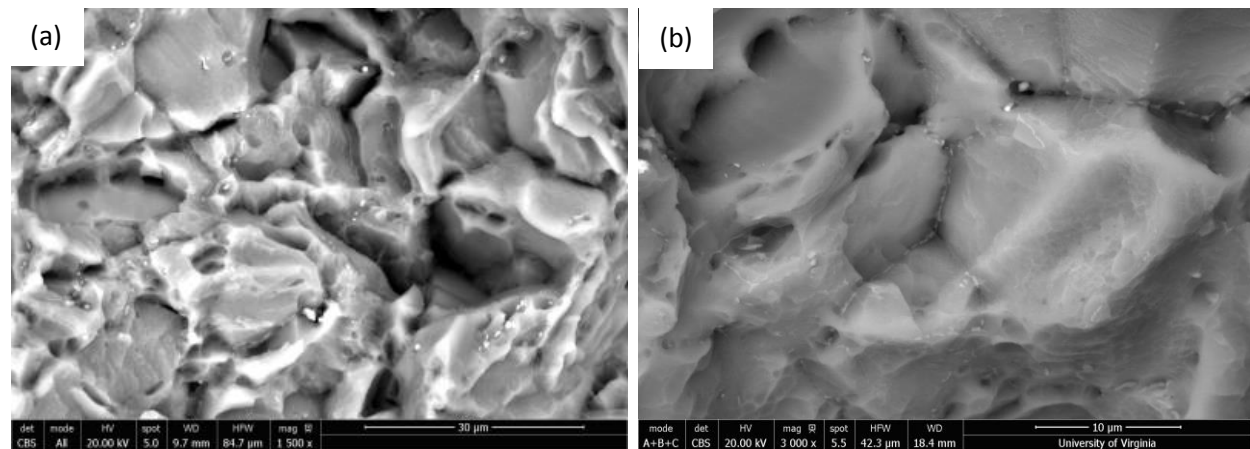


Figure 3.10: Backscattered fractographs for a T5 specimen tested in tension along RD, showing dimples and grain boundary precipitates, but absence of dispersoid clusters.

Figure 3.11 shows a micrograph of a specimen deformed in TD tension after solution heat treatment (SHT). The fracture surface looks quite different from the T5 material. It appears much smoother which is indicative of less ductile damage. The bright Y rich particles are still present and this is in agreement with an earlier study (Polesak, 2011) which showed that once formed, it was impossible to dissolve them, without melting the sample, and even then, they reappear upon solidification. Twin / grain boundary related cracks are visible and their fraction appears to be larger than in the T5 condition. Recall that this material has a weaker texture than the T5, which would promote more twinning. The extensive network of grain boundary precipitates is not visible which implies that the T3 treatment was successful in removing them. The fact that this condition shows comparable ductility as the T5 temper, indicates that these twin related cracks are not severely detrimental.

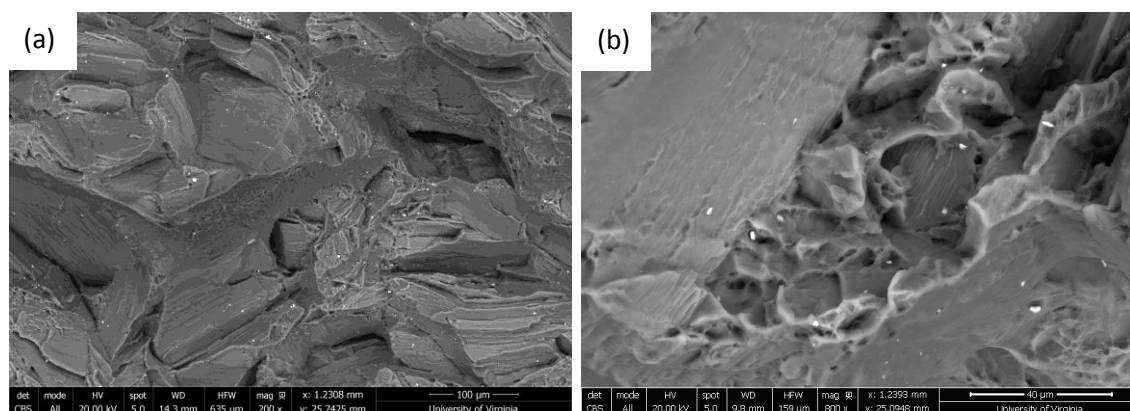


Figure 3.11: Backscattered fractographs for a T3 specimen tested in tension along TD, showing (a) smooth cracks associated with twins/grain boundaries (b) ductile dimples associated with Y rich cuboids.

In the under-aged condition, both TD and ND exhibit cracks associated with twin/grain boundaries, with little ductile damage. Note that even though the dispersoid clusters are still present in the ND specimen in under-aged condition (Figure 3.12), there are more areas which

have a rough appearance and exhibit the presence of dimples which results in a larger ductility than the TD tested in the aged condition (Figure 3.13).

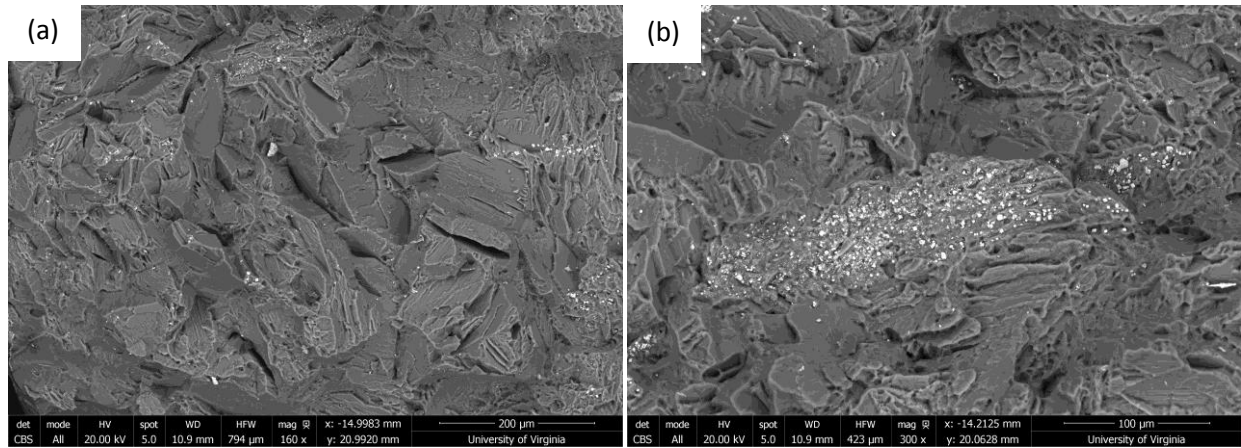


Figure 3.12: Backscattered fractographs for an under-aged (aging at 210°C for 8h) specimen tested in tension along ND, showing (a) smooth features indicative of less ductile damage and cracks associated with twins/grain boundaries. (b) the clusters of dispersoids still present after solutionizing treatment.

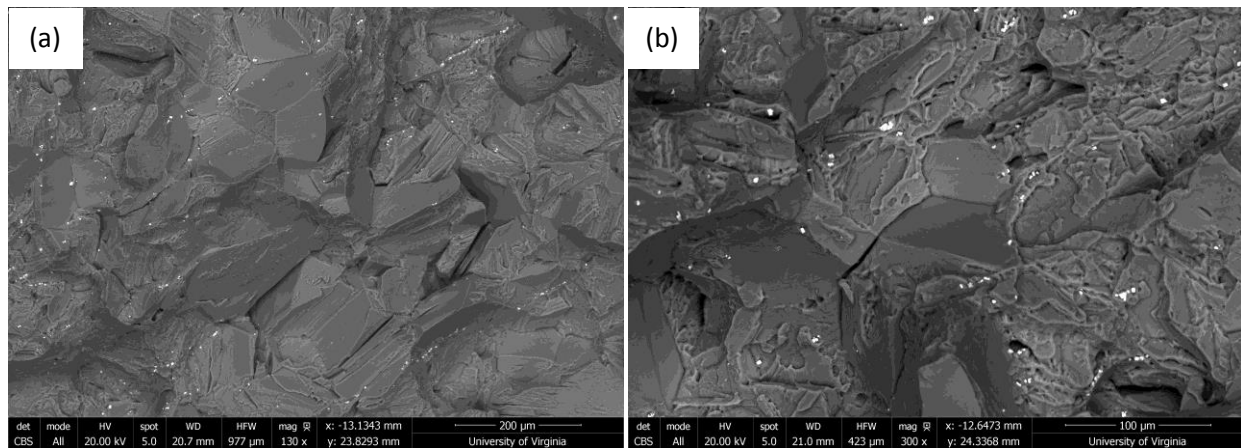


Figure 3.13: Backscattered fractographs for an under-aged (aging at 210°C for 8h) specimen tested in tension along TD, showing (a) smooth features indicative of less ductile damage and cracks associated with twins/grain boundaries. (b) some ductile dimples in between regions of smooth faceted regions.

The fractographs obtained for the TD peak-aged specimens show an increased grain boundary precipitation, and the fracture observed is essentially intergranular (Figure 3.14). At

peak-aged condition, the evidence of intergranular fracture increases, the grain boundary precipitate network reappears and this heterogeneous distribution of the precipitates seems to be responsible for the low ductility observed in this condition. The ND specimens continue to exhibit twin related cracks and some evidence of ductile damage (Figure 3.15).

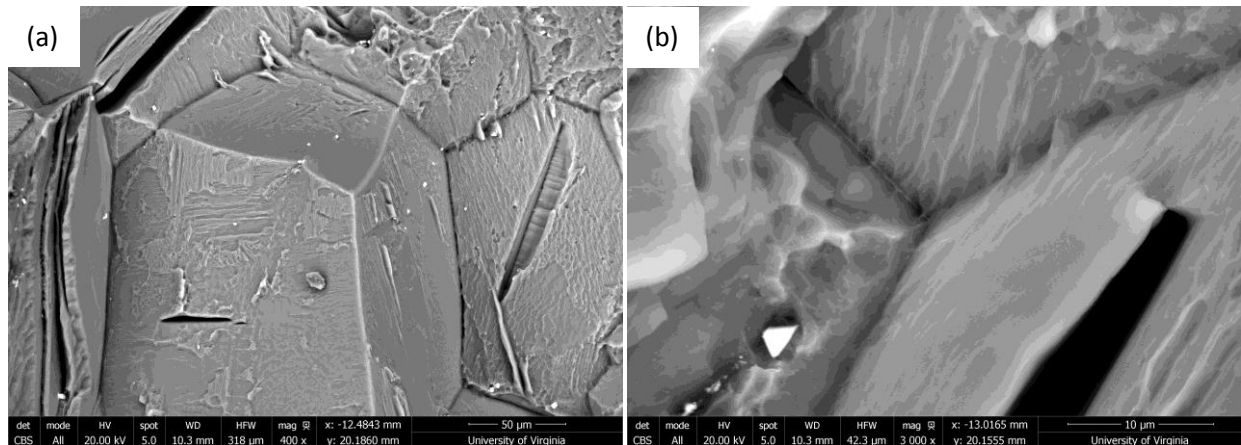


Figure 3.14: Backscattered fractographs for peak-aged (aging at 210 °C for 64h) specimen tested in tension along TD, showing (a) extensive intergranular failure with twin related cracks within the grains (b) presence of grain boundary precipitates.

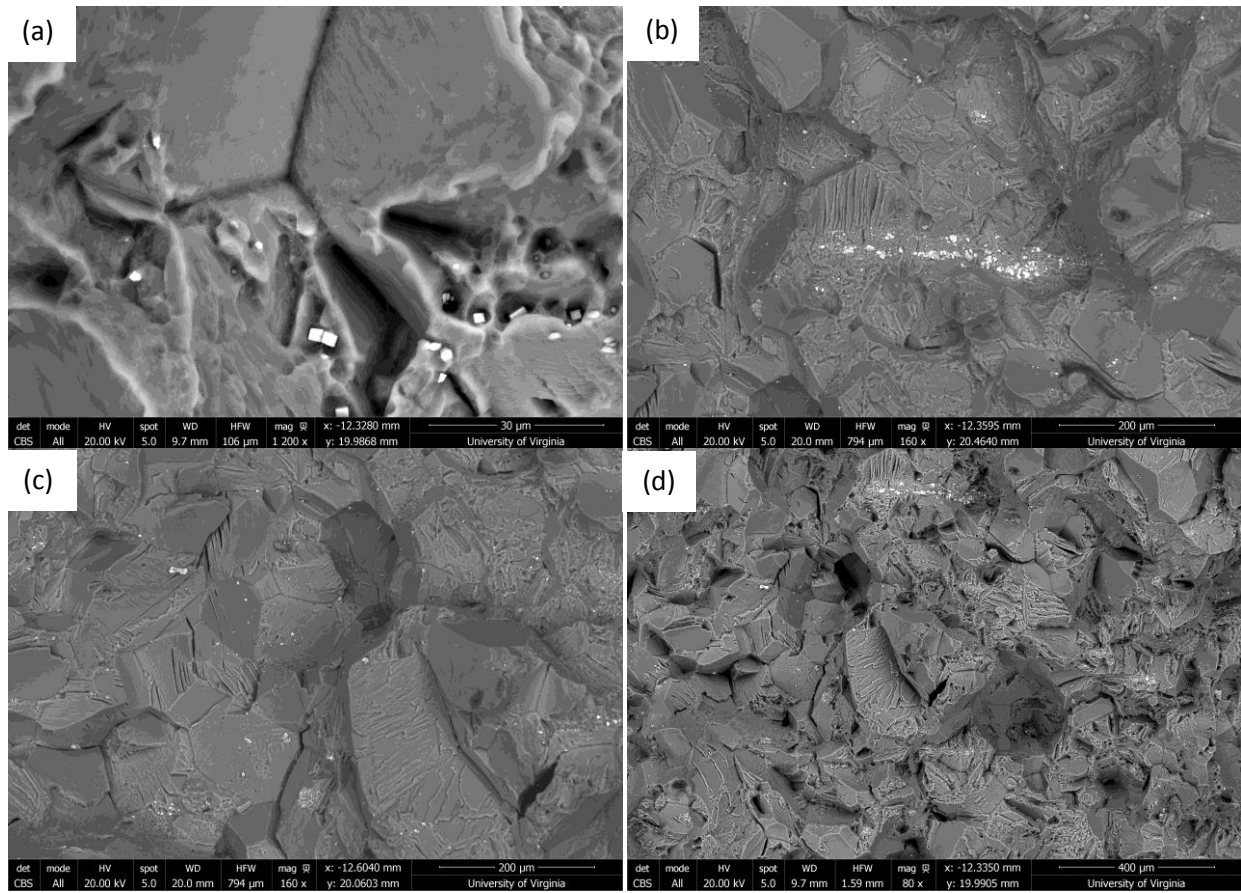


Figure 3.15: Backscattered fractographs for peak-aged (aging at 210 °C for 64h) specimen tested in tension along ND, showing (a) some ductile dimples associated with Y-rich cuboid dispersoids (b) dispersoid clusters (c) and (d) twin/grain boundary cracks.

3.5 Discussion

One rather interesting result is that hardness testing did not reveal differences in the peak strength of the various aging strategies, which were apparent in the tensile test data. For example, the T6 was shown to exhibit slightly higher hardness, but much lower strength than T5. At first this may seem contradictory. However, it is suggested that these two results can be reconciled by considering the distinct nature of the two tests in detail. Hardness testing involves probing of the material response at strain levels up to 0.3 or more (e.g., Chaudhri, 1998; Reuber et al., 2014), and the distinct hardening behavior of the different tempers (i.e., higher hardening rate of T3 and

T6, relative to T5) makes the method unreliable for probing detailed changes in the yield behavior. As will be shown in what follows, there are reasons to expect the T6 material to have a lower yield strength than the T5. First, it has a much larger grain size, so one contribution to strengthening is absent. This is particularly important for twinning mechanisms, which some authors have suggested are even more potently affected than slip (Meyers et al., 2001; Barnett et al., 2004). If twinning is an important part of the story, it is important to note that twinning can induce a very strong hardening at higher levels of strain.

3.5.1 Effect on flow behavior

In a previous study (Bhattacharyya et al., 2016), a set of initial yield and strain hardening parameters were developed to describe the constitutive response T5 material using elastoplastic self-consistent (EPSC) modeling. In that study, the relative contribution of the different strengthening mechanisms on the CRSS values of different modes were also obtained based on theoretical calculations. These together can be used to describe the effect of aging on the flow behavior of the TD and ND specimens, measured in this study. Furthermore, it has been shown that the T3 treatment weakens the texture, providing an appropriate initial texture for use in the simulations. It is to be noted that, in this simulation exercise, no fitting was carried out. The sole purpose is to show the predictive capabilities of the model developed earlier, by adjusting the CRSS values based on the microstructure parameters appropriate for the different aging treatments.

For the T3 condition, the contributions from the precipitates (42 MPa for basal, 33 MPa for prismatic and 60 MPa for $\langle c+a \rangle$ slip mode), forest dislocations (~ 1 MPa) and T5 grain size effect was subtracted off from the EPSC-T5 parameters (Table 3.2) and grain size effect for T3 (Table 3.3) was added to obtain the simulation parameters. As before, two sets of Hall-Petch

parameters were used, one based upon work of Raeisnia et al. (2010) and one based upon work of Wang and Choo (2014). Since the H-P coefficient of $\langle c+a \rangle$ slip was not obtained by Wang and Choo, the value as determined by Raeisnia et al., has been employed in simulations based on data of Wang and Choo. The new parameters thus obtained are shown in Table 3.3. For twinning, the parameters obtained for a previous study of cast and homogenized WE43 of similar grain size (Agnew et al., 2013), were used due to lack of relevant strength values.

For T6, the EPSC Voce parameters shown in Table 3.2 were adjusted for the grain size difference and employed in the simulations. Since the H-P coefficient of twinning was not obtained by Raeisnia et al., Wang and Choo's value was used in simulations based on the data of Raeisnia et al.

The simulated curves for TD (Figure 3.16) show good agreement overall with the experimentally observed flow behavior subsequent to aging. It is to be noted that the saturation stress, τ_l and initial hardening rate θ_0 were not fitted to match the data; rather the materials model previously developed to describe T5 material were used, albeit accounting for texture and grain size changes. Moreover, the experimental and the simulated results both indicate that the heat treatments did not alter the hardening behavior significantly. Regarding the ND case (Figure 3.17), the simulated flow curves over-predict flow stress. This is not surprising given that in the T5 case, a similar effect was seen. This only corroborates the fact that in order to capture twinning accurately, local stress dependence of twin nucleation has to be taken into account (Beyerlein and Tomé, 2010; Beyerlein et al., 2010; Wang et al., 2014) .

Table 3.2: Voce hardening parameters for T5 temper obtained from Bhattacharyya et al., (2016).

	τ_0	τ_1	θ_0
Basal	68	40	170
Prismatic	145	90	170
<c+a> 2 nd order	210	205	350
Tensile twin	130	0	150

Table 3.3: The effect of grain size on individual deformation modes obtained using Hall Petch coefficients Wang and Choo (2014) and Raeisinia et al. (2010), respectively.

Deformation mode	Hall Petch coefficient k (MPa-mm ^{1/2})	$\Delta\tau_{HP}$ T5 (MPa)	$\Delta\tau_{HP}$ T3 (MPa)
Basal	2.61, 0.42	19, 3	9, 1
Prismatic	5.54, 3.72	41, 28	19, 13
Pyramidal <c+a>	n/a, 4.71	n/a, 35	n/a, 16
Extension twinning	3.48, n/a	26, n/a	12, n/a

Table 3.4: CRSS values for T3 temper, obtained by subtracting the contribution of precipitates, forest dislocations, and grain size of T5 and adding T3 grain size contribution to the CRSS values given in Table 3.2.

	τ_0 <i>Raeisinia</i>	τ_0 <i>Wang</i>
Basal	23	15
Prismatic	96	89
<c+a> 2 nd order	130	(N/A)
Tensile twin	85	85

Table 3.5: CRSS values for T6 temper, obtained by subtracting the contribution of grain size of T5 and adding T3 contribution to the CRSS values given in Table 3.2.

	τ_0 <i>Raeisinia</i>	τ_0 <i>Wang</i>
Basal	65	57
Prismatic	129	122
<c+a> 2 nd order	190	(N/A)
Tensile twin	(N/A)	116

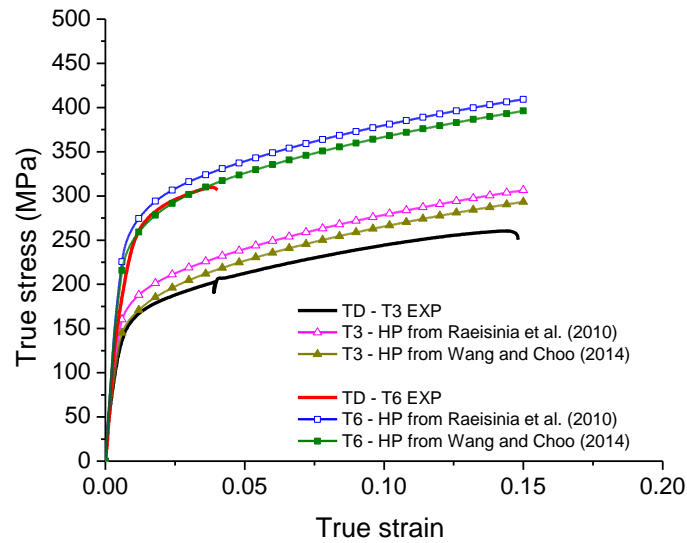


Figure 3.16: Experimental and simulated flow curves for TD tension for WE43-T3, and WE43-T6 tempers. The simulations were carried out using Voce parameters given in Tables 3.4 and 3.6

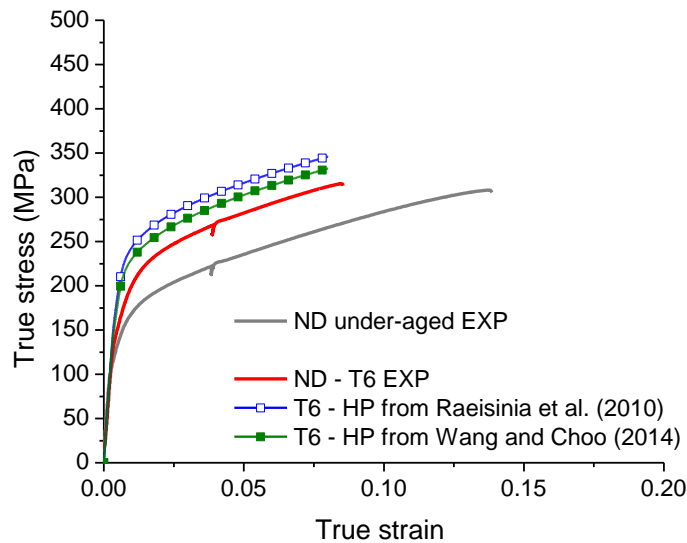


Figure 3.17: Experimental and simulated flow curves for ND tension for WE43-T6 temper and only experimental flow curve for ND tension for an under-aged specimen. The simulations were carried out using Voce parameters given in Tables 3.4 and 3.6

3.5.2 Effect on ductility

The microhardness data reveal that the T8 treatment increases the kinetics of precipitation and this is in line with previous observations on Al alloys (e.g., Gable et al., 2001) as well as modeling work on Mg-Nd (Liu et al., 2014). It is well known that dislocations affect the precipitation process by acting as a preferred nucleation site by lowering the activation energy of precipitation because the strain field of the dislocations can reduce the misfit strain of the precipitates. Furthermore, the dislocations can affect the kinetics of solute diffusion and thus accelerate the growth of the precipitates by providing easier diffusion paths along its core as well as acting as source or sink for vacancies. The first mechanism leads to a more uniform distribution of precipitates inside the grain, whereas the latter mechanism enables attaining the peak hardness/strength at lower aging durations. While the role of such treatment on ductility has not been studied here, the results of T5 temper suggest that the presence of dislocations during precipitation could improve the ductility as compared to T6. For one thing, it can lower the preference for grain boundary precipitation and the formation of a precipitate free zone in the vicinity of the grain boundaries. The fact that the type of dislocations introduced do have any significant effect on the kinetics, given that the strain energy of a dislocation is proportional to b^2 and Burger's vector of $\langle c+a \rangle$ dislocation is almost twice that of $\langle a \rangle$ type implies that may be there is not sufficient $\langle c+a \rangle$ dislocations in the matrix to produce discernable changes. Indeed, the larger Burgers vector also permits each dislocation to accommodate more strain, hence fewer dislocations are required to accommodate a given amount of strain.

The fractographs for different aging conditions reveal that the main mechanisms that are operative in this alloy are: microvoid nucleation, growth and coalescence associated with second phase particles, twin related cracks, and a ductile intergranular failure mechanism associated

with grain boundary precipitates. An additional factor relevant for the ND case is debonding associated with dispersoid clusters. Perhaps this is just a special case of microvoid nucleation, growth and coalescence, but the agglomeration of particles in a cluster/stringer makes this mechanism more catastrophic, and it is held responsible for the spallation failures observed in ballistic testing of WE43-T5 plates (Hamilton et al., 2012) As mentioned earlier in this chapter, prior work had already shown that it is impossible to remove these dispersoids which form during solidification, even with two step solutionizing heat treatments (Polesak, 2011).

One goal of the present thesis work was to determine if there was an optimal aging condition to improve the ballistic performance of the material. Given the spallation failure mechanism observed during that testing (Hamilton et al., 2012), it is suggested that examining tensile performance along the ND is a good surrogate lab test for performing this optimization. As such, it is found that the T5 and the T3 exhibit the best tensile ductility whereas T6 is the worst. It is thus envisaged that hot-rolling followed by aging leads to a more uniform distribution of the precipitates as indicated by ductile dimples within the grains, whereas T6 treatment leads to more severe grain boundary precipitation and ductile intergranular failure (Vasudévan and Doherty, 1987). The detailed role of the precipitate free zone associated with these precipitates merits further investigation. However, the present study unequivocally shows, with empirical data and reasonable physical arguments to substantiate why it is the case, that the T5 temper exhibits superior ductility as well as yield strength in comparison with the T6 more expensive heat treatment.

3.6 Conclusions

1. Solutionizing, quenching and aging leads to a slight increase in the hardness (i.e., 96 to 102 VHN, ~5%) over the conventional T5 wrought processed WE43 (hot working

followed by aging). However, solution heat treatment leads to randomization of the initial basal texture in WE43 plate. This, in turn, results in a dramatic reduction in yield strength anisotropy ($TD/ND = 1.7$ down to 1.3).

2. Stretching prior to aging of solutionized and quenched material increases the aging kinetics (peak hardness obtained after at ~8 hrs at 210°C, rather than 64 hrs). The value of the peak hardness is not enhanced by stretching prior to aging. Whether one stretches parallel to RD or compresses parallel to ND, the effect is similar.
3. Two-step aging (first at 140°C for 4 hrs, followed by 210°C) did not provide a measureable increase in hardness over the conventional one-step aging.
4. All of the samples exhibit twin-related cracks, grain boundary precipitation induced cracks, and transgranular ductile dimples. T6 samples appeared to exhibit the most intergranular ductile fracture, consistent with localization within a precipitate free zone (PFZ).
5. The T5 material has the highest ductility. T3 material is similar, despite the larger grain size and higher frequency of twin-related cracks. The ND samples tend to exhibit lower ductility in the T5 temper, which appears related to stringers of Y-containing cuboidal dispersoids.
6. Strength and flow stress *predictions* (using a previously published crystal plasticity model (Bhattacharyya et al., 2016) that accounts for the effects of initial texture, grain size, solid solution additions, and precipitates) are accurate to within 2 and 13%, respectively, for both solutionized and peak-aged material.

3.7 Acknowledgements

The authors would like to thank Dr. Bruce Davis of Magnesium Elektron, for providing the plate material explored in this study. The research at U.V.A. was sponsored by the U.S. Army Research Office under

contract number W911NF-12-1-0455 monitored by Drs. Suveen Mathaudhu and David Stepp as well as the U.S. National Science Foundation, grant number 1235259 monitored by Dr. Alexis Lewis. The views and conclusions contained in this document are those of the authors and should not be interpreted as representing the official policies, either expressed or implied, of the Army Research Laboratory or the U.S. Government. The U.S. government is authorized to reproduce and distribute reprints for government purposes notwithstanding any copyright notation hereon.

3.8 References

- Agnew, S., Whittington, W., Oppedal, A., El Kadiri, H., Shaeffer, M., Ramesh, K.T., Bhattacharyya, J., Delorme, R., Davis, B., 2014. Dynamic Behavior of a Rare-Earth-Containing Mg Alloy, WE43B-T5, Plate with Comparison to Conventional Alloy, AM30-F. *Jom* 66, 277–290. doi:10.1007/s11837-013-0830-x
- Agnew, S.R., Mulay, R.P., Polesak, F.J., Calhoun, C.A., Bhattacharyya, J.J., Clausen, B., 2013. In situ neutron diffraction and polycrystal plasticity modeling of a Mg–Y–Nd–Zr alloy: Effects of precipitation on individual deformation mechanisms. *Acta Mater.* 61, 3769–3780. doi:10.1016/j.actamat.2013.03.010
- Antion, C., Donnadieu, P., Perrard, F., Deschamps, A., Tassin, C., Pisch, A., 2003. Hardening precipitation in a Mg-4Y-3RE alloy. *Acta Mater.* 51, 5335–5348. doi:10.1016/S1359-6454(03)00391-4
- Barnett, M.R., 2007. Twinning and the ductility of magnesium alloys. Part I: “Tension” twins. *Mater. Sci. Eng. A* 464, 1–7. doi:10.1016/j.msea.2006.12.037
- Barnett, M.R., Keshavarz, Z., Beer, a. G., Atwell, D., 2004. Influence of grain size on the compressive deformation of wrought Mg-3Al-1Zn. *Acta Mater.* 52, 5093–5103. doi:10.1016/j.actamat.2004.07.015
- Beyerlein, I.J., Capolungo, L., Marshall, P., McCabe, R.J., Tomé, C.N., 2010. Statistical analyses of deformation twinning in magnesium. *Philos. Mag.* 90, 2161–2190.
- Beyerlein, I.J., Tomé, C.N., 2010. A probabilistic twin nucleation model for hcp polycrystalline metals. *Proc. R. Soc. A Math. Phys. Eng. Sci.* 466, 2517–2544.
- Bhattacharyya, J.J., Wang, F., Wu, P.D., Whittington, W.R., El Kadiri, H., Agnew, S.R., 2016. Demonstration of alloying, thermal activation, and latent hardening effects on quasi-static and dynamic polycrystal plasticity of Mg alloy, WE43-T5, plate. *Int. J. Plast.* 81, 123–151. doi:10.1016/j.ijplas.2016.01.005
- Cassada, W.A., Shiflet, G.J., Starke, E.A., 1991. The effect of plastic deformation on Al₂CuLi (T 1) precipitation. *Metall. Trans. A* 22, 299–306. doi:10.1007/BF02656799
- Chaudhri, M.M., 1998. Subsurface strain distribution around Vickers hardness indentations in annealed polycrystalline copper. *Acta Mater.* 46, 3047–3056. doi:10.1016/S1359-6454(98)00010-X
- Cho, K., Sano, T., Doherty, K., Yen, C., Gazonas, G., Montgomery, J., Moy, P., Davis, B., Delorme, R., 2009. Magnesium Technology and Manufacturing for Ultra Lightweight Armored Ground Vehicles, Army Research Laboratory ARL-RP-236.
- Deschamps, A., Bigot, A., Livet, F., Auger, P., Brechet, Y., Blavette, D., 2001. A Comparative Study of Precipitate Composition and Volume Fraction in an Al–Zn–Mg Alloy using Tomographic Atom Probe and Small-Angle X-ray Scattering. *Philos. Mag. A* 81, 2391–2414. doi:10.1080/01418610110038439
- Gable, B.M., Zhu, A.W., Csontos, A.A., Starke, E.A.J., 2001. The role of plastic deformation on the competitive microstructural evolution and mechanical properties of a novel Al-Cu-Li-X alloy. *J.*

- Light Met. 1, 1–14.
- Graf, M., Hornbogen, E., 1977. Observation of ductile intercrystalline fracture of an Al-Zn-Mg-alloy. *Acta Metall.* 25, 883–889. doi:10.1016/0001-6160(77)90174-2
- Hamilton, J., Brennan, S.T., Sohn, Y., Davis, B., Delorme, R., Cho, K., 2012. Microstructural Characteristics of High Rate Plastic Deformation in Elektron™ WE43 Magnesium Alloy.
- Kondori, B., Benzerga, A.A., 2014. Fracture Strains, Damage Mechanisms and Anisotropy in a Magnesium Alloy Across a Range of Stress Triaxialities. *Exp. Mech.* 54, 493–499. doi:10.1007/s11340-013-9812-8
- Liu, H., Gao, Y., Zhu, Y.M., Wang, Y., Nie, J.F., 2014. A simulation study of β 1 precipitation on dislocations in an Mg-rare earth alloy. *Acta Mater.* 77, 133–150. doi:10.1016/j.actamat.2014.04.054
- Ludtka, G., Laughlin, D., 1982. The influence of microstructure and strength on fracture mode and toughness of 7XXX Al alloys. *Metall. Mater. Trans. A* 13, 411–425.
- MENA, 2014a. Magnesium Elektron WE43B Data sheet 467.
- MENA, 2014b. Magnesium Elektron WE43 Data sheet 490.
- Meyers, M. a, Hringer, O. V, Lubarda, V. a, 2001. The onset of Twinning in Metals: a Constitutive Description. *Acta mater* 49, 4025–4039.
- Mordike, B.L., 2002. Creep-resistant magnesium alloys. *Mater. Sci. Eng. A* 324, 103–112.
- Nie, J.F., 2003. Effects of precipitate shape and orientation on dispersion strengthening in magnesium alloys. *Scr. Mater.* 48, 1009–1015. doi:10.1016/S1359-6462(02)00497-9
- Nie, J.-F., 2012. Precipitation and Hardening in Magnesium Alloys. *Metall. Mater. Trans. A* 43, 3891–3939. doi:10.1007/s11661-012-1217-2
- Nie, J.F., Muddle, B.C., 2000. Characterisation of strengthening precipitate phases in a Mg–Y–Nd alloy. *Acta Mater.* 48, 1691–1703. doi:10.1016/S1359-6454(00)00013-6
- Nie, J.F., Xiao, X.L., Luo, C.P., Muddle, B.C., 2001. Characterisation of precipitate phases in magnesium alloys using electron microdiffraction. *Micron* 32, 857–863. doi:10.1016/S0968-4328(00)00094-9
- Oh-ishi, K., Hono, K., Shin, K.S., 2008. Effect of pre-aging and Al addition on age-hardening and microstructure in Mg-6 wt% Zn alloys. *Mater. Sci. Eng. A* 496, 425–433. doi:10.1016/j.msea.2008.06.005
- Pardoen, T., Dumont, D., Deschamps, A., Brechet, Y., 2003. Grain boundary versus transgranular ductile failure. *J. Mech. Phys. Solids* 51, 637–665. doi:10.1016/S0022-5096(02)00102-3
- Polesak, F.J., 2011. Constitutive behavior and microstructure evolution of magnesium alloy WE43 at temperatures and strain rates relevant to hot deformation processing.
- Raeisinia, B., Agnew, S.R., Akhtar, A., 2010. Incorporation of Solid Solution Alloying Effects into Polycrystal Modeling of Mg Alloys. *Metall. Mater. Trans. A* 42, 1418–1430. doi:10.1007/s11661-010-0527-5
- Reuber, C., Eisenlohr, P., Roters, F., Raabe, D., 2014. Dislocation density distribution around an indent in single-crystalline nickel: Comparing nonlocal crystal plasticity finite-element predictions with experiments. *Acta Mater.* 71, 333–348. doi:10.1016/j.actamat.2014.03.012
- Robson, J.D., Stanford, N., Barnett, M.R., 2011. Effect of precipitate shape on slip and twinning in magnesium alloys. *Acta Mater.* 59, 1945–1956. doi:10.1016/j.actamat.2010.11.060
- Rosalie, J.M., Somekawa, H., Singh, A., Mukai, T., 2013. Increasing Volume Fraction of Precipitates and Strength of a Mg-Zn-Y Alloy by Pre-Aging Deformation. *Magnes. Technol.* 2013 323–328.
- Senn, J.W., Agnew, S.R., 2008. Texture randomization of magnesium alloys Containing rare earth elements, in: *Magnesium Technology 2008*. p. 153.
- Somekawa, H., Singh, a., Mukai, T., 2009. Fracture mechanism of a coarse-grained magnesium alloy during fracture toughness testing. *Philos. Mag. Lett.* 89, 2–10. doi:10.1080/09500830802537718
- Vasudévan, A.K., Doherty, R.D., 1987. Grain boundary ductile fracture in precipitation hardened aluminum alloys. *Acta Metall.* 35, 1193–1219. doi:10.1016/0001-6160(87)90001-0
- Wang, F., Bhattacharyya, J.J., Agnew, S.R., 2016. Effect of precipitate shape and orientation on Orowan strengthening of non-basal slip modes in magnesium alloys.
- Wang, J., Beyerlein, I.J., Tome, C.N., 2014. Reactions of lattice dislocations with grain boundaries in Mg:

- Implications on the micro scale from atomic-scale calculations. *Int. J. Plast.* 56, 156–172. doi:10.1016/j.ijplas.2013.11.009
- Wang, Y., Choo, H., 2014. Influence of texture on Hall–Petch relationships in an Mg alloy. *Acta Mater.* 81, 83–97. doi:10.1016/j.actamat.2014.08.023

4 Measuring and modeling the anisotropic, high strain rate deformation of Al alloy, 7085, plate in T711 temper

J. J. Bhattacharyya¹, S. R. Agnew¹, M. M. Lee¹, W. R. Whittington², and H. El Kadiri²

¹Materials Science and Engineering, University of Virginia, Charlottesville, Virginia, U.S.A.

²Mechanical Engineering, Mississippi State University, Mississippi, U.S.A.

4.1 Abstract

Al alloy 7085 in the T711 temper, has been proposed as a lightweight metallic armor material. The room temperature constitutive response is assessed by compression testing at quasi-static (0.001 s^{-1}) and dynamic (1000 s^{-1}) strain rates along the rolling (RD), transverse (TD), and normal (ND) directions. The flow strength, plastic strain anisotropy (r-values) and texture evolution is measured along each direction. While the flow stress exhibits only mild anisotropy, the compressive r-values revealed strong strain anisotropy, with values close to 0.4 for RD, 0.8 for TD, and 0.3-0.8 for ND, depending on details of the initial texture. Texture measurements revealed a typical hot-rolling texture with strong Brass component, as well as gradients in texture through the plate thickness. Microscopy revealed a mildly anisotropic grain shape. By employing self-consistent polycrystal plasticity simulation, it was possible to explore the relative contributions of initial crystallographic texture and anisotropic grain shape effects. The ND and TD r-values were strongly affected by anisotropic grain shape, whereas the RD is rather insensitive. Although the model reasonably described the flow behavior in all three directions, it was not capable of reproducing all aspects of the anisotropy in strain hardening and r-values. In short, the polycrystal model exaggerates the anisotropy. Previous research suggests that precipitates, which enforce a “backstress” on the surrounding microstructure, are likely responsible for reducing the plastic anisotropy. The fracture response was also found to be anisotropic, with ND showing a lower compressive ductility as compared to the RD and TD.

Keywords: B. Texture evolution B. anisotropic material B. Constitutive behavior C. Kolsky bar
C. crystal plasticity

4.2 Introduction

4.2.1 Background

The need to develop lightweight structural materials solutions for military vehicle structures and armor intensifies with the increasing cost of energy. Lighter weight vehicles (which can still meet the ballistic, blast, and crashworthiness requirements of the application) would provide larger payload capacity, greater range, and potentially greater agility to the next generation warfighter. During the last two decades, several improved aluminum alloys have been developed, primarily for aerospace applications, which have provided an opportunity to those seeking improved lightweight armor materials.

Ballistic and blast evaluations carried out on one such alloy, AA7085, by Army Research Laboratory (ARL) showed a higher performance as compared to existing AA7039 acceptance limits and lead to a new mil spec, MILDTL-32375 (Doherty et al., 2012). This new candidate armor material was tested in two different tempers: T711 for enhanced ballistic protection and T721 for improved blast protection (Gallardy, 2012). Both are in the over-aged (T7) condition, though T711 is closer to peak aged. Given such promising results, it is of interest to explore the deformation and fracture behavior in detail, as well as to develop constitutive relations which describe the behavior. To this end, the present paper presents a characterization of the homogeneous deformation response of AA7085-T711 temper, subjected to high strain rate deformation, and the role of crystallographic and morphological texture is explored.

4.2.2 Dynamic deformation of Al alloys

A significant amount of research has been carried out to evaluate the dynamic mechanical response of several Al alloys. The main focus has been to determination of the strain rate sensitivity (SRS) and fracture mechanisms of these alloys. On the one hand, solid solution strengthened alloys, such as the AA5XXX series, are known to be susceptible to the Portevin Le Chatelier (PLC) effect, which can result in negative SRS over a certain strain rate regime, under dynamic loading (Pandey et al., 2013; Kabirian et al., 2014; Baig et al., 2015; Rahmaan et al., 2016). On the other hand, precipitation strengthened alloys can exhibit a very different microstructures, depending upon their heat treatment. There may be unshearable or shearable precipitates and a range of solute levels exhibited by a single alloy. These could change significantly alter the thermally activated nature of the $\{111\}\langle 110 \rangle$ octahedral slip mode, which is intrinsically athermal, within the quasistatic strain rate and ambient temperature regime. What follows is a brief overview of such findings, with a focus on recent studies of 7000-series (Al-Zn-Mg) alloys.

Oosterkamp et al.,(2000) studied the effect of strain rate ($10^{-1} - 3 \times 10^3 \text{ s}^{-1}$) on dynamic compressive flow response for extruded AA7108 in T79 temper and found a low but slightly positive SRS. However, at strain rates $>2000 \text{ s}^{-1}$, they found a decrease in flow stress which they attributed to the occurrence of strain localization. Similar SRS values were obtained by Chen et al. (2009a), while investigating extruded AA7003 and AA7108 in T6 temper. Pedersen et al. (2008) studied the tensile response of different tempers (W, T4, T6, T7) of extruded AA7030 for strain rates up to 5 s^{-1} and found that the strain rate sensitivity and strength anisotropy of all the tempers were quite low, except the W temper material, which showed strong strain hardening anisotropy. Interestingly, all of them exhibited strong plastic strain anisotropy and the r-values

were essentially the same for various tempers. On the other hand, while comparing the anisotropy between W and T6 temper of AA7108, Lademo et al., (2002) and Reyes et al. (2006) found that both the tempers have the similar level of strength anisotropy, while the difference in r-value was greatest along 45^0 from extrusion direction. Reyes et al. (2006) also investigated AA7003 in T1 and T79 tempers and found smaller differences in the r-values. Moreover, they found strong normal strain anisotropy during through-thickness compression tests, large scatter in the data, and a large difference in the r-values of the W and T6 tempers. These aforementioned studies indicate that the r-values are more sensitive to heat treatments as compared to the strength anisotropy. Regarding the fracture mechanisms, the presence of precipitate free zones and pre-existing shear bands, can lead to strain localization and has been found to be responsible for low fracture strains (Chen et al., 2009b). El-Magd and Abouridouane (2006) studied the dynamic tension and compression behavior of AA7075 and found that the fracture strain increased at higher strain rates in compression but decreased in tension. Thus, the existing literature indicates that the 7XXX alloys exhibit low positive SRS, mild strength anisotropy, but strong strain anisotropy and evidence of shear banding. It is also evident that the normal anisotropy (both strength and strain) of these Al alloys is a less studied area, and thus, part of the present study will focus on the normal anisotropy of the T711 plate under quasistatic and dynamic loading.

4.2.3 Role of anisotropic grain shape

Wrought metals and alloys often develop strong morphological texture, i.e., anisotropic grain shape, after thermomechanical processing such as rolling, especially in cold-rolled metals and alloys or those which resist recrystallization during processing, such as many 7XXX alloys. In addition to the crystallographic texture, it has been found that the anisotropic grain shape can

contribute to the overall anisotropy of the processed material. For instance, it is well known that grain shape influences the grain-matrix interaction by altering the stress and strain partitioning between the grains and the surrounding matrix. The “relaxed constraints” (RC) models of the early 1980’s, (Honneff and Mecking, 1978; Kocks and Canova, 1981; Kocks and Chandra, 1982; Van Houtte, 1982) were developed in order to allow differing shears parallel to the long grain boundaries in rolled microstructures having predominantly pancake shaped grains. Enforcing such relaxations of kinematical constraints lead to changes in the predictions of texture development and gave better predictions as compared the “full constraints” Taylor model. The grain shape effect was addressed in a more generalized way in 1-site self-consistent models (e.g., Tiem et al., 1986; Molinari et al., 1987; Lebensohn and Tomé, 1993), where the stress and strain deviations between the grain and the matrix are related through an “interaction” tensor, which is a function of the grain shape. Thus, instead of prescribing the constraints a priori, as in RC model, the partitioning of stresses and strains are allowed to evolve based on the evolution of the grain shape. Another approach to incorporate grain shape effects is represented by the ‘2-point’ LAMEL models (Van Houtte et al., 1999, 2002), in which a pair of grains form the structural unit. Local interactions between two grains in the pair are considered and each grain can have certain shear components relaxed. More computationally intensive crystal plasticity finite element models (e.g., Mika and Dawson, 1998; Li et al., 2004;) have also been developed to address the grain shape effects.

Experimentally, Cho et al. (1999) found that the elongated grain shape of the hot-rolled Al-Li alloy in the T6 condition resulted in a larger yield strength anisotropy as compared to one with equiaxed grains. Choi et al. (2000) investigated the effect of grain shape on yield strength and plastic strain (r-value) anisotropy of AA5019A-H48 sheet and found that, in order to capture

the r -value at 45° from RD, an ellipsoidal grain shape has to be accounted for. Furthermore, they compared the effect of grain shape on individual rolling texture components and found that while the plastic strain anisotropy (r -value directionality) is increased for all the components, the brass component is influence the most, whereas the yield strength anisotropy of the copper and brass texture components are reversed. More recent crystal plasticity simulation studies on low carbon steel sheets (Delannay et al., 2009; Xie et al., 2013) and AA3103 sheets (Zhang et al., 2014) have shown that accounting for grain shape results in better predictions of the yield strength and plastic strain anisotropy. All these studies have focused on in-plane anisotropy which is of significance for sheet metal formability. In this study, the effects of grain shape are explored, not only for in-plane, but also for normal anisotropy, since through-thickness properties are important for the armor applications in view.

4.3 Experimental methods

4.3.1 Materials, texture and microstructure

A 40.64 mm (1.6 inch) thick plate of AA7085 alloy in T711 temper was provided by ALCOA Technical Center, Monroeville, Pennsylvania, U.S.A., for this study. X-ray diffraction was used to measure the crystallographic texture of the plate at various depths, from the surface to the mid-plane, in order to assess the through-thickness texture gradients. The texture was measured at the surface, one-eighth plane (~5 mm depth), one-quarter plane (~10 mm), three-eighth plane (~15 mm), and the mid-plane (~20 mm) of the plate. The measurements were made using a PANalytical X'pert Pro multipurpose diffractometer (MPD; PANalytical, Almelo, The Netherlands) with Cu K α radiation at 45 kV and 40 mA. The tube was used in point focus, with cross-slit texture optics having 2 mm horizontal and 1 mm vertical dimensions, following the Schultz reflection method, to minimize defocusing at higher χ tilts. The {111}, {200}, and {220}

incomplete ($\chi = 0^\circ$ to 80°) pole figures were obtained. The background was measured on each sample and an experimental defocusing curve was obtained from a random Ti sample, made by curing. The raw data were analyzed using MTeX to generate complete orientation distributions (ODFs) and full pole figures (Figure 4.1). The presence of a texture gradient is clearly evident. As expected, the surface texture consists of a weak $\langle 110 \rangle$ //RD shear texture, resulting from the friction between the rolls and the plate surface. The volume fraction of an individual orientation is obtained using MTeX, by integrating the product of the ODF and a Gaussian function centered on the considered orientation with a spread of 20° (Table 4.1). The ODFs are plotted as constant φ_2 sections through Euler space ($\varphi_1, \phi, \varphi_2$), using Bunge's notation (Bunge, 1982) with RD, TD and ND as sample reference axes (Figure 4.2). For this purpose, the orthotropic sample symmetry was imposed, which allows to confine the full ODF in the subspace $0 \leq \varphi_1, \phi, \varphi_2 \leq 90^\circ$.

The interior of the plate consists of a weak recrystallized Cube texture component along with the β -fiber including the copper (Cu), S and brass (Bs) orientations. However, the intensity of the β -fiber components varies through-thickness. The Cu orientations are present in similar amounts throughout, whereas the central layers ($3/8^{\text{th}}$ and midplane) have a higher volume fraction of the S and Bs orientations

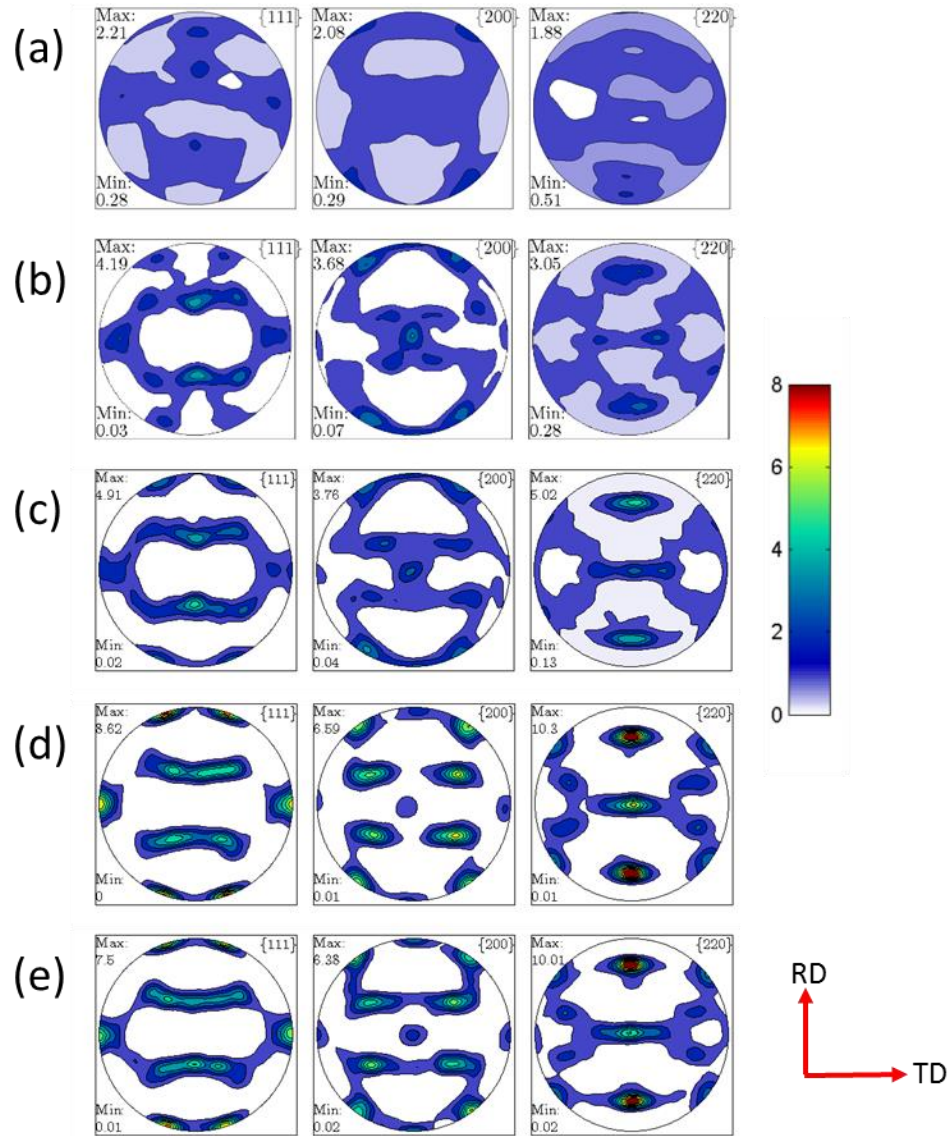


Figure 4.1: Texture gradient of AA7085-T711 plate –Recalculated experimental{111}, {200} and {220} pole figures at various depths from the surface (a) 0 mm(surface) (b) 5mm (1/8th plane) (c) 9 mm (1/4th plane) (d) 15 mm (3/8th plane) and (e) 20 mm (midplane).

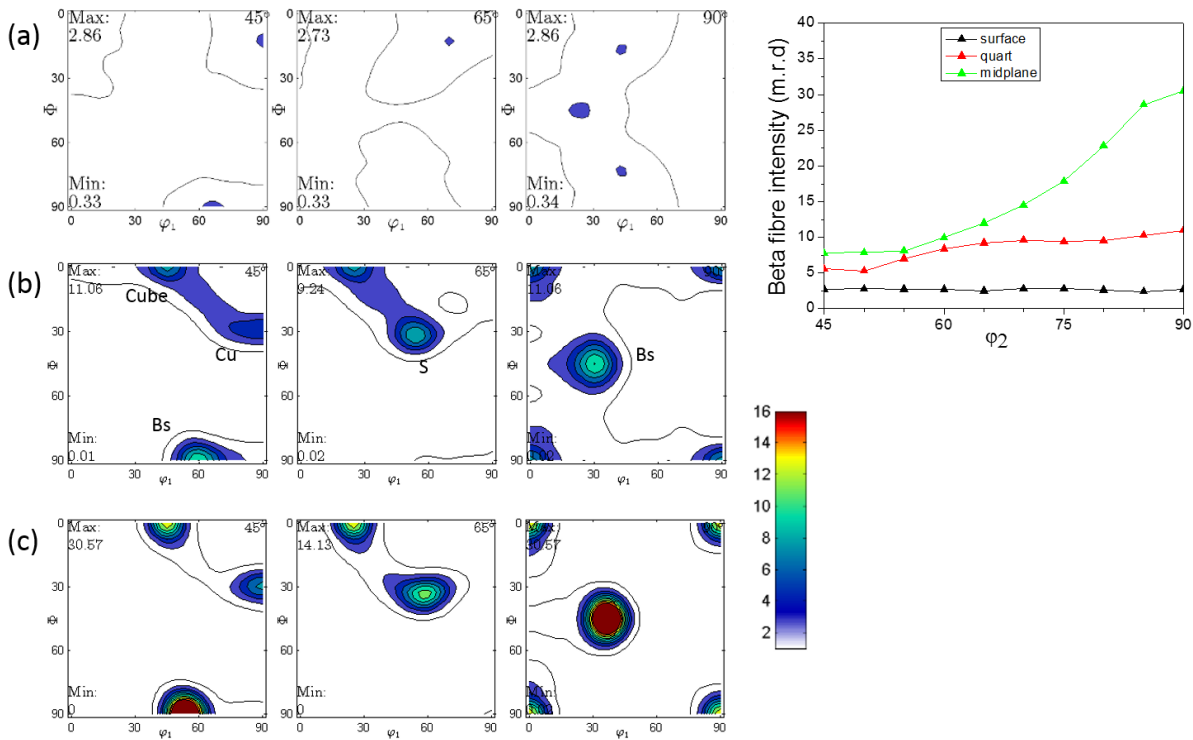


Figure 4.2: Texture gradient of AA7085-T711 plate - $\phi_2 = 45^\circ, 65^\circ$, and 90° sections (after imposing orthotropic symmetry) at: a) surface b) 1/4th plane c) midplane and d) variation of β -fibre intensity in these sections.

Table 4.1: Volume fraction of texture components calculated with 20° radius (triclinic symmetry)

Name	Indices	Bunge ($\phi_1 \Phi \phi_2$)	Surface	1/8 th	1/4 th	3/8 th	1/2
Copper	$\{112\}\langle 11\bar{1} \rangle$	$90^\circ 30^\circ 45^\circ$	7	7	9	7	11
S	$\{123\}\langle 63\bar{4} \rangle$	$59^\circ 34^\circ 65^\circ$	7	10	11	16	20
Brass	$\{110\}\langle \bar{1}12 \rangle$	$35^\circ 45^\circ 0/90^\circ$	8	11	14	27	25
Cube	$\{100\}\langle 001 \rangle$	$0^\circ 0^\circ 0/90^\circ$	4	10	11	10	11
Goss	$\{110\}\langle 001 \rangle$	$0^\circ 45^\circ 0/90^\circ$	6	6	6	3	3

Electron backscattered diffraction (EBSD) measurements were carried out on both the as-received and deformed material, in order to investigate the evolution of both microstructure and texture. The samples were cold-mounted in epoxy, mechanically ground down to 1200-grit SiC paper, polished with 3 and 1 μm oil-based diamond paste, and final polished with 0.06 μm

colloidal silica. After this metallographic procedure, a Hitachi IMP4000plus ion polisher was used to remove the deformation layer thereby improving the indexation rate. EBSD was performed within a FEI Quanta 650 FEG scanning electron microscope equipped with Oxford /HKL system with a Nordlys EBSD detector. The electron microscope was operated at 20 kV, with a working distance of 15-20 mm at a magnification of 100X. The step size and the spot size during EBSD data collection were 2.5-10 μm and 5.5 (corresponding to a beam current of 11 nA), respectively. The fraction of points successfully indexed was 85–95% and the average mean angular deviation (MAD) was 0.5° .

In order to obtain the aspect ratio (AR) of the grains, EBSD measurements were carried out on the ‘ND-RD’ and ‘RD-TD’ sections of the as-received plate. Two regions, one close to the surface and another close to the mid-plane were selected to interrogate the possibility of through-thickness gradient of grain shape. The step size for these scans was 2.5 μm . Subsequently, each grain was fitted an ellipse using HKL software and the ratio of the major and minor axes is referred to as the AR. The average value is obtained from the histogram of relative frequency against AR with a bin size of 1.

The ND-IPF maps taken from a region between the surface and $1/8^{\text{th}}$ plane (Figure 4.3a) and from a region between the $3/8^{\text{th}}$ plane and midplane (Figure 4.3b) show a partially recrystallized microstructure with large elongated grains and fine equiaxed grains. Near the surface, the predominance of ‘red’ grains indicate that majority of the grains present their $\{100\}$ poles along ND, whereas the grains near the midplane are mostly ‘green’ indicating their $\{220\}$ poles are parallel to ND. These observations are consistent with the bulk XRD texture shown in Figure 4.2. The aspect ratios (AR) of the grains were determined to be 3:2:1 (RD:TD:ND) near the surface and 5:3:1 near the midplane.

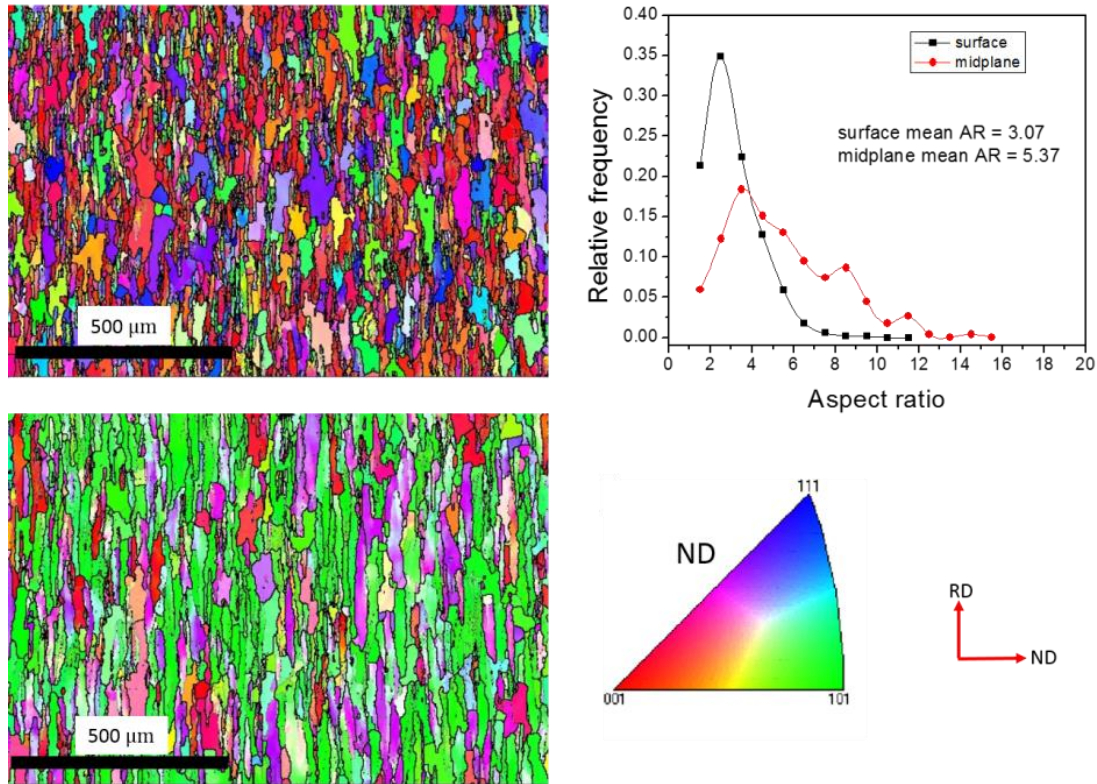


Figure 4.3: EBSD ND-IPF maps of the as-received AA7085-T711 plate obtained at: a) near the surface, showing mostly {001} oriented grains, and b) near the midplane, showing a predominance of {011} oriented grains c) relative frequency distribution of aspect ratio of the grains in the two above mentioned cases.

To obtain the deformed texture, multiple (6-8) areas of $\sim 1 \text{ mm}^2$ were scanned on the plane of the specimen containing the stress axis and the orientation distribution function (ODFs) of the individual measurements were averaged to obtain the recalculated pole figures with sufficient grain-count statistics. Band contrast and inverse pole figure (IPF) maps of different directions were constructed using HKL Channel 5 software.

4.3.2 Mechanical testing

Compression specimens, in the form of right circular cylinders of 8mm diameter and height, were wire electrical discharge machined (EDM'd) from the plate along RD, TD and ND.

The ND samples were obtained from two locations, either near the plate surface or midplane, in order to evaluate the effects of through thickness texture gradient.

Uniaxial compression tests at strain rate of 10^{-3} s^{-1} were performed using a universal testing machine, during which the axial strain was measured using a laser extensometer. A split Hopkinson pressure (or Kolsky) bar testing apparatus was used to assess the uniaxial compression behavior along RD, ND and transverse direction (TD) at a nominal strain rate of 1000 s^{-1} . The experimental set up and data analysis are discussed in detail in an earlier publication (Agnew et al., 2014). To ensure near constant strain rates, cylindrical pulse shapers of 10 mm diameter and 2 mm length cut from AA1100 alloy were used. This also helps to eliminate the high frequency Pochhammer-Chree oscillations, due to dispersion in the flow curve (Gray, 2000; Chen and Song, 2010). The condition for stress equilibrium was checked during data processing to ensure uniform loading of the specimen. The plastic strain anisotropy is assessed by measuring the compressive r-values along three orthogonal directions, following the convention of Jain and Agnew (2007):

$$r_{RD} = \epsilon_{TD}/\epsilon_{ND} \quad (4-1)$$

$$r_{TD} = \epsilon_{RD}/\epsilon_{ND} \quad (4-2)$$

$$r_{ND} = \epsilon_{TD}/\epsilon_{RD} \quad (4-3)$$

To measure the evolution of r-value with strain for the quasistatic case, the samples were unloaded at a specific strain level, and the strains along the transverse and thickness directions were measured using a digital caliper. Volume constancy ($\epsilon_{ii} < 0.001$) was enforced to ensure accurate measurements. Fractured samples were not used to assess the r values.

4.4 Modeling approach

4.4.1 The VPSC model

Polycrystal plasticity models provide an effective means of relating the single crystal constitutive behavior with that of the overall aggregate. In this case, the viscoplastic self-consistent (VPSC) model first developed by Lebensohn and Tome (1993), was used to model the deformation behavior of the AA7085-T711 plate at dynamic (1000 s^{-1}) and quasistatic (0.001 s^{-1}) strain rates. The polycrystal is represented as a collection of crystal orientations with volume fractions chosen to reproduce the experimentally measured initial texture. The model uses a single crystal constitutive equation similar to the viscoplastic rule employed by Hutchinson (1976) where the plastic strain rate $\dot{\gamma}^\alpha$ is related to the applied resolved shear stress τ^α as follows:

$$\dot{\gamma}^\alpha = \dot{\gamma}_0 \left| \frac{\tau^\alpha}{\tau_c^\alpha} \right|^{1/m} \text{sgn}(\tau^\alpha) \quad (4-4)$$

where $\dot{\gamma}_0$ is the reference slip rate, τ_c^α is the current critical resolved shear stress (CRSS) of slip system α , and sgn simply denotes the direction of the resolved stress (positive or negative). In the present study, m is not viewed as the actual strain rate sensitivity. Rather, this parameter is fixed at $1/m = 20$ and merely employed as a means of solving the “ambiguity problem” of rate independent crystal plasticity formulations (Pan and Rice, 1983; Asaro and Needleman, 1985). It will be shown later that the actual strain rate sensitivity of the flow stress is much lower than the value defined here. Hence, the simulations are carried out by setting the reference strain rate $\dot{\gamma}_0$ equal to the global straining rate enforced in the experimental tests (0.001 s^{-1} and 1000 s^{-1}) thereby eliminating the rate effects associated with the stress exponent based on the concept of Kok et al.,(2002). The actual material rate sensitivity is taken to be embedded in, τ_c^α , the CRSS.

The VPSC model incorporates an initial threshold stress τ_0^α , and the empirical Voce hardening rule for the evolution of the CRSS τ_c^α

$$\frac{d\tau_c^\alpha}{d\Gamma} = \theta_0^\alpha \left(1 - \left(\frac{\tau_c^\alpha - \tau_0^\alpha}{\tau_1^\alpha} \right) \right) \quad (4-5)$$

where $\Gamma = \sum_\alpha \gamma^\alpha$ is the accumulated shear strain in a grain, τ_c^α is the current CRSS of slip system α , $\tau_0^\alpha + \tau_1^\alpha$ is the saturation stress, and θ_0 is the initial strain hardening rate, respectively. These three parameters per deformation mode constitute the fitting parameters of the overall model. The strength increment due to strain hardening occurs via a hardening matrix, $h^{\alpha\beta}$, as follows:

$$\Delta\tau^\alpha = \frac{\partial\tau_c^\alpha}{\partial\Gamma} \sum_\beta h^{\alpha\beta} \Delta\gamma^\beta \quad (4-6)$$

where, $\delta\Gamma = \sum_\beta \Delta\gamma^\beta$. The components of the latent hardening (LH) matrix, $h^{\alpha\beta}$, determine the extent of hardening of primary system α due to activity of system β . For the FCC case, the coefficients of the hardening matrix have been experimentally determined for Al and Cu singles crystals by Kocks and Brown, (1966); Franciosi et al., (1980); Bassani and Wu, (1991) and Wu et al.,(1991). More recently, dislocation dynamics (DD) simulations have been employed to study the interaction of dislocations and obtain the hardening coefficients (Madec et al., 2003; Devincre et al., 2005, 2006). The results obtained from these two approaches differ mainly in the strength of the collinear interaction. The DD simulations results suggest that the collinear interactions are the strongest among all the interaction types. Various proportional and non-proportional loadings experiments along with dislocation density based crystal plasticity simulations have been employed to evaluate the effect of these various latent hardening coefficients (for e.g. Rousselier et al., 2010, 2012; Gérard et al., 2013; Khadyko et al., 2016). In one of these studies (Gérard et al., 2013), it was found that a high collinear interaction is required to capture the hardening for orthogonal loading in OHFC copper. However, for proportional loading of AA6060-T4, it was found that Voce hardening law with 2-parameter interaction

matrix gave satisfactory results as compared to other sophisticated hardening laws (Khadyko et al., 2016). In the current study, three different latent hardening matrices were used to see which gave the best match to the experimental data. For the first case, the hardening coefficients $h^{\alpha\beta}$, were all set to 1. This corresponds to latent hardening equal to the self-hardening rate. For the second case, based on Kocks and Brown (1966), the coefficients were set as $h^{\alpha\beta} = 1.4$ for $\alpha \neq \beta$ and $h^{\alpha\beta} = 1.0$ for $\alpha = \beta$. For the third case, the latent hardening matrix as obtained by Devincre et al.,(2006) was used, after normalizing the coefficients with respect to the self-hardening. Notably, the normalized parameters vary from 0.57 (Hirth lock) to 5.12 (collinear), whereas all others are close to 1.

To apply the self-consistent homogenization scheme based on Eshelby inclusion formalism, it is first necessary to linearize the nonlinear visco-plastic response. For a comprehensive discussion and comparison of the different linearization procedures the reader is referred to Lebensohn et al. (2007). Different linearization schemes from Secant (stiff) to Tangent (compliant) linearization were explored (results not shown in the interest of space) and it was found that affine linearization (Masson et al., 2000) gave the best overall match for the observed response, similar to the findings of Wang et al.,(2010) and Guo et al., (2015)

Using the concept of Homogeneous Effective Medium (HEM) and enforcing stress equilibrium, the linearized grain level response and the aggregate response can be related using an interaction equation:

$$(d^g - D) = -\tilde{M}:(\sigma^g - \Sigma) \quad (4-7)$$

where, the interaction tensor \tilde{M} is given by:

$$\tilde{M} = (I - S)^{-1} : S : \bar{M} \quad (4-8)$$

where d^g and D are the grain level plastic strain rate and the aggregate strain rate, respectively, and σ^g and Σ are the grain level stress and aggregate stress, respectively. S in Eq. 4-8 is the symmetric part of the Eshelby tensor and is dependent on the shape of the ellipsoid and the viscoplastic stiffness. During each straining step, the updated deformation gradient is used to update the shape of the ellipsoid i.e. the grain. Thus, the effect of the grain shape determines the Eshelby tensor which directly influences the interaction tensor and thus the effective compliance of the grain-matrix interaction.

4.4.2 Simulation methodology

To simulate uniaxial compression along RD, TD and ND, straining increments of 5×10^{-4} were imposed parallel to the loading direction at a rate consistent with the experimental testing rate while the shear strains were set to zero. The normal stresses along the two directions perpendicular to the loading direction were set to zero. All other components of stresses and strains were unknown. These boundary conditions allowed the development of normal lateral strains which was used to compute the r -value. After each straining step, the grain shapes and crystallographic orientations (i.e., texture) are updated. The predicted textures were compared with experimentally obtained textures after deformation to equivalent strain levels.

To generate yield surfaces at predefined strain levels, a set of straining directions in the principal strain space were chosen, and for each of these probes, the stress required to produce a von Mises equivalent straining increment of 0.002 was obtained using the VPSC scheme and hardening model described above. The stress values thus obtained were used to construct the yield surfaces. For a rate dependent model, there is no “yield criterion” in the strict sense.

However, the purpose is to provide an alternative visualization of the anisotropy resulting from the texture of the as-received material.

The experimental textures obtained from various depths of the AA7085-T711 plate were averaged and discretized to obtain a set of 2000 orientations with volume fractions representing the measured textures. Initially, discretized textures from each individual section were used in several simulations to see the effect of texture. Based on the results, two average textures were used subsequently. In one case, the surface, $1/8^{\text{th}}$ and $1/4^{\text{th}}$ plane textures were averaged (henceforth denoted as surf-avg) to create a representative texture of the near surface layers of the plate. Similarly, the $3/8^{\text{th}}$ and midplane textures were averaged (henceforth denoted as mid-avg) to represent the texture near the centre of the plate (Figure 4.4). Among many simulations carried out using each of these average textures (surf-avg and mid-avg), the results presented henceforth were obtained from two sets of simulations, carried out with the same Voce parameters: one with spherical grain shape and another with an ellipsoidal grain shape more representative of the initial microstructure (i.e. grain radii along RD:TD:ND of 3:2:1 for the surf-avg and 5:3:1 for mid-avg).

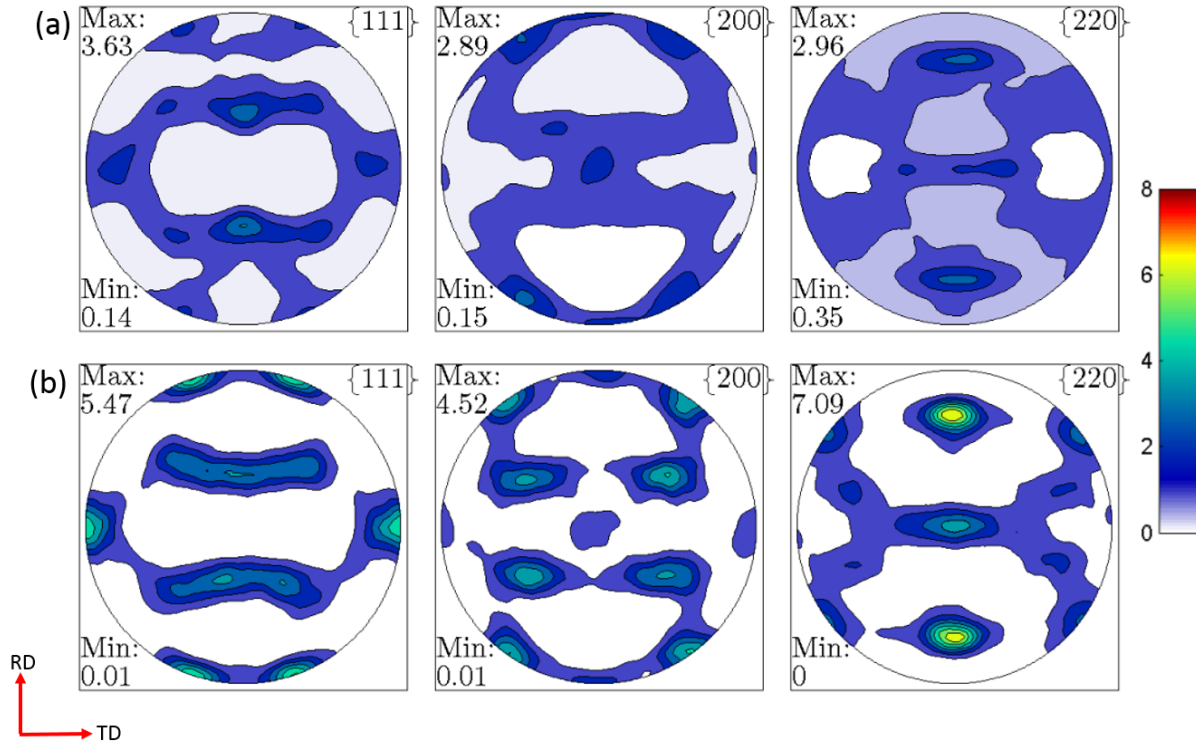


Figure 4.4: Discretized 2000 grains {111}, {200} and {220} pole figures for (a) average of surface, 1/8th and 1/4th plane (b) average of 3/8th and midplane.

4.5 Results

4.5.1 Compressive flow behavior

The flow curves at both quasistatic (QSR) and high strain (HSR) rates (Figure 4.5a and 4.5b) show subtle flow strength anisotropy with RD having a lower flow stress and hardening rate as compared to TD and ND. Multiple curves are shown to present the amount of scatter in the data. Along RD, the scatter is the least, while it is greatest for the ND case. The ND specimens extracted from near the surface exhibit a lower flow stress than the ones obtained from near the midplane. As will be demonstrated later, difference in texture is responsible for such variation of the flow stress. Interestingly, most of the mid-plane ND specimens exhibited low compressive ductility ($< 30\%$) at both 0.001 s^{-1} and 1000 s^{-1} , resulting from catastrophic shear failure, without any sign of flow softening or loss of work hardening rate while only a

small number survived to higher strain levels. On the other hand, none of the RD and TD samples failed at QSR, up to ~70% strain. Under dynamic strain rates, the near surface ND, RD and TD specimens all exhibited flow softening, albeit at different strain levels. The RD specimens showed flow softening after only ~10% strain, whereas the TD specimens were most resistant to flow softening.

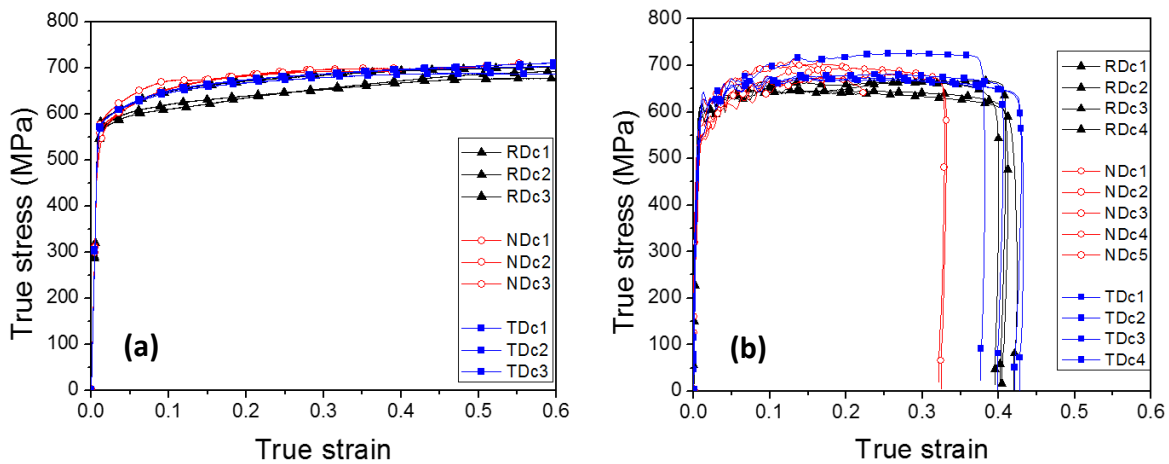


Figure 4.5: Experimental true stress-strain curves for RD, ND and TD compression at a) 0.001 s^{-1} and b) 1000 s^{-1} .

4.5.2 Modeling the quasistatic compressive response

Although the main focus of this paper concerns the dynamic behavior of 7085-T711 alloy, the quasistatic compressive data have been fitted using the VPSC code in order to determine the strain rate sensitivity at the slip system level and to determine if there is any rate dependence of texture evolution and plastic strain anisotropy. The TD compression flow curves were used to obtain the Voce parameters as shown in Table 4.2. Using these parameters, the RD and ND compression flow curves were also simulated (Figure 4.6- 4.8). For the case with isotropic grain shape and as $h^{a\beta} = 1$, it can be seen that the model underestimates the initial hardening rate and the flow stress for RD and ND. This leads to an over-prediction of the

strength anisotropy exhibited by this alloy. Accounting for the effect of grain shape does not improve the predictions, since the RD and ND flow curves remain essentially unchanged. To investigate whether latent hardening is responsible for such behavior, two cases were considered with different latent hardening coefficients. It can be seen that using $h^{a\beta} = 1.4$ gives good match for the ND case, but overestimates the TD and RD data. Using latent coefficients according to Devincre et al., (2006) gives quite similar results, and overestimates the flow stress along TD. In short, no single set of parameters were found which captured the flow anisotropy in all directions. Incorporating latent hardening where $h^{a\beta} \neq 1$ leads to an over-prediction of the flow stress anisotropy. The simulations with $h^{a\beta} = 1$ gave the best match to the experimental data, so they were used in all subsequent simulations.

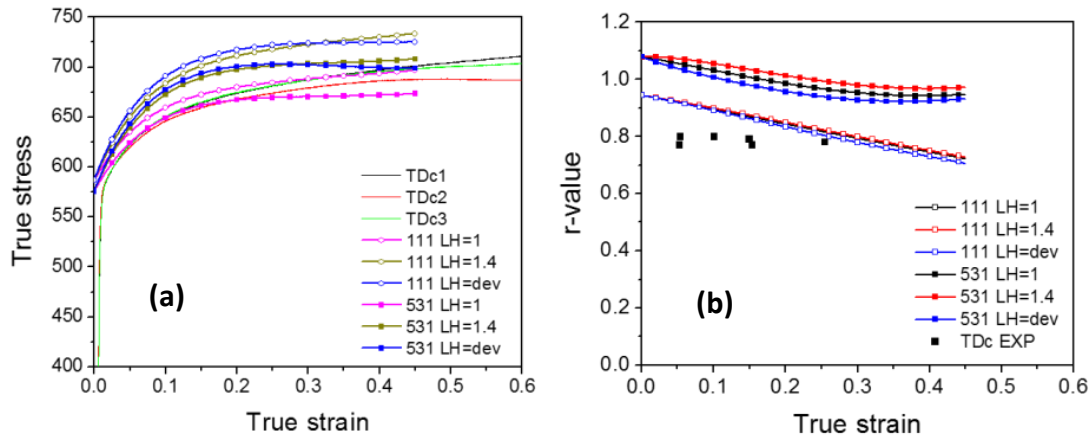


Figure 4.6: Experimental and simulated data for compression at 0.001 s^{-1} along TD a) flow curves and b) r-values. Isotropic grain shape is denoted by ‘111’ and ‘531’ represents grain shape RD:TD:ND = 5:3:1.

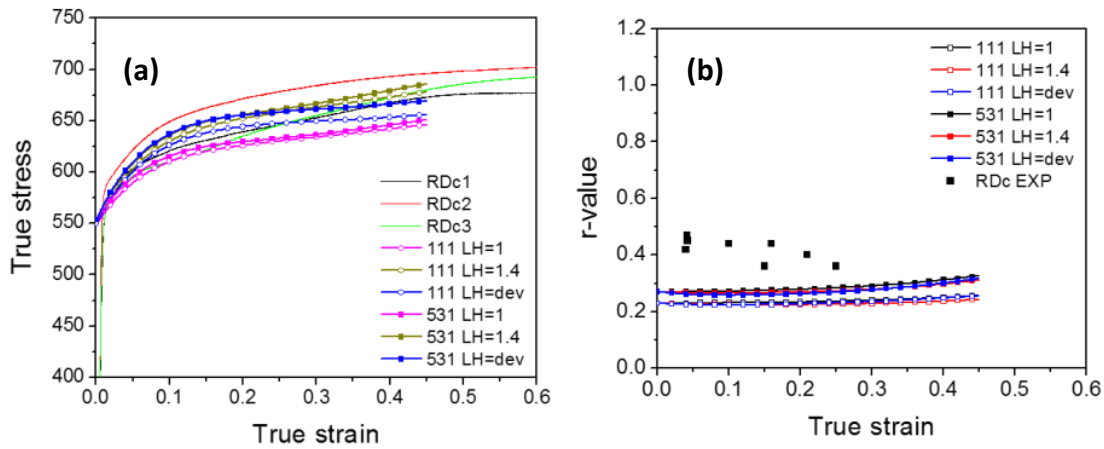


Figure 4.7: Experimental and simulated data for compression at 0.001 s^{-1} along RD a) flow curves and b) r-values. Isotropic grain shape is denoted by ‘111’ and ‘531’ represents grain shape RD:TD:ND = 5:3:1.

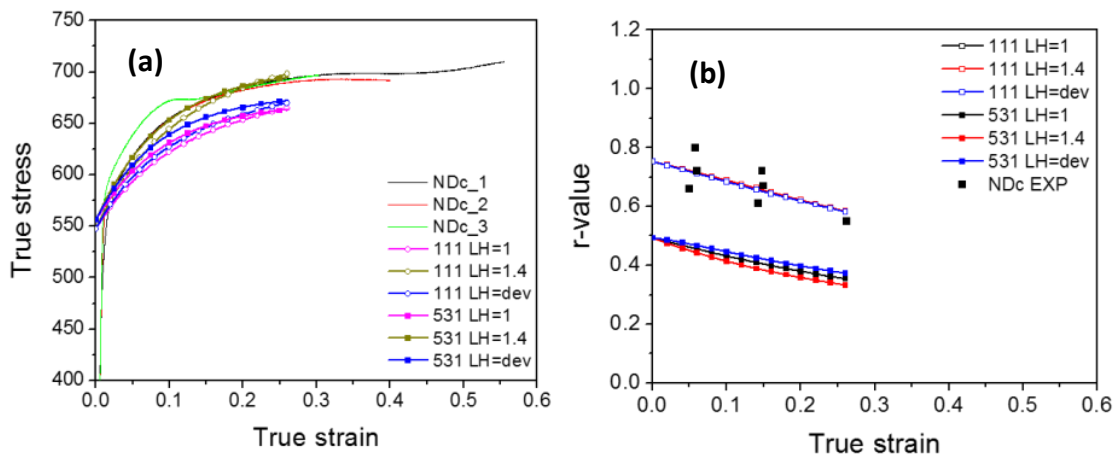


Figure 4.8: Experimental and simulated data for compression at 0.001 s^{-1} along ND a) flow curves and b) r-values. Isotropic grain shape is denoted by ‘111’ and ‘531’ represents grain shape RD:TD:ND = 5:3:1.

Since the flow curves did not provide adequate information regarding the grain shape effects, the simulated r-values were compared to the experimental data, to discern the effects of anisotropic grain shape (Figure 4.6- 4.8). For TD, using isotropic grain shape overestimated the r-values at lower strains and incorporating grain shape lead to a larger over-prediction. The effect of grain shape is larger for the TD than RD, where both isotropic and anisotropic grain shape

predicts a stronger anisotropy, i.e. a lower r-value, than what is observed experimentally. For the ND case, using isotropic grain shape gives good match with the experimental data. Comparison of experimental and simulated r-values indicates that the material is more isotropic than predicted by the crystal plasticity method employed in this work.

The experimental and simulated pole figures of a ND specimen, compressed up to 26 % strain is shown in Figure 4.9. It can be seen that the predicted pole figures qualitatively matches the experimental ones. However, the intensity of the $\{220\}$ poles are overestimated, irrespective of whether anisotropic shape effect is taken into account or not.

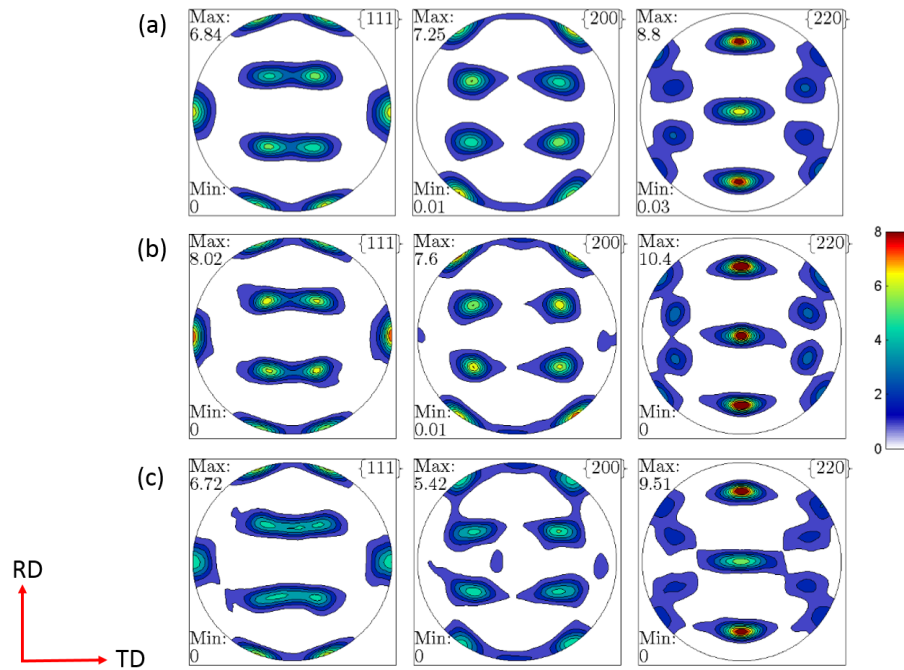


Figure 4.9: $\{111\}$, $\{200\}$ and $\{220\}$ pole figures for a specimen tested in ND compression at 0.001 s^{-1} up to 26% strain a) experimental recalculated pole figures b) simulated with isotropic grain shape c) simulated with the actual average grain shape (5:3:1).

Table 4.2: Voce hardening parameters for simulating flow curves at 0.001 s^{-1} and 1000 s^{-1} .

$\{111\}\langle 110 \rangle$	τ_0	τ_I	θ_0
0.001 s^{-1}	197	40	180
1000 s^{-1}	205	40	260

4.5.3 Modeling the dynamic compressive response

In all 3 directions, the r -values obtained at dynamic rates were same as that obtained at quasistatic rates, within experimental uncertainty. Based on the quasistatic simulation results, which provided some insight regarding the role of latent hardening, the Voce parameters for high strain rate data is obtained using the best case scenario, viz. $h^{\alpha\beta} = 1$ for both isotropic and anisotropic grain shapes. The Voce parameters presented in Table 4.2 were found to give the best match with the experimental data.

4.5.3.1 RD compression

The experimental and simulated flow curves are shown in Figure 4.10a. It was found that the Voce parameters listed in Table 4.2 provide a good description of the experimental data, irrespective of whether the actual grain shape is taken in to account. It is noted that no attempt has been made to model the flow softening exhibited by some of the specimens since the one-site, mean-field VPSC model is not capable of modeling localization phenomena. Similar to the quasistatic case, the simulated r -values do not show significant evolution with strain, in accordance with the experimental observation and the values are slightly lower than that observed (Figure 4.10b). Incorporating anisotropic grain shape increases the r -value slightly but still over-predicts the plastic anisotropy. Simulations carried out with the surf-avg texture show that the flow stress and r -values are relatively insensitive to the initial texture. The simulated textures show a good qualitative match with the experimental data (Figure 4.11a-c). It is to be noted that since the actual specimen had undergone flow softening and shear localization, so some differences between the terminal flow stress observed experimentally and that predicted by the model are to be expected.

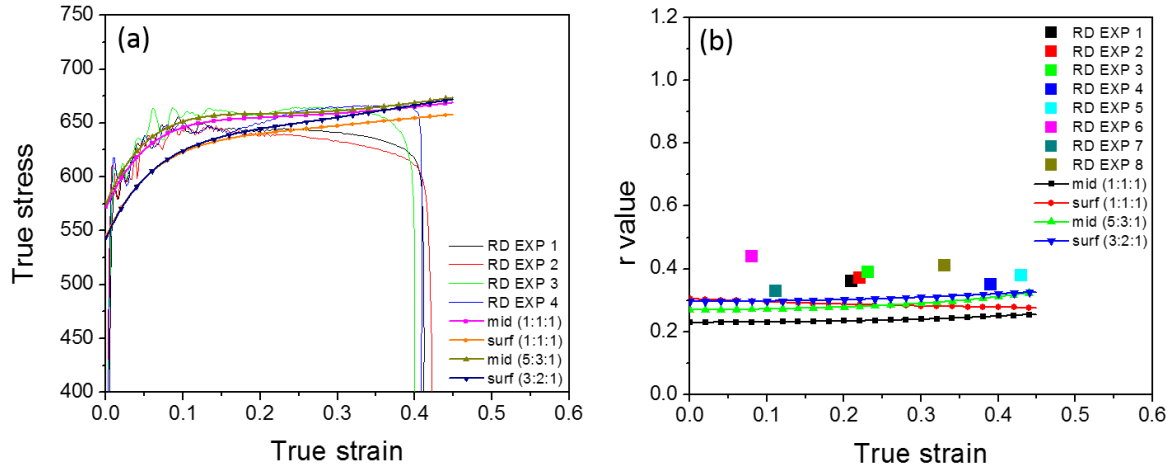


Figure 4.10: Experimental and simulated data for compression at 1000 s^{-1} along RD a) flow curves and b) r-values. ‘mid’ and ‘surf’ indicate the average texture used. The grain shape is given in parentheses.

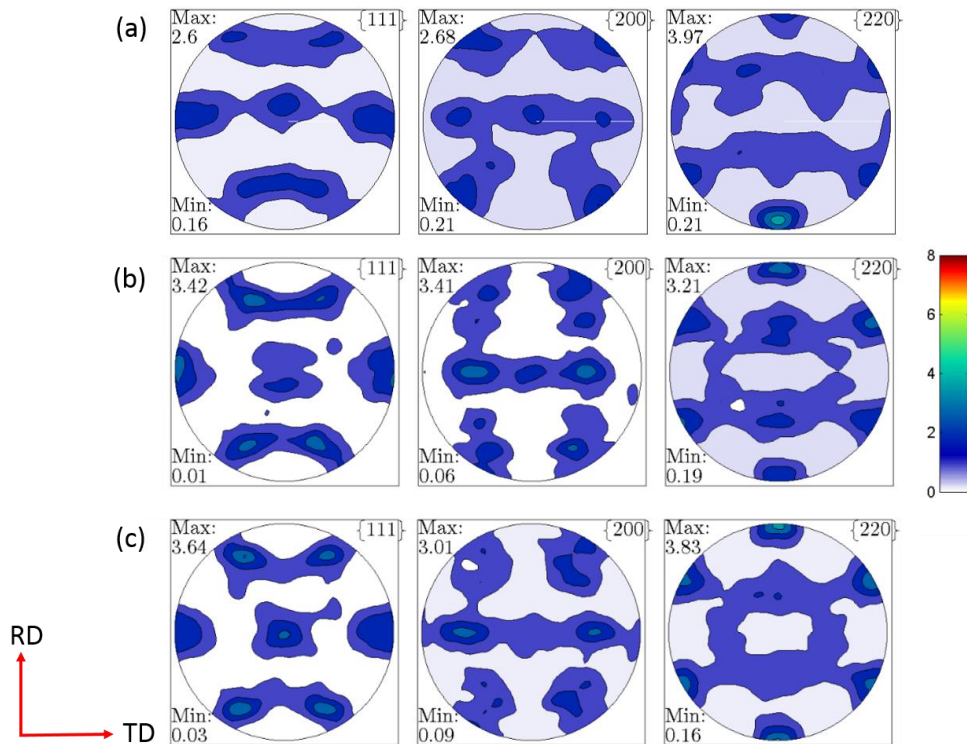


Figure 4.11: Texture evolution for RD compression after 43% strain at 1000 s^{-1} a) experimental recalculated pole figures b) simulated texture with isotropic grain shape and c) simulated texture with the actual average grain shape (5:3:1).

4.5.3.2 TD compression

The simulated TD compression flow curves show that the scatter in the flow stress observed experimentally is due to the initial texture. The effect of grain shape is more prominent in the TD case than RD, with the isotropic shape predicting a slightly higher flow stress (Figure 4.12a). The r -values, simulated with and without anisotropic grain shape, show a larger variation (Figure 4.12b) as compared to RD. However, the results of both simulations fall within the experimental scatter. As far as the texture evolution is concerned, there is some discrepancy between the experimental and the simulated pole figures. The two cases show distinct differences (Figure 4.13a-c). Notably, the splitting of the $\{111\}$ and $\{200\}$ poles towards RD, and the distribution of the $\{220\}$ poles, are in better agreement with the experimental data when the anisotropic grain shape is taken into account within simulations.

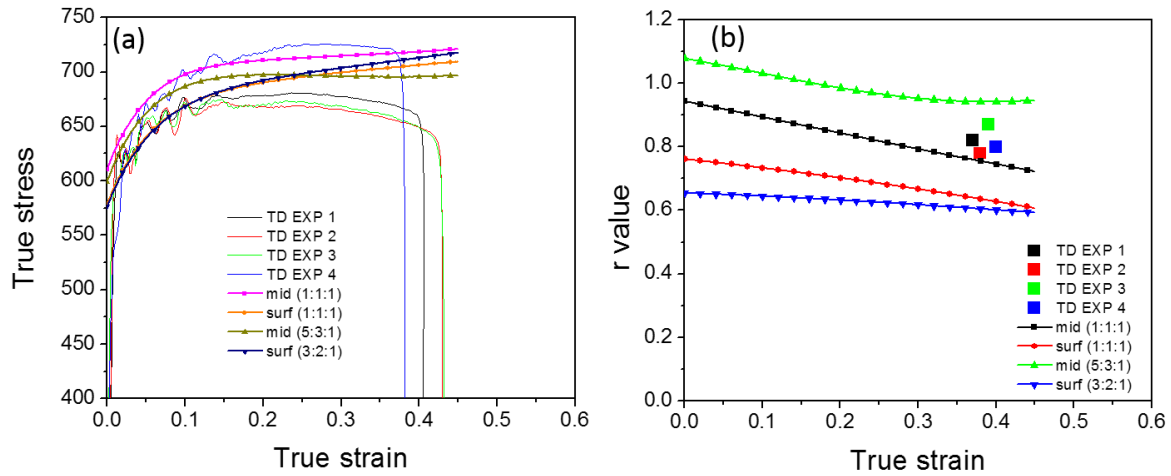


Figure 4.12: Experimental and simulated data for compression at 1000 s^{-1} along TD a) flow curves and b) r-values.

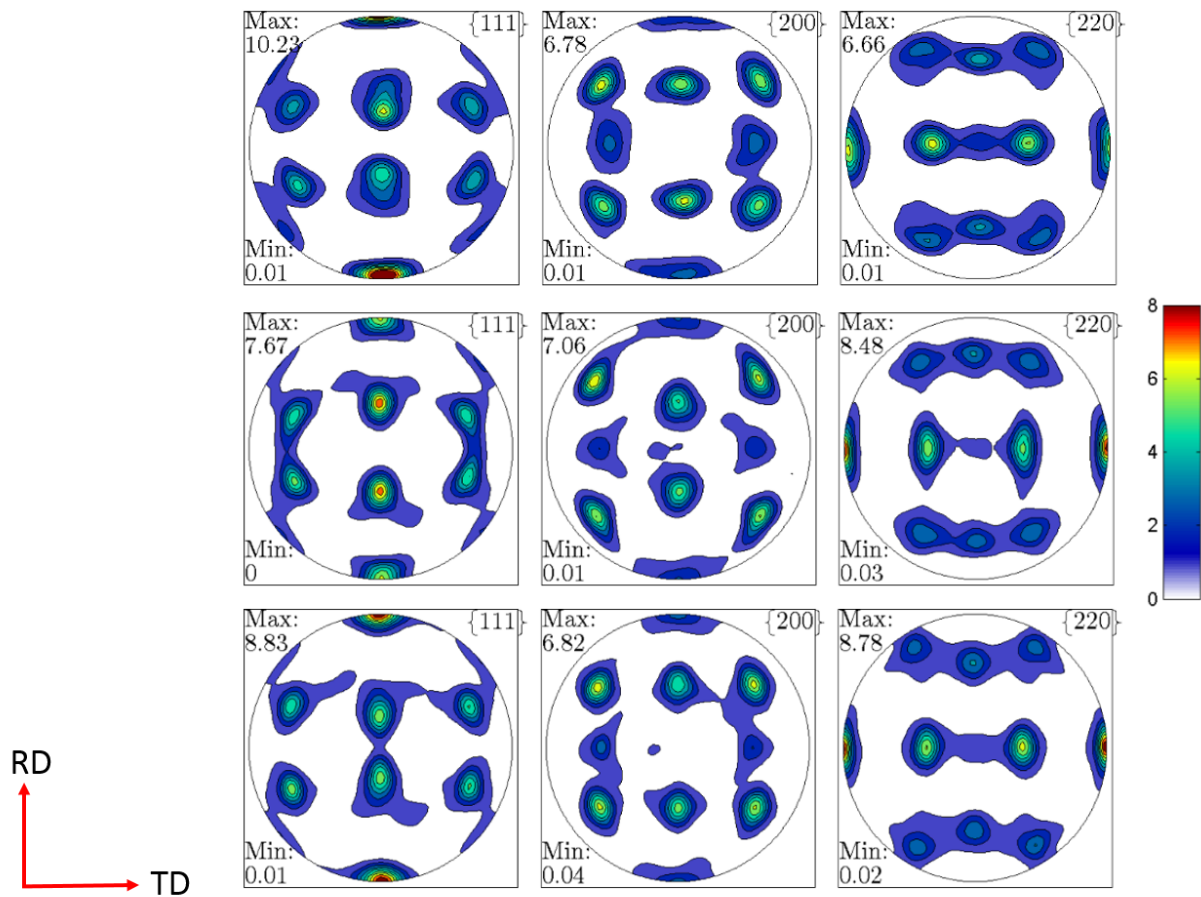


Figure 4.13: Texture evolution for TD compression after 40% strain at 1000 s^{-1} a) experimental recalculated pole figures b) simulated texture with isotropic grain shape and c) simulated texture with grain shape (5:3:1).

4.5.3.3 ND compression

The experimental and simulated flow curves confirm that the initial texture is responsible for the lower flow stress for the near surface specimens (Figure 4.14a and Figure 4.16a). By comparing with the RD and TD case, (Figure 4.10a and Figure 4.12a) it is evident that the initial texture has greatest impact on flow stress along the ND. The experimental r -values show a large amount of scatter, with the near surface specimens showing a lower r -value as compared to the near mid-plane ones (Figure 4.14b and Figure 4.16b). Note that for the ND case (both mid-plane and surface), the r -values obtained at quasistatic rates are shown along with the ones obtained at dynamic rates. This comparison confirms that the r -values are not rate dependent. Additional simulations carried out with textures from individual sections (not shown in the interest of space) indicate that the r -value for ND compression is very sensitive to the initial texture of the material, and a subtle difference can lead to a large change in the r -values. Moreover, it is found that taking account of the anisotropic grain shape results in a slightly better match with the experimentally observed r -value near the surface. However, the same approach tends to overestimate the plastic strain anisotropy near the mid-plane and leads to lower r -value predictions. The texture evolution for the surface specimens (Figure 4.15a-c) and near mid-plane ones (Figure 4.17a-c) is captured relatively well by both isotropic and anisotropic grain shape, although the latter predicts $\{200\}$ and $\{220\}$ intensities which are closer to the experiments.

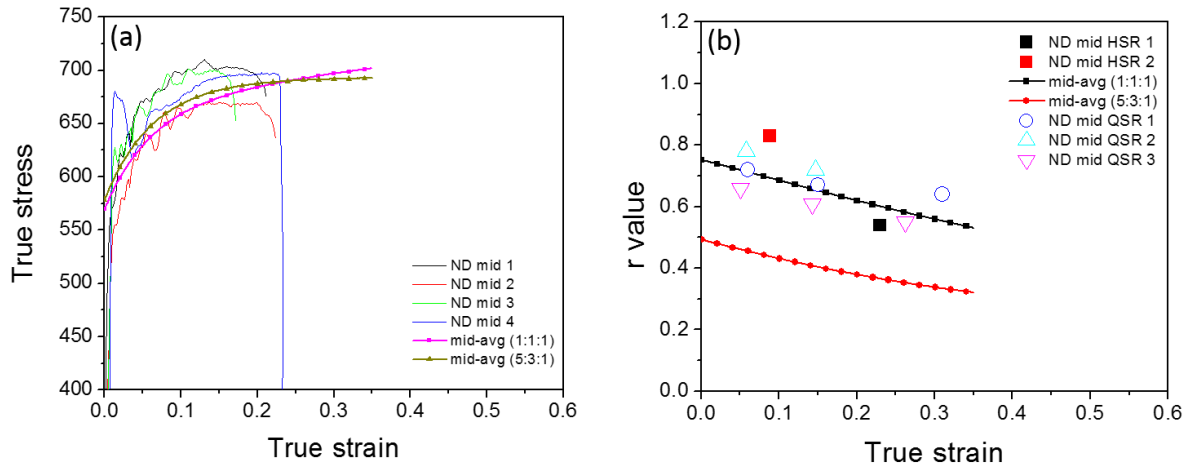


Figure 4.14: Experimental and simulated data for compression along ND from midplane a) flow curves at 1000 s^{-1} and b) r-values at 1000 s^{-1} and 0.001 s^{-1} .

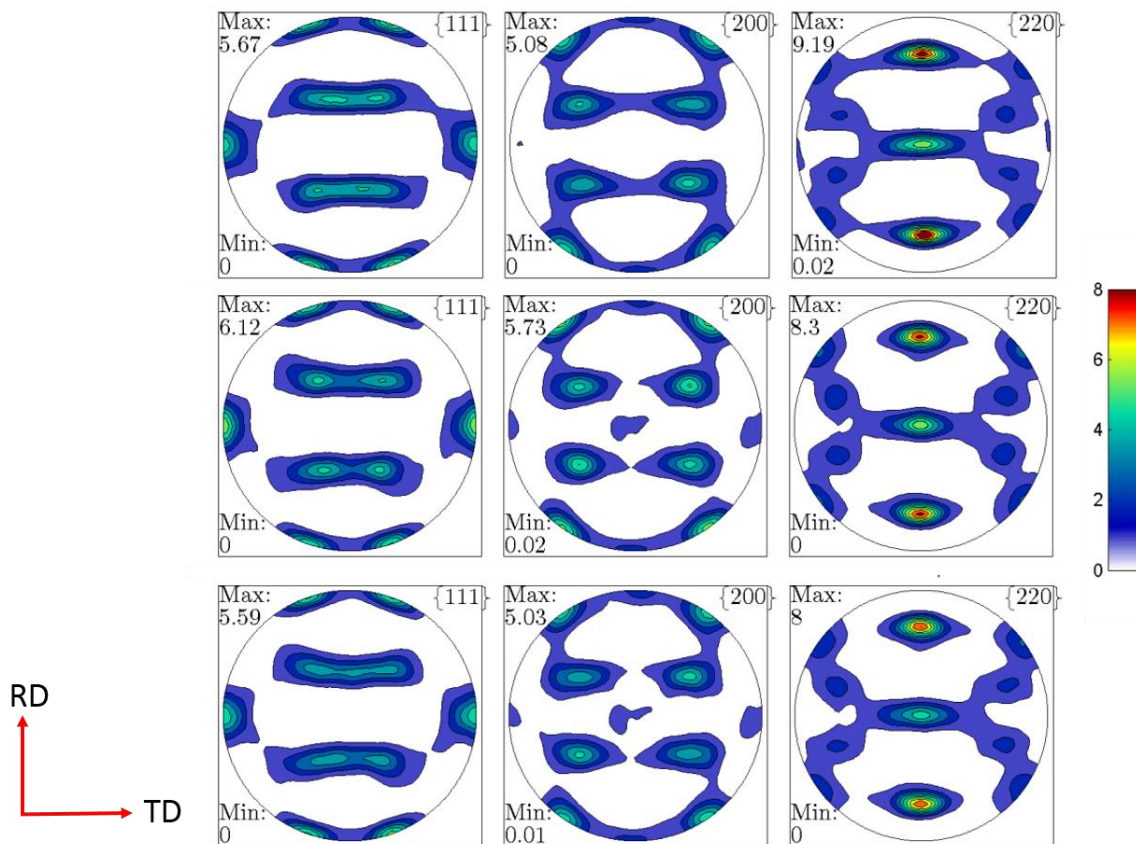


Figure 4.15: Texture evolution for a midplane ND compression specimen after 9% strain at 1000 s^{-1} a) experimental recalculated pole figures b) simulated texture with isotropic grain shape and c) simulated texture with grain shape (5:3:1).

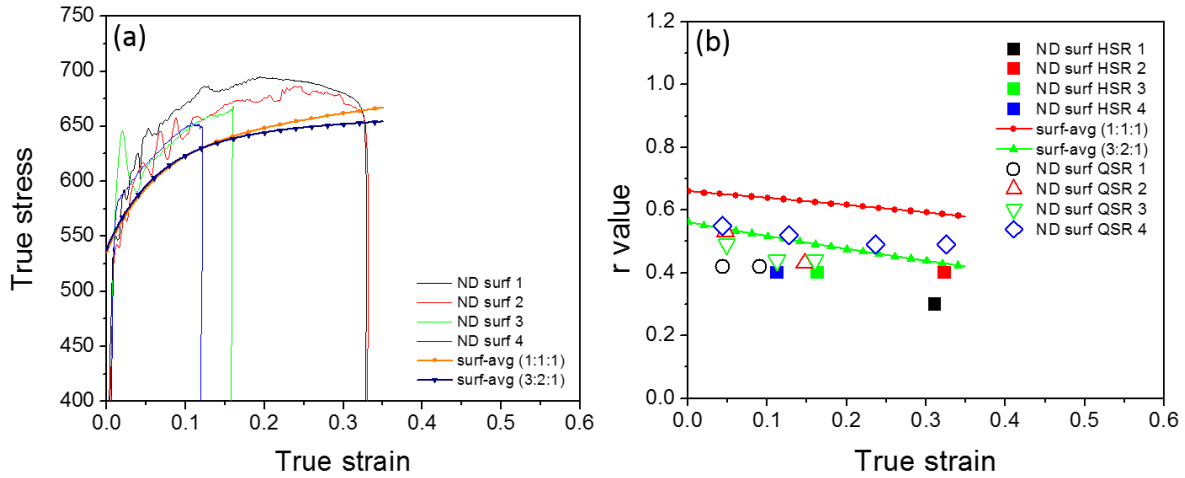


Figure 4.16: Experimental and simulated data for compression along ND from near surface a) flow curves at 1000 s^{-1} and b) r-values at 1000 s^{-1} and 0.001 s^{-1} .

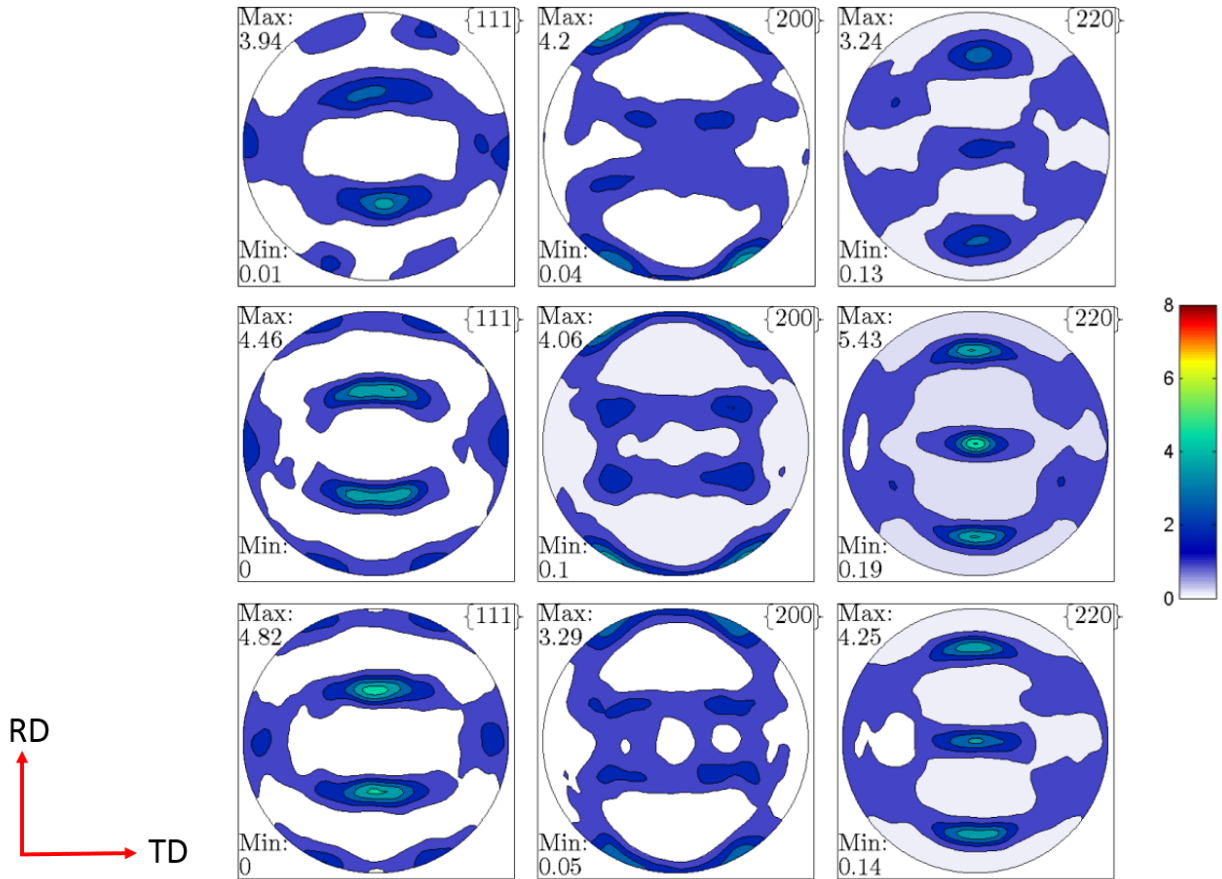


Figure 4.17: Texture evolution for a ND compression specimen extracted from near surface, after 32% strain at 1000 s^{-1} a) experimental recalculated pole figures b) simulated texture with isotropic grain shape and d) simulated texture with grain shape (3:2:1).

4.5.4 Failure and shear banding

Although failure by shear banding is not the main focus of this study, it was found that there was considerable anisotropy in the failure behavior and thus it merits a brief discussion. The ND specimens with stronger texture abruptly failed in shear at both QSR and HSR. The RD specimens, on the other hand, showed prolonged flow softening at HSR followed by shear failure. This suggests that the mechanisms leading to shear localization for the two cases may be different.

When observed along the TD plane, an EBSD RD-IPF map (Figure 4.18) of a failed RD compression specimen reveals that the major shear band is oriented at $\sim 45^\circ$ with the stress axis (i.e. RD). Additionally, there is another minor band present, oriented close to 60° about RD. The initial texture is such that during RD compression, most of the $\{112\}$ poles are parallel to the stress axis. This implies two sets of $\{111\}$ planes are at 60° with respect to the loading axis. It is thus expected that profuse slip at these two favorably oriented planes can occur. Generally, such slip activity will lead to strain hardening, until the stress level rises to activate other slip systems in harder orientations. However, the adiabatic conditions during dynamic deformation can result in an early onset of dynamic recovery and lead to loss of strain hardening. This is evident in the flow curves. This may lead to localization of flow in the favorably oriented systems, forming grain scale shear bands. With further straining these grain scale shear bands may organize to form the large shear band at 45° from the stress axis (Canova et al., 1984).

For the ND case, the shear bands formed on the TD plane with $\sim 42^\circ$ to the horizontal (RD) (Figure 4.19). Moreover, the straining direction as indicated on the yield surfaces show close proximity to the plane strain condition. Since the anisotropy present in the simulated yield surfaces are solely due to the texture of the as-received material, it is suggested that texture is

also responsible for the shear banding observed along ND. By using geometric softening arguments, Dillamore et al. (1979) have shown that in case of $\{110\} \langle 100 \rangle$ and $\{110\} \langle 112 \rangle$ texture components, the shear bands form close to, but less than, 45° from the rolling direction. For the ND case, where grain have $\{220\} \parallel$ loading axis, two sets of $\{111\}$ planes are at 35° from the loading axis leading to duplex slip, while the others are at 90° and do not contribute to strain accommodation. The limited active slip systems promote plane strain deformation, which eventually leads to localization during ND compression irrespective of the applied strain rate. This suggests that texture engineering could be a fruitful approach for applications of high strength Al alloys, which may involve significant compression in the through thickness direction.

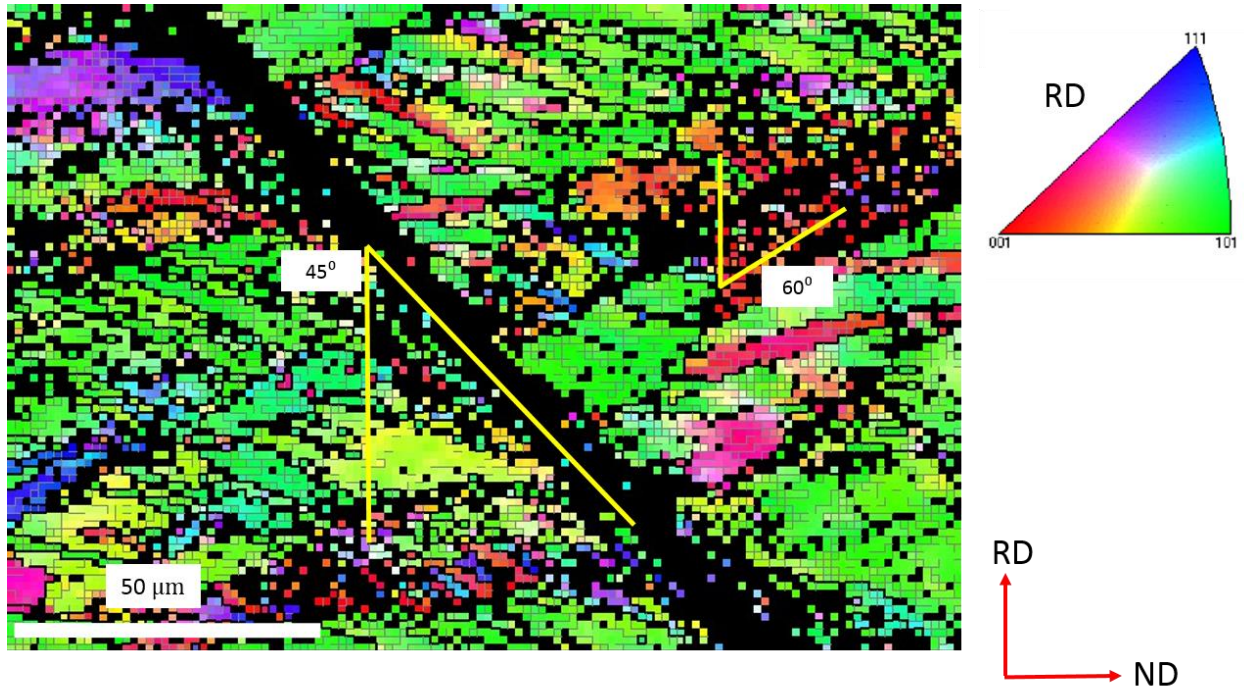


Figure 4.18: An EBSD RD-IPF map from a specimen compressed along RD up to 40 % strain at 1000 s^{-1} . The black (non-indexed) region shows a shear band on the TD plane, at an angle $\sim 45^\circ$ with the loading axis. Another shear band at angle $\sim 60^\circ$ with the loading axis is also present, identified by poorly indexed diffraction pattern.

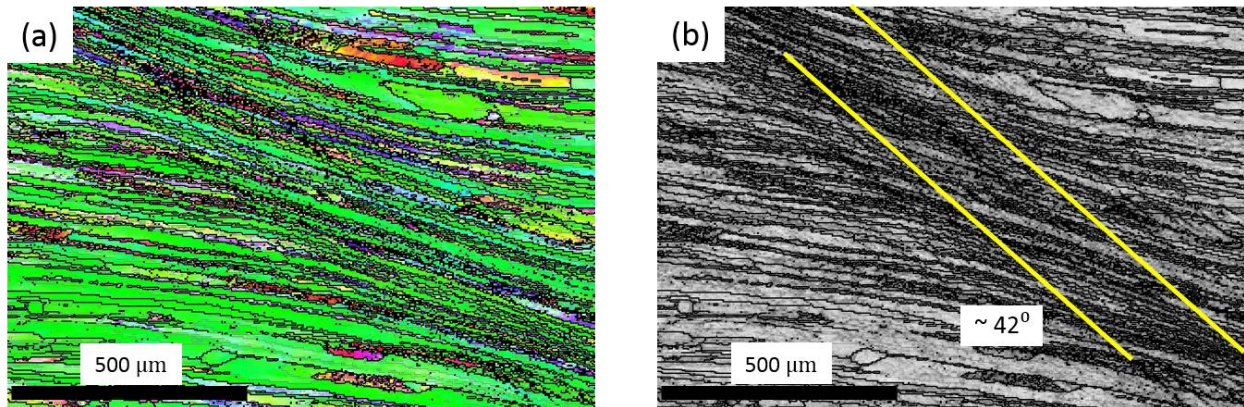


Figure 4.19: (a) ND-IPF map and (b) band contrast map of a specimen compressed to 26% strain at 0.001 s^{-1} showing diffuse shear band formation on the TD plane, oriented $\sim 42^\circ$ to the horizontal (RD). RD is to the right, ND up.

4.6 Discussion

4.6.1 Strain rate sensitivity of Al-7085-T711

The experimental and simulated results indicate that there is a slight positive strain rate sensitivity of the yield strength of this alloy. The engineering strain rate sensitivity (eSRS) of the flow stress is defined as follows:

$$m = \frac{\partial \ln \tau}{\partial \ln \dot{\gamma}} \quad (4-9)$$

and the activation volume, $V = bA$, which can be obtained by taking the derivative of the activation energy $\Delta G(\tau^*)$ with respect to stress at constant temperature and substructure (Diak et al., 1998; Caillard and Martin, 2003; Argon, 2008):

$$V = - \left[\frac{\partial (\Delta G)}{\partial \tau^*} \right]_{T,S} = kT \left(\frac{\partial \ln \dot{\gamma}}{\partial \tau^*} \right)_{T,S} = \frac{kT}{m\tau} \quad (4-10)$$

The analysis of these parameters V and m can provide insight on the rate controlling mechanisms in the plastic deformation of metals. It is necessary to determine these parameters at constant substructure in order to obtain an accurate description of the rate controlling processes, and thus, it is acknowledged that the calculations which follow are only an approximation performed in order to provide some insight about the processes involved.

Using the CRSS values obtained via inverse modeling shown in Table 4.2, a strain rate sensitivity m is 0.003 is obtained. If one instead uses the saturation stresses, i.e. $\tau_0 + \tau_1$, one obtains $m = 0.0025$, which indicates that m remains essentially constant throughout the deformation. The corresponding activation volume V is $\sim 300 b^3$. The thermodynamic parameters obtained here are consistent with earlier studies on 6XXX and 7XXX alloys (Holt et al., 1967; Lindholm et al., 1971; Khan and Meredith, 2010). It is important to note that the microstructure of a multi-component alloy such as AA7085-T711 consists of several types of precipitates (shearable and non-shearable) as well as solutes. The non-shearable precipitates are considered

to be strong obstacles and are thus responsible for increasing the athermal component of the flow stress. Considering the low Peierls resistance of the $\{110\} \langle 110 \rangle$ slip mode, interaction with solutes and with forest dislocations can potentially be the rate controlling mechanisms. The activation volume obtained here ($\sim 300 b^3$) is indicative of forest dislocation interactions as the rate controlling mechanism. However, the possibility of contributions from solute interactions and shearable precipitates cannot be ruled out, given the rather limited data used for analysis.

4.6.2 Flow behavior and strength anisotropy

A thorough examination of the texture gradient revealed that the center of the plate mainly consists of strong Brass and S components, while the Goss component is slightly higher near the surface. The EBSD measurements also revealed that there is a slight through-thickness gradient in the grain aspect ratio. The simulation results indicate that the grain shape has only a slight effect on the flow stress of the material. The effect is greatest for TD and least for the RD orientation. Incorporating grain shape effect lowers the flow stress for TD whereas it increases for the ND. As mentioned in the modeling section, the grain shape influences the mechanical response by changing the stiffness of interaction between the grain and the matrix (i.e., HEM). Tiem et al., (1986) used Kroner's isotropic elastic self-consistent solution of the Eshelby problem, to show the variation of the coefficients of the interaction tensor Q with strain for different grain shapes. Their results for a disc shaped grain showed a monotonic increase in the lateral (Q_{11} and Q_{22}) components, when compressed along the thickness direction, leading to a large increase in the stiffness of the grain-matrix interaction with deformation. One important point to note is that the actual grain-matrix interaction is dependent on both the texture evolution and grain shape effects. For the present case, where texture evolution is taken into account, the

interaction becomes slightly more compliant for TD compression leading to a lower flow stress, whereas the converse is true for the ND.

The simulation results also show the effect of initial texture on the observed flow strength variations. The largest experimental scatter is seen in case of ND and the simulation results performed with different initial textures (mid-surf and mid-avg) show a similar range of variation. The RD and TD flow stresses, on the other hand, are relatively insensitive to these variations in initial texture. Moreover, the simulation results indicate that the model captures relatively well the flow stress in RD and TD compression, but is unable to capture the higher initial hardening rate in ND case. Additional simulations incorporating latent hardening only increased the flow stress anisotropy. It is hypothesized that the precipitates present in the microstructure are responsible for the reduced strain anisotropy observed in this alloy as noted for other precipitation strengthened Al alloys (Barlat and Liu, 1998; S.H. Choi et al., 2000).

By virtue of the initial midplane texture, the TD compression specimens present a strong $\{111\}\langle uvw \rangle$ fibre along the loading axis, which leads to activation of 6 slip systems on 3 out of 4 $\{111\}$ planes, albeit with a low Schmid factor (M) of 0.27. This results in high activity of collinear slip systems, resulting in the high hardening rate for the TD case, especially when employing the latent hardening matrix suggested by modern DDD simulation (Madec et al., 2003). On the other hand, for the ND case, most grains have their $\{110\}$ poles parallel to the stress axis. It is well known (Hosford, 1964) that grains oriented with $\{110\}$ planes parallel to loading direction (Brass and Goss components), would be stressed equally, with a Schmid factor, $m = 0.41$, on $(\bar{1}11)[110]$, $(\bar{1}11)[101]$, $(111)[1\bar{1}0]$ and $(111)[10\bar{1}]$ slip systems with the resolved shear stress on the $(1\bar{1}1)$ and $(11\bar{1})$ planes and the corresponding slip systems equal to zero. This promotes duplex slip and since the coplanar hardening rate is considered to be the

same as the self-hardening, there is essentially no effect of latent hardening on the hardening behavior for this case. The RD presents an intermediate case, where some collinear slip system activity is promoted, leading to an increase in the hardening rate. The fact that the experimental data do not exhibit such anisotropy indicates that perhaps some other factors are responsible for the observed isotropy.

4.6.3 Plastic strain anisotropy and texture evolution

The plastic strain anisotropy, unlike the flow stress, is large and dependent on the loading direction. The r -values for RD and TD compression are ~ 0.4 and 0.8 respectively. For ND, the values vary from 0.3 - 0.8 . The RD r -values do not evolve as much with strain as the TD and ND and the model is able to capture the evolution well. To investigate the variation of in-plane anisotropy, additional simulations were carried out with rotated textures, representing uniaxial tests at various angles from RD (Figure 4.20). From these results, it can be seen that there is considerable variation in the in-plane anisotropy and the highest r -values is predicted along 45° from RD (Figure 4.20a). The same data has been plotted as a function of strain to show their evolution (Figure 4.20b). The r -values of most of the directions do not evolve significantly with strain, except RD30 which shows some evolution. At this point, it is worth mentioning that the evolution of r -value with strain is dependent on the texture as well as the grain shape. Thus, assuming that it remains constant with straining will not always be accurate.

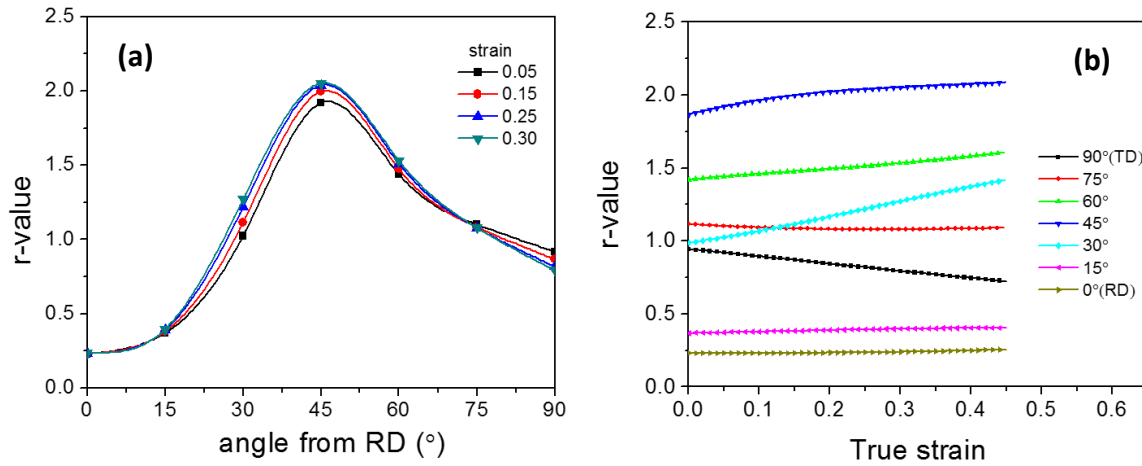


Figure 4.20: Simulated r-values of AA7085-T711: (a) in-plane variation for different strain levels and (b) evolution of in-plane r-values with strain.

Simulations carried out with different initial textures show that the r-value evolution of the ND and TD is quite sensitive, while the RD is relatively insensitive. As mentioned in the previous section, the initial texture is such that multi-slip conditions prevail for the TD case which results in r-values close to 1, promotes homogeneous deformation, and thus, resists shear localization. Hence, the TD specimens exhibit the highest compressive ductility. The RD presents $\{112\}$ pole parallel to the compression axis, which leads to a high Schmid factor of $m = 0.41$ for two sets of $\{111\}$ planes while the other two are at hard orientations with $m = 0$ and 0.27 , respectively. This leads to a low r-value, allowing strain accommodation along ND but not TD.

For the ND specimens, the initial texture leads to near plane strain deformation, e.g., for an ideally oriented Goss grain no strain is expected along TD, yielding an r-value of 0. For a Brass oriented grain, the r-value would be 0.5. However, in a real polycrystal, where other texture components are also present, the r-values are expected to deviate from the ideal values.

Indeed, the midplane specimens with a strong Brass texture, show r -values of 0.6-0.8 while the near surface specimens show r -values of 0.3-0.6. Plane stress yield surfaces calculated using the average mid-plane texture, at 4% and 12% equivalent strain, also show that for ND compression (approximated as the equi-biaxial tensile stress state) the straining direction is quite close to being plane strain (Figure 4.21). The isotropic grain shape simulation results capture this effect, predicting lower r -values for the surface, although for the latter, the r -values are slightly over-predicted. Interestingly, the anisotropic grain shape simulations further reduce the r -value, to match the experimental data.

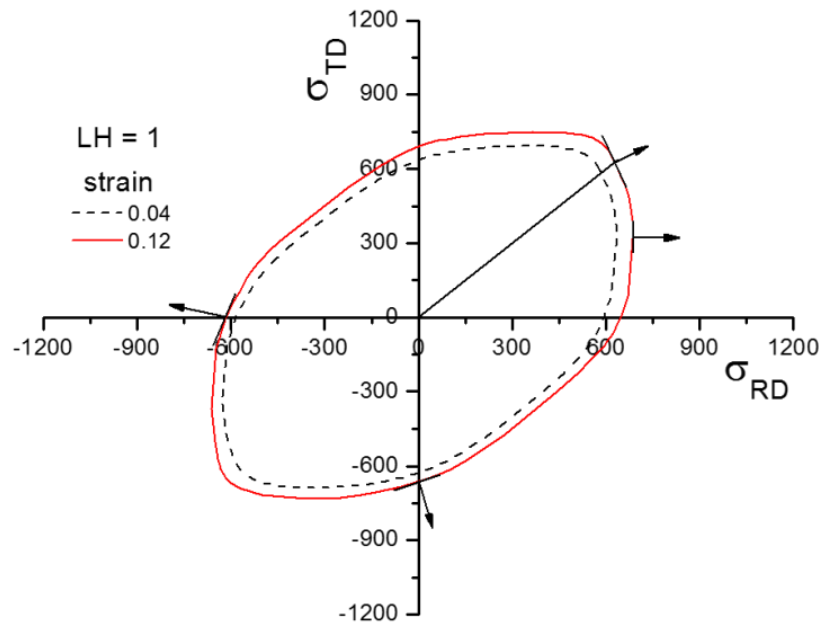


Figure 4.21: Plane stress yield surface at representative strain levels 0.04 and 0.12 for clarity. Arrows indicate the normal to the yield surface for RD and TD compression. The plane strain condition is also indicated along with the ND compression case, approximated as equibiaxial tension.

As evident from the pole figures, the texture evolution under uniaxial compression for RD, TD and ND is such that the $\{220\}$ poles tend to align with the stress axis. It is found that the experimentally observed texture evolution is captured well by the simulations. The predicted textures are slightly sharper, but it is well known (e.g, Van Houtte et al., 2005) that mean-field models cannot account for local strain heterogeneity and the associated rotation inside a grain which may be responsible for spreading of the texture (Hirsch and Lücke, 1988). A closer look at the simulated pole figures with and without grain shape effects, show that for the RD and ND case, there is qualitatively no difference. For the TD case, however, the splitting of the $\{200\}$ poles and the spread of the $\{220\}$ poles are better predicted for the anisotropic grain shape.

As a follow-on to this study, it is noted that precipitates can induce anisotropy by exerting a back stress due to their interaction with dislocations (for instance, Bate et al., 1981). As shown in earlier works on Al-Cu alloys, the backstress due to the $\{100\}$ precipitate plates can lead to a reduction in anisotropy (Barlat and Liu, 1998b; S.H. Choi et al., 2000). In more complex alloys such as AA7085 the microstructure contains a variety of precipitates with different habit planes, which can very likely alter the plastic anisotropy as well as the strain hardening behavior at early stages of deformation. The fact that the present texture based predictions of the VPSC model fail to capture all aspects of the flow stress, strain hardening and r-values, suggest that the effect of these precipitates on anisotropy needs to be taken into account, in order to accurately capture the homogeneous flow behavior of such an alloy. This aspect will be taken up in a future work.

4.7 Summary and conclusions

Experimental observation and VPSC modeling of quasistatic and high strain rate deformation behavior of AA7085-T711 plate has provided useful insights about the role of initial

texture and anisotropic grain shape on the flow strength anisotropy and plastic strain anisotropy. The key points are summarized as follows:

1. A through-thickness gradient in the crystallographic texture is present in the hot rolled plate examined. The surface has a weak $\langle 110 \rangle // \text{RD}$ shear texture, whereas the interior layers consists of a weak recrystallized Cube texture component along with the well known β -fiber consisting of Cu, S and Bs texture components. The partially recrystallized microstructure also exhibited a morphological texture with an average grain aspect ratio of 3:2:1 (RD:TD:ND) near the surface, and 5:3:1 near the midplane.

2. Compression tests along RD, TD and ND revealed mild flow anisotropy with RD having a lower flow stress and hardening rate compared to TD and ND. Moreover, the RD specimens exhibited flow softening at dynamic strain rate. The TD specimens exhibited the highest compressive ductility.

3. Significant plastic strain anisotropy was observed in this alloy, and it was found to be independent of the imposed strain rate. The r -values were ~ 0.3 - 0.4 for RD, ~ 0.8 - 0.9 for TD and 0.3 - 0.8 for ND. The ND r -values were strongly dependent on the initial texture (e.g., surface vs. mid-plane) and showed some evolution with strain.

4. The VPSC model was able to accurately describe the flow behavior along RD and TD. However, it underestimated the initial hardening rate along ND. Accounting for the anisotropic grain shape did not have any significant effect on the flow stress along all the directions investigated, and careful consideration of latent hardening effects was also unable to account for the anisotropy in strain hardening. The simulated textures qualitatively agreed with the experimental ones, and accounting for the anisotropic grain shape lead to better predictions of the texture evolution during compression along TD. The model permitted estimation of the strain

rate sensitivity of the octahedral $\{110\} \langle 011 \rangle$ slip mode was found to $m = 0.003$, consistent with the notion that it is “athermal” in the rate regime investigated.

5. Although the qualitative trends were reproduced, the model failed to capture all aspects of the plastic strain anisotropy. The material was somewhat more isotropic than that predicted by the model. Accounting for the anisotropic grain shape and possible latent hardening effects did not lead to improvement in the predictions. Simulations along untested directions showed considerable variation in the planar anisotropy. For example, the RD45 was found to have the highest r -value, and the r -value for RD30 showed considerable evolution with strain.

6. The ND specimens showed catastrophic shear failure at quasistatic and dynamic strain rate, without any sign of flow softening. Shear bands observed on the TD plane indicate geometric softening to be the prime cause for such shear localization.

Overall, it is suggested that incorporating the “backstress” effect of the precipitates within the polycrystal plasticity model could lead to improved predictions of the planar anisotropy as well as the higher initial strain hardening rate of the ND case.

4.8 Acknowledgements

The authors would like to thank ALCOA for providing the AA7085-T711 plate used in this study. The research at U.Va. and M.S.U. was sponsored by the United States Army Research Office under contract number W911NF-12-1-0455 monitored by Drs. Suveen Mathaudhu and David Stepp. The views and conclusions contained in this document are those of the authors and should not be interpreted as representing the official policies, either expressed or implied, of the Army Research Laboratory or the U.S. Government. The U.S. government is authorized to reproduce and distribute reprints for government purposes notwithstanding any copyright notation hereon.

4.9 References

- Agnew, S., Whittington, W., Oppedal, A., El Kadiri, H., Shaeffer, M., Ramesh, K.T., Bhattacharyya, J., Delorme, R., Davis, B., 2014. Dynamic Behavior of a Rare-Earth-Containing Mg Alloy, WE43B-T5, Plate with Comparison to Conventional Alloy, AM30-F. *Jom* 66, 277–290. doi:10.1007/s11837-013-0830-x
- Argon, A.S., 2008. Strengthening mechanisms in crystal plasticity. Oxford: Oxford University Press.
- Asaro, R.J., Needleman, A., 1985. Overview texture development and strain hardening in rate dependent polycrystals. *Acta Mater.* 33, 923–953.
- Baig, M., Khan, A.S., Choi, S.-H., Lee, E., 2015. Effect of Manufacturing Processes and Welding Type on Quasi-static and Dynamic Responses of Aluminum Alloys: Experiments and Modeling. *J. Dyn. Behav. Mater.* 1, 299–314. doi:10.1007/s40870-015-0025-3
- Barlat, F., Liu, J., 1998a. Precipitate-induced anisotropy in binary Al-Cu alloys. *Mater. Sci. Eng. A* 257, 47–61. doi:10.1016/S0921-5093(98)00823-5
- Barlat, F., Liu, J., 1998b. Precipitate-induced anisotropy in binary Al-Cu alloys. *Mater. Sci. Eng. A* 257, 47–61. doi:10.1016/S0921-5093(98)00823-5
- Bassani, J.L., Wu, T.-Y., 1991. Latent Hardening in Single Crystals II. Analytical Characterization and Predictions. *Proc. R. Soc. A Math. Phys. Eng. Sci.* 435, 21–41. doi:10.1098/rspa.1991.0128
- Bate, P., Roberts, W.T., Wilson, D. V., 1981. The plastic anisotropy of two-phase aluminum alloys -- I. Anisotropy in unidirectional deformation. *Acta Metall.* 29, 1797–1814.
- Caillard, D., Martin, J.L., 2003. Thermally activated mechanisms in crystal plasticity. Pergamon Materials Series Vol 8, Elsevier.
- Canova, G.R., Kocks, U.F., Stout, M., 1984. On the origin of shear bands in textured polycrystals. *Scr. Metall.* 18, 437–442.
- Chen, W.W., Song, B., 2010. Split Hopkinson (Kolsky) bar: design, testing and applications. Springer Science & Business Media.
- Chen, Y., Clausen, a. H., Hopperstad, O.S., Langseth, M., 2009a. Stress-strain behaviour of aluminium alloys at a wide range of strain rates. *Int. J. Solids Struct.* 46, 3825–3835. doi:10.1016/j.ijsolstr.2009.07.013
- Chen, Y., Pedersen, K.O., Clausen, A.H., Hopperstad, O.S., 2009b. An experimental study on the dynamic fracture of extruded AA6xxx and AA7xxx aluminium alloys. *Mater. Sci. Eng. A* 523, 253–262. doi:10.1016/j.msea.2009.06.007
- Cho, K.K., Chung, Y.H., Lee, C.W., Kwun, S.I., Shin, M.C., 1999. Effects of grain shape and texture on the yield strength anisotropy of Al-Li alloy sheet. *Scr. Mater.* 40, 651–657. doi:10.1016/S1359-6462(98)00481-3
- Choi, S.H., Barlat, F., Liu, J., 2000. Effect of Precipitates on Plastic Anisotropy of Polycrystalline Aluminum Alloys. *Mater. Sci. Forum* 331-337, 1327–1332. doi:10.4028/www.scientific.net/MSF.331-337.1327
- Choi, S.H., Brem, J.C., Barlat, F., Oh, K.H., 2000. Macroscopic anisotropy in AA5019A sheets. *Acta Mater.* 48, 1853–1863. doi:10.1016/S1359-6454(99)00470-X
- Delannay, L., Melchior, M. a., Signorelli, J.W., Remacle, J.-F., Kuwabara, T., 2009. Influence of grain shape on the planar anisotropy of rolled steel sheets – evaluation of three models. *Comput. Mater. Sci.* 45, 739–743. doi:10.1016/j.commatsci.2008.06.013
- Devincre, B., Hoc, T., Kubin, L.P., 2005. Collinear interactions of dislocations and slip systems. *Mater. Sci. Eng. A* 400-401, 182–185. doi:10.1016/j.msea.2005.02.071
- Devincre, B., Kubin, L., Hoc, T., 2006. Physical analyses of crystal plasticity by DD simulations. *Scr. Mater.* 54, 741–746. doi:10.1016/j.scriptamat.2005.10.066
- Diak, B.J., Upadhyaya, K.R., Saimoto, S., 1998. Characterization of thermodynamic response by materials testing. *Prog. Mater. Sci.* 43, 223–363. doi:10.1016/S0079-6425(98)00007-3
- Dillamore, I.L., Roberts, J.G., Bush, A.C., 1979. Occurrence of shear bands in heavily rolled cubic metals. *Met. Sci.* 73–77.

- Djapic Oosterkamp, L., Ivankovic, a., Venizelos, G., 2000. High strain rate properties of selected aluminium alloys. *Mater. Sci. Eng. A* 278, 225–235. doi:10.1016/S0921-5093(99)00570-5
- Doherty, K., Squillaciotti, R., Cheeseman, B., Placzankis, B., Gallardy, D., 2012. Expanding the Availability of Lightweight Aluminum Alloy Armor Plate Procured From Detailed Military Specifications. *ICAA13 13th Int. Conf. Alum. Alloy*. 541–546.
- El-Magd, E., Abouridouane, M., 2006. Characterization, modelling and simulation of deformation and fracture behaviour of the light-weight wrought alloys under high strain rate loading. *Int. J. Impact Eng.* 32, 741–758. doi:10.1016/j.ijimpeng.2005.03.008
- Franciosi, P., Berveiller, M., Zaoui, A., 1980. Latent hardening in copper and aluminium single crystals. *Acta Metall.* 28, 273–283. doi:10.1016/0001-6160(80)90162-5
- Gallardy, D., 2012. Ballistic Evaluation of 7085 Aluminum ARL-TR-5952.
- Gérard, C., Cailletaud, G., Bacroix, B., 2013. Modeling of latent hardening produced by complex loading paths in FCC alloys. *Int. J. Plast.* 42, 194–212. doi:10.1016/j.ijplas.2012.10.010
- Gray, G.T., 2000. Classic Split-Hopkinson Pressure Bar Testing. *Mater. Park. OH ASM Int.* 2000.
- Guo, X.Q., Wu, P.D., Wang, H., Mao, X.B., 2015. Study of Lattice Strain Evolution in Stainless Steel Under Tension: The Role of Self-Consistent Plasticity Model. *Steel Res. Int.* 85, 1–8. doi:10.1002/srin.201400570
- Hirsch, J., Lücke, K., 1988. Overview no. 76: Mechanism of deformation and development of rolling textures in polycrystalline f.c.c. metals—II. Simulation and interpretation of experiments on the basis of Taylor-type theories. *Acta Metall.* 36, 2863–2882. doi:10.1016/0001-6160(88)90173-3
- Holt, D.L., Babcock, S.G., Green, S.J., Maiden, C.J., 1967. The strain-rate dependence of the flow stress in some aluminum alloys. *ASM Trans. Q.* 60, 152–159.
- Honneff, H., Mecking, H., 1978. A method for the determination of the active slip systems and orientation changes during single crystal deformation., in: Gottstein, G., Lucke, K. (Eds.), *Texture of Materials, Proceedings of ICOTOM V*. Springer, Berlin, pp. 265–275.
- Hosford, W., 1964. Microstructural Changes During Deformation of (011) Fiber-Textured Metals. *Trans. Metall. Soc. AIME* 230, 12–15.
- Hutchinson, J.W., 1976. Bounds and Self-Consistent Estimates for Creep of Polycrystalline Materials. *Proc. R. Soc. A Math. Phys. Eng. Sci.* 348, 101–127. doi:10.1098/rspa.1976.0027
- Jain, A., Agnew, S.R., 2007. Modeling the temperature dependent effect of twinning on the behavior of magnesium alloy AZ31B sheet. *Mater. Sci. Eng. A* 462, 29–36. doi:10.1016/j.msea.2006.03.160
- Kabirian, F., Khan, A.S., Pandey, A., 2014. Negative to positive strain rate sensitivity in 5xxx series aluminum alloys: Experiment and constitutive modeling. *Int. J. Plast.* 55, 232–246. doi:10.1016/j.ijplas.2013.11.001
- Khadyko, M., Dumoulin, S., Cailletaud, G., Hopperstad, O.S., 2016. Latent hardening and plastic anisotropy evolution in AA6060 aluminium alloy. *Int. J. Plast.* 76, 51–74. doi:10.1016/j.ijplas.2015.07.010
- Khan, A.S., Meredith, C.S., 2010. Thermo-mechanical response of Al 6061 with and without equal channel angular pressing (ECAP). *Int. J. Plast.* 26, 189–203. doi:10.1016/j.ijplas.2009.07.002
- Kocks, U., Brown, T., 1966. Latent hardening in aluminum. *Acta Metall.* 14, 87–98.
- Kocks, U., Chandra, H., 1982. Slip geometry in partially constrained deformation. *Acta Metall.* 30, 695–709. doi:10.1016/0001-6160(82)90119-5
- Kocks, U.F., Canova, G.R., 1981. How many slip systems and which ?, in: *Deformation of Polycrystals: Mechanisms and Microstructures*. 2 Nd Riso Int. Symposium on Metallurgy and Materials Science. pp. 35–44.
- Kok, S., Beaudoin, A.J., Tortorelli, D.A., 2002. A polycrystal plasticity model based on the mechanical threshold. *Int. J. Plast.* 18, 715–741.
- Lademo, O.G., Hopperstad, O.S., Malo, K.A., Pedersen, K.O., 2002. Modelling of plastic anisotropy in heat-treated aluminium extrusions. *J. Mater. Process. Technol.* 125-126, 84–88. doi:10.1016/S0924-0136(02)00289-3
- Lebensohn, R.A., Tome, C.N., 1993. A self-consistent anisotropic approach for the simulation of plastic

- deformation and texture development of polycrystals: application to zirconium alloys. *Acta Metall.* 41, 2611–2624.
- Lebensohn, R.A., Tomé, C.N., Castañeda, P.P., 2007. Self-consistent modelling of the mechanical behaviour of viscoplastic polycrystals incorporating intragranular field fluctuations. *Philos. Mag.* 87, 4287–4322. doi:10.1080/14786430701432619
- Li, S., Houtte, P. Van, Kalidindi, S.R., 2004. A quantitative evaluation of the deformation texture predictions for aluminium alloys from crystal plasticity finite element method. *Model. Simul. Mater. Sci. Eng.* 12, 845–870. doi:10.1088/0965-0393/12/5/006
- Lindholm, U.S., Bessey, R.L., Smith, G. V, 1971. Effect of strain rate on yield strength, tensile strength, and elongation of three Al alloys. *J. Mater.* 6, 119–133.
- Madec, R., Devincere, B., Kubin, L., Hoc, T., Rodney, D., 2003. The Role of Collinear Interaction in Dislocation-Induced Hardening. *Science* (80-.). 301, 1879–1882. doi:10.1126/science.1085477
- Masson, R., Bornert, M., Suquet, P., Zaoui, A., 2000. An affine formulation for the prediction of the effective properties of nonlinear composites and polycrystals. *J. Mech. Phys. Solids* 48, 1203–1227. doi:10.1016/S0022-5096(99)00071-X
- Mika, D.P., Dawson, P.R., 1998. Effects of grain interaction on deformation in polycrystals. *Mater. Sci. Eng. A* 257, 62–76. doi:10.1016/S0921-5093(98)00824-7
- Molinari, a., Canova, G.R., Ahzi, S., 1987. A self consistent approach of the large deformation polycrystal viscoplasticity. *Acta Metall.* 35, 2983–2994. doi:10.1016/0001-6160(87)90297-5
- Pan, J., Rice, J.R., 1983. Rate sensitivity of plastic flow and implications for yield-surface vertices. *Int. J. Solids Struct.* 19, 973–987.
- Pandey, A., Khan, A.S., Kim, E.-Y., Choi, S.-H., Gnäupel-Herold, T., 2013. Experimental and numerical investigations of yield surface, texture, and deformation mechanisms in AA5754 over low to high temperatures and strain rates. *Int. J. Plast.* 41, 165–188. doi:10.1016/j.ijplas.2012.09.006
- Pedersen, K.O., Roven, H.J., Lademo, O.-G., Hopperstad, O.S., 2008. Strength and ductility of aluminium alloy AA7030. *Mater. Sci. Eng. A* 473, 81–89. doi:10.1016/j.msea.2007.03.089
- Rahmaan, T., Bardelcik, A., Imbert, J., Butcher, C., Worswick, M.J., 2016. Effect of strain rate on flow stress and anisotropy of DP600, TRIP780, and AA5182-O sheet metal alloys. *Int. J. Impact Eng.* 88, 72–90. doi:10.1016/j.ijimpeng.2015.09.006
- Reyes, A., Hopperstad, O.S., Lademo, O.-G., Langseth, M., 2006. Modeling of textured aluminum alloys used in a bumper system: Material tests and characterization. *Comput. Mater. Sci.* 37, 246–268. doi:10.1016/j.commatsci.2005.07.001
- Rousselier, G., Barlat, F., Yoon, J.W., 2010. A novel approach for anisotropic hardening modeling. Part II: Anisotropic hardening in proportional and non-proportional loadings, application to initially isotropic material. *Int. J. Plast.* 26, 1029–1049. doi:10.1016/j.ijplas.2010.01.001
- Rousselier, G., Luo, M., Mohr, D., 2012. Macroscopic plasticity modeling of anisotropic aluminum extrusions using a Reduced Texture Methodology. *Int. J. Plast.* 30-31, 144–165. doi:10.1016/j.ijplas.2011.10.004
- Tiem, S., Berveiller, M., Canova, G.R., 1986. Grain shape effects on the slip system activity and on the lattice rotations. *Acta Metall.* 34, 2139–2149. doi:10.1016/0001-6160(86)90159-8
- Van Houtte, P., 1982. On the equivalence of the relaxed Taylor theory and the Bishop-Hill theory for partially constrained plastic deformation of crystals. *Mater. Sci. Eng.* 55, 69–77. doi:10.1016/0025-5416(82)90085-4
- Van Houtte, P., Delannay, L., Kalidindi, S.R., 2002. Comparison of two grain interaction models for polycrystal plasticity and deformation texture prediction. *Int. J. Plast.* 18, 359–377. doi:10.1016/S0749-6419(00)00102-9
- Van Houtte, P., Delannay, L., Samajdar, I., 1999. Quantitative Prediction of Cold Rolling Textures in Low-Carbon Steel by Means of the Lamel Model. *Textures Microstruct.* 31, 109–149. doi:10.1155/TSM.31.109
- Van Houtte, P., Li, S., Seefeldt, M., Delannay, L., 2005. Deformation texture prediction: from the Taylor model to the advanced Lamel model, *International Journal of Plasticity*.

doi:10.1016/j.ijplas.2004.04.011

- Wang, H., Raeisinia, B., Wu, P.D., Agnew, S.R., Tomé, C.N., 2010. Evaluation of self-consistent polycrystal plasticity models for magnesium alloy AZ31B sheet. *Int. J. Solids Struct.* 47, 2905–2917. doi:10.1016/j.ijsolstr.2010.06.016
- Wu, T.-Y., Bassani, J.L., Laird, C., 1991. Latent Hardening in Single Crystals I. Theory and Experiments. *Proc. R. Soc. A Math. Phys. Eng. Sci.* 435, 1–19. doi:10.1098/rspa.1991.0127
- Xie, Q., Eyckens, P., Vegter, H., Moerman, J., Van Bael, a., Van Houtte, P., 2013. Polycrystal plasticity models based on crystallographic and morphologic texture: Evaluation of predictions of plastic anisotropy and deformation texture. *Mater. Sci. Eng. A* 581, 66–72. doi:10.1016/j.msea.2013.06.008
- Zhang, K., Holmedal, B., Hopperstad, O.S., Dumoulin, S., 2014. Modelling the plastic anisotropy of aluminum alloy 3103 sheets by polycrystal plasticity. *Model. Simul. Mater. Sci. Eng.* 22, 075015. doi:10.1088/0965-0393/22/7/075015

5 Effect of precipitates on anisotropy: Application to AA7085 at various tempers – Part

1: Experiments

J. J. Bhattacharyya¹, S. R. Agnew¹, B. Bittmann, and H. El Kadiri²

¹Materials Science and Engineering, University of Virginia, Charlottesville, Virginia, U.S.A.

²Mechanical Engineering, Mississippi State University, Mississippi, U.S.A.

5.1 Abstract

Commercial aluminum alloy 7085, which has been used in aerospace applications and is considered as a potential armor material is characterized under quasistatic (10^{-3} s^{-1}) and high strain rate (1000 s^{-1}) loading. Room temperature uniaxial compression tests along rolling, transverse, and normal directions (RD, TD and ND respectively) and at 45° to RD in the ND plane (henceforth denoted as only 45) were carried out for different aging conditions, in order to see the effect of aging on the flow stress and plastic strain anisotropy. The results indicate that not only the magnitude of plastic anisotropy is greatly affected along all the directions but also their evolution is temper dependent. With aging, the r-values tend towards 1, indicating that the material tends towards plastic isotropy. It is hypothesized that there is a connection between precipitate induced backstress and anisotropy. Thus, tension–compression Bauschinger tests along RD of T3 (solution heat treated) and T711 (slightly overaged) tempers with different prestrains were carried out to quantify the magnitude and investigate the evolution of the backstress. Both the T3 and T711 material showed Bauschinger effect and permanent softening; the effect in the T711 was about twice than in the T3. Analysis of the Bauschinger test data shows that the magnitude of backstress can be range from 25-225 MPa, depending upon the method used to calculate it. In both cases, the backstress saturates after $\sim 2\%$ plastic prestrain.

Keywords: plastic anisotropy, precipitates, backstress, Kolsky bar , Bauschinger effect

5.2 Introduction

Many commercial alloys are precipitation hardenable, i.e. they contain second phase particles, where their size, distribution and volume fraction can be accurately controlled via solid state phase transformation in order to tailor the mechanical properties. The most obvious effect of such precipitates is to hinder the dislocation motion and thus increase the strength of the material. The interaction of dislocations with second phase particles has been studied in great detail over the years due to its practical importance. However, besides affecting the strength, these particles have also been shown to influence the work hardening rate (e.g., Cheng et al., 2003), can lead to strong Bauschinger effect, i.e. reduction in reverse flow stress after forward straining (Bate et al., 1982; Caceres et al., 1996; Moan and Embury, 1979; Stoltz and Pelloux, 1976), and though studied much less in the past (e.g., Bate et al., 1981), can change the plastic strain anisotropy as well. In the next subsections the important aspects of the Bauschinger effect is briefly discussed followed by the effect on plastic anisotropy.

5.2.1 The Bauschinger effect

The Bauschinger effect in particle containing alloys is generally attributed to the long range internal stress developed due to additional storage of dislocation loops around a hard particle. These loops exert a stress which repels the forward motion of other dislocations on the slip plane, but facilitates their reverse motion (Brown, 1977) . It is useful to compare the Bauschinger effect in two materials using some quantitative scalar parameters. The traditional Bauschinger effect analysis, first proposed by Abel and Ham (1966) consists of treating individual hardening contributions as isotropic (i.e. non- polarized) and kinematic, where it is dependent on the straining direction. It is assumed that the forward stress σ_f is given by:

$$\sigma_f = \sigma_0 + \sigma_d + \sigma_B \quad (5-1)$$

where, σ_0 is the initial yield stress containing the contributions from friction stress, solid solution hardening and the isotropic component of precipitation hardening. σ_d is due to the strain hardening associated with the generation of forest dislocations during straining. Both these components are isotropic since it is assumed that they resist the deformation during both forward and reverse straining. The term σ_B , on the other hand, represents the long range internal stress, and is called ‘backstress’ since it opposes the forward straining in the usual manner but facilitates deformation once the strain path is reversed. Now, after some forward prestrain, if the strain path is reversed then the reverse flow stress σ_r is given by:

$$\sigma_r = \sigma_0 + \sigma_d - \sigma_B \quad (5-2)$$

since, σ_B assists the reverse straining.

From Eq. (5-1) and (5-2) the backstress σ_B can be obtained as:

$$\sigma_B = 0.5(\sigma_f - \sigma_r) \quad (5-3)$$

Typically, σ_f is the peak stress after the prestrain and σ_r is the reverse yield stress at any chosen offset. Thus, the estimate of σ_B is dependent on the choice of yield criteria.

Another commonly used stress-based parameter is β , first defined by Abel (1987), and is given by:

$$\beta = \frac{\sigma_f - \sigma_r}{\sigma_f} \quad (5-4)$$

where, as before, σ_f is the final stress value at the end of the prestrain and σ_r is measured at a chosen offset. Thus, if there is no Bauschinger effect, $\sigma_f = \sigma_r$ and $\beta = 0$. Conversely, if the material yields at zero stress upon reverse loading, then $\beta = 1$ and finally if it begins to yield during unload, $\beta = 2$. The two parameters are related as follows:

$$\sigma_B = \frac{\beta \sigma_f}{2} \quad (5-5)$$

In situations where permanent softening is observed, the amount of permanent softening $\Delta\sigma$ is defined as the difference between the magnitude of the forward and reverse flow stress at the strain value where the two flow curves become parallel. The matrix internal stress σ_B can be obtained from the permanent softening according to the relation: $\Delta\sigma = 2\sigma_B$. It has been found (Lloyd, 1977) that using the first method to obtain σ_B results in much larger values as compared to this method.

Another common parameter which is used to characterize the Bauschinger effect, is the Bauschinger strain, ε_B , generally defined as the plastic strain required to achieve the same flow stress in reverse loading as some fraction of the peak stress in forward loading (Stoltz and Pelloux, 1976). Generally, all these parameters are plotted as a function of the applied plastic prestrain to evaluate the evolution of the internal stress with deformation.

Wilson (1965) and Abel and Ham (1966) were among the first researchers to observe such Bauschinger effect in precipitate containing Al alloys. While studying Al-4% Cu alloys, they observed that the aged samples exhibit strong Bauschinger effect, whereas it was almost absent in the solutionized material. One of the first attempts to quantify the Bauschinger effect and relate it to physically measureable structural quantities was made by Wilson (1965) where he used X-ray diffraction to measure the residual internal stress. He measured the reverse strain required to annul the internal stress and then calculated the permanent softening at this strain level. He found that these two stresses are linearly related. Stoltz and Pelloux (1974, 1976) first observed this effect in commercial Al alloy 2024 and 7075. Interestingly, they found a convex shape of the reverse flow curve. Since then, several studies have investigated Bauschinger effect in Al alloys; for instance, Lloyd (1977) studied Ni and Ca intermetallics containing Al alloys and

found that grain boundary precipitates contribute less to kinematic hardening than the intragranular ones, which makes sense because there will already be a backstress associated with a grain boundary even in the absence of the grain boundary precipitate. Moan and Embury (1979) and Bate et al., (1982), used uniaxial tension-compression tests to characterize the Bauschinger effect in binary precipitates containing Al alloys. Recent studies focused on commercial alloys, for instance, Caceres et al., (1996) and Reynolds and Lyons, (1996) used tension – compression tests to investigate cast Al-Si-Mg alloy and AA8009 respectively and (Gracio et al., 2004) examined commercial AA 6022 alloy using strain reversal experiments in simple shear to characterize the Bauschinger effect.

Two important aspects that all these studies have established that, in absence of precipitates or when the precipitates are shearable, there is little or no Bauschinger effect, whereas a strong Bauschinger effect is observed when the microstructure contains non-shearable precipitates. Moreover, the magnitude of the internal stress only increases monotonically up to a few percent strain before it saturates.

5.2.2 Effect on plastic anisotropy

During monotonic loading, it has been hypothesized that the particle-induced backstress can alter the plastic anisotropy. Unlike the Bauschinger effect, only a few studies have focused on this aspect. Bate et al. (1981) while studying several binary Al alloy polycrystals, found that the strain anisotropy or r -value (width-to-thickness plastic strain ratio), in Al–4% Cu sheet, was strongly dependent on the aging condition. As the crystallographic texture was unaffected by aging, they concluded that the precipitates were responsible for the observed plastic anisotropy. Moreover, the aged specimens were more isotropic as compared to the solutionized ones, indicating that the precipitates rendered the material more isotropic. More recently, Barlat

and Liu (1998) and Choi et al., (2000) revisited this problem, and studied the simultaneous effect texture and precipitates on plastic anisotropy in Al 4% Cu alloys.

A study carried out by the present authors on AA 7085 in T711 temper, revealed that not all aspects of plastic strain anisotropy could be explained using the viscoplastic self-consistent (VPSC) crystal plasticity modeling framework, despite that fact that it accounts for texture, latent hardening, and grain shape (Bhattacharyya et al., 2016). In order to further explore the role of precipitates in this alloy, different tempers are tested at both quasistatic and dynamic strain rates. The precipitation sequence of AA 7085 and in general, 7XXX alloys is given as (Park and Ardell, 1983; Ram Prabhu, 2015): supersaturated solid solution (α) — GP-zones — metastable η' discs — equilibrium η discs (MgZn_2). Besides these precipitates, fine spheroidal Al_3Zr particles are also present in the microstructure. The present work aims at extending the previous study by characterizing the strength and strain anisotropy as well as the Bauschinger effect of AA 7085 subjected to different heat treatments.

5.3 Experimental methods

5.3.1 Materials, texture and microstructure

The material investigated in this study is AA 7085, provided by Alcoa in three different tempers: 38.1 mm (1.5 inch) thick plate of W51 (solutionized, quenched and stretched to relieve residual stress, followed by natural aging, unintentional and due to the unstable nature of the quenched state), 40.64 mm (1.6 inch) thick plate of T711 (slightly overaged to enhance ballistic resistance (Doherty et al., 2012)) and 52.4 mm (2.06 inch) thick T721 (significantly overaged to enhance blast resistance (Doherty et al., 2012)). Additionally, solution heat treatment (T3) was carried out in air, using a box furnace at 470 °C for 1 hour. The temperature was maintained

within ± 2 °C. The specimens were quenched in water at room temperature. Some of the solutionized specimens were then peak-aged (T6) at 120 °C for 24 hours.

In an earlier study, it was found that there was strong a texture gradient present along the through thickness direction of the plates. Furthermore, it was found that the plastic anisotropy, especially along the ND, was very sensitive to the initial texture. Hence, all the specimens investigated in this study were extracted from the midplane of the plates. The detailed procedure to measure the texture using X-ray diffraction technique has been described in detail elsewhere (Bhattacharyya et al., 2016). In brief, the $\{111\}$, $\{200\}$, and $\{220\}$ incomplete ($\chi = 0^\circ$ to 80°) pole figures as well as the background were obtained according to this method. The raw data were analyzed using MTeX (Hielscher and Schaeben, 2008) to generate complete orientation distributions (ODFs) and full pole figures. The T711 pole figures showing the texture gradient is presented elsewhere (Bhattacharyya et al., 2016). The pole figures for W51 and T721 are shown in Figure.5.1. Both of these mid-plane textures are similar to that which was measured in the T711, though there are fine-scale differences in the strength of the Brass, Cu, and cube texture components.

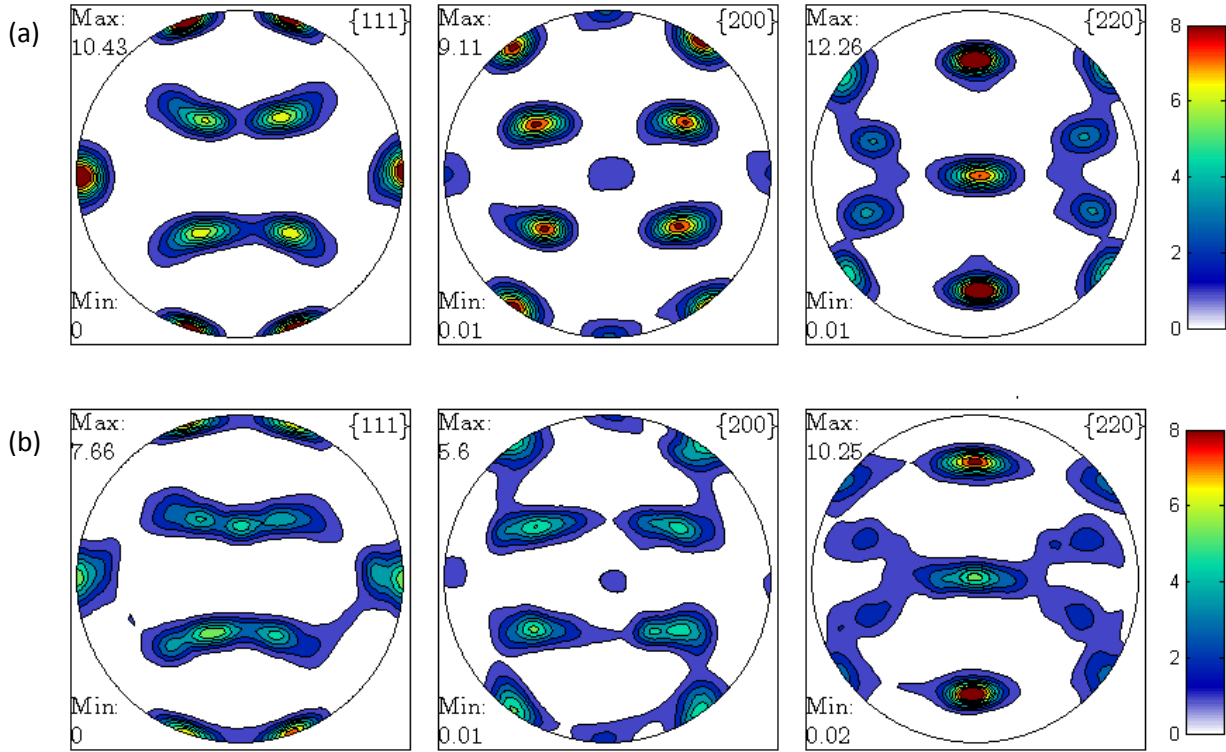


Figure 5.1: Textures measured at the plate mid-plane in the a) as-quenched and stretched temper (W51) and b) the over-aged condition known as T721.

5.3.2 Mechanical testing

The plastic strain anisotropy is assessed by measuring the compressive r-values along three orthogonal directions, following the convention of Jain and Agnew (2007):

$$r_{RD} = \epsilon_{TD} / \epsilon_{ND} \quad (5-6)$$

$$r_{TD} = \epsilon_{RD} / \epsilon_{ND} \quad (5-7)$$

$$r_{ND} = \epsilon_{TD} / \epsilon_{RD} \quad (5-8)$$

The r-value along the 45° direction is defined as:

$$r_{45} = \epsilon_{45} / \epsilon_{ND} \quad (5-9)$$

where, ϵ_{45} is the strain orthogonal to the axial and through thickness directions.

Compression specimens, in the form of right circular cylinders of 8mm diameter and height, were wire electrical discharge machined (EDM'd) from the plate along RD, TD ND and

45. Uniaxial compression tests at strain rate of 10^{-3} s^{-1} were performed using a universal testing machine, during which the axial strain was measured using a laser extensometer. The laser extensometers tags were attached to a steel block and not directly on to the sample. The block was placed in between the specimen and the platens. Hence the recorded force-displacement data included the machine compliance. To convert to true stress –strain values, the engineering stress and strain were calculated and the following correction was applied (Follansbee, 2014):

$$e_{corr} = e_{eng} - \frac{s}{E_{app}} + \frac{s}{E_{true}} \quad (5-10)$$

where, e_{corr} and e_{eng} are the is the corrected and uncorrected engineering strain, s is the engineering stress, E_{app} is the measured modulus $\sim 45 \text{ GPa}$ and E_{true} is the elastic modulus of the alloy taken to be 69.5 GPa .

Typically 3-4 specimens for a given condition were tested to examine the scatter and specimen to specimen variation. To measure the evolution of r-value with strain, the samples were unloaded at a specific strain level, typically 5%, and the strains along the transverse and thickness directions were measured using a digital caliper. Volume constancy ($\epsilon_{ii} < 0.001$) was enforced to ensure accurate measurements. Fractured samples were not used to assess the r values.

A split Hopkinson pressure (or Kolsky) bar testing apparatus was used to assess the uniaxial compression behavior along RD, ND and transverse direction (TD) at a nominal strain rate of 1000 s^{-1} . The actual strain rates varied from $1100\text{-}1400 \text{ s}^{-1}$. The specimens were strained up to $\sim 20\%$. The experimental set up and data analysis are discussed in detail in an earlier publication (Agnew et al., 2014). To ensure near constant strain rates, cylindrical pulse shapers of 10 mm diameter and 1 mm length cut from AA1100 alloy were used. This also helps to eliminate the high frequency Pochhammer-Chree oscillations, due to dispersion in the flow curve

(Gray, 2000; Chen and Song, 2010). The condition for stress equilibrium was checked during data processing to ensure uniform loading of the specimen. The r -values under dynamic loading conditions were measured post deformation instead of intermediate strain levels like the quasistatic.

The strain rate sensitivity m is calculated at 2% offset strength, using the relation:

$$m = \frac{\partial \ln \sigma(\epsilon)}{\partial \ln \dot{\epsilon}} = \frac{\ln\left(\frac{\sigma_2}{\sigma_1}\right)}{\ln\left(\frac{\dot{\epsilon}_2}{\dot{\epsilon}_1}\right)} \quad (5-11)$$

In order to quantify the magnitude of internal stresses generated due to the precipitates, two temper conditions were chosen to carry out tension-compression Bauschinger tests. The Bauschinger tests were carried out on round tensile specimens with gauge length 25 mm and diameter 6.35 mm according to ASTM E8/E8M – 15a standard. The tests were conducted by Westmoreland Mechanical Testing & Research, Inc. at strain rate of 10^{-3} s^{-1} , under ambient conditions. Two different tempers: T3 and T711 were investigated. The specimens were first loaded in tension up to various predetermined strain levels. For T3, prescribed forward strains of 0.5%, 1%, 1.5%, 2.5%, 4% and 6% were used while the T711 specimens were subjected to 1%, 1.5%, 2.5%, 4%, 5% and 6% strains. Following the tensile prestrains, the sense of deformation was reversed and all the specimens were reloaded in compression up to 1% strain.

It is well known that the magnitude of the backstress strongly depends on the definition of yield so three different strain levels were chosen to measure the yield strength, both in tension and compression. The stress at strains of 0.002 or 0.2% offset, 0.001 or 0.1% offset and 0.00025 or 250 microstrain ($\mu\epsilon$) were used to compute the backstress, according to Eq. (5-3). A yield point chosen at the proportionality limit or very small strain offset (few microstrain) results in a larger magnitude of the Bauschinger stress whereas the commonly used yield definition (0.2% offset) would reduce the value considerably. Thus in the present study, three different offset

strains: 0.00025 or 250 $\mu\epsilon$, 0.001 and 0.002 were chosen to quantify the magnitude of Bauschinger effect. For the reverse flow strength, the offsets were chosen with respect to the maximum plastic prestrain. Since permanent softening is observed in all cases, the Bauschinger strain parameter was measured based on 0.75 times the maximum forward stress. As an example, tension and compression flow curves from a T711 specimen prestrained to 5% plastic strain in tension is shown in Figure 5.2. The compressive portion is reflected about the x-axis and plotted in the first quadrant to facilitate comparison. The maximum forward stress σ_f , Bauschinger strain ϵ_B and permanent softening parameter $\Delta\sigma$ are also shown.

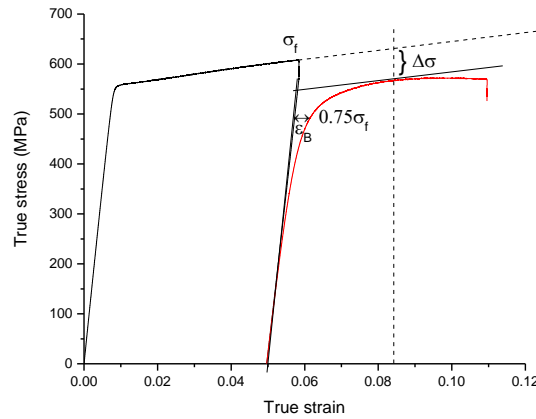


Figure 5.2: Stress strain curve obtained from Bauschinger test of a T711 specimen, where the compressive data during the reload has been plotted in the first quadrant.

5.4 Results

The data presented in this section is organized as follows. In order to see the effect on strength anisotropy with aging, the flow curves at 10^{-3} s^{-1} and at $\sim 1000 \text{ s}^{-1}$ along different loading directions for each temper investigated is presented first. Next, to elucidate the variation of plastic strain anisotropy with aging, the r -values for each loading direction are presented. Finally, the Bauschinger tests data along with the derived parameters are presented.

5.4.1 Compressive flow behavior

The uniaxial flow curves along RD, TD, ND and 45 at 10^{-3} s^{-1} and at 1000 s^{-1} for T3, W51, T6, T711 and T721 are presented in the following subsections. For T711, the RD, TD and ND data has been presented but the 45 data is new, and all tested directions are presented in the interest of completeness and to render comparisons more straightforward.

5.4.1.1 T3 temper

The flow curves at 10^{-3} s^{-1} for T3 material is shown in Figure 5.3a. 3-4 specimens were tested out of which only two flow curves for each direction are presented, for ease of reading. It is seen that the results are quite consistent. The solutionizing treatment dissolved the strengthening precipitates and resulted in a drastic decrease in the strength of the material, as compared to the aged condition (Bhattacharyya et al., 2016). The elastoplastic transition is protracted and there is nearly no yield strength anisotropy; for all the directions, the yield strength is $270 \pm 20 \text{ MPa}$. All directions exhibit good strain hardening capacity, however, they are different for different directions. The 45 direction shows the highest strain hardening followed by TD and ND, while the RD has the lowest hardening rate. The TD and ND tend to show saturation in strain hardening at $\sim 30\%$ strain.

The flow curves at 1000 s^{-1} are shown in Figure 5.3b. The values presented in Table 5.1 show slight negative strain rate sensitivity, probably because of the low strain hardening rate at dynamic rates. Another possibility for the observed negative rate sensitivity is dynamic strain ageing. Recall that the solutionized material has a large solute content in the matrix, and the effect of solutes interacting with forest dislocations can lead to dynamic strain ageing. The hardening rates saturate after about 15% strain for all the directions investigated. The flow stress anisotropy is changed with RD showing higher yield than TD and ND.

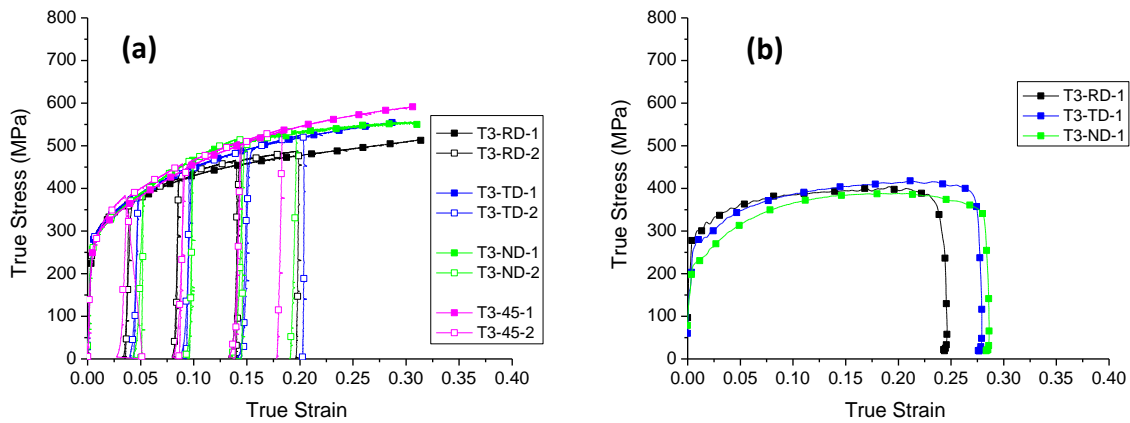


Figure 5.3: Experimental flow curves for T3 temper a) at 0.001 s^{-1} and b) at $\sim 1000 \text{ s}^{-1}$

Table 5.1: Values of strain rate sensitivity m calculated from RD flow curves, with stress values at 2% offset

Temper	m (2% offset)
T3	-0.005
W51	0.003
T711	0.002
T721	0.008

5.4.1.2 W51 temper

For the specimen which was naturally aged, (W51) the flow curves show slight yield anisotropy, where RD, TD and ND have yield strength of $\sim 450 \text{ MPa}$, whereas the 45 has a lower yield strength of only 400 MPa (Figure 5.4a). As was the case for the T3 temper, the TD, ND and 45 show a higher strain hardening rate than RD. Notably along 45, although the yield strength is lower, the stress level after $\sim 10\%$ strain is greater than RD, due to its higher strain hardening capacity. Again, all the 4 directions exhibit amount no saturation in strain hardening behavior up to $\sim 20\%$ strain, though the ND specimen failed after only $\sim 16\%$ strain in compression.

Figure 5.4b shows the flow curves at dynamic strain rates for the W51 material. In this case, the ND and TD have the highest yield strength and flow stress, while the RD and 45 is lower. The hardening rates of ND and 45 are similar and greater than TD while the RD is the lowest. The dynamic data show very similar trends as observed in case of quasistatic, indicating that the flow strength anisotropy does not exhibit obvious strain rate dependence. Given that there is a single, dominant mechanism of plastic deformation (octahedral slip), this is not surprising. The material shows only a small positive strain rate sensitivity (Table 5.1), typical of Al alloys.

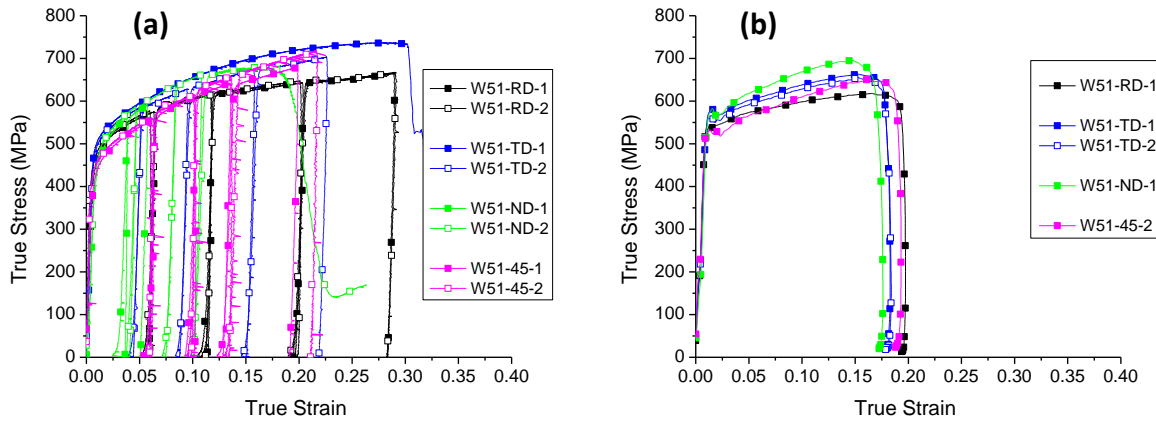


Figure 5.4: Experimental flow curves for W51 temper at a) 0.001 s^{-1} and b) $\sim 1000 \text{ s}^{-1}$.

5.4.1.3 T6 temper

Artificially aging to peakaged condition resulted in the highest strength observed among all the tempers (Figure 5.5). The yield anisotropy is large: the yield strength along RD and TD is ~ 550 MPa, whereas along ND and 45 it is ~ 475 MPa. The yielding behavior, especially for RD and TD, is sharp as compared to the T3 material. The hardening rates for RD and TD are decreased considerably, while the ND and 45 still show moderate hardening behavior, albeit lower than

other aging conditions. This is a typical behavior for precipitation strengthened alloys. The strain hardening capacity is greatly diminished (e.g., Cheng et al., 2003).

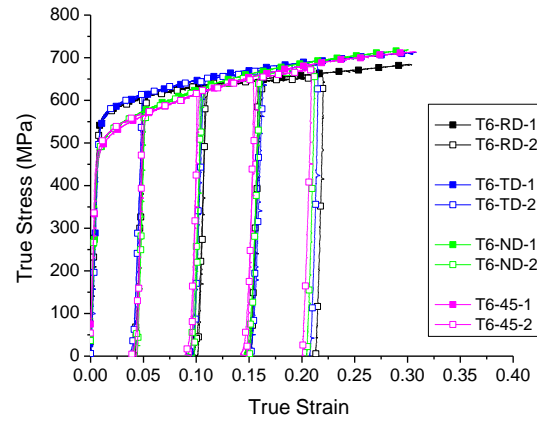


Figure 5.5: Experimental flow curves for T6 temper at 0.001 s^{-1} .

5.4.1.4 T711 temper

The RD, TD and ND results for T711 have been presented in chapter 4. In short, ND and TD exhibit the highest flow strength while the 45 has the lowest (Figure 5.6a). The hardening rate for 45 is the highest among all 4 directions. The yield strength, work hardening behavior and the level of strength anisotropy are very similar to that of the T6 temper. The dynamic data (Figure 5.6b), also shows similar trends as the quasistatic; 45 direction shows the highest hardening rate and the strain rate sensitivity is slightly positive.

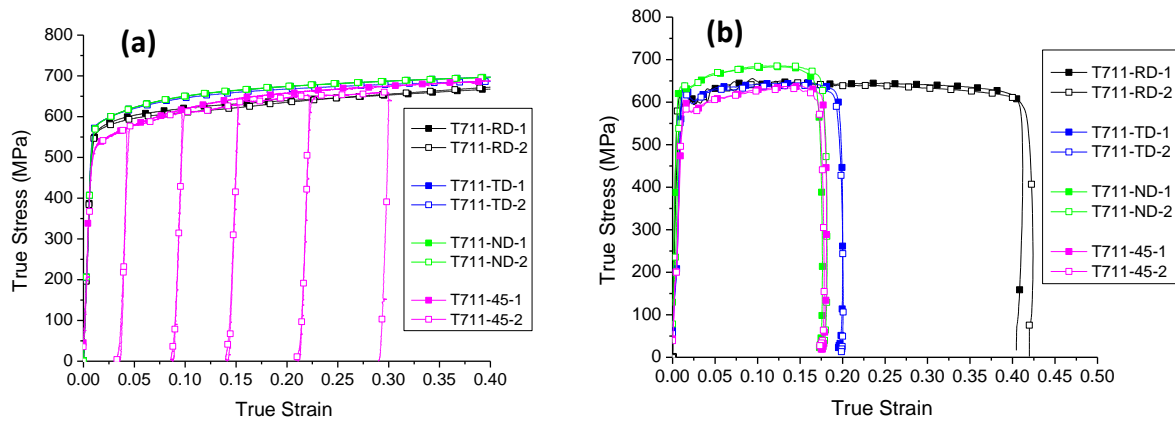


Figure 5.6: Experimental flow curves for T711 temper at a) 0.001 s^{-1} and b) $\sim 1000 \text{ s}^{-1}$

5.4.1.5 T721 temper

Upon further aging, the strength of the material has decreased (Figure 5.7a). There is very little yield anisotropy between RD, TD and ND. The yield strength for all the directions is ~ 400 MPa. However, in this case, the 45 specimen exhibits a lower hardening rate than the other 3 directions. Notably, the hardening response is also quite different from the solutionized and the peak-aged conditions. Along all the directions, the specimens exhibit rapid strain hardening up to $\sim 5\%$ strain followed by saturation and almost perfect plastic behavior. This type of flow behavior is typical of non-shearable precipitate containing materials, where the initial rapid strain hardening is due to buildup of internal stresses around the precipitates and once the relaxation occurs, the strain hardening rate decreases (Cheng et al., 2003; Poole et al., 2007).

Under dynamic conditions, (Figure 5.7b), the flow curves exhibit flow softening after 10% strain. This is expected since the material exhibited quite low strain hardening at the quasistatic strain rate. Flow localization, due to near adiabatic conditions under dynamic loading, is likely to start at earlier stages, in the absence of strain hardening. Like the other tempers, the

flow strength shows slight positive rate sensitivity (Table 5.1) and the strength anisotropy remains the same.

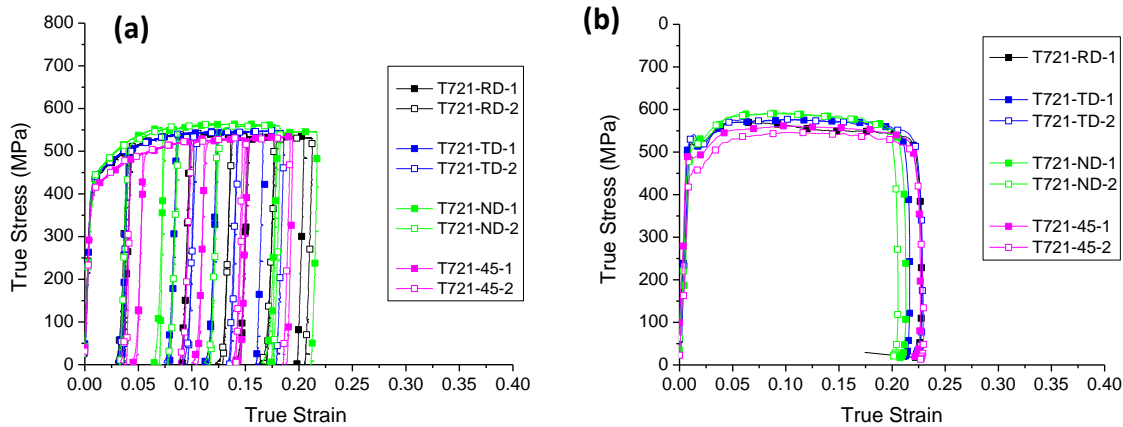


Figure 5.7: Experimental flow curves for T721 temper at a) 0.001 s^{-1} and b) $\sim 1000 \text{ s}^{-1}$.

5.4.2 Plastic strain anisotropy (r-value)

In the following subsection, the variation of r-values with strain for different tempers are presented for all the 4 loading directions tested.

The r-values along RD for all the tempers investigated are much less than 1 (Figure 5.8a), indicating low thinning resistance, which is common in Al alloys. However, there is a subtle variation in the r-values among the tempers. For the T3 material, lowest r-values are observed; starting from ~ 0.18 at plastic strains $< 5\%$ they gradually increase up to 0.3 and apparently saturates. The naturally aged W51 shows quite similar trend, although there is some scatter in the data. It starts from ~ 0.25 and gradually rises to 0.35 after about 25% strain. Contrary to the naturally aged specimen, the T6 and T711 material exhibits a higher r-value of 0.35 and essentially remains constant with straining. The most interesting behavior is exhibited by the overaged T721 material where it starts from ~ 0.25 at early stages of deformation but rapidly increase to ~ 0.5 within 20% strain.

Thus, these results suggest that not only the magnitude of the r -values but also their evolution with strain is temper dependent. The r -values at dynamic strain rates show a similar trend, although they appear to be slightly lower (at a given strain level) as compared to their quasistatic counterparts. The T3 and W51 specimens exhibit the lowest r -values, and it subsequently increases as the material is aged for longer durations.

The r -values along TD for all the tempers are also less than 1 but greater than the values for RD (Figure 5.8b). The r -values tend towards 1 with aging. Unlike RD, the TD r -values for all the tempers show a steady increase with strain. For the T3 material, r -values starting from ~ 0.4 at plastic strains $< 5\%$ increase up to 0.7 at $\sim 25\%$ strain. The naturally aged W51 again shows some scatter but follows the same trend in general. There is essentially no difference in the r -values for the W51 and the T6 material; both exhibiting r -values of 0.6-0.7 within the strain range investigated. The r -value for T711 remains quite constant at ~ 0.8 throughout straining whereas, the overaged T721 material the r -value for starts from ~ 0.6 and steadily increases to ~ 0.8 within 20% strain.

The r -values at dynamic strain rates compares very well with the quasistatic data, indicating that there is no strain rate dependency of the r -values at least within the rate regime investigated. The T3 and W51 essentially have the same r -values along TD, whereas the T711 and T721 are considerably different. Unlike the RD case, the TD r -value data suggests that although the magnitude of the r -values varies with the temper, their evolution with strain is less sensitive to the heat treatment.

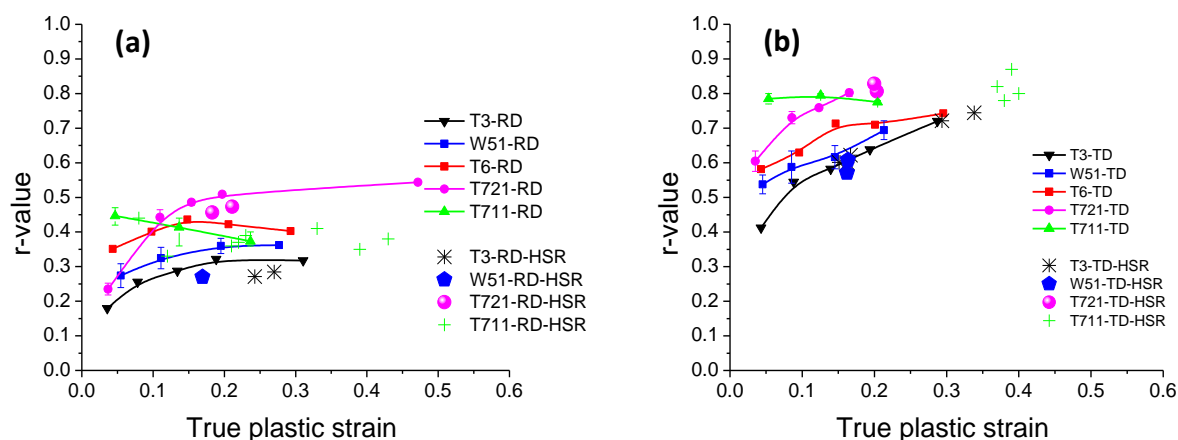


Figure 5.8: The variation of r-value as a function of plastic strain, for T3, W51, T6, T711 and T721 temper, at both quasistatic and dynamic strain rates a) along RD b) along TD

The r-values for the ND samples show a wide range of scatter, with the overaged T721 having r-values closer to 1, followed by the slightly overaged T711 (Figure 5.9a). All except the T6 temper shows a slight decreasing trend. The high strain rate data, in general, falls in line with the quasistatic and thus in agreement with the conclusion that the r-values are essentially rate independent. It is worth mentioning that in the previous study it was found that the ND r-values were highly sensitive to the initial texture of the material. Although it is known that aging treatment does not lead to any appreciable changes in the texture, it is worth remembering that the as-received plates of W51 and T721 were of different thicknesses, and thus even though they have qualitatively the same texture, the texture strength and thus the volume fraction of individual texture components of the two materials are different. Furthermore, the solutionizing heat treatment used to produce the T3 and T6 conditions from commercially produced W51 temper could have induced some recrystallization and grain growth sufficient to alter the texture. X-ray diffraction measurements of the texture in the T3 temper suggest that a slight texture modification was induced. The previous study showed that these slight variations can lead to

large changes in the ND r-values hence the influence of texture in the data presented here may not be completely neglected.

The r-values for the 45 specimens are all greater than 1 and vary between ~ 1.4 to ~ 2 , depending on the heat treatment (Figure 5.9b). The T3 material shows the largest r-values among all the tempers investigated; ~ 2 at low strains, which gradually decrease to 1.7 after 30% plastic strain. The W51 shows a constant r-value of ~ 1.6 throughout straining. For the peakaged (T6) specimen, the r-values are ~ 1.55 and also remain relatively constant with straining. For the two overaged tempers investigated, T711 and T721, the r-values show rapid evolution like in case of RD, where they start from ~ 1.75 and rapidly decrease. The T721 tends to monotonically decrease to ~ 1.4 , whereas the T711 seems to saturate or perhaps even increase at higher strain levels. The dynamic r-values exhibit a similar trend, with a slight larger scatter. Just like the earlier cases, it is evident that with aging, the r-values tend towards 1, indicating that the material becomes more isotropic.

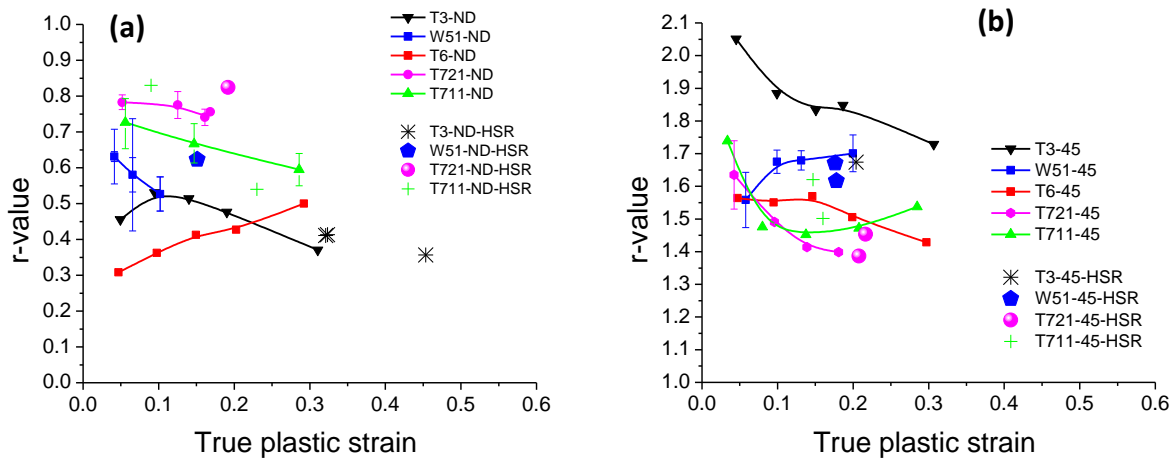


Figure 5.9: The variation of r-value as a function of plastic strain, for T3, W51, T6, T711 and T721 temper, at both quasistatic and dynamic strain rates a) along ND b) along 45

5.4.3 Bauschinger tests

The results for the Bauschinger tests for T3 and T711 are presented in this section. First, the tension-compression flow curves are presented. The different parameters derived from this data are presented next. Figure 5.10 shows the flow curves for the T3 material for different prestrains. The forward tension curves show linear hardening while the reverse flow curves in compression are flatter. Some of this distinction may be due to buckling of the rather high aspect ratio tensile test bars (4:1, gage length to diameter), so the compressive data are viewed with some suspicion beyond about 2% compressive plastic strain. The yield is quite gradual for both forward and reverse loading. In case of T711 (Figure 5.11), the forward curves exhibit a rather sharp yield with much lower hardening rate, but the reverse curves show a more rounded behavior.

If the initial tensile yield behavior of the T711 tempered material is compared with the initial compressive yield behavior (520 MPa in compression vs. 555 MPa in tension for 0.1% offset) (Figure 5.6), one can see that it has a “built-in” Bauschinger effect from its thermomechanical history. Recall that the commercial practice is to solutionize, quench and stretch, to relieve the residual stresses induced by quenching. This stretching appears to induce backstresses that cause the subsequent tensile yield to be abrupt, while compressive yield exhibits the more gradual. This apparent “built-in” Bauschinger effect is ignored in the subsequent quantitative analysis. However, it should be born in mind when making qualitative comparisons of the various tempers. For example, the solutionizing heat treatment used to produce the T3 and T6 material relieves any such built-in stress state present in the commercially produced tempers.

During the initial tensile loading, the yield strengths for the T3 material were found to be ~295, 325 and 346 MPa at 250 $\mu\epsilon$, 0.001 and 0.002 offsets. For the T711, the corresponding yield strengths were 520, 554 and 560 MPa. Similarly, the yield strength in compression is also measured. These values as well as other quantities mentioned in the experimental section are calculated from the data and are presented in Table 5.2. From this data it is seen that, for all the offset strain levels used, the compressive yield strength values are lower than the maximum flow stress attained during tension, indicating the presence of Bauschinger effect, even in the T3 material. It can be seen that upon compressive loading, there is a transient region (which lasts for ~ 1.5% strain in this case), where the hardening rate is much higher than that in tension. Subsequently, the compression curve becomes essentially parallel to the tension but at a lower stress level, indicative of permanent softening. These features are observed for all the prestrains applied and for both T3 and T711 material.

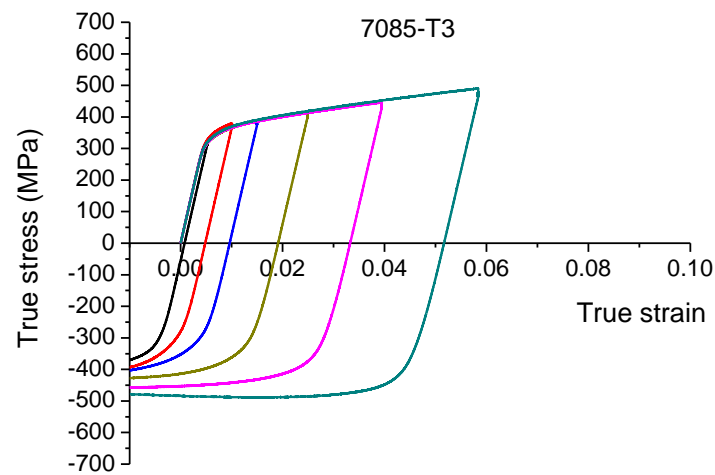


Figure 5.10: Tension compression flow curves for T3 material after different prestrains.

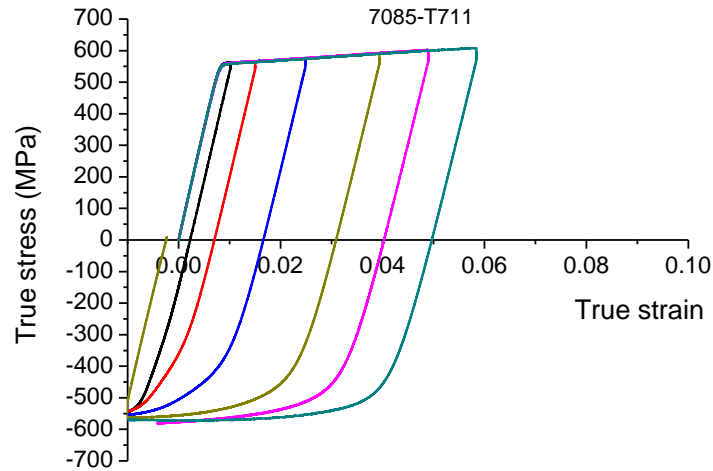


Figure 5.11: Tension compression flow curves for T711 material after different prestrains.

The backstress as given in Table 5.2 is plotted against the plastic prestrain for the different offsets (Figure 5.12a). As expected, the offset used to determine the reverse yield strength has a large impact on the magnitude of the backstress. The general trend is the same in every case; the backstress increases up to about 1% plastic prestrain after which it tends to saturate. The largest backstress of ~ 225 MPa is observed for the T711 material with a $250 \mu\epsilon$ offset. Moreover, it is seen that for a given offset the backstress calculated for T711 is about twice that of the T3 material.

Table 5.2: Various Bauschinger parameters computed for T3 and T711 material.

Total prestrain	Plastic prestrain ϵ_p	Max tensile stress σ_f	Compressive yield strength σ_r			$\sigma_B = (\sigma_f - \sigma_r)/2$			B strain ϵ_B	Permanent softening $\Delta\sigma$
T711										
			0.002	0.001	250 $\mu\epsilon$	0.002	0.001	250 $\mu\epsilon$		
0.01	0.00227	563	476	347	185	43.8	108.0	189.2	0.00129	35.0
0.015	0.00703	564	365	291	140	99.5	136.3	212.0	0.00308	33.6
0.025	0.01663	576	383	297	125	96.5	139.5	225.5	0.00396	40.1
0.04	0.0309	591	368	269	88	111.5	161.0	251.8	0.00336	59.5
0.05	0.04029	602	417	262	136	92.4	169.9	233.0	0.00307	67.4
0.06	0.04967	607	396	290	145	105.9	158.7	231.2	0.00258	66.0
T3										
0.005	0.000786	316	338	312	257	-10.9	2.1	29.5	6E-05	26.8
0.010	0.00483	379	316	286	225	31.7	46.5	77.0	0.00093	29.5
0.015	0.00963	388	311	277	210	38.6	55.5	89.0	0.00124	35.6
0.025	0.01913	414	328	290	196	42.9	61.6	108.6	0.00132	30.9
0.040	0.03327	446	353	304	198	46.8	71.0	124.0	0.00142	43.5
0.060	0.05168	490	388	319	188	51.0	85.4	151.2	0.026703	36.7

If, on the other hand, the permanent softening parameter is used to compute the internal stress, then the values are much lower (Figure 5.12b). Interestingly, for the T3 material, the values are ~15 MPa and is constant with strain, whereas for the T711 material, the internal stress shows a gradual increase from 15 MPa up to 35 MPa at about 3.5% plastic prestrain, where it apparently saturates. Here also, the difference in magnitude of the internal stress between the T3 and T711 is close to a factor of 2.

The final parameter extracted from the experimental data is the Bauschinger strain, which is plotted as a function of the applied plastic prestrain (Figure 5.13). The data shows a different trend for T3 and T711 material. For T3, a clear saturation behavior is observed after 1% plastic prestrain. The T711, on the other hand, show an increase in the Bauschinger strain up to about 1.5% plastic prestrain after which it decreases.

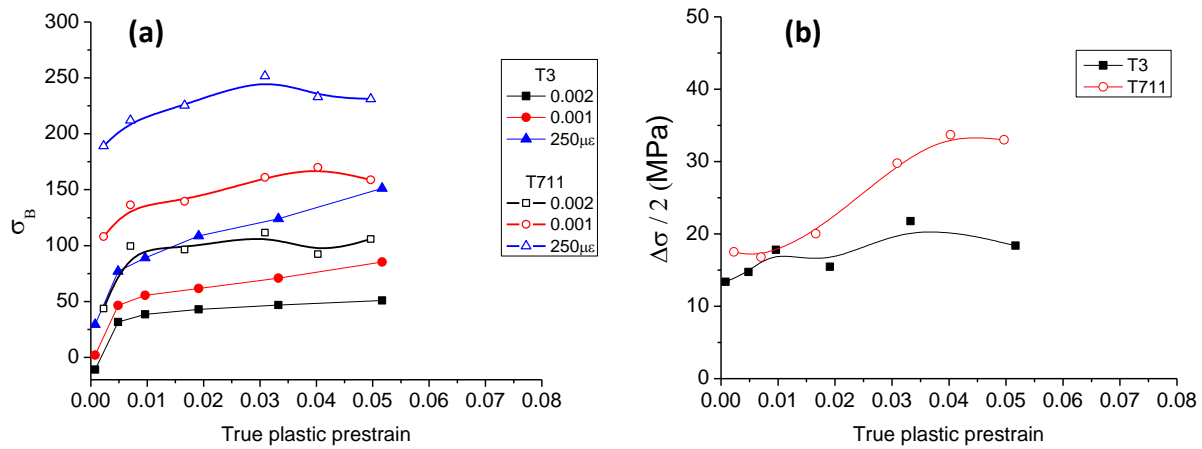


Figure 5.12: The variation of backstress as a function of plastic prestrain and offset used to obtain compressive yield stress. a) computed according to Eq. 5-3 and b) based on permanent softening

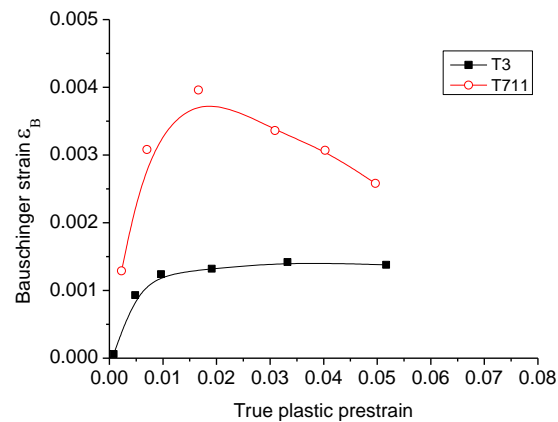


Figure 5.13: Evolution of Bauschinger strain as a function of plastic prestrain

5.5 Discussion

The temper dependence of strength and strain anisotropy as well as the Bauschinger effect of AA 7085 has been investigated. In the following subsections, the results are discussed first in terms of the anisotropy and then the Bauschinger effect.

5.5.1 The strength and strain anisotropy

The flow curve data reveals a systematic variation in the flow strength, strain hardening and particularly in the plastic anisotropy evolution for different heat treatment conditions. The general trend is quite clear. The peak-aged condition is characterized by flow curves which show abrupt yield, the highest strength anisotropy, and the lowest hardening rates. In the solutionized state, the yield behavior is more gradual, the strength and strength anisotropy is lowest, and the highest strain hardening capacity is the highest. All other aging conditions lie intermediate to these two extremes. It is found that the 45 specimens are softest in all cases, except T6 where they show similar behavior as the ND. It is interesting to note that, starting from the solutionized condition, the flow strength anisotropy increases up to the T6 condition, after which it decreases again in the overaged condition.

The r -values for all the directions tend towards 1 with aging, i.e. the presence of the second phase particles increases the strength as well as modifies the strain anisotropy of the material. RD, TD and 45 all show consistent trends, except ND, which has been found to be very sensitive to the initial texture ((Reyes et al., 2006; Bhattacharyya et al., 2016, in review). Another noteworthy point is that the r -values, particularly for the overaged condition show rapid evolution with strain, which is not observed in single phase alloys, where they remain almost constant throughout straining, at least for small strain levels, where texture evolution is minimal. Furthermore it is observed that for the non-overaged conditions (T3, W51 and T6), the degree to

which the r -values are affected varies with the loading direction. However, the r -values for the overaged condition are significantly different for all the directions. This may be a reflection of the fact that different metastable precipitates phases appear and are replaced by equilibrium phases and each of these phases resists, to varying degrees, being sheared by the dislocations. Once over-aged, the precipitates are non-shearable at least up to a few percent strains (Moan and Embury, 1979), and hence, the effects of the internal stress become more apparent in the over-aged condition. Indeed, the internal stresses of interest are those which develop because there are particles which remain elastic, despite being embedded in a plastic medium.

This empirical result helps to explain previous observation that conventional crystal plasticity modeling (with the viscoplastic self-consistent code known as VPSC), which accounts for the initial texture, over-estimates the strain anisotropy. Those prior predictions better describe the strain anisotropy in the T3 and W51 tempers. Whereas the T6, T711 and T721 tempered materials have an increasing population of shearable and non-shearable precipitates. The key feature which will determine the anisotropy is slip system selection. The degree to which the precipitates serve to alter the slip system selection, the more they will alter the observed strain anisotropy. There are two ways we can imagine this to occur. For shearable precipitates, the grains may tend to activate fewer slip systems, exhibiting a more planar slip behavior, and altering the way internal strains are distributed amongst the grains. For non-shearable precipitates, backstresses may develop with straining which quickly “shut down” the initially active slip systems and force the grains to adopt other initially latent slip systems. This latter possibility will be explored in detail in a subsequent modeling work.

5.5.2 Bauschinger data

The level of internal stresses observed in this study is found to be dependent upon the offset strain employed. If Eq. 5-3 is used, the values lie between 25 to 225 MPa. On the other hand, if only the permanent softening is of interest, the values lie between 10-35 MPa. Both sets of values imply a strong contribution of kinematic hardening to strain hardening of the materials investigated. This has been observed in the past (Lloyd, 1977; Proudhon et al., 2008; Fribourg et al., 2011) and can be understood if one considers that the very small offsets used in Eq. 5-3 represents the transient behavior of the Bauschinger effect, whereas the permanent softening is measured after some reverse plastic strain has occurred. This type of permanent softening has been observed in pure Al (Hasegawa et al., 1975) and has been explained in terms of breakdown of dislocation structures upon stress reversal, leading to a loss in dislocation density, which does not recover to its original value until large reverse strains are applied (Beyerlein and Tome, 2007). In the transient regime, on the other hand, the contribution from reversible dislocation motion cannot be ignored.

Queyreau and Devincre (2009) used dislocation dynamics to investigate the Bauschinger effect in the transient regime and have highlighted the importance of annihilation of Orowan loops by backward moving dislocations. The elastic attraction followed by annihilation enables the dislocation to overcome the obstacle without having to exert any extra stress. This results in very low flow stress during the early stages of reverse loading. Hence using small offsets for reverse yield strength gives large internal stress values. As straining continues, new loops are stored, not all of which are annihilated by the dislocations, leading to the rapid hardening. At the same time, the dislocation structures that generated during prestraining also evolve. The permanent softening phenomenon in single phase alloys has generally been attributed to the loss

in dislocation density due to dissolution of substructures. However, when there are non-shearable precipitates present, it is interesting to investigate whether the particles sustain some level of stresses throughout, even after they are sheared, which additionally contributes to permanent softening besides the contribution from dislocations. One of the concepts, which will be explored in future modeling, is the degree to which these effects can be captured by more coarse-scale micromechanical modeling of the internal stresses within elastic inclusions (precipitates, idealized as Eshelby's ellipsoidal inhomogeneity) within a matrix having elasto-plastic properties governed by the standard rules of small-strain anisotropic crystal plasticity as formulated by Hill (1965).

Irrespective of the method by which the internal stress is calculated, the values saturate once the plastic prestrain exceeds $\sim 2\%$. This can be explained by considering the fact that a finite number of loops that can be stored around the particle. At this point, other factors such as recovery due to cross slip or climb, or even particle shearing due to the local stress concentration cannot be ruled out. The final parameter which characterizes the Bauschinger effect is the strain at which a fraction of the forward stress is restored. For both cases, the magnitudes are quite low and a part of this is because $0.75\sigma_f$ has been chosen to measure them. Even then, the strain for T3 is about 3 times lower than that of T711, indicating that for a given prestrain, the T3 material regains the original configuration much faster than T711. For both cases, the strain increases up to a 1-1.5% prestrain, indicating that it requires a larger reverse strain to restore the target stress value. On further pre-straining, the T3 shows a saturation type behavior, whereas the T711 shows a decrease. This implies that it becomes easier for the material to recover the original behavior. This observation requires further investigation and direct measurements of the stress in the second phase (using in-situ x-ray or neutron diffraction for example) and specifically how it

evolves, once the saturation behavior is observed, would certainly benefit from explaining what happens at larger prestrain levels.

5.6 Conclusion

1. AA 7085 is a relatively new aerospace structural alloy, which exhibits a typical hot rolling texture consisting of strong brass and S components, which only varies slightly from one temper to another (T3, T6, T711, and T721).
2. The strength anisotropy increases with increasing level of aging.
3. Conversely, the strain anisotropy (as characterized by r-values along RD, TD, ND, & 45° to RD) tend toward isotropy with increasing levels of aging.
4. As has been observed in other Al alloy systems, the Bauschinger effect increases with aging. As such, we observe a correlation between the strain anisotropy, which increasingly departs from standard crystal plasticity predictions, and the increased level of backstress induced by second phase particles.
5. The strength and strain anisotropy observations are essentially common between quasistatic and dynamic ($\sim 1000 \text{ s}^{-1}$) strain rates, which greatly simplifies the characterization of the effect.
6. The strain rate sensitivity was found to be low and positive for all the tempers investigated, except T3, which exhibited a slight negative rate sensitivity. It is hypothesized that the high solute content in the matrix interacts with dislocations to produce a dynamic strain ageing effect.
7. All the tempers, when compared to quasistatic loading, exhibit lower hardening rates under dynamic rates, which suggests that the adiabatic conditions are responsible for the strain softening effect.

8. Crystal plasticity models designed for examining fatigue problems (e.g., the hysteresis loops of low cycle fatigue testing) have tended to incorporate the effects of backstress (e.g., Meric et al., 1991; Wollmershauser et al., 2012). The present work highlights the need to account for such backstresses, even in cases involving higher levels of plasticity (such as modeling of metal forming, crash, ballistics, etc.) where strain anisotropy is often of keen interest.

5.7 Acknowledgements

The authors would like to thank ALCOA for providing the AA7085 plates, in W51, T711 and T721 tempers, used in this study. The authors would like to thank Frederic Barlat and Shi-Hoon Choi for suggesting us to look into this topic in detail and Md. Shamssujjoha and Josiah Winter for measuring the texture of the T3 material. The research at U.Va. and M.S.U. was sponsored by the United States Army Research Office under contract number W911NF-12-1-0455 monitored by Drs. Suveen Mathaudhu and David Stepp. The views and conclusions contained in this document are those of the authors and should not be interpreted as representing the official policies, either expressed or implied, of the Army Research Laboratory or the U.S. Government. The U.S. government is authorized to reproduce and distribute reprints for government purposes notwithstanding any copyright notation hereon.

5.8 References

- Abel, A., 1987. Historical perspectives and some main features of the Bauschinger effect. *Mater. forum* 10, 11–26.
- Abel, A., Ham, R., 1966. The cyclic strain behaviour of crystals of aluminum-4 wt.% copper-i. the bauschinger effect. *Acta Metall.* 14, 1489–1494. doi:10.1016/0001-6160(66)90170-2
- Agnew, S., Whittington, W., Oppedal, A., El Kadiri, H., Shaeffer, M., Ramesh, K.T., Bhattacharyya, J., Delorme, R., Davis, B., 2014. Dynamic Behavior of a Rare-Earth-Containing Mg Alloy, WE43B-T5, Plate with Comparison to Conventional Alloy, AM30-F. *Jom* 66, 277–290. doi:10.1007/s11837-013-0830-x
- Barlat, F., Liu, J., 1998. Precipitate-induced anisotropy in binary Al-Cu alloys. *Mater. Sci. Eng. A* 257, 47–61. doi:10.1016/S0921-5093(98)00823-5
- Bate, P., Roberts, W.T., Wilson, D. V, 1981. The plastic anisotropy of two-phase aluminum alloys -- I. Anisotropy in unidirectional deformation. *Acta Metall.* 29, 1797–1814.
- Bate, P., Roberts, W.T., Wilson, D., 1982. The plastic anisotropy of two-phase aluminium alloys - II Anisotropic behavior in load reversal tests. *Acta Metall.* 30, 725–737.
- Beyerlein, I.J., Tome, C.N., 2007. Modeling transients in the mechanical response of copper due to strain

- path changes. *Int. J. Plast.* 23, 640–664. doi:10.1016/j.ijplas.2006.08.001
- Bhattacharyya, J.J., Agnew, S.R., Lee, M., Whittington, W.R., El Kadiri, H., 2016. Measuring and modeling the anisotropic, high strain rate deformation of Al alloy, 7085, plate in T711 temper, in review.
- Bhattacharyya, J.J., Wang, F., Wu, P.D., Whittington, W.R., El Kadiri, H., Agnew, S.R., 2016. Demonstration of alloying, thermal activation, and latent hardening effects on quasi-static and dynamic polycrystal plasticity of Mg alloy, WE43-T5, plate. *Int. J. Plast.* 81, 123–151. doi:10.1016/j.ijplas.2016.01.005
- Brown, L.M., 1977. Orowan's explanation of the Bauschinger effect. *Scr. Metall.* 11, 127–131. doi:10.1016/0036-9748(77)90291-5
- Caceres, C., Griffiths, J.R., Reiner, P., 1996. The influence of microstructure on the Bauschinger effect in an Al-Si-Mg casting alloy. *Acta Metall.* 44, 14–23.
- Chen, W.W., Song, B., 2010. Split Hopkinson (Kolsky) bar: design, testing and applications. Springer Science & Business Media.
- Cheng, L.M., Poole, W.J., Embury, J.D., Lloyd, D.J., 2003. The influence of precipitation on the work-hardening behavior of the aluminum alloys AA6111 and AA7030. *Metall. Mater. Trans. A* 34, 2473–2481. doi:10.1007/s11661-003-0007-2
- Choi, S.H., Barlat, F., Liu, J., 2000. Effect of Precipitates on Plastic Anisotropy of Polycrystalline Aluminum Alloys. *Mater. Sci. Forum* 331-337, 1327–1332. doi:10.4028/www.scientific.net/MSF.331-337.1327
- Doherty, K., Squillaciotti, R., Cheeseman, B., Placzankis, B., Gallardy, D., 2012. Expanding the Availability of Lightweight Aluminum Alloy Armor Plate Procured From Detailed Military Specifications. ICAA13 13th Int. Conf. Alum. Alloy. 541–546.
- Follansbee, P.S., 2014. Fundamentals of Strength—Principles, Experiment, and Application of an Internal State Variable Constitutive Model. the Minerals. Met. Mater. Soc. John Wiley Sons, Inc., Hoboken.
- Fribourg, G., Brechet, Y., Deschamps, A., Simar, A., 2011. Microstructure-based modelling of isotropic and kinematic strain hardening in a precipitation-hardened aluminium alloy. *Acta Mater.* 59, 3621–3635. doi:10.1016/j.actamat.2011.02.035
- Gracio, J.J., Barlat, F., Rauch, E.F., Jones, P.T., Neto, V.F., Lopes, A.B., 2004. Artificial aging and shear deformation behaviour of 6022 aluminium alloy. *Int. J. Plast.* 20, 427–445. doi:10.1016/S0749-6419(03)00095-0
- Gray, G.T., 2000. Classic Split-Hopkinson Pressure Bar Testing. Mater. Park. OH ASM Int. 2000.
- Hasegawa, T., Yakou, T., Karashima, S., 1975. Deformation behaviour and dislocation structures upon stress reversal in polycrystalline aluminium. *Mater. Sci. Eng.* 20, 267–276.
- Hielscher, R., Schaeben, H., 2008. A novel pole figure inversion method: Specification of the MTEX algorithm. *J. Appl. Crystallogr.* 41, 1024–1037. doi:10.1107/S0021889808030112
- Hill, R., 1965. A self-consistent mechanics of composite materials. *J. Mech. Phys. Solids* 13, 213–222. doi:10.1016/0022-5096(65)90010-4
- Jain, A., Agnew, S.R., 2007. Modeling the temperature dependent effect of twinning on the behavior of magnesium alloy AZ31B sheet. *Mater. Sci. Eng. A* 462, 29–36. doi:10.1016/j.msea.2006.03.160
- Lloyd, D.J., 1977. The Bauschinger effect in polycrystalline aluminum containing coarse particles. *Acta Metall.* 25.
- Meric, L., Poubanne, P., Cailletaud, G., 1991 Single crystal modeling for structural calculations. Part 1: model presentation. *J. Eng. Mat. Technol.* 113, 162–170
- Moan, G.D., Embury, J.D., 1979. A study of the Bauschinger effect in Al-Cu alloys. *Acta Metall.* 27, 903–914.
- Park, J.K., Ardell, A.J., 1983. Microstructures of the commercial 7075 Al alloy in the T651 and T7 tempers. *Metall. Trans. A* 14, 1957–1965. doi:10.1007/BF02662363
- Poole, W.J., Wang, X., Lloyd, D.J., Embury, J.D., 2007. The shearable – non-shearable transition in Al – Mg – Si – Cu precipitation hardening alloys: implications on the distribution of slip, work hardening and fracture. *Philos. Mag.* 37–41. doi:10.1080/14786430500154935

- Proudhon, H., Poole, W.J., Wang, X., Bréchet, Y., 2008. The role of internal stresses on the plastic deformation of the Al-Mg-Si-Cu alloy AA6111. *Philos. Mag.* 88, 621–640. doi:10.1080/14786430801894569
- Queyreau, S., Devincere, B., 2009. Bauschinger effect in precipitation-strengthened materials: A dislocation dynamics investigation. *Philos. Mag. Lett.* 89, 419–430. doi:10.1080/09500830903005433
- Ram Prabhu, T., 2015. An overview of high-performance aircraft structural al alloy-AA7085. *Acta Metall. Sin. (English Lett.* 28, 909–921. doi:10.1007/s40195-015-0275-z
- Reyes, A., Hopperstad, O.S., Lademo, O.-G., Langseth, M., 2006. Modeling of textured aluminum alloys used in a bumper system: Material tests and characterization. *Comput. Mater. Sci.* 37, 246–268. doi:10.1016/j.commatsci.2005.07.001
- Stoltz, R.E., Pelloux, R.M., 1976. The Bauschinger effect in precipitation strengthened aluminum alloys. *Metall. Trans. A* 7, 1295–1306.
- Stoltz, R.E., Pelloux, R.M., 1974. Cyclic deformation and bauschinger effect in AlCuMg alloys. *Scr. Metall.* 8, 269–275. doi:10.1016/0036-9748(74)90250-6
- Wilson, D., 1965. Reversible work hardening in alloys of cubic metals. *Acta Metall.* 13, 807–814. doi:10.1016/0001-6160(65)90145-8
- Wollmershauser, J.A., Clausen, B., Agnew, S.R., 2012. A slip system-based kinematic hardening model application to in situ neutron diffraction of cyclic deformation of austenitic stainless steel. *Int. J. Fatigue* 36, 181–193. doi:10.1016/j.ijfatigue.2011.07.008

6 Effect of precipitates on anisotropy: Application to AA7085 at various tempers – Part 2: Modeling

6.1 Abstract

A model taking into account the kinematic hardening effect of an elastic inclusion within an elastoplastic single crystal has been incorporated into the elastoplastic self-consistent (EPSC) polycrystal modeling framework. This model has been used to quantitatively describe the effect of non-shearable precipitates on the generalized plasticity. This model was validated by the experimental results presented in Part 1 (chapter 5). By taking into account the kinematic hardening contribution, it is demonstrated that the model can qualitatively describe the plastic anisotropy as well as the flow behavior for AA 7085 in different tempers. While it is acknowledged that shearable precipitates play an important role in strengthening alloys like AA 7085, the kinematic hardening effect of the highly loaded precipitates, including those which may be non-shearable, is demonstrated to have a largely unrecognized, but measureable impact on anisotropy.

Keywords: plastic strain anisotropy, backstress, precipitation hardening, self-consistent modeling, strain incompatibility.

6.2 Introduction

In the first part of the series of two papers, experimental results pertaining to AA 7085 subjected to various heat treatments was presented. The results clearly indicate the dependence of flow stress anisotropy and plastic strain anisotropy (r-value) on the temper condition of the material. Although this phenomena has been observed before in several Al alloys (Bate et al., 1981; Hosford and Zeisloft, 1972; Jobson and Roberts, 1977), the modeling efforts devoted to capture and predict this phenomena has been limited to a single effort at the ALCOA technical

center which employed a phenomenological continuum plasticity approach, rather than the crystal plasticity based approach presented here.

The interaction of precipitates with dislocations is a well-established field and has been studied by a number of researchers (e.g. Friedel, 1964; Bacon et al., 1973; Gleiter and Hornbogen, 1968; Ardell, 1985; Takahashi and Ghoniem, 2008, to name a few). It is fairly now well established that the presence of precipitates leads to a changes in the solute distribution, decreases the mean free path of the dislocations, creates additional storage of dislocations due to strain incompatibility, and hence, affects dynamic recovery. The presence of non-shearable particles/precipitates leads to an additional storage of dislocation loops around them (Ashby, 1970; L.M. Brown and Stobbs, 1971; Brown and Clarke, 1975), which exerts a stress that repels the forward motion of other dislocations on the slip plane, but facilitates their reverse motion. This additional stress is commonly called ‘backstress’ due to its directional nature, which leads to Bauschinger effect as well as a change in the activity of slip systems, which in turn, affects the plastic anisotropy.

Several types of models have been implemented in the past which incorporate the effects of particles/precipitates in the description of the hardening behavior. They can be broadly classified into two categories: 1) strain gradient plasticity based models which take into account the geometrically necessary dislocations (GNDs) (Ashby, 1970) associated with the particles (for instance, Busso et al., 2000; Yassar et al., 2007) and 2) the ‘elastic inclusion model’, where the particle/precipitate is treated as an elastic ellipsoidal inclusion embedded in the crystalline matrix (Brown and Clarke, 1975). One advantage of the latter strategy is that it can be relatively straightforward to implement. The early applications were limited to isotropic elasticity where the particle and the matrix have same elastic constants. The model of Brown and Clarke (1975)

based on Eshelby's inclusion formalism (Eshelby, 1957) where the eigenstrain, ε^* is assumed to be equal to the unrelaxed plastic strain in the material. Thus, for an ellipsoidal inclusion with uniform eigenstrain ε^* , the total strain in the inclusion $\varepsilon^{I,e}$ is obtained according to Eshelby's solution:

$$\varepsilon_{ij}^I = S_{ijkl} \varepsilon_{kl}^* \quad (6-1)$$

where S is the Eshelby tensor, taking into account the shape and orientation of the ellipsoid.

Therefore, the elastic strain in the inclusion ε_e^I is given as (for small-strain deformation):

$$\varepsilon_{ij}^{I,e} = \varepsilon_{ij}^I - \varepsilon_{ij}^* = S_{ijkl} \varepsilon_{kl}^* - \varepsilon_{ij}^* = (S_{ijkl} - I_{ijkl}) \varepsilon_{kl}^* \quad (6-2)$$

Subsequently, the stress in the inclusion follows from Hooke's law:

$$\sigma_{ij}^I = C_{ijkl} (\varepsilon_{kl}^I - \varepsilon_{kl}^*) = C_{ijkl} (S_{klmn} \varepsilon_{mn}^* - \varepsilon_{kl}^*) = -Q_{ijkl} \varepsilon_{kl}^* \quad (6-3)$$

where C is the elastic stiffness tensor and Q is the accommodation tensor given by:

$$Q_{ijkl} = C_{ijmn} (I_{mnkl} - S_{mnkl}) \quad (6-4)$$

In this formulation, the value of unrelaxed plastic strain is assumed to be equal to that of the total plastic strain in the material. This is an assumption which is only valid for very small strains, where limited relaxation occurs (Brown and Clarke, 1975; Bate et al., 1981).

This 'elastic inclusion model' in its original form has been used by several researchers, e.g. (Bate et al., 1981; Brown and Clarke, 1975; Moan and Embury, 1979) to explore the role of precipitates in Al containing alloys. In recent years, it has been incorporated in phenomenological continuum plasticity models, for instance, (Barlat and Liu, 1998a; Choi et al., 2000) as well as in crystal plasticity formulations (Schmitt et al., 1997; Bonfoh et al., 2003; Han et al., 2004, 2006; Sehitoglu et al., 2005; Anjabin et al., 2014).

The crystal plasticity framework provides several advantages in comparison to phenomenological continuum models. At the grain level, the deformation is described by the

crystallography of dislocation slip or twinning, which are the fundamental mechanisms of plasticity. Furthermore, the polycrystalline aggregate is represented by its crystallographic texture. Together, these two factors can result in anisotropic elastic and plastic properties, at the macro (polycrystal) level. In addition, the crystal plasticity models inherently capture intergranular stresses (e.g, Mulay et al., 2011), because a grain oriented favorably with respect to the loading axis can have a different stress state as compared to a unfavorably oriented ‘hard’ grain. Furthermore, these models are not restricted to any particular strain paths as they take into account texture evolution. These features are not present in continuum plasticity models. And even though these continuum models are computationally efficient, the number of fitting parameters is quite large and literally dozens of experiments are typically required to fully calibrate the comprehensive models, such as the so-called Yld89, Yld96 and Yld2003 models proposed by Barlat et al. (1989 ;1997; 2003).

In the present work, the elastoplastic self-consistent (EPSC) model, originally developed by Turner and Tome (1994), has been modified to incorporate the hardening behavior due to the presence of elastic inclusion. First, the initial EPSC infinitesimal strain formulation of Turner and Tome is briefly described, followed by the derivation of the modified single crystal behavior and finally a comparison between the original EPSC, the new model and experimental data is presented.

6.3 The EPSC model

The purpose of this section is to introduce the equations which are implemented in the original EPSC model, to facilitate comparison with the modified model. The details are given in (Hutchinson, 1970; Turner and Tomé, 1994). In the EPSC model, a ‘grain’ represents a collection of physical grains having a particular orientation and is approximated as an anisotropic

elastoplastic ellipsoidal inclusion. This grain is embedded in an anisotropic homogeneous effective medium (HEM) which represents the polycrystalline aggregate. The grain level and aggregate level response are connected using modified Eshelby equivalent inclusion formalism.

6.3.1 Grain level constitutive behavior

Under isothermal conditions and restriction to infinitesimal strain, the constitutive relation of a grain c , is given by the differential form of Hooke's law, relating the stress increment $d\sigma^c$ to the *elastic* strain increment:

$$d\sigma_{ij}^c = C_{ijkl}^c [d\varepsilon_{ij}^c - \sum_s m_{ij}^\alpha d\gamma^\alpha] \quad (6-5)$$

where, \mathbf{C}^c is the elastic stiffness tensor of the crystal c , $d\boldsymbol{\varepsilon}^c$ is the total strain increment in crystal c , and the total plastic shear increment is given by $\sum_\alpha m_{ij}^\alpha d\gamma^\alpha$; i.e. shear increment $d\gamma^\alpha$ on slip system α , resolved by the Schmid tensor \mathbf{m}^α and summed over all active slip systems. The Schmid tensor \mathbf{m}^α is given by the symmetric part of the dyadic product of the unit slip direction \mathbf{b}^α and unit slip plane normal, \mathbf{n}^α :

$$m_{ij}^\alpha = \frac{1}{2} (\mathbf{n}_i \mathbf{b}_j + \mathbf{n}_j \mathbf{b}_i) \quad (6-6)$$

The model allows only positive shear on a given slip system, the negative shear is accommodated by a positive shear on the opposite system (thus, the normal twelve octahedral slip systems within the FCC crystal are counted as 24 forward and backward slip systems). For a slip system to be potentially active it should satisfy the Schmid's law, i.e. the resolved shear stress $\tau^\alpha (= \mathbf{m}^\alpha : \boldsymbol{\sigma}^c)$ on the slip system α should equal the critical resolved shear stress (CRSS) τ_{cr}^α . Moreover, the system has to remain loaded, i.e. the stress has to remain on the yield surface throughout the straining step, while the yield surface evolves due to strain hardening (known as the consistency condition). For loading, these conditions are written as:

The Schmid criterion: $m_{ij}^\alpha \sigma_{ij}^c = \tau_{cr}^\alpha$ (6-7)

The consistency condition: $m_{ij}^\alpha d\sigma_{ij}^c = d\tau_{cr}^\alpha$ (6-8)

If the above two criteria are satisfied, then

$$d\gamma^\alpha > 0 \quad (6-9)$$

For a slip system that is unloading, the consistency condition is:

$$m_{ij}^\alpha d\sigma_{ij}^c < d\tau_{cr}^\alpha \text{ and } d\gamma^\alpha = 0 \quad (6-10)$$

The evolution of the CRSS, $d\tau_{cr}^\alpha$ is dependent on the shear rates of all active slip systems (henceforth Σ_β always means sum over active slip systems) and is given by the following equation (Hill, 1966):

$$d\tau_{cr}^\alpha = \Sigma_\beta V^\alpha(\Gamma) h^{\alpha\beta} d\gamma^\beta \quad (6-11)$$

where, $h^{\alpha\beta}$ is the latent hardening matrix which defines how much slip in system α hardens slip system β , $V^\alpha(\Gamma)$ is empirical Voce strain hardening rule which determines the evolution of the current threshold stress, starting from an initial threshold stress τ_0^α , as:

$$V^\alpha(\Gamma) = \frac{\partial \tau_v^\alpha}{\partial \Gamma} = \theta_0^\alpha \left(1 - \left(\frac{\tau^\alpha - \tau_0^\alpha}{\tau_1^\alpha} \right) \right) \quad (6-12)$$

$\Gamma = \Sigma_\alpha \gamma^\alpha$ is the total shear strain in a grain, τ_v^α is the current threshold strength of system α , $\tau_0^\alpha + \tau_1^\alpha$ is the saturation stress, and θ_0 is the initial strain rate. Thus, there are three fitting parameters per slip mode. Notably, Kocks and Mecking (2003) describe how this slip system level strain hardening rule can be related to dislocation theory.

In order to use the Eshelby formalism, the constitutive relation given in Eq. (6-5) has to be linearized according to:

$$d\sigma_{ij}^c = L_{ijkl}^c d\varepsilon_{kl}^c \quad (6-13)$$

where, L^c is the grain level incremental elastoplastic stiffness tensor. Prior to yielding, $L^c = C^c$ and after yielding, one may combine Eq. (6-5) with (6-12), obtaining:

$$L_{ijkl}^c = C_{ijkl}^c (I_{ijkl} - \sum_{\alpha} m_{ij}^{\alpha} G_{kl}^{\alpha}) \quad (6-14)$$

where, the tensor G^{α} , relates the slip increments in system α , $d\gamma^{\alpha}$, to the crystal strain increment, $d\varepsilon^c$:

$$d\gamma^{\alpha} = G_{ij}^{\alpha} d\varepsilon_{ij}^c \quad (6-15)$$

Substituting Eqs. (6-5) and (6-10) in the consistency condition, Eq. (6-8), one obtains:

$$m_{ij}^{\alpha} C_{ijmn}^c d\varepsilon_{mn}^c = \sum_{\beta} \left(m_{ij}^{\alpha} C_{ijmn}^c m_{mn}^{\beta} + V^{\alpha}(\Gamma) h^{\alpha\beta} \right) d\gamma^{\beta} \quad (6-16)$$

Denoting $\left(m_{ij}^{\alpha} C_{ijmn}^c m_{mn}^{\beta} + V^{\alpha}(\Gamma) h^{\alpha\beta} \right)$ as $X^{\alpha\beta}$ and comparing with Eq. (6-14) one obtains:

$$G_{mn}^{\alpha} = \sum_{\beta} (X^{-1})^{\alpha\beta} m_{ij}^{\beta} C_{ijmn}^c \quad (6-17)$$

6.3.2 Self-consistent formulation

At the aggregate level, the linearization of constitutive equation is similar to that of the grain level:

$$d\sigma_{ij} = L_{ijkl} d\varepsilon_{kl} \quad (6-18)$$

where, $d\sigma$ and $d\varepsilon$ are the incremental stresses and strains in the aggregate and L is the overall incremental elastoplastic stiffness tensor of the homogeneous effective medium (the aggregate), which is not known *a priori*. The equivalent inclusion method relates the total incremental strain in a grain to that in the aggregate by an interaction equation:

$$(d\sigma_{ij}^c - d\sigma_{ij}) = -\beta L_{ijkl}^* (d\varepsilon_{kl}^c - d\varepsilon_{kl}) \quad (6-19)$$

where L^* is called the interaction stiffness, and is given by:

$$L_{ijkl}^* = L_{ijmn}(S_{mnkl}^{-1} - I_{mnkl}) \quad (6-20)$$

where S is the elastoplastic Eshelby tensor, which takes into account the shape and orientation of the grain ellipsoid with respect to the aggregate reference frame and I is the fourth-rank identity tensor. β is a scalar parameter that is used to scale the interaction stiffness in order to adjust the strength of the interaction between the grains and the equivalent medium. For example, setting $\beta = 0$ implies infinitely compliant interaction with no stress deviations and thus would allow each grain to have the same stress increment as the aggregate, i.e. the lower bound estimate akin to Sachs (1928). On the other hand, $\beta = \infty$ results in an infinitely stiff interaction, which permits large variations in the stress increments of individual grains, while restricting any strain deviations, i.e. the upper bound estimate of Taylor-Lin theory (1957). Substituting the constitutive equations (6-13) and (6-18) into (6-19) a localization equation relating the strain increment in the grain to that in the aggregate can be written as:

$$d\varepsilon_{ij}^c = A_{ijkl}^c d\varepsilon_{kl} \quad (6-21)$$

where, the strain concentration tensor A^c is given by:

$$A_{ijmn}^c = (L_{ijkl}^c + L_{ijkl}^*)^{-1} (L_{klmn} + L_{klmn}^*) \quad (6-22)$$

The localization equation gives the strain increment in each grain, for given medium stiffness L and imposed strain rate. However, since L is not known *a priori* and is dependent on the responses of the individual grains, a self-consistent iterative method is used to obtain it. The condition of self-consistency enforces that the volume weighted averages (denoted as ' $\langle \rangle$ ') of the stress and strain increments of all the constituent grains equals the magnitudes of that of the aggregate:

$$d\varepsilon = \langle d\varepsilon^c \rangle \quad (6-23)$$

$$d\sigma = \langle d\sigma^c \rangle \quad (6-24)$$

From Eq. (6-18), (6-21) and (6-23) a self-consistent expression for the elastoplastic stiffness can be obtained as (Hutchinson, 1970):

$$L_{ijkl} = \langle L_{ijmn}^c A_{mnkl}^c \rangle \quad (6-25)$$

6.4 Grain with elastic particles

Conceptually, the presence of elastic particles embedded in the matrix can affect the behavior in two ways; first, the particles will share a part of the applied stress and thus, reduce the amount of stress in the matrix. So, the matrix will flow at a larger applied stress than it would in the absence of the particles. This load sharing effect has been used extensively by the composite community in order to model the behavior of two phase composites (for instance, Withers et al., 1989; Corbin and Wilkinson, 1994).

The next effect is more subtle; since the matrix and the particles do not deform by the same amount, a gradient of strain develops around the particles. This incompatibility between the elastically deforming particle and the plastically deforming matrix, gives rise to the presence of geometrically necessary dislocations (GNDs) (Ashby, 1970). This additional storage of Orowan loops around non-shearable precipitates and its effect on strain hardening has been addressed using a Kocks- Mecking type formulation as proposed by Estrin (1996) and later used by others; (Cheng et al., 2003; Simar et al., 2007; Fribourg et al., 2011). However the analytical approach has one major disadvantage; it treats the isotropic and kinematic hardening behavior in an uncoupled way. Although all these models can capture the flow curve along a particular loading direction, it would be not possible to capture the complete strength and strain anisotropy evolution for a given material, using such a model. Nevertheless, these analytical models do

provide useful insight, which can be incorporated in crystal plasticity based models. In the following subsections, a constitutive model for a composite grain containing elastic particles, based on the formulation by Schmitt et al., (1997) and Bonfoh et al., (2003) is described and modified in order to render it more numerically stable. Subsequently, a modification of the formulation to take into account the effect of saturation of backstress due to relaxation is presented similar to that suggested by Barlat et al., (Barlat and Liu, 1998a; Choi et al., 2000) is presented.

6.4.1 The heterogeneous grain

Let us assume that the volume fraction of the particles (e.g., precipitates) is f , then, the total strain increment in a grain $d\boldsymbol{\varepsilon}^c$ is partitioned between the matrix (elastoplastic) and the precipitate (elastic) according to a simple rule of mixtures:

$$d\boldsymbol{\varepsilon}_{ij}^c = f d\boldsymbol{\varepsilon}_{ij}^{ppt} + (1 - f) d\boldsymbol{\varepsilon}_{ij}^m = f d\boldsymbol{\varepsilon}_{ij}^{ppt} + (1 - f) d\boldsymbol{\varepsilon}_{ij}^{m,el} + d\boldsymbol{\varepsilon}_{ij}^{m,pl} \quad (6-26)$$

Introducing Hooke's law yields:

$$d\boldsymbol{\varepsilon}_{ij}^c = f \mathbf{C}_{ijkl}^{ppt}{}^{-1} d\boldsymbol{\sigma}_{kl}^{ppt} + (1 - f) \mathbf{C}_{ijkl}^m{}^{-1} d\boldsymbol{\sigma}_{kl}^m + (1 - f) d\boldsymbol{\varepsilon}_{ij}^{m,pl} \quad (6-27)$$

where, $d\boldsymbol{\varepsilon}^{ppt}$, $d\boldsymbol{\sigma}^{ppt}$ and \mathbf{C}^{ppt} are the incremental total (elastic only) strain, stress and elastic stiffness of the particle, respectively, and $d\boldsymbol{\varepsilon}^m$, $d\boldsymbol{\varepsilon}^{m,el}$, $d\boldsymbol{\varepsilon}^{m,pl}$, $d\boldsymbol{\sigma}^m$ and \mathbf{C}^m are the incremental total, elastic and plastic strain, stress and elastic stiffness of the matrix respectively.

The plastic strain increment in the matrix is given by the usual form: (see Eq. 6-5)

$$d\boldsymbol{\varepsilon}_{ij}^{m,pl} = \sum_{\alpha} m_{ij}^{\alpha} d\gamma^{\alpha} \quad (6-28)$$

Since the particle is elastic, the total plastic strain increment of the heterogeneous grain is only due to that in the matrix:

$$d\varepsilon_{ij}^{c,pl} = (1 - f) \sum_{\alpha} m_{ij}^{\alpha} d\gamma^{\alpha} = \sum_{\alpha} m_{ij}^{\alpha} d\gamma^{\alpha,c} \text{ where, } d\gamma^{\alpha,c} = (1 - f)d\gamma^{\alpha} \quad (6-29)$$

The total stress increment in the heterogeneous grain $d\sigma^c$ can be written in a similar manner using the rule of mixtures:

$$d\sigma_{ij}^c = f d\sigma_{ij}^{ppt} + (1 - f) d\sigma_{ij}^m \quad (6-30)$$

from which the matrix stress can be obtained as:

$$d\sigma_{ij}^m = \frac{d\sigma_{ij}^c - f d\sigma_{ij}^{ppt}}{1 - f} \quad (6-31)$$

6.4.2 Yield criteria for the heterogeneous grain

A slip system within the matrix of the equivalent grain is potentially active once the resolved shear stress $\tau^{\alpha,m}$ is equal to the CRSS of that system. That is:

$$\tau^{\alpha,m} = m_{ij}^{\alpha} \sigma_{ij}^m = \tau_{CRSS,m}^{\alpha} \quad (6-32)$$

where, $\tau_{CRSS,m}^{\alpha}$ is the critical resolved shear stress of the matrix. Substituting Eq. (6-31) into (6-32) gives:

$$m_{ij}^{\alpha} (\sigma_{ij}^c - f \sigma_{ij}^{ppt}) = (1 - f) \tau_{CRSS,m}^{\alpha} = \tau_{CRSS,c}^{\alpha} \quad (6-33)$$

where $\tau_{CRSS,c}^{\alpha}$ is now the CRSS of the heterogeneous grain.

Comparing with the single crystal case, Eq. (6-8), the yield function for the heterogeneous grain now includes a ‘backstress’, $f\sigma^{ppt}$, which provides kinematic hardening along with the regular hardening term, which in itself can be anisotropic, if different $\tau_{CRSS,c}^{\alpha}$ for different slip systems is considered, (through the latent hardening matrix).

Next, if one recalls the consistency condition, i.e., the stress must remain on the yield surface throughout the straining step, one obtains:

$$m_{ij}^s d\sigma_{ij}^m = d\tau_{CRSS,m}^s \quad (6-34)$$

where,

$$d\tau_{CRSS,m}^s = \sum_{\beta} V^{\alpha}(\Gamma) h^{\alpha\beta} d\gamma^{\beta} \quad (6-35)$$

As mentioned earlier, the particles induce strain incompatibilities which evolve with straining. In order to take account of that Bonfoh et al., (2003) proposed that the stress increment in the equivalent grain differs from that in the matrix. The matrix stress increment can be expressed as (Schmitt et al., 1997; Bonfoh et al., 2003):

$$d\sigma_{ij}^m = d\sigma_{ij}^c + P_{ijkl}^c d\epsilon_{kl}^m \quad (6-36)$$

where, \mathbf{P}^c is a polarization tensor, and $\mathbf{P}^c: \mathbf{d}\boldsymbol{\epsilon}^m$ describes the stress increments due to the strain incompatibility. Using Eq. (6-34-6-36) the consistency condition becomes:

$$m_{ij}^{\alpha} (d\sigma_{ij}^c + P_{ijkl}^c d\epsilon_{kl}^m) = d\tau_{CRSS,m}^s \quad (6-37)$$

$$m_{ij}^{\alpha} [d\sigma_{ij}^c + P_{ijkl}^c (d\epsilon_{kl}^{m,el} + d\epsilon_{kl}^{m,pl})] = d\tau_{CRSS,m}^s \quad (6-38)$$

$$m_{ij}^{\alpha} [d\sigma_{ij}^c + P_{ijkl}^c (C_{ijkl}^m)^{-1} d\sigma_{kl}^m + \sum_{\alpha} m_{ij}^{\alpha} d\gamma^{\alpha}] = \sum_{\beta} V^{\alpha}(\Gamma) h^{\alpha\beta} d\gamma^{\beta} \quad (6-39)$$

To this end, it can be assumed (Schmitt et al., 1997; Bonfoh et al., 2003; Qu and Cherkaoui, 2006) that there are stress concentration tensors, \mathbf{B} , which relate the stress increment of the precipitate and the matrix to the stress increment in the grain, i.e.

$$d\sigma_{ij}^{ppt} = B_{ijkl}^{ppt} d\sigma_{kl}^c \text{ and } d\sigma_{ij}^m = B_{ijkl}^m d\sigma_{kl}^c \quad (6-40)$$

and strain concentration tensors, \mathbf{T} , that relate the strain increment of the precipitate and the matrix to the strain increment in the grain.

$$d\epsilon_{ij}^{ppt} = T_{ijkl}^{ppt} d\epsilon_{kl}^c \text{ and } d\epsilon_{ij}^m = T_{ijkl}^m d\epsilon_{kl}^c \quad (6-41)$$

The strain concentration tensor for the particle, \mathbf{T}^{ppt} can be derived as (Bonfoh et al., (2003):

$$T_{ijop}^{ppt} = (I_{ijop} + S_{ijkl}^{ppt} L_{klmn}^c)^{-1} (C_{mnop}^{ppt} - L_{mnop}^c) \quad (6-42)$$

using a self-consistent approximation for the behavior of the precipitate containing grain itself.

In this equation, \mathbf{S}^{ppt} is the Eshelby tensor for the particle which depends on the particles shape

(e.g. disc, rod, sphere) and the orientation of the particle with respect to the grains crystallographic coordinates (can be used to specify orientation relationships).

Once the expression for stress and strain concentration tensors are known, it is relatively straightforward to relate the two using the constitutive relations for the particle and grain as:

$$B_{ijop}^{ppt} = C_{ijuv}^{ppt} T_{uvmn}^{ppt} (L_{mnop}^c)^{-1} \quad (6-43)$$

Using Eq. (6-30), the relationship between B_{ijkl}^m and B_{ijkl}^{ppt} can be obtained as:

$$I_{ijkl} = f B_{ijkl}^{ppt} + (1 - f) B_{ijkl}^m \quad (6-44)$$

or,

$$B_{ijkl}^m = (I_{ijkl} - f B_{ijkl}^{ppt}) / (1 - f) \quad (6-45)$$

Note the similarity between Eq. (6-45) and Eq. (6-31).

Thus, the consistency condition, Eq. (6-39) becomes,

$$m_{pq}^\alpha \left[d\sigma_{pq}^c + P_{pqmn}^c \left(C_{mni}^m \right)^{-1} \frac{(I_{ijkl} - f B_{ijkl}^{ppt})}{(1-f)} d\sigma_{kl}^c + \sum_\alpha m_{mn}^\alpha d\gamma^\alpha \right] = \sum_\beta V^\alpha(\Gamma) h^{\alpha\beta} d\gamma^\beta \quad (6-46)$$

Using Eq. (6-29) and rearranging, one obtains:

$$m_{ij}^\alpha [(1 - f) I_{ijuv} + P_{ijkl}^c C_{klmn}^m]^{-1} (I_{mnuv} - f B_{mnuv}^{ppt}) d\sigma_{uv}^\alpha = \sum_\beta (V^\alpha(\Gamma) h^{\alpha\beta} - m_{ij}^\alpha P_{ijkl}^c m_{kl}^\alpha) d\gamma^{\beta,c} \quad (6-47)$$

The hardening behavior of each slip system is now a function of both the Voce hardening term (including latent hardening effects) and is modified by the polarizing (kinematic) effect of the precipitates.

$$H^{\alpha\beta} = V^\alpha(\Gamma) h^{\alpha\beta} - m_{ij}^\alpha P_{ijkl}^c m_{kl}^\beta \quad (6-48)$$

and

$$d\tau_{CRSS,c}^{\alpha} = \sum_{\beta} H^{\alpha\beta} d\gamma^{\beta,c} \quad (6-49)$$

One can define another fourth rank tensor, \mathbf{U} , which describes the effects of the precipitate stress state the strain incompatibility through and \mathbf{B}^{ppt} and \mathbf{P}^c , respectively:

$$U_{ijuv} = (1 - f)I_{ijuv} + P_{ijkl}^c C_{klmn}^m{}^{-1} (I_{mnuv} - fB_{mnuv}^{ppt}) \quad (6-50)$$

The final expression for the consistency condition of the heterogeneous grain is:

$$m_{ij}^s U_{ijuv} d\sigma_{uv}^c = d\tau_{CRSS,c}^s \quad (6-51)$$

which replaces Eq. (6-8) the single phase, single crystal case. It is worth noting that the hardening matrix, $H^{\alpha\beta}$, appearing in the modified consistency condition contains a contribution from the strain incompatibility between the particles and the matrix, in the form of the tensor \mathbf{P} and the tensor \mathbf{U} includes the influence of the evolution of the particle stress σ^{ppt} , through the stress concentration tensor.

6.4.3 Constitutive relation of the equivalent grain

Assuming the stiffness of the precipitate and the matrix are equal i.e. $\mathbf{C}^{ppt} = \mathbf{C}^m = \mathbf{C}^c$, then using Eq.(6-27) and (6-28) the total strain in the grain simplifies to:

$$d\varepsilon_{ij}^c = C_{ijkl}^c{}^{-1} d\sigma_{kl}^c + (1 - f) d\varepsilon_{kl}^{m,pl} \quad (6-52)$$

$$\text{or, } d\varepsilon_{ij}^c = C_{ijkl}^c{}^{-1} d\sigma_{kl}^c + (1 - f) \sum_{\alpha} m_{kl}^{\alpha} d\gamma^{\alpha} \quad (6-53)$$

Therefore,

$$C_{ijkl}^c{}^{-1} d\sigma_{kl}^c = d\varepsilon_{ij}^c - (1 - f) \sum_{\alpha} m_{ij}^{\alpha} d\gamma^{\alpha} \quad (6-54)$$

Thus, the constitutive relation, for the heterogeneous grain becomes:

$$d\sigma_{ij}^c = C_{ijkl}^c : [d\varepsilon_{kl}^c - \sum_{\alpha} m_{kl}^{\alpha} d\gamma^{\alpha,c}] = C_{ijkl}^c : (d\varepsilon_{kl}^c - d\varepsilon_{kl}^{c,pl}) \quad (6-55)$$

which again has to be linearized in the usual way:

$$d\sigma_{ij}^c = L_{ijkl}^c : d\varepsilon_{kl}^c \quad (6-56)$$

where, \mathbf{L}^c is now the instantaneous elasto-plastic stiffness tensor of the equivalent grain c . In what follows next, the expression for \mathbf{L}^c is derived.

Using Eq. (6-53) and Eq. (6-55), \mathbf{L}^c can be obtained as:

$$L_{mnkl}^c = C_{mni j}^c (I_{ijkl} - \sum_{\alpha} m_{ij}^{\alpha} Q_{kl}^{\alpha}) \quad (6-57)$$

$$\text{where, } d\gamma^{\alpha,c} = Q_{ij}^{\alpha} d\varepsilon_{ij}^{\alpha} \quad (6-58)$$

Comparing with Eq. (6-17), it can be seen that the tensor \mathbf{Q}^{α} is the heterogeneous grain counterpart of tensor \mathbf{G}^{α} of the single crystal case. This tensor obtains the shear increments of the equivalent grain in terms of the imposed strain increments. As before, by substituting the Hooke's law Eq. (6-54) in the consistency condition Eq. (6-49) one obtains,

$$m_{ij}^{\alpha} U_{ijuv} C_{uvmn}^c [d\varepsilon_{mn}^c - \sum_{\alpha} m_{mn}^{\alpha} d\gamma^{\alpha,c}] = \sum_{\beta} H^{\alpha\beta} d\gamma^{\beta,c} \quad (6-59)$$

Which upon rearranging and simplifying

$$m_{ij}^{\alpha} U_{ijuv} C_{uvmn}^c d\varepsilon_{mn}^c - m_{ij}^{\alpha} U_{ijuv} C_{uvmn}^c \sum_{\alpha} m_{mn}^{\alpha} d\gamma^{\alpha,c} = \sum_{\beta} H^{\alpha\beta} d\gamma^{\beta,c} \quad (6-60)$$

$$m_{ij}^{\alpha} U_{ijuv} C_{uvmn}^c d\varepsilon_{mn}^c = \sum_{\beta} \left(m_{ij}^{\alpha} U_{ijuv} C_{uvmn}^c m_{mn}^{\beta} + H^{\alpha\beta} \right) d\gamma^{\beta,c} \quad (6-61)$$

$$\text{Denoting } X^{\alpha\beta} = \left(m_{ij}^{\alpha} U_{ijuv} C_{uvmn}^c m_{mn}^{\beta} + H^{\alpha\beta} \right) \quad (6-62)$$

$$m_{ij}^{\alpha} U_{ijuv} C_{uvmn}^c d\varepsilon_{mn}^c = \sum_{\beta} X^{\alpha\beta} d\gamma^{\beta,c} \quad (6-63)$$

$$d\gamma^{\beta,c} = \sum_{\alpha} (X^{-1})^{\alpha\beta} m_{ij}^{\beta} U_{ijuv} C_{uvmn}^c d\varepsilon_{mn}^c \quad (6-64)$$

Comparing Eq. (6-58) and Eq. (6-64),

$$Q_{mn}^{\alpha} = \sum_{\beta} (X^{-1})^{\alpha\beta} m_{ij}^{\beta} U_{ijuv} C_{uvmn}^c \quad (6-65)$$

Finally the heterogeneous grain elastoplastic stiffness becomes:

$$L_{ijmn}^c = C_{ijpq}^c \left(I_{pqmn} - \sum_{\alpha} m_{pq}^{\alpha} \sum_{\beta} (X^{-1})^{\alpha\beta} m_{pq}^{\beta} U_{pq\alpha\beta} C_{uvmn}^c \right) \quad (6-66)$$

The derivation for the tensor \mathbf{P}^c has been discussed in detail by Bonfoh et al., (2003). In short, using the expression for the stress concentration tensor Eq. (6-40), and subtracting $d\boldsymbol{\sigma}^m$ from both sides, one obtains

$$d\sigma_{kl}^m = d\sigma_{ij}^c + \left(I_{ijkl} - (B_{ijkl}^m)^{-1} \right) L_{klmn}^m d\varepsilon_{mn}^m \quad (6-67)$$

which on comparing with Eq.(6-36), yields the expression for \mathbf{P}^c as:

$$P_{ijmn}^c = \left(I_{ijkl} - (B_{ijkl}^m)^{-1} \right) L_{klmn}^m \quad (6-68)$$

To eliminate the terms containing matrix properties, using Eq. (6-26) and Eq. (6-40) one obtains:

$$(L_{ijkl}^c)^{-1} d\sigma_{kl}^c = f (C_{ijkl}^{ppt})^{-1} d\sigma_{kl}^{ppt} + (1 - f) (L_{ijkl}^m)^{-1} d\sigma_{kl}^m \quad (6-69)$$

which on rearranging and substitution into Eq. (6-68) gives P^c as;

$$P_{ijop}^c = f (I_{ijuv} - B_{ijuv}^{ppt}) \left((L_{uvop}^c)^{-1} - f (C_{uvmn}^{ppt})^{-1} B_{mnop}^{ppt} \right)^{-1} \quad (6-70)$$

Up until now, the equations presented are derived from rigorous micromechanical formulation as presented originally by Schmitt et al., (1997) and later expanded by Bonfoh et al., (2003). In the next section, some modifications of the relevant equations are presented, first in order to overcome some numerical difficulties and secondly, to capture the physics associated with the experimental data presented in the first part of the series.

6.5 Modifications

The equations that have been presented in the previous section require the use of the compliance of the equivalent heterogeneous grain $(\mathbf{L}^{c^{-1}})$. Now, the elastoplastic stiffness associated with the grain decreases with strain, as evident from the experimental data, especially for the aged specimens, where even the polycrystal response is almost perfectly plastic. The reduction in the stiffness value is drastic; starting from the elastic stiffness of ~ 70 GPa it reduces

to less than 100 MPa, i.e., by almost 3 orders of magnitude. This makes the stiffness matrix very *ill-conditioned* and virtually impossible to invert without introducing large numerical errors. In what follows next, the relevant equations were reformulated to eliminate the need to invert the grain stiffness as $(\mathbf{L}^c)^{-1}$ to get around this problem.

6.5.1 Eliminating the grain compliance

Starting from the relationship between the stress and strain concentration tensors:

$$B_{ijop}^{ppt} = C_{ijuv}^{ppt} T_{uvmn}^{ppt} (L_{mnop}^c)^{-1} \quad (6-71)$$

and substituting in the expression for \mathbf{P}^c , Eq.(6-70) and simplifying one obtains:

$$P_{ijop}^c = f \left(I_{ijop} - C_{ijuv}^{ppt} T_{uvmn}^{ppt} (L_{mnop}^c)^{-1} \right) \left((L_{qruv}^c)^{-1} (I_{uvop} - f T_{uvop}^{ppt}) \right)^{-1} \quad (6-72)$$

Using standard rules of matrix inversion, and commutative properties of double contraction:

$$P_{ijop}^c = f (L_{ijop}^c - C_{ijuv}^{ppt} T_{uvmn}^{ppt}) (I_{mnop} - f T_{mnop}^{ppt})^{-1} \quad (6-73)$$

Similarly, substituting Eq. (6-71) and Eq. (6-42) in the expression for U reduces to:

$$U_{abrs} = (1 - f) I_{abrs} + P_{abef}^c (C_{efgh}^c)^{-1} \left(I_{ghrs} - f C_{ghij}^{ppt} \left(I_{ijop} + S_{ijkl}^{ppt} L_{klmn}^c \right)^{-1} (C_{mnop}^{ppt} - L_{mnop}^c) \right)^{-1} (L_{oprs}^c)^{-1} \quad (6-74)$$

From which $(\mathbf{L}^c)^{-1}$ can be eliminated to give:

$$U_{xyop} = (1 - f) I_{xyop} + P_{xyab}^c (C_{abuv}^c)^{-1} \left(I_{uvop} - f C_{uvij}^{ppt} \left(L_{ijop}^c + S_{ijmn}^{ppt} (C_{mnop}^{ppt} - L_{mnop}^c) \right)^{-1} \right) \quad (6-75)$$

Finally the expression for the strain concentration tensor \mathbf{T}^{ppt} can be expressed in a more symmetric form:

$$T_{ijop}^{ppt} = (I_{ijop} + S_{ijkl}^{ppt} L_{klmn}^c{}^{-1} C_{mnop}^{ppt} - S_{ijop}^{ppt})^{-1} \quad (6-76)$$

$$T_{pqmn}^{ppt} = \left(S_{pqkl}^{ppt} L_{klij}^c{}^{-1} \left(C_{ijmn}^{ppt} + L_{ijkl}^c S_{klmn}^{ppt}{}^{-1} - L_{ijmn}^c \right) \right)^{-1} \quad (6-77)$$

$$T_{pqmn}^{ppt} = \left(C_{mnop}^{ppt} + L_{ijkl}^c S_{klmn}^{ppt}{}^{-1} - L_{ijkl}^c \right)^{-1} \left(L_{ijkl}^c - L_{ijkl}^c S_{klmn}^{ppt}{}^{-1} + L_{ijkl}^c \right) \quad (6-78)$$

$$T_{pqmn}^{ppt} = \left(C_{ijmn}^{ppt} + L_{ijkl}^c \left(S_{klmn}^{ppt}{}^{-1} - I_{klmn} \right) \right)^{-1} \left(L_{mnop}^c + L_{ijkl}^c \left(S_{klmn}^{ppt}{}^{-1} - I_{klmn} \right) \right) \quad (6-79)$$

Denoting

$$L_{ijkl}^c \left(S_{klmn}^{ppt}{}^{-1} - I_{klmn} \right) = L_{ijmn}^{*ppt} \quad (6-80)$$

the strain concentration tensor can be written in a similar form as Eq.(6-20) and (6-22):

$$T_{ijkl}^{ppt} = \left(C_{ijop}^{ppt} + L_{ijop}^{*ppt} \right)^{-1} \left(L_{opkl}^c + L_{opkl}^{*ppt} \right) \quad (6-81)$$

6.5.2 Incorporating relaxation effects

The polarization tensor \mathbf{P} derived earlier takes into account the strain mismatch that is generated between the elastic particle and the elastoplastic matrix. Now, the evolution of \mathbf{P} with straining is governed by the instantaneous elastoplastic stiffness of the grain, as well as the strain concentration tensor \mathbf{T}^{ppt} . Physically, this takes into account the effect of dynamic recovery that determines the net accumulation of dislocations, and hence the strain hardening rate, (in the form of the Voce hardening law). However, in the presence of the particles, there is an additional recovery which takes place which has been observed experimentally (e.g., Brown and Stobbs, 1971; Atkinson et al., 1974), and the present formulation does not account for this. Thus, the final modification that has to be incorporated is the relaxation of the strain/stress concentration due to these physical phenomena.

The experiments (Wilson, 1965; Moan and Embury, 1979; Bate et al., 1982) and even the results presented in this thesis (previous chapter) show that the effect of this particle induced

internal stress is prominent only for up to a few percent strains, after which it saturates. The generally accepted physical explanation is that there is a maximum number of dislocation loops that can accumulate around a particle, which is proportional to size of the particle (Ashby, 1970). Before this critical number of loops is achieved, the stress due to the pile up increases and once the limit is reached, several things can happen; the particle can shear, the particle-matrix interface can de-bond or the stress concentration can activate secondary slip systems or produce prismatic loops, all of which relaxes the stress that developed due to the pile up (Brown and Stobbs, 1971, 1976; Brown and Clarke, 1975) . Barlat and Liu, (1998b) and Choi et al., (2000) have applied a simple exponential decay function to the backstress in their continuum model, to capture the effect of such relaxation mechanisms. Interestingly, Proudhon et al., (2008) derived an analytical model for the evolution of the unrelaxed plastic strain with applied strain, and came up with an exponential relationship. Thus, an exponential decay term is, for simplicity, assumed to be a function of the equivalent strain of the heterogeneous grain and the saturation strain, is multiplied to the strain concentration tensor derived earlier as:

$$T_{ijkl}^{ppt} = (C_{ijop}^{ppt} + L_{ijop}^*)^{-1} (L_{opkl}^c + L_{opkl}^*) \exp\left(-\frac{\varepsilon_{VM}^{c,p}}{\varepsilon_{sat}}\right) \quad (6-82)$$

where, $\varepsilon_{VM}^{c,p}$ is the Von-Mises equivalent *plastic* strain in the heterogeneous grain *c*, and ε_{sat} is the saturation stress value which can, in principle, be obtained from Bauschinger tests. This way, although the relaxation behavior is accounted for empirically, there are no arbitrary fitting parameters involved in the model, each has a specific physical meaning.

The saturation strain value can be obtained from a plot of backstress as a function of plastic prestrain, as suggested by Moan and Embury, (1979). This plot was calculated for different offset compressive yield strengths and was presented in the experimental paper (chapter 5). Although this data is for T711, a similar trend can be assumed to hold for the T721, both being in

the overaged state. According to this data, the backstress obtained from different offset values, tend to exhibit saturation around 2% strain. Definitely more data points are required to obtain an exact estimate, but the goal here is to investigate the effects of incorporating relaxation, not to exactly model the experimental data.

6.6 Simulation methodology

The individual textures presented earlier for T711, W51 and T721 have been discretized in to 2000 grains and have been used in the simulations, in order to account for any effect of the texture. In order to simulate the 45° orientation specimens, the textures have been rotated by 45° about ND and used. The particles were assumed to be spheres; with cube-on-cube (100 II 100) orientation relationship, with respect to the crystal coordinate system of the surrounding grain. It is worth mentioning that 7000 series alloys contain precipitates (η' and η) which are typically plate shaped as well as spherical Al_3Zr dispersoids (Park and Ardell, 1983; Srivatsan et al., 1997). Even though the formulation is completely general, and can treat any arbitrarily shaped ellipsoid on any given habit plane, however, accounting for the different variants is non-trivial, especially for a commercial alloy where different shaped precipitates/dispersoids with different orientation relationships are present. Furthermore, it is computationally expensive since the Eshelby tensor \mathbf{S}^{ppt} as well as the strain concentration relations have to be calculated for each variant and averaged in an appropriate manner. The aim here is to demonstrate the effect of these precipitates, and not to quantitatively model the particular material in question. For this same reason, an arbitrary but plausible (Deschamps et al., 2001; Dumont et al., 2004) elastic precipitate volume fraction of 0.05 is chosen for the simulations. Note that the main strengthening effects of shearable and non-shearable precipitates are already accounted for by the level of the critical resolved shear stress for dislocation motion. (Recall the analysis of the

strengthening impact of precipitates on the strength of slip systems within Mg alloy, WE43-T5, presented in chapter 3.)

The simulation of uniaxial compression has been described elsewhere (Bhattacharyya et al., 2016). In short, straining increments of 1×10^{-4} were imposed parallel to the loading direction while the shear strains and the normal stresses along the two directions perpendicular to the loading direction were set to zero. All other components of stresses and strains were unknown. These boundary conditions allowed the development of normal lateral strains which was used to compute the r -value. Since the effect of the backstress is only dominant up to first few percent strains, all the simulations were restricted to less than 10% strain. Moreover, since the formulation is based on small strain assumptions, texture evolution was not considered in any of the cases, including the simulations carried out using original EPSC, so that a direct comparison can be made. The effect of texture evolution during large strain deformation was already considered using VPSC modeling in chapter 4. At the risk of redundancy, this chapter is concerned with exploring the possibility that discrepancies in the VPSC predictions were due to neglect of precipitate-induced backstresses on the anisotropy.

For the Bauschinger tests, the forward tension curve was fitted to obtain the Voce parameters, and then simulations were carried out with the same parameters for different prestrain levels after which the material was unloaded to zero macroscopic stress and subsequently loaded in compression up to 3.5% strain. No attempt was made to fit the hardening behavior upon reload, since it is well known that not all of the operative physical mechanisms are accounted for in this present model. In order to capture such details, the dislocation based intragranular backstresses have to be taken into consideration (e.g., Wollmershauser et al., 2012; Zecevic and Knezevic, 2015), in addition to the coarser effects considered here. Furthermore, as

mentioned in chapter 5, the data at strain levels larger than 2% compressive strain are considered untrustworthy since some buckling was observed during the tests. Thus, the sole purpose of fitting the Bauschinger tests data was to see the effect of the intergranular backstresses that are inherently present in the model.

6.7 Results

In the following sections the performance of the model is investigated and compared to the original EPSC model, where precipitate induced effects are not considered. First, comparison of the EPSC model with the Bauschinger data of the T3 samples is presented. Next, the original EPSC model is used to investigate the flow behavior and anisotropy of the W51 material (which had undergone significant natural aging). Next, the simulation results for the T721 material are presented using both the original and modified EPSC model. For the modified model, two sets of results are presented, one with the relaxation effects and another without considering the relaxation effects.

6.7.1 Modeling Bauschinger effect

As shown in Eq. (6-19), the interaction strength between the grains and the medium can be modified by changing the β parameter. Initially, the β parameter was set to 1 and simulations were carried out to fit the Bauschinger test data for the T3 material. A linear hardening rule was found adequate to fit the data. The results (Figure 6.1) show that the model overestimates the Bauschinger effect, i.e. it model predicts a lower yield strength than observed experimentally. This can be explained as follows. When a stiff interaction is considered, the stress rate deviations allowed are larger, and hence, larger intergranular residual stresses are developed after unloading which leads to premature yielding in reverse loading.

A more compliant interaction, on the other hand, reduces the stress deviations and the grains develop similar stress states as the macroscopic aggregate, thus reducing the intergranular residual stress levels. It has generally been observed that the level of intergranular residual stresses in aluminum alloys are small (Pang et al., 1998; Dawson et al., 2001). Hence, the T3 Bauschinger test data was modeled using the lowest level of $\beta = 0.5$ for which EPSC remains numerically stable, as shown in Figure 6.2. It is admitted that internal strain data, typically obtained using *in-situ* diffraction, would be needed to verify this assumption. Nevertheless, the improved level of agreement between the model and experiment, especially at low prestrain levels, is encouraging. All subsequent simulations were carried out using this value of β .

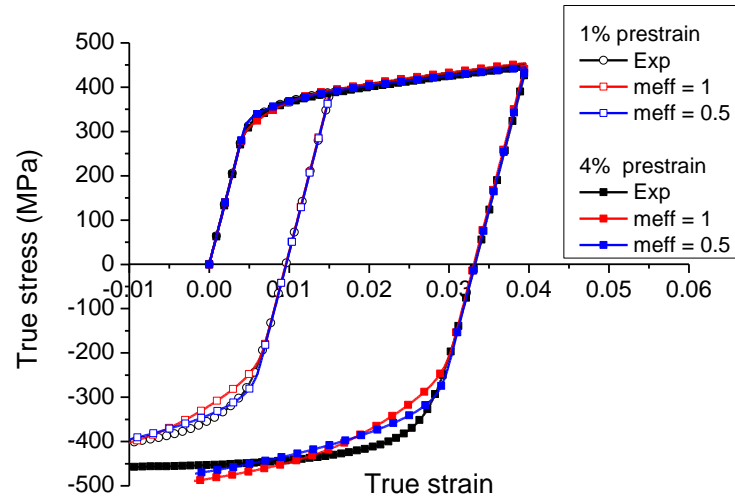


Figure 6.1: Experimental and simulated tension-compression curves for the T3 material, after 1.5% and 3.5% prestrains, showing the effect of β parameter.

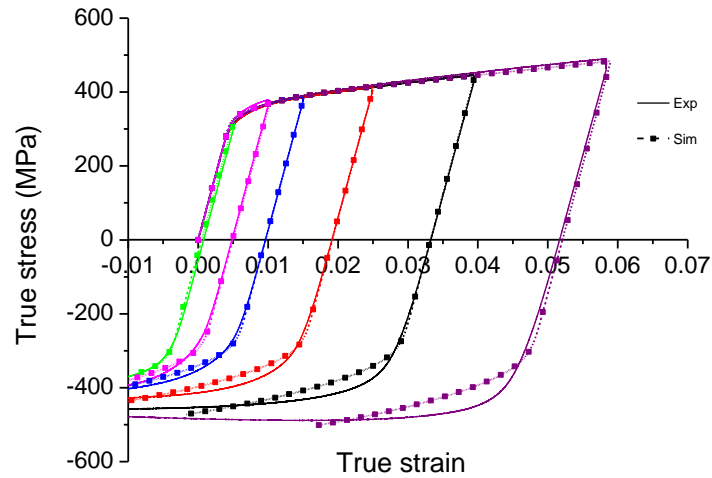


Figure 6.2: Experimental tension-compression curves for the T3 material after different prestrains, along with simulations, carried out using $\beta = 0.5$.

6.7.2 Modeling W51

In order to evaluate the capabilities of the EPSC model, for a case where the volume fraction of non-shearable precipitates should be minimal, though shearable precipitates are undeniably present, the W51 material was chosen. The TD flow curves were used to fit the Voce

parameters, and then the same parameter set is used to predict the flow curves and r-values of the RD, ND and 45 directions (Figure 6.3 and 6.4). The results show that the model is able to successfully predict the yield as well as the strain hardening behavior along RD, while for the 45 direction, although it captures the yield, it underestimates the hardening behavior, resulting in a slightly lower flow stress overall. In case of ND (Figure 6.4), the model under-predicts the yield strength as well as fails to capture the rapid strain hardening, resulting in an underestimation of the flow stress by ~ 50 MPa. Problems with modeling the ND have abounded in this study of AA 7085, and through thickness variations in the texture are one likely culprit.

As far as the strain anisotropy is concerned (Figures 6.5 and 6.6), the model does capture the ND r-values quite well (~ 0.6 both), does a relatively good job for the RD (~ 0.35 exp. vs 0.2 simulated) and the 45 direction (~ 1.6 exp. vs 1.8 simulated) However, it underestimates the anisotropy along the TD, where it predicts r-values of 1. With this as a benchmark, the model's performance for when precipitates effects are present will be tested next.

Table 6.1: Voce hardening parameters for $\{111\}\langle 110 \rangle$ slip mode for T3, W51 and T721 simulations.

	τ_0	τ_1	θ_0
T3 Bauschinger test - $\beta = 1$	130	-	200
T3 Bauschinger test - $\beta = 0.5$	144	-	320
W51 - TD			
No particles (original EPSC)	195	80	250
T721 - TD			
No particles (original EPSC)	172	60	250
0.05 vol. fraction, no saturation	161	5	61
0.05 vol. fraction, saturation at 2% strain	161	50	170

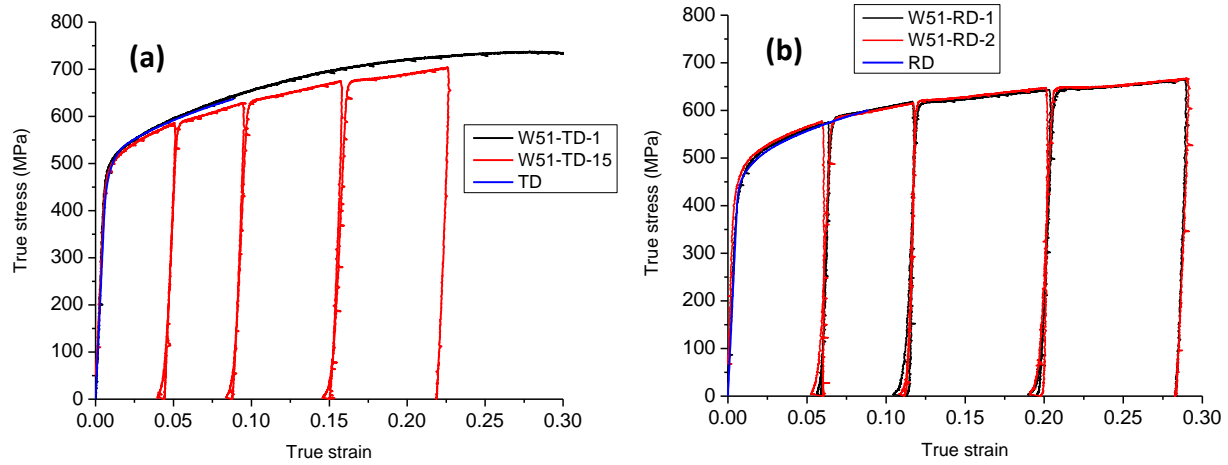


Figure 6.3: Experimental and simulated flow curves for W51 a) (fitted) along TD b) predicted along RD

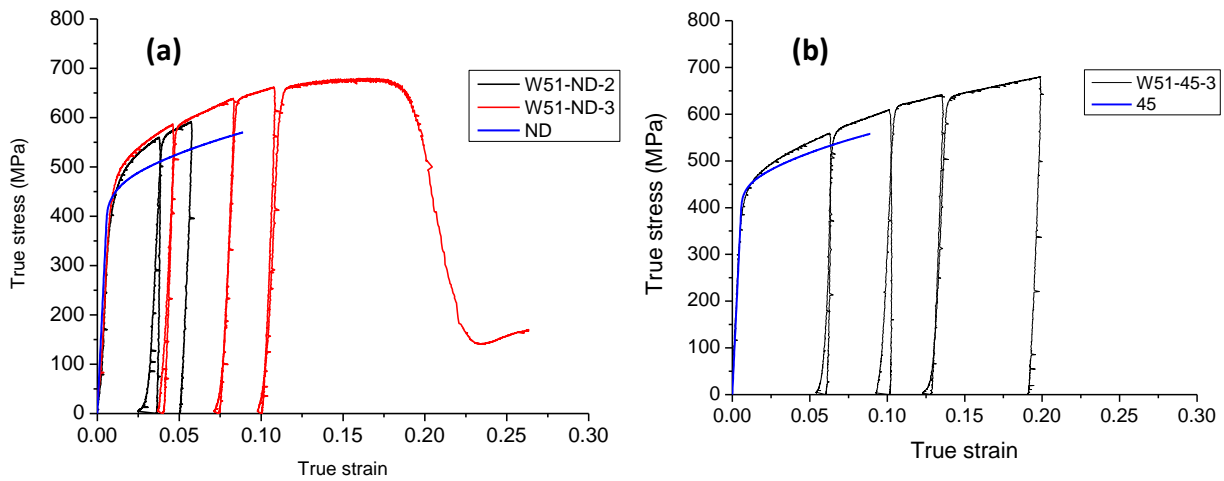


Figure 6.4: Experimental and predicted flow curves for W51 a) along ND and b) along 45.

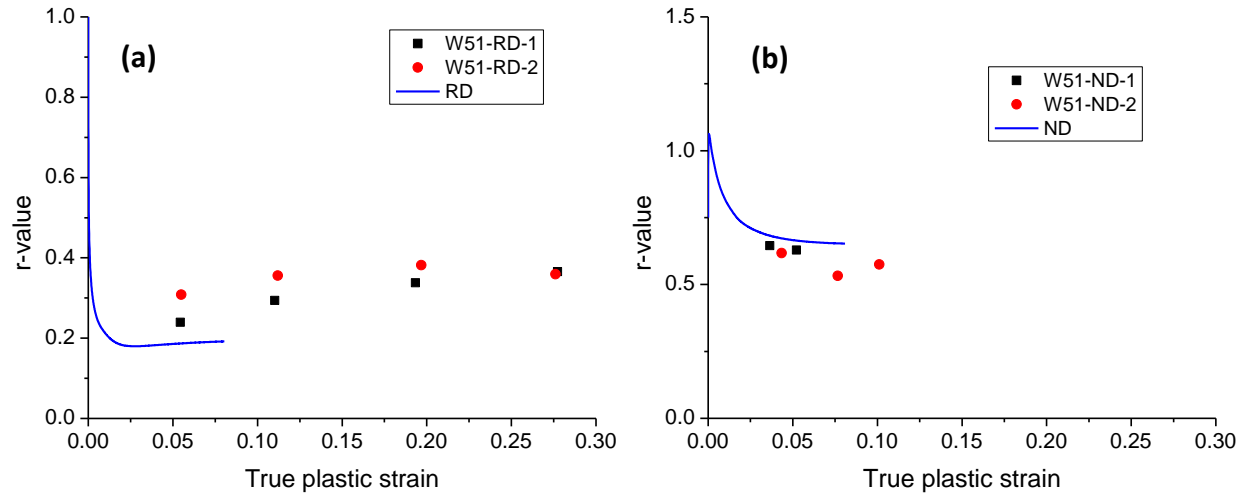


Figure 6.5: Experimental and predicted r-values for W51 a) along RD and b) along ND

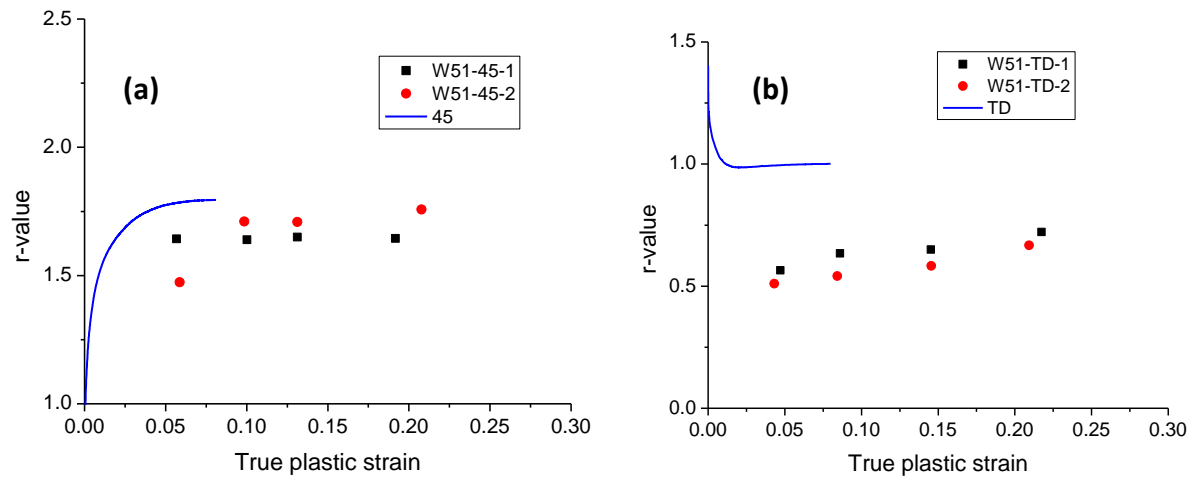


Figure 6.6: Experimental and predicted r-values for W51 a) along 45 and b) along TD

6.7.3 Modeling T721

Similar to the W51 case, the TD flow curves were fitted to obtain the Voce parameters (Table 6.1) and then the RD, ND and 45 responses were predicted and compared with the experimental data (Figures 6.5 - 6.10). The simulation results of the original EPSC model show that the predicted flow curves for all the directions are now underestimated, albeit to different extents. The general trend is quite similar to W51; it is least under-predicted along RD and most along ND. Notably, it fails to capture the initial rapid strain hardening along the RD. The r -values (Figures 6.11 and 6.12) are also not captured as well as the W51 case; along RD (~ 0.45 exp. vs 0.27 simulated), along 45 (~ 1.5 exp. vs 1.8 simulated) and for ND (~ 0.8 exp. vs 1.0 simulated). By incorporating a precipitate volume fraction of 0.05 , the predictions are qualitatively improved, i.e. the r -values and flow stresses shift in the right direction. In all cases, it predicts a lower flow stress and strain anisotropy, which is in accordance with the experiments. By incorporating the saturation, the hardening behavior becomes more parabolic. After the initial rapid rise, the hardening rate decreases in a manner that is similar to that observed experimentally. This is a direct result of the decaying off of the strain concentration which reduces the strong polarization of the stresses. If no relaxation is considered, then backstresses increase with straining, leading to high hardening rates.

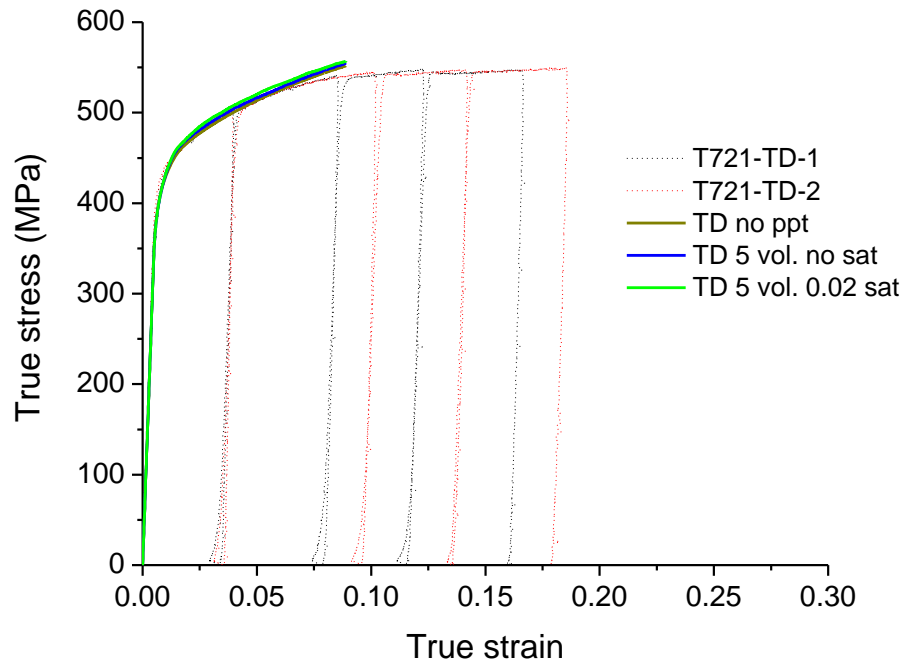


Figure 6.7: Experimental and simulation (fitted) flow curves for T721 along TD.

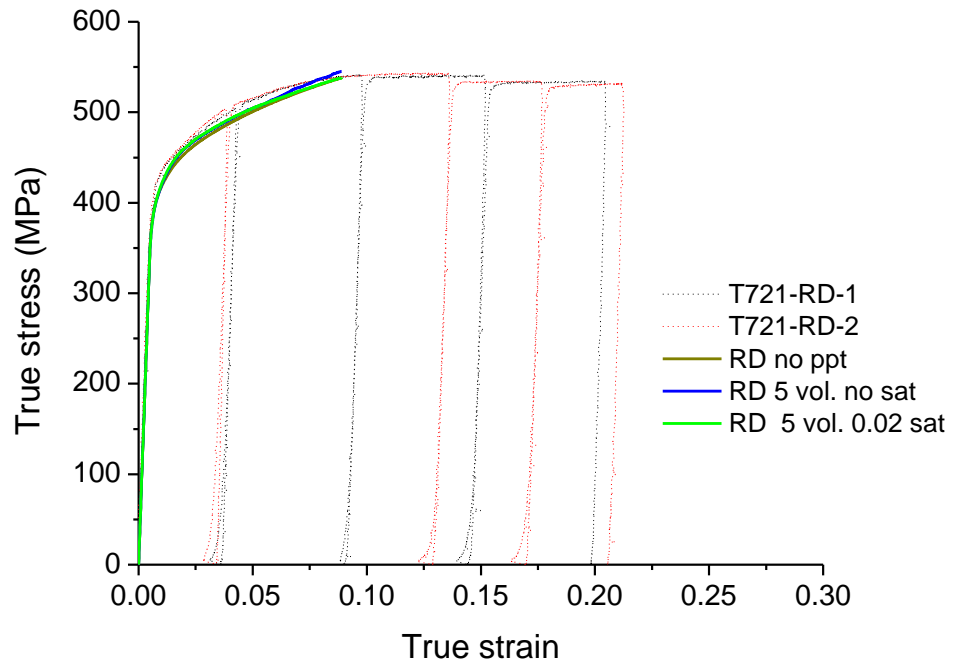


Figure 6.8: Experimental and predicted flow curves for T721 along RD

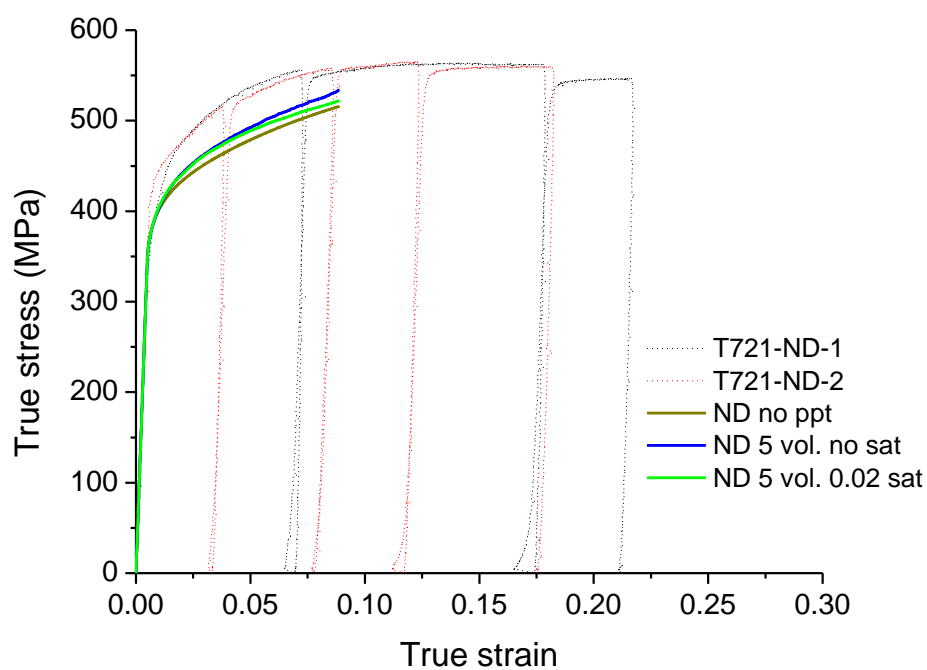


Figure 6.9: Experimental and predicted flow curves for T721 along ND.

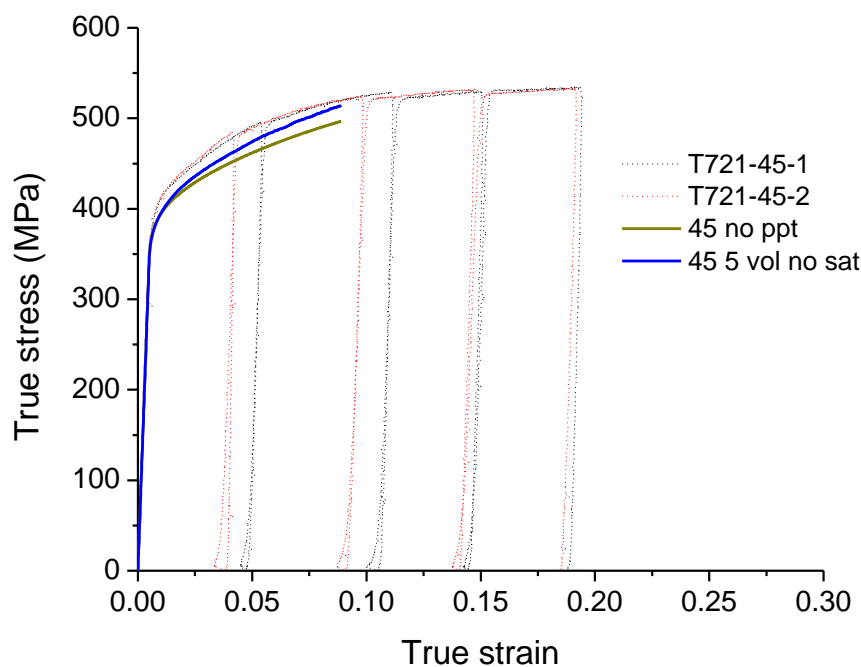


Figure 6.10: Experimental and predicted flow curves for T721 along 45 direction.

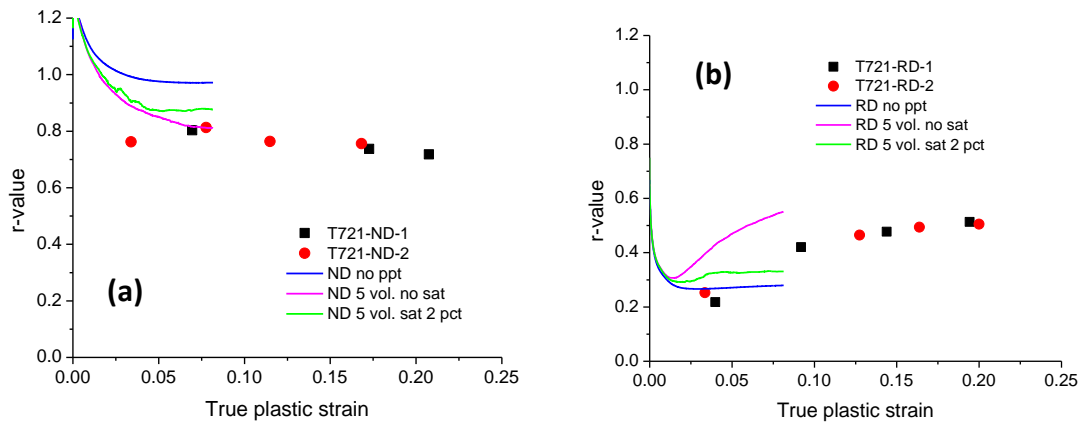


Figure 6.11: Experimental and predicted r-values for T721 a) along ND and b) along RD.

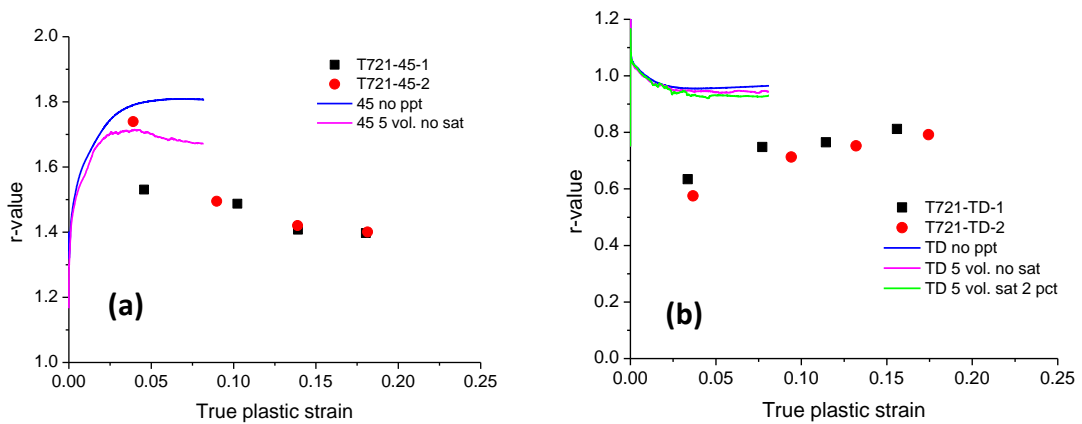


Figure 6.12: Experimental and predicted r-values for T721 a) along 45 and b) along RD.

6.8 Discussion

6.8.1 Bauschinger effect

By comparing the experimental and simulated Bauschinger plots for T3 (Figure 6.2), it is evident that not all aspects after strain reversal are captured. By lowering the strength of the interaction between the grains and the aggregate, the behavior is qualitatively improved, but subtle details, like the early yield in compression followed by a rapid hardening is not captured. It is well known (Mughrabi, 1983; Bate and Wilson, 1986; Abel, 1987) that the lower yield

strength upon strain reversal is due to the intragranular backstresses generated by dislocations pile ups formed during prestraining. The changes in the strain hardening rate which follows following the yield upon strain reversal is controlled by the rate of annihilation of dislocations which eventually leads to permanent softening (Hasegawa et al., 1975; Gracio et al., 2004; Beyerlein and Tome, 2007), which was observed in this study also (chapter 5). Although the goal of this study was not to specifically model the Bauschinger effect, it was of interest to see the contribution from intergranular stresses. The modeling results suggest that in an almost elastically isotropic material like Al, the contribution from intergranular stresses are quite low, at least in the case of heavily alloyed and solutionized AA 7085. However, there appears to be a substantial contribution from the dislocation based intragranular backstresses, given the discrepancies observed between model and experiment presented for the case of T3. Now, recall that the magnitude of backstresses in T711 were about twice than that observed in T3, which could be due to the additional internal stresses developed in presence of the precipitates. Thus, in order to capture all the aspects of strain reversal, in a precipitate containing alloy like the one used in this study, a dislocation based model (e.g., (Beyerlein and Tome, 2007; Wollmershauser et al., 2012; Kitayama et al., 2013; Zecevic and Knezevic, 2015) which also takes into account the precipitate contributions has to be used.

6.8.2 Role of precipitates on anisotropy

The simulation results for W51 (minimum influence from non shearable precipitates) suggest that the anisotropy observed is relatively well captured by the original model. The predicted flow curves are quite well captured, except along ND. The r-values for all directions save the TD are relatively well captured, which suggests that the anisotropic behavior is mainly due to the crystallographic texture present in the material. On the other hand, for T721, the flow

curve along RD is relatively well captured, but the r -values are underestimated. This suggests that something other than the texture is influencing the strain anisotropy. Once a small volume fraction of precipitates/particles are introduced, the model predictions qualitatively shift in the correct direction. For all the directions except TD, the new model captures both the flow strength and the plastic strain anisotropy. This suggests that the precipitate-induced backstress is indeed responsible for the reduction in anisotropy. Furthermore, if one observes the Voce parameters for T721 (Table 6.1), it can be seen that if no relaxation is considered; almost the whole contribution to strain hardening comes from the particle induced stresses. While it might be true for first few percent strain, at higher (>5%) strains, it seems somewhat unrealistic, since increases in the dislocation density also produces strain hardening. Furthermore, as mentioned earlier, incorporating the relaxation, results in a decreasing hardening rate, similar to what is observed experimentally. When compared to the simulation results without saturation, not only the ‘2% saturation’ simulation results match the experimental data better, but also it is considered to be closer to reality.

6.9 Conclusions

The effect of precipitate-induced backstress on the strength and strain anisotropy of a precipitation hardenable alloy 7085 in various tempers was explored using a modified EPSC modeling approach. The simulation results presented in this article provide some useful insights regarding modeling of the anisotropic behavior in such materials. The key points are summarized below:

1. The simulations results for Baushinger tests show that the contribution of intergranular backstresses to strain reversal behavior is quite low. Even for T3 temper material, where precipitates induced effects are minimum. The EPSC model with low interaction strength (β

= 0.5) describes the experimental data well for small pre-strain levels ($\epsilon < 0.01$). At higher pre-strains there appear to be significant effects due to dislocation based intragranular backstresses.

2. The original EPSC model can predict the much of the anisotropy exhibited by W51 material, which does not have non-shearable precipitates. Only the TD predictions of r-values strongly depart from those measured experimentally.
3. For T721 (overaged) material, the traditional EPSC model predicts a stronger anisotropy, both for flow stress and r-values, than observed experimentally.
4. A micromechanical model has been incorporated in the EPSC framework and using this model, it is shown that by incorporating a small volume fraction (0.05) of second phase particles, the trend toward isotropy is reproduced.
5. When the backstresses are allowed to continue to build up without relaxation, the modified EPSC model predicts unrealistic levels of strain hardening. By incorporating an exponential decay in the backstress due to dislocation relaxation effects, it is shown that the observed trends in predicted anisotropy are retained, without attributing all the hardening contribution to the precipitates.
6. Finally, outstanding disagreement between the model and experiment suggest that the effects of dislocation-based intragranular backstresses must also be considered along with the precipitate induced effects.

6.10 Acknowledgements

The authors would like to thank ALCOA for providing the AA7085 plates in W51, T711, and T721 tempers, used in this study. We would also like to thank Dr. Laurent Capolungo at Los Alamos National Laboratory for helpful discussions about numerical challenges. The research at U.Va. and M.S.U. was sponsored by the United States Army Research Office under contract number W911NF-12-1-

0455 monitored by Drs. Suveen Mathaudhu and David Stepp. The views and conclusions contained in this document are those of the authors and should not be interpreted as representing the official policies, either expressed or implied, of the Army Research Laboratory or the U.S. Government. The U.S. government is authorized to reproduce and distribute reprints for government purposes notwithstanding any copyright notation hereon.

6.11 References

- Abel, A., 1987. Historical perspectives and some main features of the Bauschinger effect. *Mater. forum* 10, 11–26.
- Anjabin, N., Karimi Taheri, A., Kim, H.S., 2014. Crystal plasticity modeling of the effect of precipitate states on the work hardening and plastic anisotropy in an Al-Mg-Si alloy. *Comput. Mater. Sci.* 83, 78–85. doi:10.1016/j.commatsci.2013.09.031
- Ardell, A., 1985. Precipitation Hardening. *Metall. Trans. A* 16, 2131–2165.
- Ashby, M., 1970. The deformation of plastically non-homogeneous materials. *Philos. Mag.* 21, 399–424. doi:10.1007/s13398-014-0173-7.2
- Atkinson, J., Brown, L., Stobbs, W.M., 1974. The work-hardening of copper-silica IV. The Bauschinger effect and plastic relaxation. *Philos. Mag.* 30, 1247–1280.
- Bacon, D.J., Kocks, U.F., Scattergood, R.O., 1973. The effect of dislocation self-interaction on the Orowan stress. *Philos. Mag.* 28, 1241–1263.
- Barlat, F., Brem, J.C., Yoon, J.W., Chung, K., Dick, R.E., Lege, D.J., Pourboghrat, F., Choi, S.-H., Chu, E., 2003. Plane stress yield function for aluminum alloy sheets—part 1: theory. *Int. J. Plast.* 19, 1297–1319. doi:10.1016/S0749-6419(02)00019-0
- Barlat, F., Lian, K., 1989. Plastic behavior and stretchability of sheet metals. Part I: A yield function for orthotropic sheets under plane stress conditions. *Int. J. Plast.* 5, 51–66.
- Barlat, F., Liu, J., 1998a. Precipitate-induced anisotropy in binary Al-Cu alloys. *Mater. Sci. Eng. A* 257, 47–61. doi:10.1016/S0921-5093(98)00823-5
- Barlat, F., Liu, J., 1998b. Precipitate-induced anisotropy in binary Al-Cu alloys. *Mater. Sci. Eng. A* 257, 47–61. doi:10.1016/S0921-5093(98)00823-5
- Barlat, F., Maeda, Y., Chung, K., Yanagawa, M., Brem, J.C., Hayashida, Y., Lege, D.J., Matsui, K., Murtha, S.J., Hattori, S., Becker, R.C., Makosey, S., 1997. Yield function development for aluminum alloy sheets. *J. Mech. Phys. Solids* 45, 1727–1763. doi:10.1016/S0022-5096(97)00034-3
- Bate, P., Roberts, W.T., Wilson, D. V., 1981. The plastic anisotropy of two-phase aluminum alloys -- I. Anisotropy in unidirectional deformation. *Acta Metall.* 29, 1797–1814.
- Bate, P., Roberts, W.T., Wilson, D., 1982. The plastic anisotropy of two-phase aluminium alloys - II Anisotropic behavior in load reversal tests. *Acta Metall.* 30, 725–737.
- Bate, P.S., Wilson, D. V., 1986. Analysis of the bauschinger effect. *Acta Metall.* 34, 1097–1105. doi:10.1016/0001-6160(86)90220-8
- Beyerlein, I.J., Tome, C.N., 2007. Modeling transients in the mechanical response of copper due to strain path changes. *Int. J. Plast.* 23, 640–664. doi:10.1016/j.ijplas.2006.08.001
- Bhattacharyya, J.J., Agnew, S.R., Lee, M., Whittington, W.R., El Kadiri, H., 2016. Measuring and modeling the anisotropic, high strain rate deformation of Al alloy, 7085, plate in T711 temper, in review.
- Bonfio, N., Carmasol, A., Lipinski, P., 2003. Modeling of intra-crystalline hardening of materials with particles. *Int. J. Plast.* 19, 1167–1193. doi:10.1016/S0749-6419(02)00015-3
- Brown, L., Clarke, D., 1975. Work hardening due to internal stresses in composite materials. *Acta Metall.* 23, 821–830.

- Brown, L.M., Stobbs, W.M., 1976. The work-hardening of copper-silica V. equilibrium plastic relaxation by secondary dislocations. *Philos. Mag.* 34, 351–372. doi:10.1007/s13398-014-0173-7.2
- Brown, L.M., Stobbs, W.M., 1971. The work hardening of copper-silica I. A model based on internal stresses, with no plastic relaxation. *Philos. Mag.* 23, 1185–1199.
- Brown, L.M., Stobbs, W.M., 1971. The work-hardening of copper-silica II. The role of plastic relaxation. *Philos. Mag.* 23, 1201–1233. doi:10.1007/s13398-014-0173-7.2
- Busso, E.P., Meissonnier, F.T., O'Dowd, N.P., 2000. Gradient-dependent deformation of two-phase single crystals. *J. Mech. Phys. Solids* 48, 2333–2361. doi:10.1016/S0022-5096(00)00006-5
- Cheng, L.M., Poole, W.J., Embury, J.D., Lloyd, D.J., 2003. The influence of precipitation on the work-hardening behavior of the aluminum alloys AA6111 and AA7030. *Metall. Mater. Trans. A* 34, 2473–2481. doi:10.1007/s11661-003-0007-2
- Choi, S.H., Barlat, F., Liu, J., 2000. Effect of Precipitates on Plastic Anisotropy of Polycrystalline Aluminum Alloys. *Mater. Sci. Forum* 331–337, 1327–1332. doi:10.4028/www.scientific.net/MSF.331-337.1327
- Corbin, S.F., and Wilkinson, D.S., 1994. the Influence of Particle Distribution on the Mechanical Response of a Particulate Metal Matrix Composite. *Acta Metall.* 42, 1311–1318.
- Dawson, P., Boyce, D., MacEwen, S., Rogge, R., 2001. On the influence of crystal elastic moduli on computed lattice strains in AA-5182 following plastic straining. *Mater. Sci. Eng. A* 313, 123–144. doi:10.1016/S0921-5093(01)00967-4
- Deschamps, A., Bigot, A., Livet, F., Auger, P., Brechet, Y., Blavette, D., 2001. A Comparative Study of Precipitate Composition and Volume Fraction in an Al–Zn–Mg Alloy using Tomographic Atom Probe and Small-Angle X-ray Scattering. *Philos. Mag. A* 81, 2391–2414. doi:10.1080/01418610110038439
- Dumont, D., Deschamps, a., Bréchet, Y., Sigli, C., Ehrström, J.C., 2004. Characterisation of precipitation microstructures in aluminium alloys 7040 and 7050 and their relationship to mechanical behaviour. *Mater. Sci. Technol.* 20, 567–576. doi:10.1179/026708304225016662
- Eshelby, J.D., 1957. The Determination of the Elastic Field of an Ellipsoidal Inclusion, and Related Problems. *Proc. R. Soc. A Math. Phys. Eng. Sci.* 241, 376–396. doi:10.1098/rspa.1957.0133
- Estrin, Y., 1996. “Dislocation-density-related constitutive modeling,” in: Krausz, A., Krausz, K. (Eds.), *Unified Constitutive Laws of Plastic Deformation*. Academic Press, Inc, pp. 82–84.
- Fribourg, G., Brechet, Y., Deschamps, A., Simar, A., 2011. Microstructure-based modelling of isotropic and kinematic strain hardening in a precipitation-hardened aluminium alloy. *Acta Mater.* 59, 3621–3635. doi:10.1016/j.actamat.2011.02.035
- Friedel, J., 1964. *Dislocations*, New York. Pergamon.
- Gleiter, H., Hornbogen, E., 1968. Precipitation hardening by coherent particles. *Mater. Sci. Eng.* 2, 285–302.
- Gracio, J.J., Barlat, F., Rauch, E.F., Jones, P.T., Neto, V.F., Lopes, A.B., 2004. Artificial aging and shear deformation behaviour of 6022 aluminium alloy. *Int. J. Plast.* 20, 427–445. doi:10.1016/S0749-6419(03)00095-0
- Han, C.S., Kim, J.H., Chung, K., Kang, T.J., 2006. Modeling the plastic deformation of crystals with thin precipitates. *Int. J. Solids Struct.* 43, 2398–2421. doi:10.1016/j.ijsolstr.2005.06.032
- Han, C.S., Wagoner, R.H., Barlat, F., 2004. On precipitate induced hardening in crystal plasticity: theory. *Int. J. Plast.* 20, 477–494. doi:10.1016/j.ijplas.2003.11.002
- Hasegawa, T., Yakou, T., Karashima, S., 1975. Deformation behaviour and dislocation structures upon stress reversal in polycrystalline aluminium. *Mater. Sci. Eng.* 20, 267–276.
- Hill, R., 1966. Generalized constitutive relations for incremental deformation of metal crystals by multislip. *J. Mech. Phys. Solids* 14, 95–102. doi:10.1016/0022-5096(66)90040-8
- Hosford, W.F., Zeisloft, R.H., 1972. The anisotropy of age-hardened Al-4 Pct Cu single crystals during plane-strain compression. *Metall. Trans.* 3, 113–121.
- Hutchinson, J., 1970. Elastic-Plastic Behavior of Polycrystalline Metals and Composites. *Proc. R. Soc. London A Math. Phys. Eng. Sci.* 319, 247–272.

- Jobson, P., Roberts, W.T., 1977. Directionality in a precipitation-hardened alloy. *Metall. Mater. Trans. A* 8, 2013–2014.
- Kitayama, K., Tomé, C.N., Rauch, E.F., Gracio, J.J., Barlat, F., 2013. A crystallographic dislocation model for describing hardening of polycrystals during strain path changes. Application to low carbon steels. *Int. J. Plast.* 46, 54–69. doi:10.1016/j.ijplas.2012.09.004
- Lin, T.H., 1957. Analysis of elastic and plastic strains of a face-centred cubic crystal. *J. Mech. Phys. Solids* 5, 143–149. doi:10.1016/0022-5096(57)90058-3
- Moan, G.D., Embury, J.D., 1979. A study of the Bauschinger effect in Al-Cu alloys. *Acta Metall.* 27, 903–914.
- Mughrabi, H., 1983. Long-Range Wall and Cell Structures and Internal Stresses in Deformed Metal Crystals *Acta Metall.* 31, 1367–1379.
- Mulay, R.P., Clausen, B., Agnew, S.R., 2011. In-situ neutron diffraction study of the bauschinger effect in B2 structured CoZr. *Metall. Mater. Trans. A Phys. Metall. Mater. Sci.* 42, 60–70. doi:10.1007/s11661-010-0389-x
- Pang, J.W., Holden, T., Mason, T., 1998. In situ generation of intergranular strains in an Al7050 alloy. *Acta Mater.* 46, 1503–1518. doi:10.1016/S1359-6454(97)00369-8
- Park, J.K., Ardell, A.J., 1983. Microstructures of the commercial 7075 Al alloy in the T651 and T7 tempers. *Metall. Trans. A* 14, 1957–1965. doi:10.1007/BF02662363
- Proudhon, H., Poole, W.J., Wang, X., Bréchet, Y., 2008. The role of internal stresses on the plastic deformation of the Al–Mg–Si–Cu alloy AA6111. *Philos. Mag.* 88, 621–640. doi:10.1080/14786430801894569
- Qu, J., Cherkaoui, M., 2006. *Fundamentals of micromechanics of solids*. John Wiley & Sons, Inc., Hoboken, NJ.
- Russell, K.G., Ashby, M.F., 1970. Slip in aluminum crystals containing strong, plate-like particles. *Acta Metall.* 18, 891–901. doi:10.1016/0001-6160(70)90017-9
- Sachs, G., 1928. *Z. Verein Deutsch Ingen* 72, 734.
- Schmitt, C., Lipinski, P., Berveiller, M., 1997. Micromechanical modelling of the elastoplastic behavior of polycrystals containing precipitates— Application to hypo- and hyper-eutectoid steels. *Int. J. Plast.* 13, 183–199. doi:10.1016/S0749-6419(95)00007-0
- Sehitoglu, H., Foglesong, T., Maier, H.J., 2005. Precipitate effects on the mechanical behavior of aluminum copper alloys: Part II. Modeling. *Metall. Mater. Trans. a-Physical Metall. Mater. Sci.* 36A, 763–770.
- Simar, A., Brechet, Y., de Meester, B., Denquin, A., Pardoën, T., 2007. Sequential modeling of local precipitation, strength and strain hardening in friction stir welds of an aluminum alloy 6005A-T6. *Acta Mater.* 55, 6133–6143. doi:10.1016/j.actamat.2007.07.012
- Srivatsan, T.S., Sriram, S., Veeraraghavan, D., Vasudevan, V.K., 1997. Microstructure, tensile deformation and fracture behaviour of aluminium alloy 7055. *J. Mater. Sci.* 32, 2883–2894. doi:10.1023/A:1018676501368
- Takahashi, A., Ghoniem, N.M., 2008. A computational method for dislocation-precipitate interaction. *J. Mech. Phys. Solids* 56, 1534–1553. doi:10.1016/j.jmps.2007.08.002
- Turner, P.A., Tomé, C.N., 1994. A study of residual stresses in Zircaloy-2 with rod texture. *Acta Metall. Mater.* 42, 4143–4153. doi:10.1016/0956-7151(94)90191-0
- Wilson, D., 1965. Reversible work hardening in alloys of cubic metals. *Acta Metall.* 13, 807–814. doi:10.1016/0001-6160(65)90145-8
- Withers, P.J., Stobbs, W.M., Pedersen, O.B., 1989. The Application of the Eshelby Method of Internal Stress Determination to Short Fiber Metal Matrix Composites. *Acta Metall.* 37, 3061–3084.
- Wollmershauser, J.A., Clausen, B., Agnew, S.R., 2012. A slip system-based kinematic hardening model application to in situ neutron diffraction of cyclic deformation of austenitic stainless steel. *Int. J. Fatigue* 36, 181–193. doi:10.1016/j.ijfatigue.2011.07.008
- Yassar, R.S., Mesarovic, S.D., Field, D.P., 2007. Micromechanics of hardening of elastic-plastic crystals with elastic inclusions: I - Dilute concentration. *Int. J. Plast.* 23, 1901–1917.

doi:10.1016/j.ijplas.2007.03.013

Zecevic, M., Knezevic, M., 2015. A dislocation density based elasto-plastic self-consistent model for the prediction of cyclic deformation: Application to AA6022-T4. *Int. J. Plast.* 72, 200–217.

doi:10.1016/j.ijplas.2015.05.018

7 Conclusions and future work

7.1 Overall contribution

In the present work, the constitutive behavior of two different precipitation hardenable alloys; magnesium alloy WE43 and aluminum alloy 7085, has been investigated at quasistatic and dynamic strain rates. The strategy employed is crystal plasticity modeling along with experimental methods which is used to calibrate as well as validate the model. A strong emphasis was on anisotropy of the alloys, the origin of which is quite different for the two alloys investigated. In Mg alloys, presence of multiple slip modes, as well as twinning, makes the single crystal behavior highly anisotropic. Al being face centered cubic, has only 1 slip mode, the octahedral $\{111\}\langle 110 \rangle$ mode, which makes the single crystal much more isotropic, compared to Mg.

In chapter 2, EPSC modeling of quasistatic and high strain rate deformation behavior of WE43T5 plate has provided useful insights about the grain level deformation mechanisms and the role of individual strengthening mechanisms that are operative in this alloy. The quasistatic modeling results suggest that the basal slip and extension twinning in this alloy are strengthened greatly, whereas harder prismatic and $\langle c+a \rangle$ slip modes are relatively less strengthened. This is one reason why WE43-T5 exhibits lower anisotropy than conventional Mg alloys. The hardening of the twinning mode has a great effect on the behavior. For example, there is an absence of the characteristic sigmoidal shape, reduced tension compression strength asymmetry, and lower twin volume fraction as compared to conventional alloys. By examining the effect of various strengthening mechanisms, it is found that the precipitates have a profound effect in strengthening the slip modes and solute atoms were emphasized as key strengtheners of the $\langle c+a \rangle$ and extension twinning modes. The modeling results show that the observed higher twin

volume fraction at higher strain rate is due to the slight positive rate sensitivity of prismatic slip, resulting in its lower activity, and thus twinning has to accommodate the strain.

Another interesting observation, the strength modeling exercise revealed, is that although the plate shaped precipitates in this alloy are capable of increasing the CRSS of basal slip as well as other slip modes, they are present in low number density /volume fraction, which results in low age hardenability. Thus in order to explore the possibilities of increasing the low number density/ volume fraction several heat treatment strategies were employed, as described in Chapter 3. It was found that neither the conventional T6 treatment (solutionizing, quenching followed by aging), nor the T8 (solutionizing, quenching stretching prior to aging) nor the two step aging treatments (pre-aging at a lower temperature) lead to a substantial increase in the peak hardness. However, the latter two procedures increase the kinetics of precipitation, and thus enable to reach the peak hardness at a much shorter aging time. One advantage of the solution heat treatment is that it weakens the initial basal texture in WE43 plate, resulting in a dramatic reduction in yield strength anisotropy ($TD/ND = 1.7$ down to 1.3). A key achievement of the modeling work presented in chapter 2 is the strength and flow stress *predictions*, for both solutionized and peak-aged material, are accurate to within 13% or better.

A goal of the present thesis work was to determine if there was an optimal aging condition to improve the ballistic performance of the material, given the spallation failure mechanism observed during that testing (Hamilton et al., 2012). The results presented in chapter 3 show that the WE43-T5 ND samples tend to exhibit lower ductility, due stringers of Y-containing cuboidal dispersoids, lying on the ND plane. These results suggest that the key to avoid spallation in ballistic tests is to improve the ND ductility. Perhaps optimizing the alloy

content to reduce the amount of dispersoids, or performing thermomechanical treatments to disintegrate them and smear them out evenly can be a strategy to improve the ND ductility.

The fracture behavior for all the heat treatment conditions explored in this study, exhibit twin-related cracks, grain boundary precipitation induced cracks, and transgranular ductile dimples. It is found that the T5 and the T3 exhibit the best tensile ductility whereas T6 is the worst. It is shown qualitatively, that the T6 treatment leads to more severe grain boundary precipitation and ductile intergranular failure, which adversely affects the ductility, whereas hot-rolling followed by aging (T5) leads to a more uniform distribution of the precipitates as indicated by ductile dimples within the grains.

In the second part of this dissertation, the quasistatic and high strain rate deformation behavior of AA7085 for five different tempers (T3, W51, T6, T711 and T721) has been investigated. Preliminary crystal plasticity modeling of T711 material, using VPSC code, revealed that not all aspects of plastic anisotropy could be captured. The material was somewhat more isotropic than that predicted by the model. Accounting for the anisotropic grain shape and possible latent hardening effects did not lead to improvement in the predictions. It was then hypothesized that particle induced “backstress” (which the model did not account for) is responsible for the discrepancy between the model and the experiment. Further experiments on the other tempers, confirmed that the plastic anisotropy is strongly dependent on the ageing conditions. It is found that the overaged materials were indeed more isotropic than what texture alone would result in. In order to model this effect, a micromechanical two-phase model has been incorporated within the elastoplastic self-consistent (EPSC) model. It was demonstrated that by incorporating a small volume fraction (0.05) of second phase particles, the isotropic behavior can be qualitatively well captured. Another aspect that was investigated was the role of

the relaxation of the backstresses. It is known from the literature that the Orowan loops that pile up against the non-shearable particles are responsible for the observed ‘backstress’. It is also known that they are only stable up to few percent strains, after which various relaxation mechanisms tend to rearrange them to a lower energy configuration. This leads to saturation of the backstress at higher strains. By incorporating this relaxation effect, the simulations gave the best and physically plausible results, as compared to the case without relaxation as well as the original single phase EPSC model. When relaxation effects are not considered, the modified EPSC model predicts that all the strain hardening observed is due to the presence of second phase particles, which is unrealistic at higher strain levels.

The dynamic tests data permitted the estimation of the strain rate sensitivity of the octahedral $\{110\} \langle 011 \rangle$ slip mode for the different tempers investigated. The rate sensitivity m for W51, T711 and T721, was found to quite low, ranging from 0.002 to 0.008, and is consistent with the notion that it is “athermal” in the rate regime investigated. The slight negative rate sensitivity in the T3 temper ($m = -0.005$) is probably due to dynamic strain aging phenomena due to high solute content in the matrix in T3 condition. All the specimens exhibited strain softening at higher strain levels, under dynamic loading. The extent of strain softening varied with the loading direction; while RD was most susceptible to shear localization, the 45 direction showed continued strain hardening at dynamic strain rates. This observation can be explained in terms of texture and their behavior at quasistatic rates, where they exhibited the same trend. It is thus suggested that the low work hardening rate of RD along with adiabatic conditions make it more susceptible to shear localization.

7.2 Future work

The modeling effort in chapter 2 has identified some key aspects of the single crystal behavior that merits further investigation. It has been found that the $\langle c+a \rangle$ and twinning modes in WE43 is quite strong and this has been attributed to the presence of rare earth solutes. However, the mechanism of solute interaction with the $\langle c+a \rangle$ and twinning dislocations is still not clear. Thus, it is worthwhile to investigate such interactions using tools like molecular dynamics (MD) or discrete dislocation dynamics (DDD), which can provide useful quantities like interaction energies between the solute and dislocations. Such an attempt has been made in recent years which investigated the effect of solutes on the basal slip (used in Section 2.6.3.2 of chapter 2), but it needs to be extended further for non-basal slip and twinning.

Another important aspect that was revealed is that the the polycrystal plasticity model in its current form, cannot precisely capture the flow stress along all directions simultaneously, when extension twinning is the dominant deformation mode (i.e. for ND tension, RD and TD compression). Thus, it appears that it is necessary to take into account the stress associated with twin nucleation which is sensitive to the local stress state and cannot be addressed in such mean field approach.

The third issue that merits investigation is the latent hardening due to dislocation-dislocation as well as dislocation-twin interaction. In chapter 2, it was necessary to incorporate latent hardening effects in order to capture the plastic strain anisotropy during in-plane tension. More specifically, the fact that basal slip mode is hardened considerably by both prismatic and $\langle c+a \rangle$ slip modes, whereas the $\langle c+a \rangle$ mode is not strongly hardened by either basal or prismatic, as suggested by DDD simulations, had to be incorporated. . However, an outstanding question is why is it not always necessary to incorporate this effect? Also, do the latent hardening

coefficients vary with straining? A similar challenge was faced while modeling the constitutive behavior of Al T711 in chapter 4. Again, DDD simulations suggest a low coplanar interaction in face centered cubic metals, but it was found to be inadequate to capture the constitutive response of the alloy in question. It is thus suggested that a dislocation dynamics based crystal plasticity model should be used to explore such questions.

Furthermore, the strain rate sensitivities determined using the present approach has a large error associated with them. Furthermore, to obtain the rate sensitivity at constant substructure, rate jump tests are required, which is a challenge in the strain rate regimes, investigated in this study. Thus it is suggested that single crystal experiments should be performed in order to probe the thermally activated regimes (at low temperatures, or very high strain rates) of the basal and twinning modes.

Regarding the fracture behavior of the alloy, detailed role of the precipitate free zone associated with these precipitates merits further investigation. Especially the dependence of strain localization on the width and composition of the precipitate free zone needs to be identified.

Shear localization during dynamic deformation of the Al alloys, needs to be further investigated. Especially, information about the temperature rise during straining using thermal imaging would provide a better idea about the temperature distribution within the specimen.

Finally, crystal plasticity models which incorporate the effects of intragranular backstresses has to be tested for materials containing non-shearable precipitates, in order to capture all of the generalized Bauschinger effect. The present work highlights the need to account for such backstresses, even in cases involving higher levels of plasticity (such as

modeling of metal forming, crash, ballistics, etc.) where strain anisotropy is often of keen interest.

8 Appendix A

8.1 Experimental - Split Hopkinson Pressure Bar

The high-strain-rate ($1000\text{--}2000\text{ s}^{-1}$) tension and compression tests have been carried out using a Split-Hopkinson pressure bar (SHPB), also known as the Kolsky Bar. The following is a brief overview of Hopkinson bar theory and data analysis. A detailed description of the apparatus, high rate material testing and the governing theory can be found in the following references (Meyers, 1994; Gray, 2000a; Gama, Lopatnikov, & Gillespie, 2004;). The SHPB is a high-strain-rate testing apparatus whose operating principle is based on elastic wave propagation in materials. Typically, the apparatus consists of three bars; the striker bar, the incident bar, and the transmitted bar and are made out from the same material (same cross-sectional area and acoustic impedance defined by $z = \rho C_0$, where ρ is the density and C_0 is the speed of sound in the bar material). It is important that the bars undergo only elastic deformation during the whole experiment. The specimen, which has a lower acoustic impedance than the bars, is sandwiched between the incident and the transmitted bar.

The apparatus used for dynamic compression testing is shown schematically in Figure 8.1 (G.T. Gray, 2000).

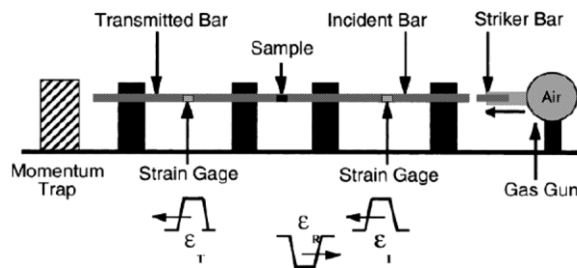


Figure 8.1: A schematic of the compression Split Hopkinson Pressure Bar (G.T. Gray, 2000).

In compression tests, the striker bar is propelled by the gas gun and impacts the incident bar, which generates a compressive stress wave. If L is the length of the striker bar, then the time taken for the compressive wave to travel back to the free end of the striker bar, reflect and return as a unloading tensile wave is: $T = 2L/C_0$, which is the total loading duration of the specimen. Thus by changing the length of the striker bar, different strains can be imparted to the specimen. This incident wave propagates down the bar where it encounters the sample. At this point, due to impedance mismatch between the specimen and the bars, a portion of the wave is transmitted through the specimen into the transmitter bar as a compressive stress wave while the rest of it is reflected as a tensile wave. The fraction of the wave that is transmitted is dependent on the impedance and geometric difference between the bar and the specimen. Strain gauges on each bar record the strain time history of the passing waves. The raw data obtained from the test is the signal histories of the strain gages. Thus, a calibration procedure, which converts the measured signals into strain, has to be carried out. Once the strain histories are known, the constitutive response of the material can be calculated based on 1D elastic stress wave propagation in the bars (Meyers, 1994; G.T. Gray, 2000; Gama et al., 2004).

8.2 Calibration

The calibration procedure is necessary for a new installation, or if the bars or strain gages are changed. This procedure enables one to relate the signal measured in the gages to the strain in the bars. The striker bar upon impact generates a stress wave σ in the incident bar whose magnitude is related to the particle velocity, v_p . Using the relationship between wave velocity, C_0 , Young's modulus, E and density ρ :

$$C_0 = \sqrt{\frac{E}{\rho}} \quad (8-1)$$

and Hooke's law along with the definition of strain:

$$\sigma = E\varepsilon = E \frac{\partial u}{\partial x} \quad (8-2)$$

where u is the particle displacement and σ and ε are the axial stress and strain respectively.

Using Chain rule in Eq. (8-2) and substituting Eq. (8-1) we get,

$$\sigma = E \frac{\partial u}{\partial t} \frac{\partial t}{\partial x} = \frac{E v_p}{C_0} = c \rho v_p \quad (8-3)$$

Since by definition, the particle velocity $v_p = \frac{\partial u}{\partial t}$ and wave velocity $C_0 = \frac{\partial x}{\partial t}$

The relation between the particle velocity v_p and the velocity imparted to the striker bar, V , can be obtained using law of conservation of momentum:

Momentum before impact: $mV = (\rho AL)V$ and momentum after impact $= \rho A \cdot 2L \cdot v_p$.

Therefore, $V = 2v_p$ which gives:

$$\sigma = C_0 \rho \frac{V}{2} \quad (8-4)$$

This strain in the bar can be calculated as:

$$\varepsilon_{calc} = \frac{\sigma}{E} = \frac{C_0 \rho V}{2E} = \frac{V}{2C_0} \quad (8-5)$$

The strain calibration factor then is:

$$K_\varepsilon = \frac{\varepsilon_{calc}}{\varepsilon_{measured}} \quad (8-6)$$

The strain calibration factor can be obtained from what is called a ‘bars apart’ test, where the striker bar impacts the incident and the transmitted bar separately. The strain versus time profile for such a test is shown in Figure 8.2. The transmitted bar is kept separated. The incident wave, upon reaching the free end of the bar, reflects completely as a tensile wave, which is picked up by the strain gage on the incident bar. To obtain the $\varepsilon_{measured}$, the raw compressive wave signal is smoothed and then averaged over the region where it is almost constant.

The velocity of the striker bar V in Eq. (8-5) can be measured accurately using laser tags. The other unknown term in Eq. (8-5) is the wave velocity, C_0 . One can accurately measure the distance between the strain gage from the bar end, d , and can determine the duration, t , between the rise of the compressive wave and that of the reflected wave, then the wave velocity can be obtained as: $C_0 = d/t$. Once all these values are known, the calibration factor can be obtained using Eq. (8.6).

For the apparatus used in this study, the wave velocity obtained by using this method is 4850.3 m/s. Besides, the calibration factor, one can also calculate and compare the incident pulse duration, if the striker length is known. For a striker bar of length 540 mm (used in the present study), a loading duration of 223 μ s is predicted by the formula: $2L/C_0$, which compares well with the value obtained experimentally (230 μ s).

Finally another parameter that is of interest is the transmission factor K_t which is the ratio of the strain in the incident to that in the transmitted bar. This calibration factor is obtained using what is called a ‘bars together’ test, where there is no specimen and the incident and the transmitted bar is in contact with each other. Due to the same impedance, the incident wave should completely pass into the transmitted bar, without any loss, but in reality it is often not the

case. There is often a negligible reflected pulse resulting from slight misalignment of the bars, as shown in Figure 8.3.

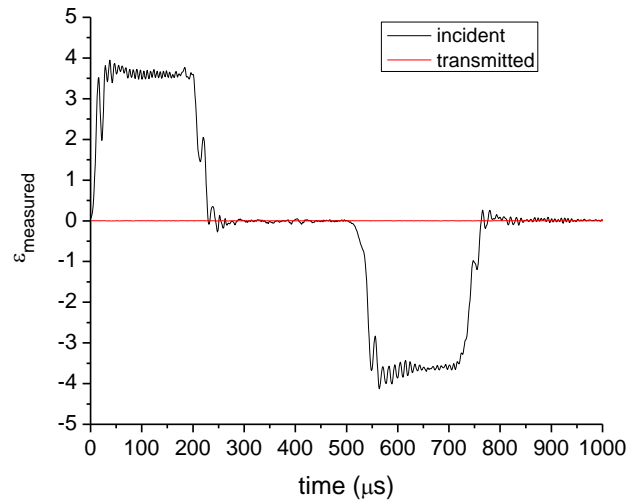


Figure 8.2: A ‘bars apart’ test raw data showing the signal measured by strain gages attached to the incident and transmitted bar. The compressive incident wave is chosen as positive.

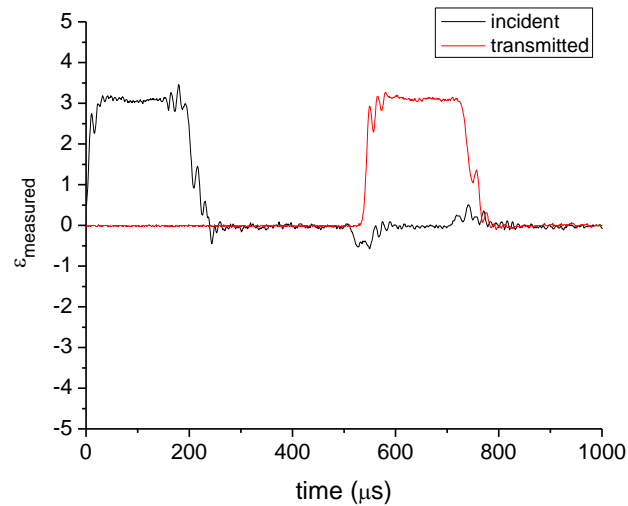


Figure 8.3: A ‘bars together’ test raw data showing the signal measured by strain gages attached to the incident and transmitted bar. The compressive incident wave is chosen as positive.

Once again, the strains can be found out by smoothing and averaging the flat portion of the data for both incident and transmitted signal.

$$K_t = \frac{\varepsilon_{incident}}{\varepsilon_{transmitted}} \quad (8-7)$$

For the present study, the value of K_t is found to be 1.008.

8.3 Constitutive response

Once the calibration procedure is complete, the material stress-strain response can be calculated from the difference in velocities of the bar ends (V_1 , V_2) and forces (F_1 , F_2) acting on the ends of the specimen. As the stress wave reaches the bar end, the velocity of the incident bar end approaches V_1 . The engineering strain rate of the sample, $\dot{\varepsilon}_s$, is then given by:

$$\dot{\varepsilon}_s(t) = \frac{V_1(t) - V_2(t)}{L_s} \quad (8-8)$$

where, V_1 and V_2 are the velocities of the bar ends. Since measurement of the velocity at the end of the bars is difficult, a method based on 1D elastic stress wave propagation in the bars is generally applied.

The stress, strain and strain rate of the specimen, is determined from the incident strain, ε_I , the reflected strain, ε_R , and the transmitted strain, ε_T , histories in the bar. The velocities at the interface are related to the strain according to:

$$V_1(t) = C_0[\varepsilon_I(t) - \varepsilon_R(t)] \quad (8-9)$$

$$V_2(t) = C_0\varepsilon_T(t) \quad (8-10)$$

Note that here $t = 0$ is defined to be when the incident wave reaches the bar end. For $t > 0$, the incident and reflected waves are superimposed in the incident bar, so V_1 is reduced.

Combining equations (8-8), (8-9) and (8-10) the strain rate in the specimen can be written in terms of the strain histories as:

$$\dot{\varepsilon}_s(t) = \frac{C_0}{L_s} [\varepsilon_I(t) - \varepsilon_R(t) - \varepsilon_T(t)] \quad (8-11)$$

The strain can be obtained by integrating equation (8.11):

$$\varepsilon_s(t) = \int \left(\frac{C_0}{L_s} [\varepsilon_I(t) - \varepsilon_R(t) - \varepsilon_T(t)] \right) dt \quad (8-12)$$

If F_1 and F_2 are the forces applied at the specimen ends by the bars, then they are related to the strains as:

$$F_1(t) = A_b E_b [\varepsilon_I(t) + \varepsilon_R(t)] \quad (8-13)$$

$$F_2(t) = A_b E_b \varepsilon_T(t) \quad (8-14)$$

where, A_b and E_b are respectively the cross sectional area and Young's Modulus of the bars.

Note again, it has been assumed that the bars are of same dimensions and made from the same material.

The stress in the specimen is based on the average force acting on it which is expressed as:

$$\sigma_s(t) = \frac{1}{2} \left(\frac{F_1(t) - F_2(t)}{A_s} \right) \quad (8-15)$$

where, and A_s is the cross sectional area of the sample.

Therefore, using equations (8-13) - (8-15), the stress in the sample is obtained as:

$$\sigma_s(t) = \frac{A_b E_b}{2A_s} [\varepsilon_I(t) + \varepsilon_R(t) + \varepsilon_T(t)] \quad (8-16)$$

For equilibrium to exist $F_1(t) = F_2(t)$ and principles of conservation of momentum dictates:

$$\varepsilon_T(t) = \varepsilon_I(t) + \varepsilon_R(t) \quad (8-17)$$

Therefore, under equilibrium, equations (7-11), (7-12) and (7-16) simplify to:

$$\dot{\varepsilon}_s(t) = 2 \frac{C_0}{L_s} \varepsilon_R(t) \quad (8-18)$$

$$\varepsilon_s(t) = -2 \int \left(\frac{C_0}{L_s} \varepsilon_R(t) \right) dt \quad (8-19)$$

$$\sigma_s(t) = \frac{A_b E_b}{A_s} \varepsilon_T(t) \quad (8-20)$$

Thus the stress, strain and strain rate of the sample can be determined from the known bar properties and recorded strain gauge signals. From equation (8-19), it can be seen that the maximum strain achieved is a function of the reflected strain wave duration and amplitude.

For high strain rate tensile tests, the apparatus set up is slightly different. A schematic of the apparatus as adopted from (Isakov et al., 2014) is presented in Figure 8.4. The tensile SHPB is comprised of a striker tube, an incident bar and a transmitted bar. Upon impacting the flange, the striker creates an elastic tensile wave in the incident bar. As the incident wave reaches the end of the bar, a portion is reflected, with the remainder being transmitted through the sample into the transmitted bar (Nemat-Nasser et al., 1991). The three strain-time histories of the elastic waves are recorded with strain gauges on each bar. The stress-strain calculation is performed using the same relations as discussed for the compression test.

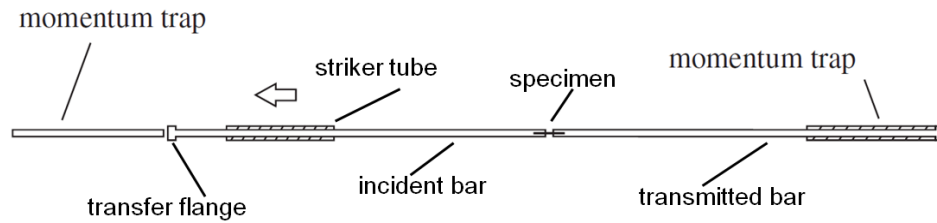


Figure 8.4: A schematic of the tension Split Hopkinson Pressure Bar (Isakov et al., 2014). The arrow indicates the direction in which the striker tube moves.

8.4 SHPB data analysis - Assumptions

Before discussing the assumptions, another important factor that needs to be taken in to consideration is the specimen geometry. As the apparatus is made out of slender bars, the ‘machine’ stiffness of SHPB is quite low as compared to conventional universal testing machines. Thus the specimen size plays a crucial role in the response. While choosing the specimen design two aspects are considered to be important: minimizing friction and reducing inertia effects. The optimal specimen design, which minimizes errors due to inertia as well as friction effects, is the one which minimizes the areal mismatch between the specimen and the bar and have a specimen aspect ratio (L/D) between 0.5 and 1.0 (Davies and Hunter, 1963; G. T. Gray, 2000).

Several assumptions were made for the analysis described in the previous section and these assumptions must be validated to be used for a split Hopkinson bar test (Gama et al., 2004; G.T. Gray, 2000). First, the specimen was assumed to be at equilibrium during the experiment. This means that the sample is in a uniform stress state. One method which is used to determine if dynamic equilibrium is achieved is to compare the force history in the incident and transmitted

bars. If the forces are approximately equivalent then equilibrium is said to exist (Song and Chen, 2005).

Davies and Hunter (1963) established that equilibrium is achieved after a "ring-up time" when the loading pulse travels back and forth inside the specimen more than π times. As this ring-up time is necessary prior to being able to analyze the experimental data, the elastic behavior of the specimen and its yield strength cannot be determined for dynamic tests. Several techniques have been used to reduce the ring-up time. One of them is to reduce the size of the specimen, as its length is proportional to the ring-up time (Gama et al., 2004). Another method is to increase the rise time of the incident pulse. This is done by using a "pulse shaper", which consists in placing a soft metal shim between the incident bar and the striker (G.T. Gray, 2000). Figure 8.5 shows the variation of strain rate for tests with and without a pulse shaper. The pulse shaper used is a disc of 10 mm diameter and 1 mm length, cut from AA1100 alloy. The test where a pulse shaper is used shows a gradual rise in the strain rate and once it reaches the maximum value, it remains constant throughout straining. Another noteworthy feature is that the high frequency oscillations that are present when no pulse shaper is used, is eliminated.

Another assumption made during the split Hopkinson bar analysis is that there are only longitudinal waves propagating in the axial direction of the bar. During an actual impact between the striker and the incident bar, several types of waves, such as spherical or surface waves, are generated and propagate at different velocities in every direction (Meyers, 1994). Davies (Davies, 1948) applied the solution to elastic wave propagation in an infinitely long cylinder to SHPB and found that the assumption is valid after 10 diameters distance along the length of the bar. Therefore, if the incident bar is long enough, the stress wave can be considered as a 1D wave. Finally, a comparison between data collected at University of Virginia (UVa), Mississippi

State University and Army Research Laboratory (ARL) for the same material (7085-T711-TD) is shown in Figure 8.6, which show the consistency and reproducibility of the results.

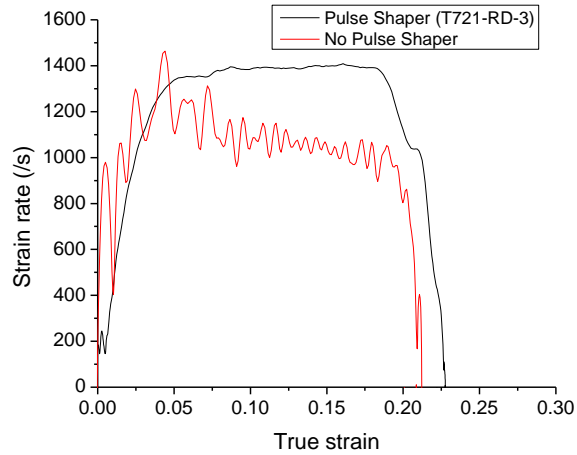


Figure 8.5: The variation of strain rate with strain for tests with and without a pulse shaper, showing constant strain rate as well as high frequency oscillations are eliminated when a pulse shaper is used.

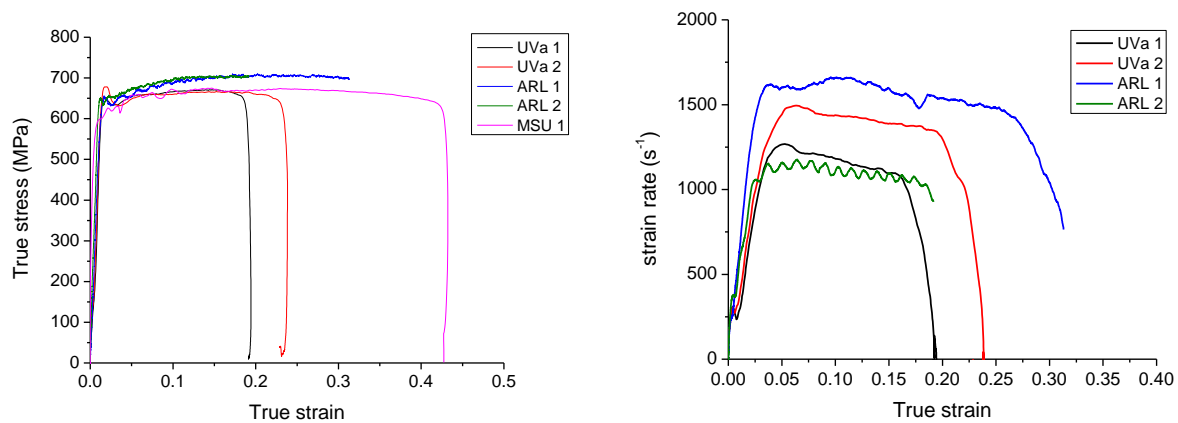


Figure 8.6: Dynamic test results for AA7085-T711 along TD obtained at UVa, MSU and ARL (a) Flow curves (b) strain rate as a function of strain.

8.5 References

- Davies, E.D.H., Hunter, S.C., 1963. The dynamic compression testing of solids by the method of the split Hopkinson pressure bar. *J. Mech. Phys. Solids* 11, 155–179. doi:10.1016/0022-5096(63)90050-4
- Davies, R., 1948. A critical study of the Hopkinson pressure bar. *Philos. Trans. R. Soc. London. Ser. A, Math. Phys. Sci.* 240, 375–457.
- Gama, B.A., Lopatnikov, S.L., Gillespie, J.W., 2004. Hopkinson bar experimental technique: A critical review. *Appl. Mech. Rev.* 57, 223. doi:10.1115/1.1704626
- Gray, G.T., 2000. Classic Split-Hopkinson Pressure Bar Testing. Mater. Park. OH ASM Int. 2000. 462–476.
- Gray, G.T., 2000. Classic Split-Hopkinson Pressure Bar Testing. Mater. Park. OH ASM Int. 2000.
- Isakov, M., Hiermaier, S., Kuokkala, V., a, P.T.R.S., 2014. Improved specimen recovery in tensile split Hopkinson bar. doi:10.1098/rsta.2013.0194
- Meyers, M.A., 1994. *Dynamic Behavior of Materials*. John Wiley & Sons.
- Nemat-Nasser, S., Isaacs, J.B., Starrett, J.E., 1991. Hopkinson Techniques for Dynamic Recovery Experiments. *Proc. R. Soc. A Math. Phys. Eng. Sci.* doi:10.1098/rspa.1991.0150
- Song, B., Chen, W., 2005. Split Hopkinson pressure bar techniques for characterizing soft materials 2, 113–152.